Gas Phase Infrared Photodissociation Spectroscopy of Mass-Selected Ionic Clusters:

Metal Oxides and Microhydrated Anions

Am Fritz-Haber-Institut
der Max-Planck-Gesellschaft
entstandene und

im Fachbereich Physik
der Freien Universität Berlin
eingereichte Dissertation
von

Torsten Wende

Berlin, 2012

Zusammenfassung

Der zentrale Schwerpunkt dieser Arbeit ist die Strukturaufklärung von Metalloxidclustern im Rahmen des Sonderforschungsbereiches 546 „Struktur, Dynamik und Reaktivität von Übergangsmetalloxid-Aggregaten" (1999–2011). Das Ziel des SFB 546 war die Entwicklung eines tieferen Verständnisses der Zusammenhänge zwischen Struktur und Reaktivität in katalytischen Systemen. Ein weiterer Schwerpunkt dieser Arbeit ist die Charakterisierung des Solvatisierungsverhaltens von Anionen in Wasserclustern auf molekularer Ebene, indem schrittweise einzelne Wassermoleküle an das zu untersuchende Anion angelagert werden. Um Einblicke in die Clusterstruktur zu gewinnen, werden Schwingungsspektren von massenselektierten, geladenen Clustern in der Gasphase mithilfe der Infrarot-Photodissoziationsspektroskopie (IR-PD) gemessen (Kapitel 1.3). Die Kopplung eines Ionenfalle-Tandemmassenspektrometers (Kapitel 2) mit dem freien Elektronenlaser *FELIX* erlaubt es, Schwingungsspektren von gekühlten Ionen in einem breiten spektralen Bereich zu messen (100–4000 cm^{-1}). Die folgende Strukturzuordnung beruht auf einem Vergleich zwischen experimentellen und simulierten Spektren verschiedener Isomere, die mit quantenchemischen Methoden berechnet werden.

Zur Strukturuntersuchung der Metalloxidcluster wird die Botenatommethode angewendet, bei der ein schwach gebundenes Edelgasatom als Sonde zur Messung der Molekülschwingungen dient (Kapitel 1.3). Trotz ihrer Reaktionsträgheit können Edelgasatome die Struktur des Clusters beeinflussen. Am Beispiel der Vanadiumoxidcluster $V_3O_{6-8}{}^+$ (Kapitel 3) wird gezeigt, dass die Wechselwirkung zwischen dem Ion und dem Edelgasatom, je nach Art des Botenatoms zu einer Änderung der energetischen Reihenfolge der Isomere führen kann. Die Untersuchung zeigt weiterhin, dass die Beiträge mehrerer Isomere in einem Schwingungsspektrum isoliert werden können, indem die Anzahl der bindenden Edelgasatome systematisch variiert wird.

Die ersten Schwingungsspektren von Cer enthaltenden Gasphasenclustern wurden gemessen. Diese Spektren ermöglichen eine Bewertung verschiedener Dichtefunktionale hinsichtlich ihrer Beschreibung lokaler Ce-4f Zustände. Diese Studie zeigt, dass sogar kleine Cluster mit 2–5 Ceratomen bereits festkörperähnliche Eigenschaften aufweisen. Die geometrischen Strukturen von Ceroxidclustern (Kapitel 4) stellen nur leicht modifizierte Fragmente der Ceroxidoberfläche dar und sind daher interessante Systeme für zukünftige Reaktivitätsstudien, um katalytische Prozesse auf Ceroxidoberflächen nachzubilden. In den gemischten Metalloxidclustern $[(CeO_2)(VO_2)_2]^+$ und $[(Ce_2O_3)(VO_2)]^+$ werden die Ce-Atome und nicht die V-Atome bevorzugt reduziert (Kapitel 5). Dies unterstützt die Annahme, dass die hohe Reduzierbarkeit von Ce^{+4} entscheidend ist für die fördernde Rolle von Ceroxid als Trägermaterial in Vanadiumoxidkatalysatoren.

Die Kombination aus IR-PD Spektroskopie und Moleküldynamiksimulationen erlaubt es, die Zusammenhänge zwischen Konformationsänderungen von Dicarboxylatdianionen in Wasserclustern und den zugehörigen spektroskopischen Merkmalen systematisch zu studieren (Kapitel 6). Die relativen Intensitäten der symmetrischen (ν_S) und antisymmetrischen (ν_A) Carboxylatstreckschwingungen stellen empfindliche Messsonden für die Konformation der Dianionen dar. Die schrittweise Anlagerung einzelner Wassermoleküle an das nackte Dianion führt zu einem Konformationsübergang von einer linearen zu einer gefalteten Struktur, sobald eine kritische Clustergröße erreicht ist. Diese Konformationsänderung äußert sich in einem deutlichen Intensitätseinbruch der ν_S Absorptionsbande. Der Konformationsübergang wird sowohl durch die Größe des Wasserclusters als auch durch die Kettenlänge der Dianionen bestimmt. Die Studie zeigt, dass die gefalteten Strukturen durch Bildung zusätzlicher H-Brücken zwischen dem Dianion und den Wassermolekülen stabilisiert werden.

Summary

The central goal of the present thesis is the structural characterization of metal oxide clusters in the framework of the *Dedicated Research Center "Structure, Dynamics and Reactivity of Transition Metal Oxide Aggregates"* (SFB 546, 1999–2011), funded by the German Research Foundation. The SFB 546 aimed at developing a detailed understanding of the relationships between structure and reactivity in catalytic systems. A second goal of this thesis is the characterization of the solvation behavior of anions in water clusters at the molecular level, one water molecule at a time. In order to gain insights into the cluster structure, vibrational spectra of mass-selected gas phase cluster ions are measured by way of infrared photodissociation (IR-PD) spectroscopy (Chapter 1.3). The use of an ion trap–tandem mass spectrometer (Chapter 2) combined with the Free Electron Laser for Infrared eXperiments *FELIX* (The Netherlands), allows for the measurement of vibrational spectra of cryogenically-cooled ions over a wide spectral range (100–$4000 \, \text{cm}^{-1}$). The subsequent structural assignment is based on a comparison between experimental and simulated spectra of different isomers derived from quantum chemical calculations.

The structures of metal oxide clusters are investigated using the messenger atom technique, where a weakly bound rare gas atom is used as a probe to measure a vibrational spectrum of the cluster ion (Chapter 1.3). Although rare gas atoms are chemically inert, they can have an influence on the structure of the cluster ion. The study of vanadium oxide clusters $V_3O_{6-8}^+$ (Chapter 3) demonstrates that the interaction between a rare gas atom and the ion can change the energetic ordering of the isomers, depending on which rare gas atom is used. It is also shown that the contributions from multiple isomers to the vibrational spectrum can be isolated by systematically varying the number of rare gas atoms attached to the cluster.

The first vibrational spectra of gas phase cerium-containing clusters are presented. The spectra represent ideal benchmarks for assessing the applicability of different density functionals, which differ in the description of localized Ce-4f states. The study reveals that even small clusters with 2–5 cerium atoms have properties similar to the bulk. The geometric structures of cerium oxide clusters $Ce_mO_n^+$ (Chapter 4) represent only "slightly modified" fragments of bulk ceria, making them interesting systems for reactivity studies to mimic catalytic processes on ceria surfaces. In the mixed metal oxide clusters $[(CeO_2)(VO_2)_2]^+$ and $[(Ce_2O_3)(VO_2)]^+$ the cerium atoms are preferentially reduced (Chapter 5). This key finding supports that the high reducibility of Ce^{+4} accounts for the promoting role of ceria in supported vanadium oxide catalysts.

The combination of IR-PD spectroscopy with molecular dynamics simulations allows for the systematic study of the relationships between conformational changes of dicarboxylate dianions ^-OOC–$(CH_2)_m$–COO^- in water clusters and the corresponding spectroscopic features (Chapter 6). The relative intensities of the symmetric (ν_S) versus antisymmetric (ν_A) carboxylate stretching modes represent a sensitive probe for the conformations of the dianions. The addition of water molecules to the dianion, one at a time, leads to a conformational transition from a linear to a folded structure, once a critical solvent number is reached. The conformational change is reflected in a significant drop of the ν_S band intensity. The conformational transition depends on the solvent number as well as on the chain length of the dianions. The study shows that the stability of the folded conformation is attributed to the formation of additional solute-solvent (rather than solvent-solvent) hydrogen bonds in the cluster.

Contents

Abbreviations

ADE adiabatic detachment energy.

CID collision-induced dissociation.

CRDS cavity ring-down spectroscopy.

CT charge transfer.

DFM difference frequency mixing.

DFT density functional theory.

ESI electrospray ionization.

FEL free electron laser.

FELIX free electron laser for infrared experiments.

FWHM full width at half maximum.

HBs hydrogen bonds.

HREEL high resolution electron energy loss.

IR infrared.

IR-MPD infrared multiple photon dissociation.

IR-PD infrared photodissociation.

IR-VPD infrared vibrational predissociation.

IVR intramolecular vibrational relaxation.

MCP multichannel plate.

MD molecular dynamics.

MPE multiple photon excitation.

ODH oxidative dehydrogenation.

PES photoelectron spectroscopy.

QC quantum chemical.

RET ring electrode trap.

RF radio frequency.

TMP turbomolecular pump.

TOF time-of-flight.

TOF-MS time-of-flight mass spectrometer.

Introduction

The central aim of the work presented in this thesis is the structural investigation of ionic clusters in the gas phase, using a combination of modern spectrometric and spectroscopic techniques. Gas phase studies allow for characterizing the properties of clusters under well-defined conditions. The intrinsic properties and their evolution with cluster size can be investigated in the absence of any perturbing interaction with an environment. Beyond that, the interaction of a particle with its environment can systematically be studied, e.g, by adding solvent molecules in a stepwise fashion, typically referred to as microsolvation. The clusters investigated in this thesis contain a countable number of atoms, from just a few up to hundred atoms. At these sizes every individual atom contributes to the properties of the cluster, i.e., its properties can significantly change upon addition or removal of a single atom or molecule. Moreover, the cluster properties lie in the *non-scalable* regime meaning that they cannot be derived from properties of larger particles. Clusters are thus extensively studied to unravel how physical and chemical properties emerge from a single atom or molecule to macroscopic particles [1–4].

We apply infrared (IR) spectroscopy (Chapter 1) in order to characterize the structure of mass-selected cluster ions in the gas phase. With this method, structural information of a molecule is obtained by studying its vibrational properties using IR radiation. However, the densities of mass-selected ions are rather low and, thus, a special experimental approach, referred to as infrared photodissociation (IR-PD) spectroscopy (Chapter 1.3), is employed to measure vibrational spectra of gas phase ions. Several technical tools and devices are essential in order to perform the experiments. The setup consists of a tandem mass spectrometer (Chapter 2) that serves to produce, mass-select and thermalize the cluster ions as well as to probe their molecular vibrations. The latter is achieved by combining the spectrometer with an intense, tunable IR light source, e.g., a free electron laser (FEL).

Most of our experiments were carried out at the FOM Institute for Plasma Physics Rijnhuizen (Nieuwegein, The Netherlands) using the free electron laser *FELIX* (Chapter 2.5). To this end, the instrument and its experimental equipment were transported to the FELIX user facility. The results described in the present thesis comprise two topics: the structures of transition metal oxide clusters (Chapters 3–5) and the microhydration of negative ions (Chapter 6). The following sections aim at giving a general overview of both topics.

Structures of Transition Metal Oxide Clusters

Transition metal oxides exhibit a pronounced variability in their structure and chemical reactivity. Metal oxide aggregates are thus extensively used as building blocks for nanostructured materials important for many technical applications, e.g., nanosensors [5], coatings [6] or fuel

cells [7]. Nanomaterials are especially relevant in heterogeneous catalysis [8–11]. The development of new and more efficient catalysts represents a central goal in this field. This is due to the fact, that catalysts are essential in many industrial processes. For instance, the production of many chemicals and drugs involves catalytic processes. Catalysts are also indispensable in areas like environmental protection and renewable energy generation (e.g. fuel cells).

Among the transition metals, vanadium plays an important role in metal oxide catalysis [12]. Vanadium oxide based catalysts are used in the synthesis of important chemicals. A prominent example is sulfuric acid, H_2SO_4, which is one of the most produced chemicals in the world. Furthermore, vanadium oxides are also used in the purification of exhaust gases arising from power plants.

Although vanadium oxide catalysts are extensively used in the chemical industry, many of their microscopic properties are still not well understood. However, understanding catalytic processes at the molecular level is essential in order to develop tailored catalysts. Metal oxide catalysts are complex systems whose activity and selectivity depend on many parameters, in particular on the surface properties. Typically, nano-sized aggregates of the active metal oxide are deposited on the surface of oxide supports, such as silica (SiO_2), alumina (Al_2O_3), titania (TiO_2) or ceria (CeO_2). Using nanoparticles as the active species is advantageous, because their large surface-to-volume ratio yields higher activities. Furthermore, the deposited aggregates are not necessarily uniform but differ with respect to size and composition. In fact, irregular surfaces and defects are assumed to be crucial for obtaining high activities. Thus, several questions arise, for example, what are the structural properties of the deposited particles? Which structures yield particularly high reactivities? The efficiency of the catalyst also depends on the properties of the support material, generally referred to as the *metal oxide–support effect*. The exact origin and mechanism of this effect are still under debate. Does the support stabilize certain structures of the active species or does it actually participate in the catalytic reaction?

It remains challenging to elucidate such complex correlations directly from investigations on real catalysts with currently available surface science techniques. Instead, well-defined model systems are suitable to specifically investigate the intrinsic properties and interactions of a catalytic system. These tasks were addressed within the DFG-funded *Dedicated Research Center SFB 546 "Structure, Dynamics and Reactivity of Transition Metal Oxide Aggregates"* (1999–2011). The SFB 546 aimed at delevoping a detailed understanding of the relationship between structure and reactivity of transition metal oxide aggregates. Due to their relevance in heterogeneous catalysis, the SFB 546 focused on the characterization of vanadium oxide systems, from gas phase clusters to thin films and real catalysts. The present thesis evolved as part of the sub-project A3 *"Clusters in the Gas Phase"*.

At the beginning of the SFB 546, a generally applicable method was developed to identify the structure of mass-selected gas phase clusters. This method relies on the synergy of experimental and theoretical investigations. The combination of a tandem mass spectrometer and the free electron laser FELIX allows for measuring IR spectra of mass-selected clusters with high sensitivity. This experimental technique was developed and optimized in our group [13]. The comparison between experimental and simulated vibrational spectra allows for assessing quantum chemical (QC) calculations and assigning geometric structures. Based on this method, structural motifs of vanadium oxide clusters, aluminum oxide clusters as well as binary vanadium/titanium oxide clusters were successfully identified [14–23]. The structural investigations of metal oxide clusters are conducted in close collaboration with the Quantum Chemistry group of Prof. Joachim Sauer (Humboldt Universität zu Berlin), in which density

functional theory (DFT) calculations are performed.

Following the initial comprehensive studies of metal oxide clusters, the primary focus of the present thesis lies on the structural characterization of vanadium oxide clusters, cerium oxide clusters as well as mixed vanadium/cerium oxide clusters in the gas phase. Cerium oxide is one of the most reactive rare earth metal oxides and plays an important role in many catalytic applications. It is commonly used as a support material for metals and metal oxides in heterogeneous catalysis. As already mentioned above, the support is generally not chemically inert, but can have an effect on the catalytic reaction. Among all typical support materials, ceria has a pronounced ability to directly participate in catalytic processes [24]. For example, the dehydrogenation of propane to propene is observed to be particularly efficient when vanadium oxide is supported on ceria [25]. The reactivity of ceria is connected to its chemical reducibility, i.e., the interplay between the oxidation states Ce^{4+}/Ce^{3+}. Vanadia supported on ceria represents thus a prototypical system to study the metal oxide–support effect. However, the description of localized Ce-4f states is challenging. In this regard, vibrational spectroscopy on gas phase clusters can contribute to assess QC methods.

Throughout this thesis, the so-called *messenger atom technique* (Chapter 1.3) is applied in order to investigate the structures of metal oxide clusters. This method involves the formation of a weakly bound ion-rare gas atom complex, where the rare gas atom serves as a probe to measure a vibrational spectrum of the cluster ion. This experimental approach is a key method to obtain well-resolved IR spectra. Although rare gas atoms are chemically inert, the ion-rare gas atom interaction may influence the vibrational spectrum of the cluster ion. The investigation of trinuclear vanadium oxide clusters $V_3O_{6-8}{}^+$ exemplifies how the presence of a messenger atom can affect the structure of the cluster ion. The geometric structures of $V_3O_{6-8}{}^+$ are markedly messenger-dependent, which is shown in Chapter 3.

Chapter 4 addresses the structural characterization of cerium oxide cluster cations $Ce_mO_n{}^+$ ($m = 1$–5). The IR spectra of mass-selected cluster ions are measured as a function of size and stoichiometry. This study is the first spectroscopic investigation of cerium oxide clusters in the gas phase. The experimental vibrational frequencies, extracted from the IR spectra, are used as benchmarks to test different DFT calculations. This combined experimental-computational study allowed for an unambiguous assignment of the geometric structures, demonstrating that even small clusters with 2–5 cerium atoms have structural properties reminiscent of the bulk ceria. Based on these results, binary metal oxide clusters $(CeO_2)(VO_2)^+$, $(CeO_2)(VO_2)_2{}^+$ and $(Ce_2O_3)(VO_2)^+$ are studied to mimic the active site–support effect in the gas phase. The clusters have a tailored electronic structure. The first cluster contains no electron in either the Ce-f or V-d orbitals. As the number of valence electrons is increased, the question arises, which orbital the additional electrons prefer, i.e., is vanadium or cerium preferentially reduced? The corresponding results are the subject of Chapter 5.

Identifying Binding Motifs in Hydrated Ions

There is a lively interest involving many branches of the physical sciences, to develop a detailed understanding of how ions are solvated in water at the molecular level. When salt molecules, for instance table salt (NaCl), are mixed with water, they undergo dissolution. The NaCl molecules dissociate into oppositely charged ions, namely Na^+ cations and Cl^- anions, which become surrounded by shells of water molecules. Another example are acid molecules, e.g., sulfuric acid (H_2SO_4), which dissociate into protons H^+ and conjugate base anions $HSO_4{}^-$

$$NO_3^-(H_2O)_3 \qquad NO_3^-(H_2O)_4 \qquad HCO_3^-(H_2O)_3 \qquad SO_4^{2-}(H_2O)_{12}$$
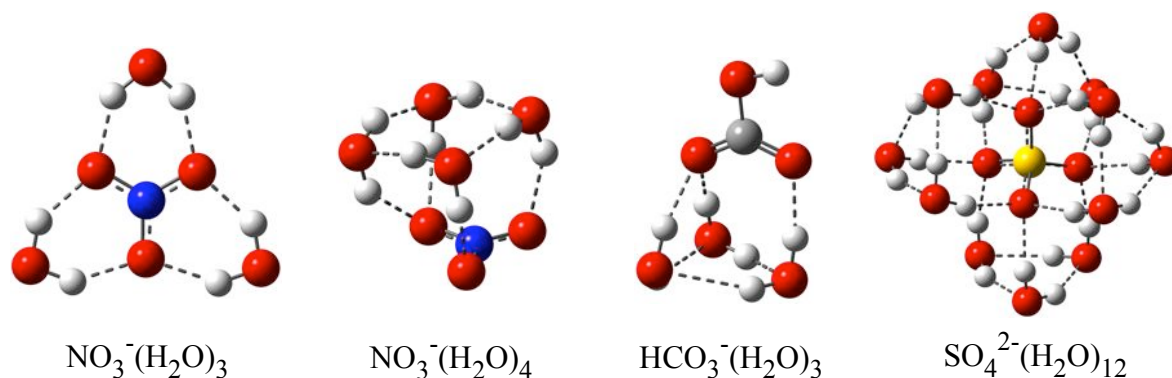
Figure 1: Characteristic structural motifs of microhydrated nitrate (NO_3^-), bicarbonate (HCO_3^-) and sulfate (SO_4^{2-}) anions determined in our group.

and SO_4^{2-}. What is the origin of this process? It lies in the strong polarity of water molecules, which results in their ability to form hydrogen bonds (HBs) with polar molecules and ions. The hydration shell is formed due to energetic reasons, because the ion-water HBs are stronger than the water-water HBs. The properties of the hydrated ions differ from those of the unsolvated ions and depend on the structure of the surrounding hydration network. A molecular-level understanding of ion hydration is thus important to elucidate chemical processes. For instance, potassium channels are present in the cell membranes of all living organisms. These channels only respond to hydrated K^+ ions and thus control the K^+ concentration inside the cell. The channel mimics the hydration shell of K^+ ions such that only these specific ions can pass the channel [26, 27]. Ion hydration plays also an important role in atmospheric chemistry. Hydrated molecular ions like nitrate (NO_3^-) and sulfate (SO_4^{2-}) are typical constituents of aerosol particles in the troposphere that originate from natural and anthropogenic processes [28, 29]. These ions can be formed by dissolution of adsorbed acid molecules, HNO_3 or H_2SO_4, on the aerosol surface. Such aerosol particles strongly influence the earth's climate, promoting cloud formation or chemical reactions important for many atmospheric cycles. The chemical properties are primarily governed by the nature of the aerosol surface. The question remains how the water molecules are coordinated around the ions? Are they present on the surface or inside the aerosol particle?

It is difficult to extract detailed microscopic information directly from IR spectroscopy on bulk solutions or vapor/water interfaces. A solution contains many different ions which interact with each other and the water molecules. Spectroscopy on solutions therefore probes an average of many solute-solute and solute-solvent interactions. Furthermore, the ions are already fully hydrated and influences of a single water molecule in the hydration shell cannot be extracted. Gas phase vibrational spectroscopy on size-selected ion-water complexes, on the other hand, allows characterizing the solute-solvent and solvent-solvent interactions at the molecular level in a stepwise fashion, one water molecule at a time. The electrospray technique allows transferring hydrated ions from solution into the gas phase without fragmentation. The source conditions can be carefully adjusted in order to control the degree of hydration, from the bare ion to ions with many water molecules. The tandem mass spectrometer aids to mass-select a hydrated complex of interest which is then isolated and spectroscopically probed.

A primary focus in our group is the structural investigation of microhydrated conjugate base anions [30–37]. These investigations are accomplished in close collaboration with the

group of Prof. Dan Neumark (University of California, Berkeley). These studies address several questions, e.g., how many water molecules comprise the first hydration shell? Are the ions symmetrically or asymmetrically hydrated? How is the geometric structure of the ion influenced by the presence of the hydrogen-bonded network? The hydration motifs strongly depend on the interplay between the ion-water and water-water interactions. Figure 1 illustrates some identified binding motifs of microhydrated nitrate, bicarbonate (HCO_3^-) and sulfate ions. In the $NO_3^- \cdot (H_2O)_3$ complex, the nitrate ion is symmetrically surrounded by three water molecules. Surprisingly, this hydration motif significantly changes when just a single water molecule is added to the complex. A small water network composed of a four-membered water ring is formed representing a particularly stable motif (Figure 1) [32]. Although the bare bicarbonate ion has a similar geometric structure compared to nitrate, different binding motifs are observed. In contrast to nitrate, the first three water molecules asymmetrically solvate bicarbonate forming a stable three-membered water ring at the CO_2 moiety (Figure 1) [33]. The results suggest that both ions, nitrate and bicarbonate, prefer surface solvation. In contrast, in microhydrated sulfate dianions the number of ion-water HBs is maximized over the water-water hydrogen bonding. As a consequence, sulfate dianions prefer to be internally solvated, illustrated for the complex $SO_4^{2-} \cdot (H_2O)_{12}$ in Figure 1 [38, 39]. These results exemplify that the evolution of the hydration shell strongly depends on the nature of the solvated anion.

The microhydration of molecular anions can also affect their stability or conformation. In this regard, multiply charged anions are particularly interesting species. For instance, the isolated SO_4^{2-} ion is unstable in the gas phase and decays via electron loss on the nanosecond time scale [40, 41]. This is due to the strong, repulsive Coulomb interaction between the excess charges. However, SO_4^{2-} can be stabilized by the presence of three or more water molecules [42]. Hence, it is the environmental stabilization which accounts for the presence of sulfate dianions in the atmosphere.

The second part of this thesis addresses the structural investigation of microhydrated dicarboxylate dianions $^-OOC-(CH_2)_m-COO^-$. These dianions consist of two charged carboxylate groups which are separated by a hydrophobic, aliphatic chain. Since both charge centers are separated, these dianions are stable in the gas phase. These systems allow for a systematic investigation of the intramolecular Coulomb repulsion, because the charge separation can be controlled by the chain length [43, 44]. Furthermore, dicarboxylate dianions serve as model systems to study solvent-mediated effects. Chapter 6 focuses on the investigation of solvent-induced conformational changes, which is conducted in collaboration with the group of Prof. Angel Rubio (Universidad del País Vasco, Spain). In the unsolvated dianions both charge centers repel each other resulting in a linear conformation of the molecule. With increasing level of hydration, both negative charge centers become solvated leading to charge screening. In larger solvated clusters the solute-solvent and solvent-solvent interactions can be sufficiently strong to overcome the Coulomb repulsion. At this point, a conformational transition can occur.

Chapter 1

Infrared Spectroscopy

IR spectroscopy is a widely used method that probes molecular vibrations allowing to determine the structure of molecules. Throughout this thesis IR photodissociation spectroscopy is employed to investigate molecular vibrations of mass-selected ions in the gas phase. This chapter aims at describing the theoretical concepts of this experimental technique. It begins with a brief introduction in the theory of molecular vibrations (Section 1.1). Section 1.2 addresses the question how IR spectra of mass-selected ions can be generally obtained. This leads to the concept of action spectroscopy involving IR photodissociation as one established approach. Within the present thesis, the photodissociation experiments are classified into (i) IR multiple photon dissociation and (ii) IR vibrational predissociation. The underlying mechanisms of both methods are qualitatively described in Section 1.3. In the last part some general remarks on the structural assignments based on quantum chemical calculations are given.

1.1   Vibrational Modes

The vibrational properties of a molecule are directly correlated to its structure, because they are sensitive to the chemical composition and properties of the intramolecular bonds (bonding strengths, lengths and angles). A vibrational spectrum thus represents a unique *fingerprint* that allows distinctly identifying a molecule or molecular group. In total, a polyatomic molecule consisting of N atoms has $3N - 6$ vibrational degrees of freedom ($3N - 5$ for linear molecules). The vibrations of the atoms in the molecule are completely governed by the molecular potential V which contains information about the interactions between the atoms. An exact description of the forces acting between the atoms is usually not possible. For many molecules the *harmonic approximation* proves to be satisfactory to theoretically describe the vibrations of the system. Within this approach the intramolecular bonds are considered to be completely elastic, i.e., all atoms undergo small harmonic oscillations around their equilibrium position obeying *Hooke's law*. From a mathematical point of view, the molecular potential V is expanded in a Taylor series around the equilibrium position of the atoms [45]. In the harmonic approximation only the second order terms are considered yielding

$$V \cong \frac{1}{2} \sum_{i,j}^{3N-6} \left. \frac{\partial^2 V}{\partial \xi_i \partial \xi_j} \right|_0 \xi_i \xi_j, \tag{1.1}$$

where ξ_i represent the $3N - 6$ coordinates necessary to describe the vibrations of the system. The second derivatives of the potential correspond to the *force constants* which determine the motion of a single atom in the molecule subject to all its neighbors. The force constants are used to derive the vibrational frequencies of the molecule. The relation is particularly simple for a diatomic molecule. Here, the vibration is described by $V(\xi) = \frac{1}{2}k\xi^2$ and the vibrational frequency ν is obtained from the force constant k according to $k = (2\pi\nu)^2\mu$ where μ is the reduced mass. However, for polyatomic molecules the relation becomes more complex. Solving Newton's equations of motion, it can be shown that the $3N - 6$ vibrational degrees of freedom of a nonlinear molecule correspond to $3N - 6$ *independent* vibrational modes which are referred to as *normal modes* [45]. Each normal mode represents a simple harmonic oscillator with a characteristic frequency ν_i. It describes a concerted motion of many atoms in the molecule. Those atoms oscillate in phase with the same frequency ν_i but different amplitudes such that the center of mass of the molecule remains stationary. The oscillatory motion is described by a single coordinate, referred to as *normal coordinate*, which linearly depends on the atomic displacements Δx_j, Δy_j and Δz_j as well as the masses m_j ($j = 1, 2, \ldots, N$). A normal mode is usually illustrated by means of arrows indicating the relative displacements of the atoms. This is exemplified for the normal modes of the water molecule in Figure 1.2. A quantum mechanical treatment shows that the vibrational energy of a molecule is not continuously
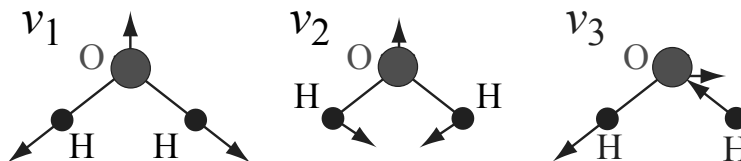
Figure 1.2: Normal modes of the water molecule H_2O: symmetric stretching mode (ν_1), water bending mode (ν_2) and antisymmetric stretching mode (ν_3). Picture adapted from Ref. [46].

variable but is quantized [45]. The energy levels of a normal mode are given by

$$E_i = h\nu_i \left(n_i + \frac{1}{2} \right) \qquad (i = 1, 2, \ldots, 3N - 6), \tag{1.2}$$

where h is Planck's constant, ν_i the vibrational frequency and n_i the vibrational quantum number which can have only integer values $(0, 1, 2, \ldots)$. As can be seen from Eq. (1.2), within the harmonic approximation all vibrational levels are equally spaced.

The vibrational modes of a molecule can be probed upon the interaction with electromagnetic radiation in the IR region. The molecule can absorb photons when the frequency of the radiation is in resonance with a normal mode which leads to transitions between the vibrational levels. Not all normal modes of a molecule are necessarily observed in an IR spectrum. An important criterion is that the dipole moment of the molecule changes along the normal coordinate. If this condition is fulfilled, a normal mode is called *IR active* otherwise it is referred to as *IR inactive*. For instance, all normal modes of H_2O shown in Figure 1.2 are IR active and can be observed in its IR spectrum. The more the dipole moment changes during the vibration, the more effectively the vibration is activated resulting in an intense IR absorption band. In mathematical terms, the absorption intensity is proportional to $|\partial M/\partial Q|^2$, the square of the change in dipole moment M with respect to the change in the normal coordinate Q [45]. Within the harmonic approximation transitions are allowed between adjacent vibrational levels of a single vibrational mode, that is the vibrational quantum number n_i can only change by one, $\Delta n_i = \pm 1$ [46].

Although the fundamental vibrational properties of molecules can often be understood within the harmonic approximation, it cannot account for all properties of real molecules, such as dissociation. The vibrations of real molecules are governed by an *anharmonic* potential owing to the anharmonic nature of real chemical bonds. For a diatomic molecule, the anharmonicity can be described by the empirical *Morse potential* [47] given by the formula

$$V = D_e \left[1 - e^{-\sqrt{\frac{k}{2D_e}}(R - R_e)} \right]^2. \tag{1.3}$$

The Morse potential function is illustrated in Figure 1.3. At small internuclear distances R the Coulomb repulsion of the nuclei dominates and the potential energy is high. At the equilibrium spacing R_e, the potential energy between the atoms is most attractive. However, when increasing the distances beyond R_e, the attractive force becomes zero leading to bond breaking at a dissociation energy D_e. The vibrational level spacing is no longer constant but decreases with increasing vibrational quantum numbers (Figure 1.3). The corrected energy levels are given by

$$E = h\nu \left(n + \frac{1}{2} \right) \left[1 - \chi_{anharm} \left(n + \frac{1}{2} \right) \right], \tag{1.4}$$

determined by the anharmonicity constant χ_{anharm} [46].

Due to anharmonicity, the normal modes in a polyatomic molecule are not independent anymore. They are coupled to each other which plays an important role in the photodissociation experiments used throughout in this thesis to probe molecular vibrations (Section 1.3).
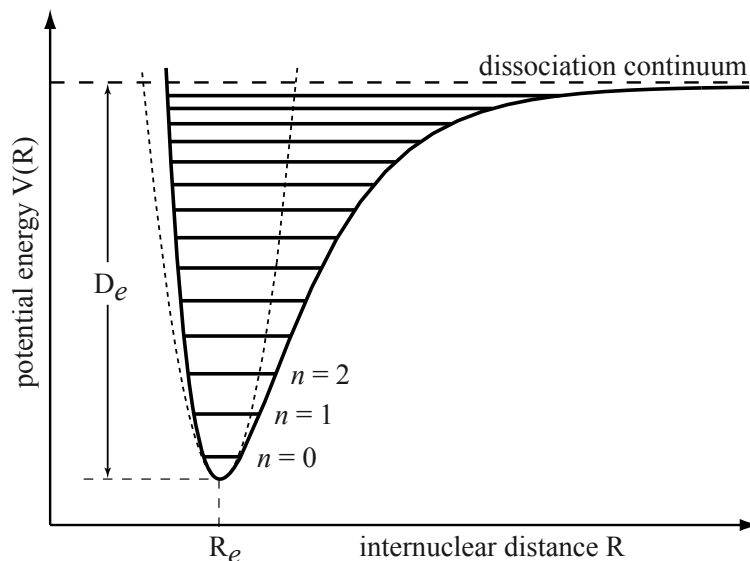
Figure 1.3: Potential energy of a diatomic molecule. The Morse potential function (solid line) adequately describes the anharmonic nature of the molecular potential. The harmonic oscillator potential function (dotted line) is only valid for small displacements from the equilibrium position R_e. The picture is adapted from Ref. [48].

1.2 Infrared Spectroscopy of Gas Phase Ions

Direct Absorption Spectroscopy. A common technique for recording vibrational spectra of molecules is direct absorption IR spectroscopy. This method allows for determining the frequency-dependent absorption cross section $\sigma(\nu)$ by measuring the attenuation of IR light. The absorption $I(\nu)/I_0(\nu)$ of the light intensity by the sample is described by *Lambert-Beer's law*

$$\frac{I(\nu)}{I_0(\nu)} = e^{-\sigma(\nu)\cdot n \cdot l}, \tag{1.5}$$

with the intensity of the incoming and transmitted light, $I_0(\nu)$ and $I(\nu)$, respectively, the density of absorbing particles n and the path length l. A general problem of direct absorption measurements in the gas phase concerns the limited sensitivity. Owing to the small IR absorption cross sections of gas phase molecules, rather high number densities ($\geq 10^{10}$ molecules/cm^3) are required for recording an absorption spectrum. The sensitivity can be enhanced when the absorption cell is placed inside an optical cavity allowing the light to pass the cell multiple times, referred to as cavity ring-down spectroscopy (CRDS) [49]. Casaes et al. employed IR CRDS to measure the ν_6 band of C_9 clusters in a supersonic molecular beam [50]. In these experiments, the minimum detectable particle density is estimated to be 10^9 molecules/cm^3.

Action Spectroscopy. In the present work, vibrational spectra of charged particles are investigated. The maximum number density of ions is usually limited to 10^6 ions/cm^3 which is close to the *space-charge limit* (10^8 ions/cm^3) [51]. These densities are generally too low for applying direct absorption measurements. Therefore, alternative methods are necessary for recording IR spectra of gas phase ions. With the increasing availability of intense and tunable IR laser systems, e.g, IR FELs and tabletop solid-state IR laser systems (Section

2.5), IR *action spectroscopy* has been established as an alternative approach. Rather than detecting the direct absorption of light, action spectroscopy relies on measuring the response of the molecule to photon absorption. Several processes can occur such as emission of photons (fluorescence), electrons (ionization) and fragments (dissociation).

1.3 Infrared Photodissociation Spectroscopy

IR-PD is the most commonly applied technique of action spectroscopy, in which the dissociation of molecules is monitored to measure their IR spectra. IR-PD spectroscopy has been employed throughout this thesis. In the following, an introduction to this experimental technique is given based on Ref. [14, 15, 52–55].

The IR-PD process is schematically described as follows,

$$AB^{+/-} \xrightarrow{n \cdot h\nu_{IR}} \left(AB^{+/-}\right)^* \longrightarrow A^{+/-} + B. \qquad (1.6)$$
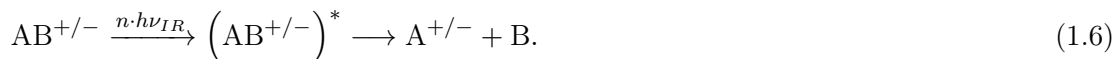
Parent ions of interest $(AB^{+/-})$ are irradiated with an intense IR laser pulse. When the laser is resonant with a fundamental vibrational transition the cluster starts absorbing photons of frequency ν_{IR}. Thereby the internal energy of the cluster increases. The number of absorbed photons n needed to induce fragmentation, typically depends on the specific dissociation threshold of the cluster. When the internal energy exceeds the dissociation threshold, the cluster dissociates leading to the formation of charged $(A^{+/-})$ and neutral fragments (B). The IR spectrum is derived by measuring the parent and fragment ion yield in dependence on the laser frequency. Owing to the great sensitivity of ion detectors, ions can be detected with nearly $100\,\%$ efficiency, which allows studying gas phase ions with low number densities.

Similar to Lambert-Beer's law (Eq. (1.5)), the ratio of the population $N\left(\nu\right)/N_0$ of the parent ion with and without IR radiation can be described by the following relation

$$\frac{N\left(\nu\right)}{N_0} \propto e^{-\sigma(\nu) \cdot F(\nu)} \qquad (1.7)$$

with the photon fluence $F\left(\nu\right)$ and the absorption cross section $\sigma\left(\nu\right)$ [55]. The relation (1.7) shows that the measurement of $\sigma\left(\nu\right)$ does not depend on the number density of ions but rather on the number of photons per cm^2, i.e. the fluence, in contrast to direct absorption measurements (see above).

1.3.1 Infrared Multiple Photon Dissociation

Since the IR photon energy is generally smaller than the dissociation energy of a molecule, several photons need to be absorbed to induce fragmentation. The underlying process is typically referred to as infrared multiple photon dissociation (IR-MPD). Its efficiency depends on the properties of the molecule, e.g., the size and initial internal energy, as well as on the properties of the light source. In particular, the vibrational excitation of a molecule is governed by the anharmonicity of the potential. For polyatomic molecules the IR-MPD mechanism is most commonly described by a sequential non-coherent absorption process which is divided into three (overlapping) regions: resonant region, quasi-continuum region and the dissociation region (Figure 1.4) [56].
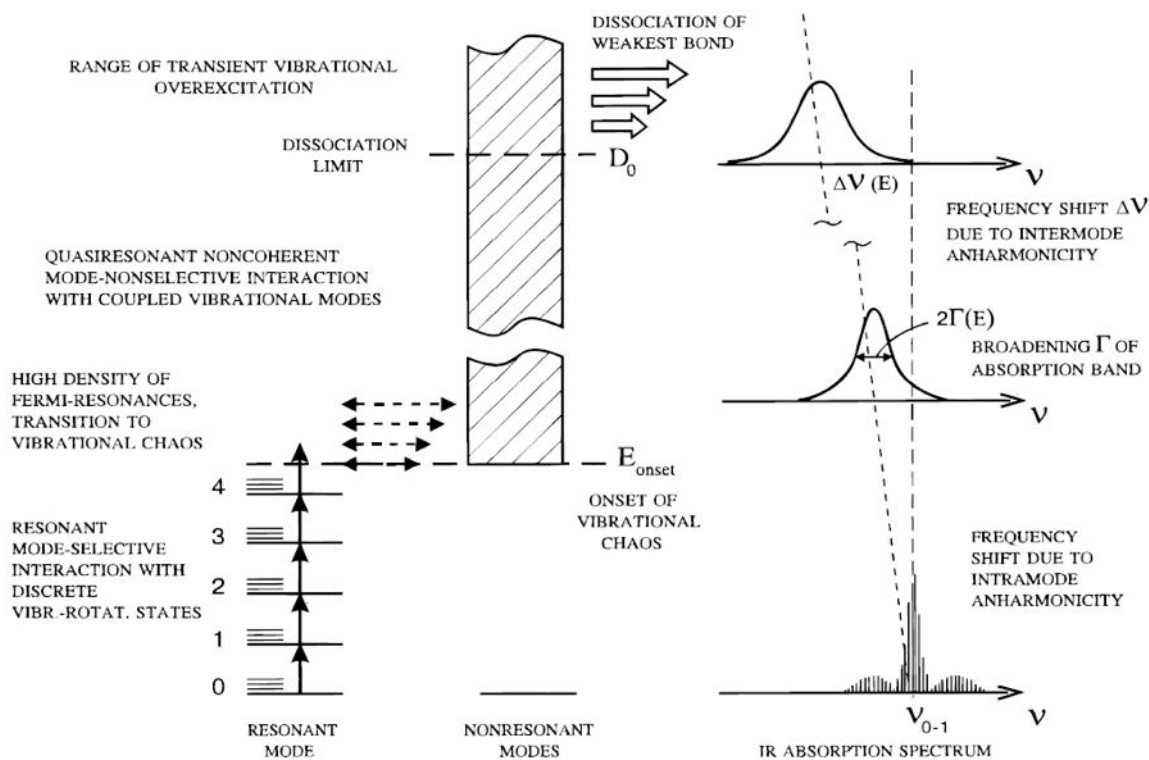
Figure 1.4: Main features of the mechanism underlying IR multiple photon excitation and dissociation of a polyatomic molecule. Reprinted with permission from Ref. [56]. Copyright (1998) American Chemical Society.

Resonant Region. The initial excitation of the molecule is governed by incoherent resonant absorption of multiple photons (left-hand side, Figure 1.4) involving vibrational transitions between the first discrete energy levels of a single vibrational mode ($n_i = 0 \rightarrow n_i = 1 \rightarrow n_i = 2 \rightarrow \ldots$). For polyatomic molecules, small anharmonic shifts of the vibrational levels can be compensated, for instance by the bandwidth of the laser or by changes in the rotational quantum number of the molecule. The latter is facilitated by the presence of many vibrational-rotational sublevels. Further absorption of photons in the resonant region can take place until the vibrational transitions are shifted out of resonance with the excitation range of the laser. At this point, the excitation is prevented which is referred to as the *anharmonicity bottleneck*. However, for many molecules the absorption of a few photons is already sufficient to reach the quasi-continuum of states.

Quasi-Continuum Region. The quasi-continuum region (middle, Figure 1.4) is characterized by a high density of rovibrational states $\rho(E_i)$ which is reached at high internal energies E_i of the molecule. As the internal energy increases, $\rho(E_i)$ roughly scales with E_i^K where K is the number of vibrational degrees of freedom [15]. Therefore, even small molecules containing only a few atoms can quickly reach a density of many states per cm^{-1} at internal energies of $>1000\,\text{cm}^{-1}$. Reaching the quasi-continuum of states is important in order to sustain the absorption of photons and further excite the molecule. As the molecule climbs up the vibrational ladder, the IR-excited vibrational mode can couple to other vibrational degrees of

freedom due to anharmonic coupling and the absorbed photon energy spreads throughout the molecule (indicated by broken arrows in Figure 1.4). The underlying mechanism is called *intramolecular vibrational relaxation* (IVR) and is fast at high densities of states. The population of the IR-excited vibrational mode is rapidly removed and the excited molecule escapes the anharmonic bottleneck, thus facilitating the absorption of more photons.

The IVR rate is an important parameter for the entire IR-MPD mechanism since it can limit the rate of photon absorption. To ensure efficient absorption of many photons, IVR has to proceed on a timescale that is shorter than the temporal width of the laser pulse. For polyatomic molecules the IVR process typically takes place on a timescale of 10^{-11}–10^{-12} s [52, 53]. For example, such IVR lifetimes are short compared to the macropulse length of FELIX ($5\,\mu$s) which is primarily used for the photodissociation experiments presented here.

Owing to the IVR mechanism the absorption transitions may be broadened (right-hand side, Figure 1.4). The line width ΔE of a transition depends on the lifetime Δt of the excited vibrational mode. Both units are related according to the Heisenberg relation $\Delta E \Delta t \approx \hbar$. For example, an IVR rate, $1/\Delta t$, of $10^{12}\,\mathrm{s}^{-1}$ corresponds to a line width of $\Delta E \approx 5.3\,\mathrm{cm}^{-1}$. For comparison, in the present experiments FELIX is typically operated using a spectral bandwidth of $\leq 10\,\mathrm{cm}^{-1}$. Thus, the observed line widths in these measurements are rather limited by the laser source.

Dissociation Region. In principle, the highly excited molecules can undergo different cooling processes including the emission of light (radiative cooling) and the emission of particles (evaporative cooling). In the latter case, the molecule can emit electrons (ionization) or neutral fragments (dissociation). Which of these competing cooling channels is experimentally observed depends on the properties of the molecule and its degree of excitation. The rate of photon emission approximately scales with E_i^4, according to the *Stefan-Boltzmann law*, and is the dominant cooling channel at lower internal energies. In contrast, at higher energies dissociation or ionization of the molecule will dominate because the corresponding rate constants grow exponentially with E_i [57]. For most molecules dissociation is much faster than the emission of electrons because their dissociation energy is lower than their ionization energy.

The relevant cooling channel of all molecular ions investigated in this thesis is dissociation via evaporation of neutral fragments. When the internal energy exceeds the dissociation energy, the molecule reaches the continuum of states (middle, Figure 1.4) and fragmentation becomes energetically allowed. Typically, the dissociation process involves breaking of the weakest bond in the molecule. However, at sufficiently high laser fluence several competing dissociative channels might open up. Even though the vibrational energy of the molecule has reached the dissociation threshold, the fragmentation is not necessarily observed in the experiment. In fact, similar to the IVR rate, the dissociation rate has to be compared to the experimental time window. In the present experiments, the timescale is basically determined by the interaction time with the IR radiation which is on the order of microseconds when FELIX is used. For the dissociation rate to fall into this experimental time window, the molecule has to be excited well above the dissociation threshold [53].

1.3.2   Example: Ion-Water Complexes

IR-PD of microhydrated ions is governed by multiple photon excitation (MPE). Thermal heating of these complexes typically results in evaporation of water molecules. The number of photons needed to break the ion-water or water-water bonds in the complex depends on the
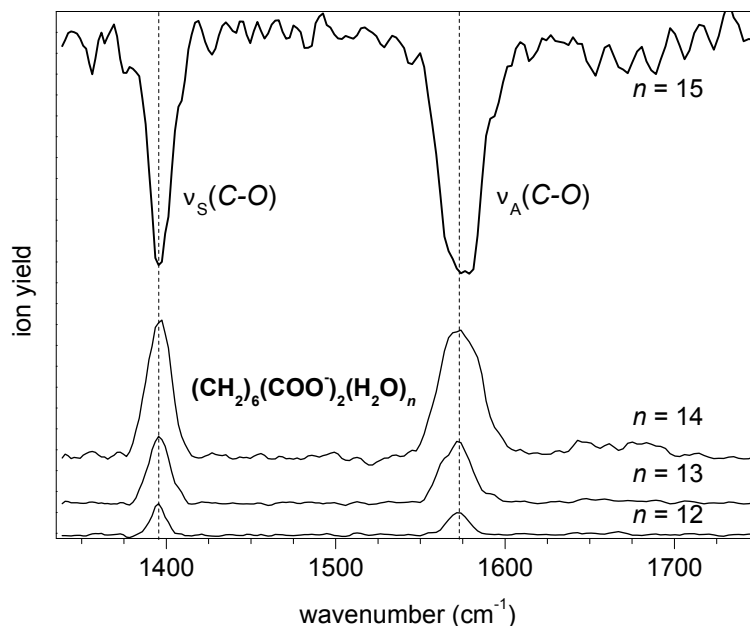
Figure 1.5: Stepwise evaporation of water molecules in microhydrated suberate dianions $(CH_2)_6(COO^-)_2(H_2O)_n$. Multiple photon excitation of the symmetric ($\nu_S(C–O)$) and antisymmetric ($\nu_A(C–O)$) carboxylate stretching vibrations in the $n = 15$ complex induces dissociation indicated by the depletion of the ion signal (top trace). The vibrational energy is efficiently transfered to the water-water network in the complex such that loss of multiple water molecules occurs during the interaction with FELIX. This is indicated by the formation of the smaller complexes $n = 12 - 14$ (lower traces).

dissociation energy but also on the spectral range in which the IR spectrum is measured. In ion-water complexes of conjugate base anions, such as nitrate ions NO_3^- [32], bicarbonate ions HCO_3^- [33] and dicarboxylate dianions $^-OOC\text{-}(CH_2)_m\text{-}COO^-$ (Chapter 6), the hydrogen-bonded water molecules are typically bound with 0.5–1 eV (or about 4000–8000 cm^{-1}). The water molecules bind even stronger (near 2 eV) to ions containing a positively charged metal center like the $[MgNO_3]^+$ ion pair [34]. Hence, in the fingerprint region of the complexes, typically 500–2000 cm^{-1}, absorption of 2–8 IR photons is needed to reach a dissociation threshold of 4000 cm^{-1}. The IR-MPD experiments reveal two interesting processes. First, the complexes can undergo sequential evaporation of several water molecules. With increasing level of hydration the water molecules typically become more loosely bound and, thus, sequential dissociation is quite likely for larger ion-water complexes. Second, specific absorption bands are sometimes not observed in an IR-MPD spectrum of smaller complexes. For instance, this is the case for the librational modes of the water molecules.

Sequential Dissociation. Sequential evaporation of water molecules is especially observed for microhydrated suberate dianions $^-OOC–(CH_2)_6–COO^-(H_2O)_n$ (Chapter 6). The $n = 15$ complex shall serve as an example to illustrate this process. Figure 1.5 shows the depletion spectrum (top trace) of $n = 15$ measured in the region of the carboxylate stretching vibrations. MPE of the symmetric ($\nu_S(C–O)$) and antisymmetric ($\nu_A(C–O)$) modes results in the sequential loss of three water molecules, thereby forming the complexes $n = 12–14$ (lower traces, Figure 1.5). Basically, this behavior relies on two aspects, namely, fast IVR owing to

the large cluster size as well as long interaction time with the FELIX laser pulse. Loss of the first water molecule can quickly occur during the laser pulse. After dissociation, the formed fragment $n = 14$ is further resonantly excited and dissociates again. This process continues until the smallest observed fragment $n = 12$ is formed.

Isomerization. Multiple photon absorption can induce structural changes in microhydrated ions that contain water molecules bound in a bidentate fashion. Absorption of the first few photons followed by fast IVR may be sufficient to break one of the two H-bonds while the complex remains still below the dissociation limit. Thus, a conformational change is induced which can shift absorption frequencies of the complex. In particular, when the excited vibrational mode shifts out of resonance with the laser, no further photon absorption occurs and the dissociation of the complex is prevented. For example, IR-MPD studies on microhydrated nitrate, bicarbonate and bisulfate ions [32, 33, 36] reveal that the water librational modes ($<800\,\mathrm{cm}^{-1}$) are strongly affected. As a consequence, these modes do not appear in the IR-MPD spectrum. The effect is most commonly observed for the smaller complexes where all water molecules are bound in a bidentate fashion.

1.3.3 Infrared Vibrational Predissociation

Messenger Technique. In contrast to ion-water complexes, covalently bound metal oxide clusters can have dissociation energies of several eV. The IR-MPD efficiency for these strongly bound systems is reduced, because several tens of photons need to be absorbed to reach the dissociation continuum. An alternative approach which allows circumventing MPE is the so-called *messenger technique* introduced by Lee and coworkers [58, 59]. The dissociation threshold is substantially lowered when a weakly bound ligand, referred to as messenger, is attached to the cluster ion. Rare gas atoms are typically used as a messenger species but it can also be an inert molecule like H_2. Ideally, the vibrational modes of the cluster ion ($AB^{+/-}$) remain unperturbed and its IR signature is obtained via dissociation of the ion-messenger complex ($AB^{+/-}\cdot M$) as depicted in Eq. (1.8),

$$AB^{+/-} \cdot M \xrightarrow{h\nu_{IR}} \left(AB^{+/-}\right)^* \cdot M \xrightarrow{IVR} AB^{+/-} + M. \tag{1.8}$$
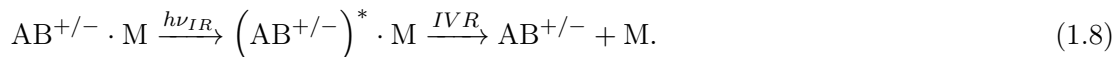
The cluster ion $AB^{+/-}$ is excited by resonant photoabsorption. Ideally, the ion-messenger interaction is weak enough to reach the dissociation limit by absorption of a single photon. The absorbed energy is redistributed among all vibrational modes via IVR. Ultimately, dissociation occurs by breaking the weak ion-messenger bond. The vibrational spectrum is then obtained by recording the ion yield of $AB^{+/-}$ as a function of the photon energy $h\nu_{IR}$.

The method offers several advantages arising from the weak ion-messenger interaction. First, ion-messenger binding energies are typically lower than $0.2\,\mathrm{eV}$, especially when lighter rare gas atoms (He, Ne) are used. Therefore, in the fingerprint region ($500–2000\,\mathrm{cm}^{-1}$), only a few photons are absorbed and IR spectra can be measured in (or near) the linear regime. Second, IVR is usually slow in ion-messenger complexes because of lower internal energies, and lifetime broadening of vibrational transitions is significantly reduced. The excitation energy is trapped for a long time within the excited vibrational mode before it couples to the van der Waals modes of the messenger. Under these conditions the complex is said to undergo infrared vibrational predissociation (IR-VPD) [60]. For example, IR-VPD of rare gas atom tagged cerium oxide cluster cations (Chapter 4) and binary cerium/vanadium oxide

cluster cations (Chapter 5) results in line widths between 6–$10\,\mathrm{cm}^{-1}$, limited by the spectral bandwidth of the laser and dynamical effects. If the bandwidth of the laser is sufficiently small, IR-VPD spectra can even be measured with rotational resolution, for instance, demonstrated in the early work on $H_3O^+\cdot(H_2)$ by Lee and coworkers [59].

Note that IR-MPD and IR-VPD are not mutually exclusive. As mentioned above, IR-VPD in the mid-IR region may involve absorption of more than a single photon and IR-MPD may involve predissociation. Nonetheless, throughout this thesis the term IR-VPD will be used in the context of rare gas tagging.

Rare Gas Atom Tagging. Making use of the above-mentioned advantages, the IR signatures of metal oxide cluster cations presented in this thesis are investigated employing rare gas atom tagging. Using tunable FEL radiation, this technique was first applied to monovanadium oxide cluster cations [17, 61]. The IR-VPD spectra were measured of the corresponding ion-He atom complexes. Among the rare gas atoms, helium represents the ideal messenger as due to its small polarisability the perturbation on the cluster ion remains small. The cluster properties can be significantly affected when heavier rare gas atoms like argon or krypton are used, which typically leads to strong shifts of the vibrational frequencies [54, 62]. Different rare gas atoms can actually stabilize different cluster isomers, although they have been thought to be chemically inert. Such isomer-selectivity was previously observed by Fuji et al. in their IR-VPD study on messenger-tagged $H^+(H_2O)_6$ clusters [63]. Similar effects are observed for metal oxide clusters investigated in this thesis. For instance, the structures of vanadium oxide clusters $V_3O_{6-8}{}^+$ are markedly messenger-dependent which is discussed in more detail in Chapter 3.

1.3.4 Example: Predissociation of $VPO_4{}^+\cdot He_2$[1]

IR-VPD spectroscopy on the helium-tagged complex $VPO_4{}^+\cdot He_2$ shall serve as an example to illustrate that even a weakly bound He atom can influence the vibrational transitions of the bare cluster ion. Figure 1.6 shows the IR-VPD spectrum (top panel) of $VPO_4{}^+\cdot He_2$, which is obtained by monitoring the loss of a single He atom. The spectrum is measured in the spectral region from 900 to $1500\,\mathrm{cm}^{-1}$ using a tabletop IR laser system (Section 2.5). Four absorption bands (labeled A–D) are observed which are unambiguously assigned to vibrational modes of a V–$(O)_2$–P four-membered ring isomer containing a terminal $V{=}O$ and $P{=}O$ double bond (bottom, Figure 1.6): bands A ($1445\,\mathrm{cm}^{-1}$) and B ($1064\,\mathrm{cm}^{-1}$) are attributed to the $P{=}O$ and $V{=}O$ stretching vibrations, respectively, while band C ($1043\,\mathrm{cm}^{-1}$) and D ($957\,\mathrm{cm}^{-1}$) correspond to in-plane deformation modes of the ring. The DFT calculations for the helium-tagged ring isomer reveal that both helium atoms preferentially bind to the V atom (middle, Figure 1.6). The ion-He atom interaction particularly affects the vibrational frequencies of the ring vibrations, which exhibit a significant blue-shift, e.g., band C is predicted to shift by $+10\,\mathrm{cm}^{-1}$ (see dashed vertical lines in Figure 1.6). Thus, the positions of the experimental bands C and D are even better reproduced if the ion-He atom interaction is taken into account.

Furthermore, the vibrational transitions yield different experimental line widths. For instance, the $P{=}O$ stretching band has a width of $11\,\mathrm{cm}^{-1}$ (FWHM), representing the narrowest feature in the spectrum, while band C appears noticeably broader with a width of $18\,\mathrm{cm}^{-1}$.

---

[1]The IR-VPD measurements were performed in our group as part of a collaboration with Prof. Helmut Schwarz and Nicolas Dietl (Technische Universität Berlin). The theoretical results presented here are provided by Dr. Ling Jiang.
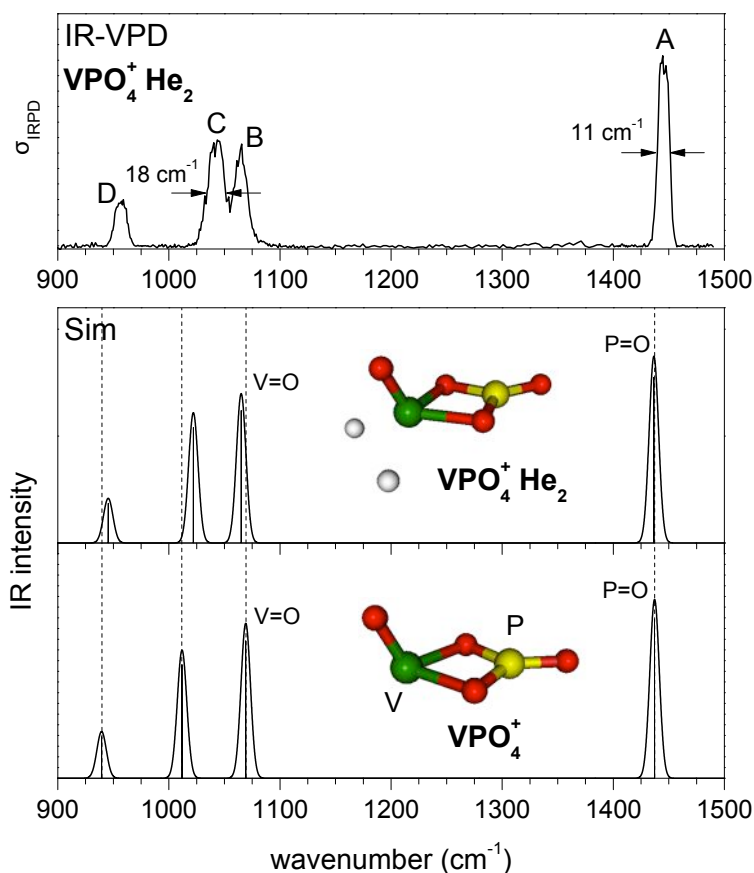
Figure 1.6: Predissociation of the helium-tagged complex $VPO_4^+\cdot He_2$. The IR-VPD spectrum (top) is well reproduced by the simulated (B3LYP+D/TZVPP) linear absorption spectrum of the helium-tagged ring isomer of VPO_4^+ (bottom). The ring vibration band C is most strongly affected upon tagging, leading to a significant blue-shift (see dashed vertical lines). In contrast, the vibrational frequency of the P=O stretching mode remains unperturbed. This finding may suggest that band C couples stronger to the dissociation channel, leading to a larger experimental line width of band C compared to band A.

The line widths exceed the spectral bandwidth of the laser ($\sim 2\,\mathrm{cm}^{-1}$) and may thus be limited by, for instance, the rotational band contour and/or dynamical effects. As already shown above, the ring vibration band C is most strongly affected upon tagging, in contrast to the P=O stretching vibration, which remains unperturbed. This finding may suggest, that band C couples stronger to the dissociation channel, i.e., loss of He atoms. Hence, IVR could proceed faster which then noticeably broadens band C.

1.3.5   General Strategy for Structural Assignment

The structural assignment is based on the comparison between experimental and simulated IR spectra, as already exemplified in Figure 1.6. Aided by QC calculations, different structural isomers are optimized and the vibrational frequencies and intensities are commonly derived within the harmonic approximation. The resulting stick spectra are typically convoluted using a gaussian line shape function in order to account for line-broadening effects (laser bandwidth, rotational envelope, IVR). The linear absorption spectra are then compared with

the experimental results with respect to the number of absorption bands, their positions and intensities.

The quantitative agreement between experimental IR-PD spectra and calculated linear absorption spectra basically depends on the number of photons involved in the dissociation process. IR-VPD of rare gas-tagged complexes is ideally governed by single photon absorption or involves just a few photons. Therefore, IR-VPD spectra often reflect the linear absorption spectrum quantitatively, especially when light rare gas atoms (He, Ne) are used. Generally it allows for an unambiguous structural assignment [14]. When many photons are needed, the efficiency of the dissociation process can be significantly reduced. In an IR-MPD spectrum, the relative band intensities may therefore differ from those in the linear spectrum. Furthermore, the number of photons needed to dissociate the molecule changes within the fingerprint region (see example 1.3.2). Hence, band intensities in the lower frequency range may be much more reduced. Nonetheless, earlier IR-MPD studies show that the IR-MPD spectrum often resembles the linear absorption spectrum [52, 64]. This is particularly observed for larger molecular systems characterized by a high density of vibrational states. The excitation energy can quickly be redistributed already after absorption of a single photon which thus becomes the rate determining step in the IR-MPD process.

Chapter 2

Experimental Setup

The IR-PD experiments described in the present thesis have been performed using an instrumental setup that combines a cryogenically cooled radio frequency (RF) ring electrode ion trap with a tandem mass spectrometer [65]. This setup will be described in the following chapter, which is divided as follows. First, a description of the ion sources used in the IR-PD experiments is given. A cryogenically cooled single target laser ablation source was designed and set up as part of my PhD research and is discussed. Section 2.2 gives a brief overview of the operating principle of the tandem mass spectrometer. The spectrometer consists of several different RF multipole devices which serve to guide, mass-select and trap ions. Section 2.3 provides a theoretical background of RF multipole devices and introduces their experimental applications. The fourth section explains the ion detection scheme. IR-PD spectroscopy requires a light source that provides tunable and intense IR radiation. Section 2.5 presents two IR light sources which have been used in the IR-PD measurements, i.e., the free electron laser FELIX and a tabletop solid-state IR laser system.

2.1   Cluster Sources

Several interchangeable ion sources are presently available for the formation of atomic and molecular clusters in our lab. Here, I describe the laser vaporization source, as well as the electrospray ionization source, which I used extensively throughout this work.

2.1.1   Laser Vaporization
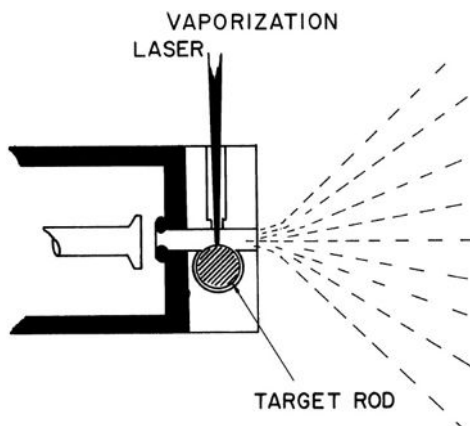
Figure 2.1: Schematic cross-section of a standard laser vaporization source developed by Smalley and coworkers. Reprinted with permission from Ref. [66]. Copyright (1982) American Chemical Society.
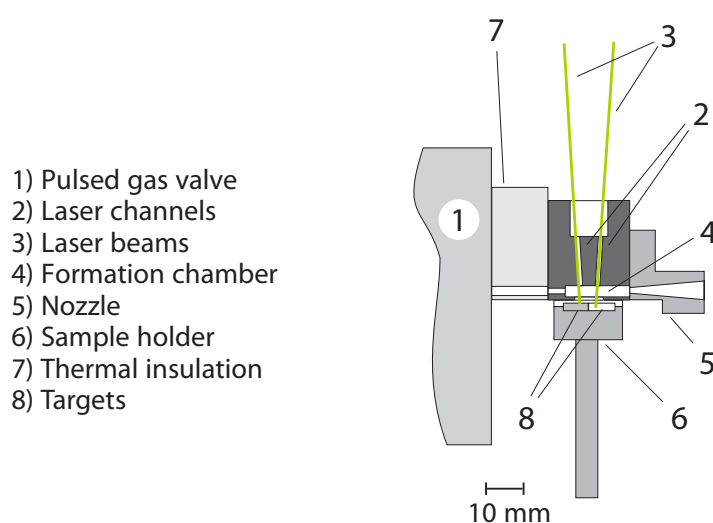
The first laser vaporization source was developed in the early eighties by Smalley et al. [67, 68]. Figure 2.1 shows a schematic of the original design which also illustrates the principle of operation. A small portion of a metallic material is vaporized by focusing a pulsed laser beam through an inlet channel onto the surface of a target rod. A dense metal plasma is formed which is then entrained in a flow of an inert carrier gas injected by a pulsed valve. The gas mixture expands within a confining channel that is tangent to the target rod and perpendicular to the laser inlet channel. The confinement keeps the density of the carrier gas sufficiently high to enable thermalization and clustering through three-body collision processes. At the end of this channel the gas expands freely into a vacuum forming a supersonic beam.

Today, laser vaporization is a standard technique for producing metal-containing clusters [69]. Over the years, the source design and operation have been optimized in order to improve cluster formation. Different types of laser vaporization sources have been developed, including sources that either use rod [70], disk [71–73], wire [74] or even liquid [75] targets. Bimetallic clusters can be formed by vaporization of a bimetallic target or using a dual target source [76–78]. The performance of a laser vaporization source depends on many parameters. In order to obtain a stable cluster signal each laser pulse needs to hit a new spot on the surface and therefore the target has to be moved prior to each laser pulse which prevents the laser from burning holes [68]. The synchronization between the vaporization laser and the valve opening represents an important parameter which affects the efficiency of the plasma cooling and thus the cluster size distribution. The choice of the vaporization laser with regard to the pulse width has a major effect on the vaporization process [66]. If a nanosecond laser pulse is used only the early portion of the laser pulse efficiently forms a metal plasma above the surface of the target. On this short time scale the plasma cannot expand fast enough and therefore continues

to absorb light which leads to the formation of a super-heated plasma. As the hot plasma becomes optical dense the target is shielded from further ablation. In contrast, longer laser pulses in the microsecond range vaporize the material more efficiently but dominantly lead to the ejection of liquid droplets. Since the metal vapor can expand during the long laser pulse the formation of a saturated metal atom vapor is hindered. Therefore nanosecond pulsed lasers are commonly used for laser ablation although relatively hot cluster beams are produced. In order to improve the cooling efficiency of the clusters different design modifications have been discussed in the literature. A better thermalization is achieved by introducing a pre-expansion zone [79, 80] or by varying the length of the clustering channel (typically a few centimeters) [81]. The heat transfer from the vapor to the walls is enhanced due to an increased number of collisions with the carrier gas resulting in an colder cluster beam. Another example is the introduction of a large cavity or thermalization chamber already before the channel [70, 71]. This modification separates the cluster formation processes from the expansion. Apart from the standard design discussed so far, vaporization sources are reported where the incoming laser beam is coaxial to the molecular beam axis. This setup reduces cluster losses due to extended wall deposits as well as the leakage of carrier gas due to the absence of a laser inlet channel [73].

Dual-Target Dual-Laser Vaporization Source

For the IR-PD experiments on cerium oxide and mixed cerium/vanadium oxide clusters (see Chapters 4 and 5) a dual-target dual-laser vaporization source was used in collaboration with the group of Prof. Peter Lievens (Katholieke Universiteit Leuven, Belgium) [77, 82]. An outline of the source is illustrated in Figure 2.2. It contains an elongated cylindrical formation chamber of 17 mm with a diameter of 3 mm. Small rectangular plate targets of about $7 \times 24\,mm^2$ are used. The cerium and vanadium targets are mounted side by side and pressed against a 6 mm long slit in the formation chamber by means of a target holder. Opposite to the slit two laser channels are drilled under an angle of 5° through which two independent laser beams (second

1) Pulsed gas valve
2) Laser channels
3) Laser beams
4) Formation chamber
5) Nozzle
6) Sample holder
7) Thermal insulation
8) Targets

10 mm

Figure 2.2: Outline of the dual-target dual-laser vaporization source. Picture is taken from Ref. [82].

harmonic of two Nd:YAG lasers) are aligned and focused onto the targets. A conical nozzle terminates the formation room. Carrier gas pulses are provided by a pulsed supersonic valve (R. M. Jordan Co.) which is operated at a repetition rate of 10 Hz. The gas valve and the source are thermally insulated by means of a 15 mm Teflon block allowing to cool the nozzle by liquid nitrogen. In order to avoid hole drilling in the targets, the target holder is moved in a rectangular closed loop pattern using two vacuum compatible stepper motors.

Single Target Laser Vaporization Source

A central goal of my thesis work was the design, construction and implementation of a cryogenically-cooled dual target laser vaporization source for the formation of metal oxide aggregates. Two different types of metal oxide clusters are formed in two separate clustering channels and are then combined further downstream in an aggregation chamber. This configuration has already been used to produce bimetallic clusters [78, 83]. A first step to that goal is the construction of a cryogenically-cooled single rod laser vaporization source. The new design feature of this source is the implementation of a cold head which serves to control the temperature of the aggregation chamber in the range from 20 K to 300 K. This source was used for the IR-VPD experiments on vanadium oxide clusters (Chapter 3) as well as on iron oxide clusters (preliminary results are shown in Appendix B).

General Overview. Figure 2.3 shows the source inside the vacuum chamber. It is mounted directly onto the second stage of a 4 K cold head of a closed-cycle He cryostat (*Sumitomo Heavy Industries*, RDK-205D). The cold head is inserted from the top and mounted onto an adjustment flange (not shown in Figure 2.3), which allows for an external adjustment of the whole source assembly under vacuum in three dimensions relative to the skimmer. The distance between the cooled nozzle and the skimmer is typically 3 cm. In order to provide the source with electrical and gas connections a multiple feedthrough flange is connected to
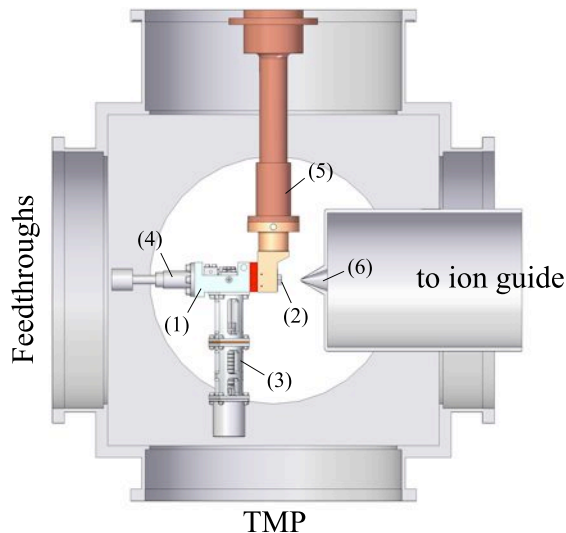
Figure 2.3: Cutaway view of the source chamber. The laser vaporization source is attached to a cold head. The following parts are shown: laser vaporization source (1), cooled nozzle (2), rotation/translation screw mechanism (3), pulsed valve (4), cold head (5), skimmer (6).

the front port of the chamber. Vaporization is induced by the second harmonic (532 nm) of a Q-switched Nd:YAG laser (*Quantel*, BRIO) which provides 3–6 ns pulses with pulse energies of up to 40 mJ at a fixed repetition rate of 50 Hz. The pulse energy can be continuously attenuated with a commercial beam attenuator with Brewster type polarizers (*Altechna*). In this way, the laser can be operated with the optimal timing between flash lamp and Q-switch to reduce shot-to-shot fluctuations. The pulsed laser beam enters the chamber through a 70 mm diameter borosilicate glass (4 mm thick) which is mounted onto a ISO-K DN250 flange attached to a side port of the chamber. A lens ($f = 40$ cm) is mounted onto a translation stage and used to focus the beam through the laser inlet channel onto the target.
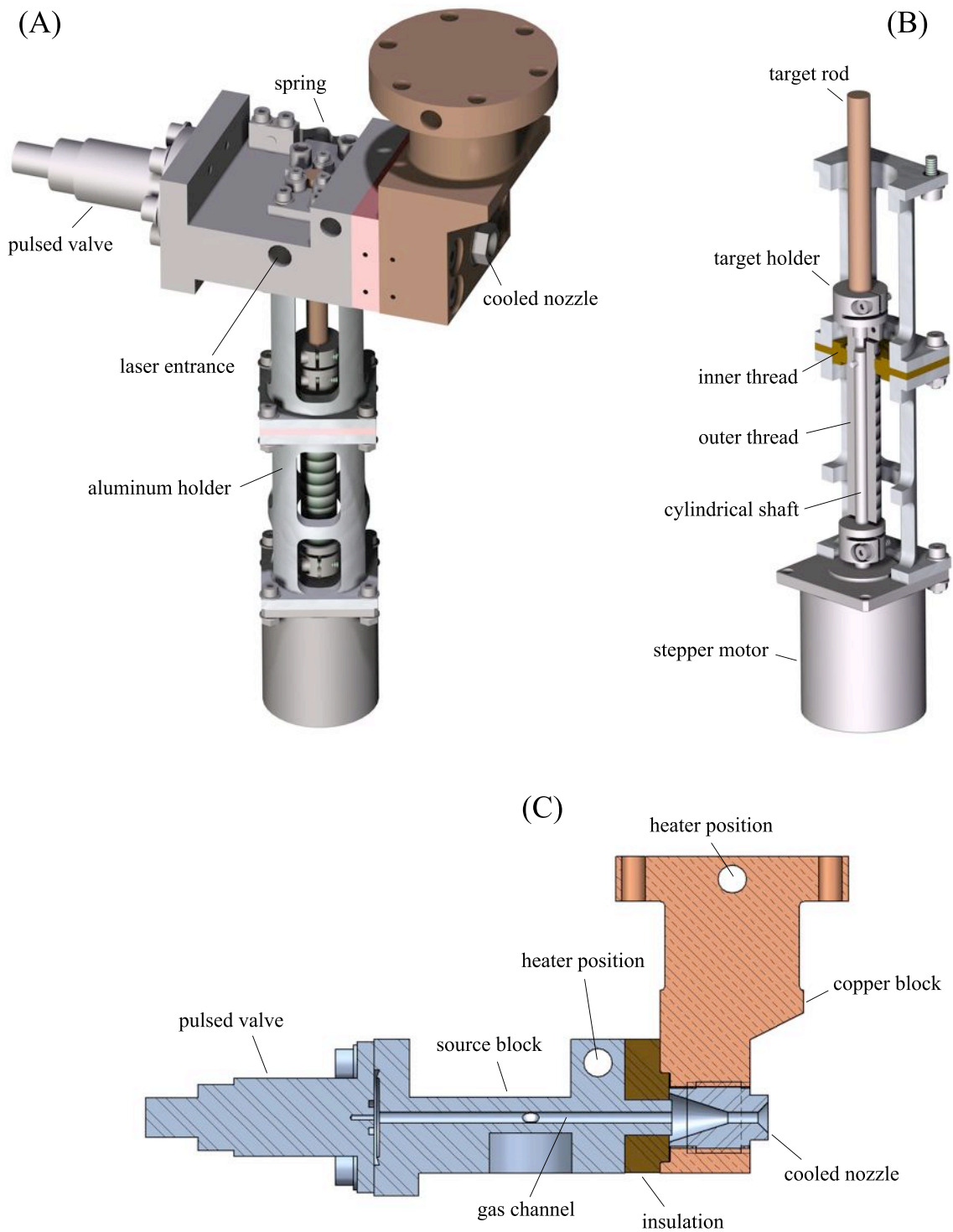
Source Design. Figure 2.4 shows the assembly of the laser vaporization source. The setup is divided into a source unit, a cooling unit and a motion system. The main body of the source unit is made of a $66.5 \times 50 \times 35$ mm^3 stainless-steel block (source block, Figure 2.4C). Following the standard design three orthogonal intersecting channels are drilled through the block. The target rod is moved within a vertical channel of 6.4 mm in diameter. Three small ball bearings mounted on top of the main body mainly serve to guide the rod during the motion. More precisely, one ball bearing, fixed on a movable metal plate, is pressed against the rod mediated by a spring plate ensuring a smooth rotational motion. The typical diameter of the target rod is 6.2 mm, but 1/4" rods could be used as well depending on their straightness. One horizontal channel serves as an opening for the incoming laser beam (laser entrance, Figure 2.4A). This channel has a M5 thread for an adapted set screw containing a drilled channel through which the laser beam is focused. Different set screws with openings from 0.5 mm to 1.5 mm are available and can be easily exchanged. The end of the horizontal channel can be closed by using an adapted M4 cylinder head screw, in order to decrease the leakage of the carrier gas during operation. The second horizontal channel is 2.5 mm in diameter and is used to mix the metal plasma with the carrier gas (gas channel, Figure 2.4C). The gas pulses are provided by a solenoid valve (*Parker*, Series 99) which is mounted to one end of the gas channel. In order to ensure thermalization and clustering the gas mixture flows about 30 mm within the gas channel before it terminates in a cooled nozzle.

The source unit is mounted to the cooling unit. A cross section of this assembly is presented in Figure 2.4C. Both units are thermally insulated from each other by a 8 mm thick polyimide block (Vespel® SP-21). The main body of the cooling unit is a OFHC[1] copper block and serves to cool a stainless steel nozzle which is screwed in the block. Differently shaped nozzles can easily be exchanged. To enhance thermalization and promote the formation of e.g. messenger-tagged clusters a conical converging-diverging nozzle with an orifice of 2.5 mm is used. The whole assembly is directly attached to a cold head by means of a 52 mm diameter flange. A heating cartridge (*Janis Research*, 50 W/50 Ω UHV heater) installed close to the interface between the cold head and the copper block allows for a continuous temperature control over the range from about 20 K to 350 K. The mode of operation can be extended by replacing the insulating material by for instance stainless steel or copper. In this way the source unit can be cooled as well. A second heater cartridge is implemented in the source block enabling to control the temperature gradient. The temperatures of both units are read out using silicon diodes (*Lake Shore*, DT-670-SD).

A screw-thread motion system situated inside the vacuum chamber is directly mounted to the bottom of the source block and generates a translational rotation of the target rod.

---

[1]OFHC = oxygen-free high thermal conductivity

(A)

(B)

spring

pulsed valve

cooled nozzle

laser entrance

aluminum holder

target rod

target holder

inner thread

outer thread

cylindrical shaft

stepper motor

(C)

heater position

heater position

copper block

pulsed valve

source block

cooled nozzle

gas channel

insulation

Figure 2.4: Schematic 3D-view of the laser vaporization source.

The assembly is illustrated in Figure 2.4B. The key features are based on the source design described in the thesis of P. Grüne [54]. The rotation is induced by a cryo stepper motor suitable for low temperature applications in ultra high vacuum (*Phytron*, VSS32-UHVC). The rotation of the motor shaft is directly transfered to a cylindrical shaft which is inserted in a machined M10 × 0.5 fine thread screw (20 threads/cm). A small pin at the end of the shaft transfers the motion to the thread screw which turns in a fixed internal thread (8 threads), thereby inducing a translational rotation. The rod is fixed to the thread screw by means of a target holder. The rod, target holder, thread screw and cylindrical shaft are fixed by means of couplings. In order to meet the criterion of a smooth rotational motion the dimensions of each mechanical part are carefully tolerated. High demands are put on the coaxial alignment of each part with respect to the motor shaft. To this end the internal thread is fixed in-between two aluminum holders. The stepper motor is mounted to one end and its position can be aligned in order to center the cylindrical shaft within the fine thread screw. Finally the whole assembly is mounted to the source block. Its final position can be adjusted as well to properly align the rod position within the vertical bore. The length of the assembly is about 145 mm, limited by the vacuum chamber. Dimensions have been optimized to maximize the stroke which is 40 mm (which requires a 58 mm long rod).

The quality of the motion strongly depends on the materials used for the thread screw and the internal thread. Whereas the thread screw is made of stainless steel different materials (Vespel® SP-21, bronze, Teflon) have been tested for the internal thread. In order to minimize wear and mechanical friction during rotation Vespel® SP-21 has proven to be the best material. The polymer is filled with 15 % graphite which yields a low friction coefficient.

Operation. The up and down motion of the rod is computer-controlled via a programmable stepper motor controller (*Phytron*, MCC-2). A power supply (*Phytron*, PS 5-48) provides the required current and voltages. LabView is used for defining the motion loop and setting the motor parameters. The applied torque is mainly determined by the step resolution and the motor current. For instance, the maximum torque of 40 mNm is achieved in full step mode at 1.2 A. In contrast, setting the step resolution to 1/16 the torque is already reduced by about 50 %. Note that a minimum required torque for this assembly is calculated to be about 1 mNm if only the friction between screw and thread is considered. However, the following two effects enhance the friction of the system. First, the rod translates in-between the ball bearings. Second, it was found that the rotation of the motor shaft exhibits a small nutation which couples to the thread screw. As one ball bearing is pressed against the rod, the nution is significantly reduced but causes tilting. Thereby the friction inside the thread is enhanced and can lead to jamming. Therefore, the length of the internal thread has been varied in order to minimize the risk of jamming upon tilting. It was found that 4 mm (8 threads) provides enough backlash which improves the handling especially with regard to the alignment. A longer thread of > 8 mm easily causes the drive to get stuck. A stable operation is typically achieved using a step resolution of 1/8 and a run current of 0.4 A (corresponding to a torque of approximately 8 mNm). The stepping frequency is set to 50 Hz in accordance with the laser repetition rate providing a fresh spot for each laser pulse. The turning speed is then about 2 turns per minute yielding a smooth ablation trace on the target. The fine thread allows for an optimal use of the target.

A smooth motion of the rod is important for a stable operation of the source. The rod should be aligned close to the gas channel in order to minimize the gas leakage past the rod.

Fine adjustment of the ball bearings serve to keep the rod in position during the rotation. It is convenient to do the alignment outside the chamber. Targets of a similar diameter can be exchanged without removing the source from the vacuum chamber.

The applied run current of 0.2–0.4 A results in a significant heat production of the motor. The temperature of the motor winding is monitored by a type K thermocouple and read out using a control unit (*Eurotherm* Typ 2132 implemented in *FHI ELAB* #4653.2) which provides the motor controller with an interlock signal once the temperature of the winding exceeds the specified limit of 40 °C. In order to keep the temperature below this limit the motor needs to be cooled. To this end the motor housing is surrounded by a copper clamp which is attached to the first stage of the cold head.

In the normal mode of operation the temperature of the nozzle is controlled using a temperature controller (*Lakeshore*, Model S331). The nozzle can be cooled down to 20 K while the temperature of the source block is kept at 290 K using a home-built 50 W power supply (*FHI ELAB*, #4790).

The parameters of the gas pulses provided by the solenoid valve are mainly determined by the backing pressure, the opening time and the opening gap. The valve is operated with a home-built pulsed nozzle driver (*FHI ELAB*, #3984.1) providing voltage pulses in order to define the opening gap and time. During operation the valve is triggered with 50 Hz and stable operation is achieved using a rather low voltage of about 200 V and a maximum opening time of 300 µs. Best operation (indicated by a stable pressure in the source chamber) is obtained when thermal equilibrium is reached. The time delay between the valve and the laser is crucial to the cluster formation and is adjusted for each cluster size with microsecond precision. Generally, the time delay is adjusted such that the laser pulse coincides with the peak intensity of the carrier gas pulse. Smalley et al. proposed to fire the laser on the leading edge of the rising carrier gas pulse [71]. In our experiments the valve is typically triggered 100 µs to 300 µs before the Q-switch of the laser. For the formation of metal oxide clusters a backing pressure of typically 8 bar helium seeded with O_2 is used.

The laser beam is aligned and focused through the inlet channel onto the target. An opening of 1.5 mm is found to be suitable in order to prevent the hole from being covered with material deposits induced by ablation. The pulse energies used for the ablation target are varied in the range from 10 mJ to 20 mJ, depending on the target material. Final adjustment of the lens position (distance to the target) is made by monitoring the ion signal. In order to obtain the same ion intensities during the up and down motion the laser beam needs to be carefully horizontally aligned. This is best done by monitoring the ion signal before and after the turning point of the rod.

Formation of Metal Oxide Clusters. Figure 2.5 illustrates typical cluster distributions for vanadium oxide clusters $V_mO_n^+$ and iron oxide clusters $Fe_mO_n^+$. Using a carrier gas of typically 0.25 % O_2 seeded in helium, oxygen-rich clusters are efficiently produced in the mass range from 100 to 700 amu. Both mass spectra exhibit several (overlapping) peak progressions associated to clusters with different numbers of metal atoms. The strongest ion signal of each progression is labeled. Furthermore, preliminary measurements were carried out to produce metal copper clusters Cu_n^+ (Figure A.2 in the appendix). The appendix also includes design considerations in order to improve the ion signal stability.
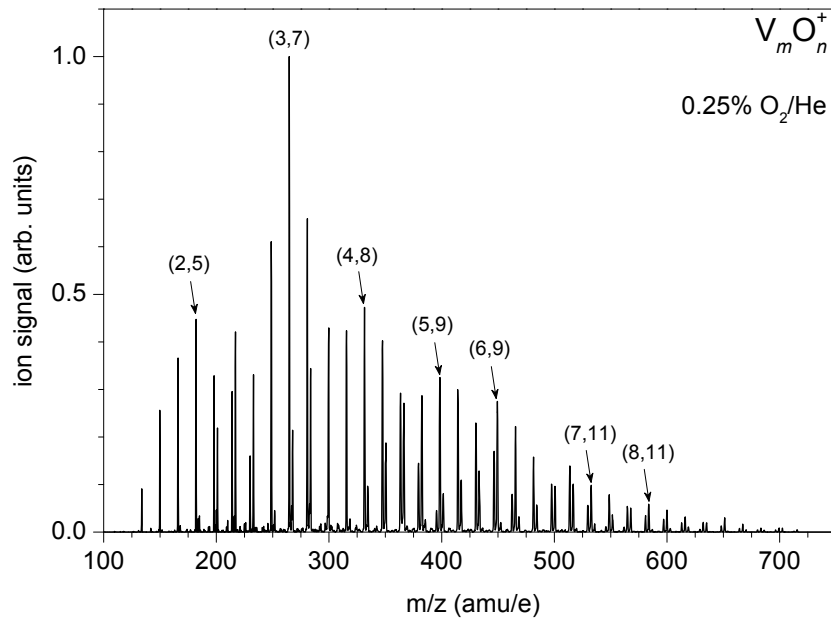
(a)
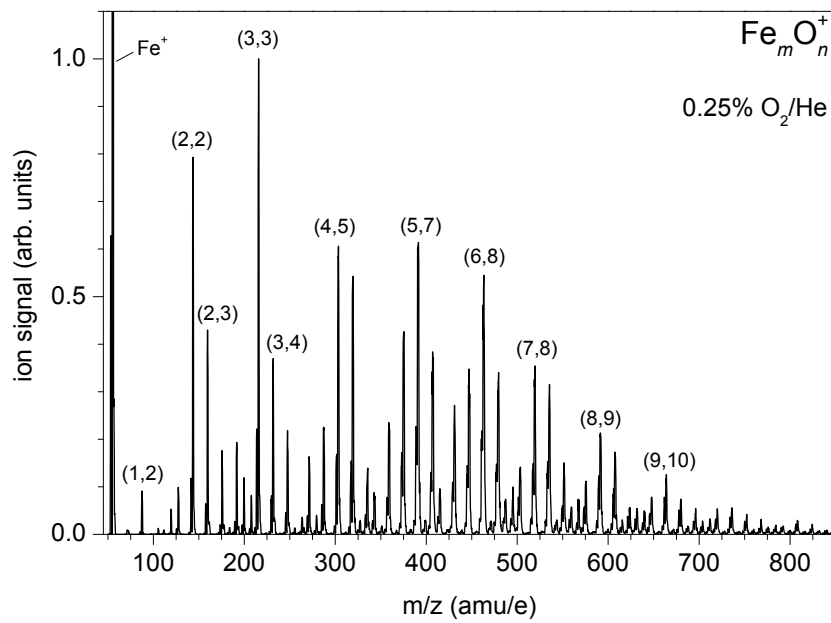
(b)

**Figure 2.5:** Typical mass spectra of vanadium oxide clusters **(a)** and iron oxide clusters **(b)**.

2.1.2   Electrospray Ionization

Electrospray ionization (ESI) is a standard technique in mass spectrometry to produce gas phase ions from a solution. It is a soft ionization technique which is capable to transfer weakly-bound compounds without fragmentation into the gas phase [84]. John B. Fenn improved the electrospray technique and combined it with mass spectrometry which revolutionized the quantitative investigation of biologically relevant macromolecules [85, 86]. In the present thesis, the ESI technique has been applied in order to investigate microhydrated ions, e.g. dicarboxylate dianions $^-$OOC-$(CH_2)_m$COO$^-$ (Chapter 6). In the following, a description of the Z-spray source implemented in the experiments is given.

Z-Spray Source.   The source was taken from a commercial Waters *Quattro Ultima* mass spectrometer. The main elements of this source are schematically illustrated in Figure 2.6. An aqueous solution which already contains preformed ions is pumped at a constant flow rate (10–20 µl/h) into a stainless steel capillary (*1* and *2*, Figure 2.6). An applied intense electric field deforms the liquid at the capillary tip and promotes the formation of a jet of small charged droplets. The capillary is typically provided with a high voltage of 2–3 kV depending on the solvent. Usually, a solvent mixture of water and acetonitrile (50:50) is used which reduces the surface tension of the liquid and facilitates the droplet ejection at lower voltages. Within the atmospheric pressure region of the source, the droplets shrink due to solvent evaporation resulting in multiple fission cycles until the gas phase ions are formed [87, 88]. A flow of
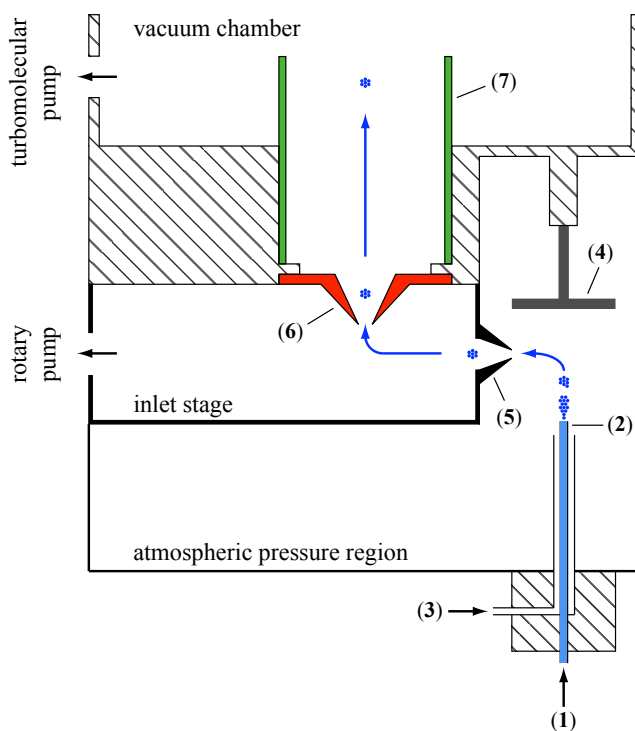
Figure 2.6: Schematic view of the Z-spray source. The main elements of the source are indicated: (1) sample solution, (2) stainless steel capillary, (3) nebulizer gas, (4) grounded baffle, (5) sample cone attached to the source block, (6) extraction cone, (7) cylindrical lens. Typically applied voltages are given in the text.
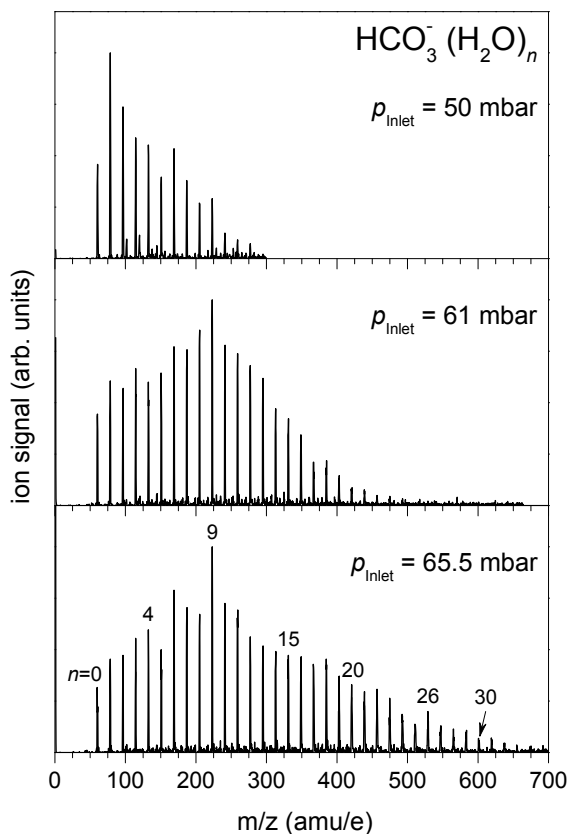
Figure 2.7: Mass spectra of microhydrated bicarbonate anions $HCO_3^-(H_2O)_n$ measured for inlet pressures p_{inlet} = 50, 61 and 65.5 mbar, demonstrating that the degree of microhydration can be tuned by varying p_{inlet}.

nitrogen gas (*3*, Figure 2.6) surrounding the capillary is provided in order to support the evaporation. A small 700 μm diameter sample cone (*5*, Figure 2.6) installed perpendicular to the spray samples the ion beam and serves as the opening to the first pumping stage, referred to as inlet stage. This arrangement separates the charged species from the neutrals. To this end, the sample cone and source block are provided with a voltage U_1 (40–100 V). An extraction cone (*6*, Figure 2.6) with an opening of 1 mm is mounted perpendicular to the inlet stage. It is electrically isolated from the source block and provided with a second voltage U_2 (0–60 V). The ions enter the vacuum chamber ($p < 10^{-2}$ mbar) and pass a cylindrical lens (*7*, Figure 2.6) provided with a third voltage U_3 (0–60 V) that serves to focus the ions into the tandem mass spectrometer for further mass analysis.

The transmission of the ions into the mass spectrometer depends on the applied voltages which are chosen such that $U_1 > U_2 > U_3$. These voltages are kept at the lowest value possible in order to keep the kinetic energy of the ions small. The pressure in the inlet stage, p_{inlet}, represents a sensitive parameter for tuning the degree of hydration. Figure 2.7 illustrates how the solvation of bicarbonate anions (HCO_3^-) is affected when p_{inlet} is increased. At 50 mbar hydrated ions containing up to 12 water molecules are observed while the monohydrated ion is preferentially formed. Increasing p_{inlet} to 65 mbar leads to a broad distribution of hydrated ions which shows a maximum at nine water molecules. The high pressure facilitates the formation of microhydrated ions containing up to 30 water molecules.

The underlying mechanism induced by the pressure inside the inlet stage remains unclear. The following mechanism is conceivable in order to explain the effects of p_{inlet} on the observed ion distribution. Before the ions enter the inlet stage, the solvation number distribution is primarily governed by thermal evaporation of solvents in the atmospheric pressure region. This means that the degree of solvation is determined by the thermal stability of the clusters, i.e., the ratio of the internal energy to the binding energy of a solvent molecule [89]. Once the ions enter the inlet stage, their transmission efficiency may be influenced by p_{inlet}. At higher pressures the ions experience frequent but low-energy collisions with the neutral gas. These gentle conditions reduce the amount of fragmentation leaving the larger, more weakly-bound complexes intact. Transmission of the larger clusters is then enhanced. In contrast, at lower pressures the complexes undergo less but high-energy collisions resulting in fragmentation, namely loss of water molecules, and small complexes are mainly observed. This phenomenon has already been discussed in studies that investigated the formation of non-covalent protein assemblies in dependence on the source pressure [90].

2.2   Tandem Mass Spectrometer
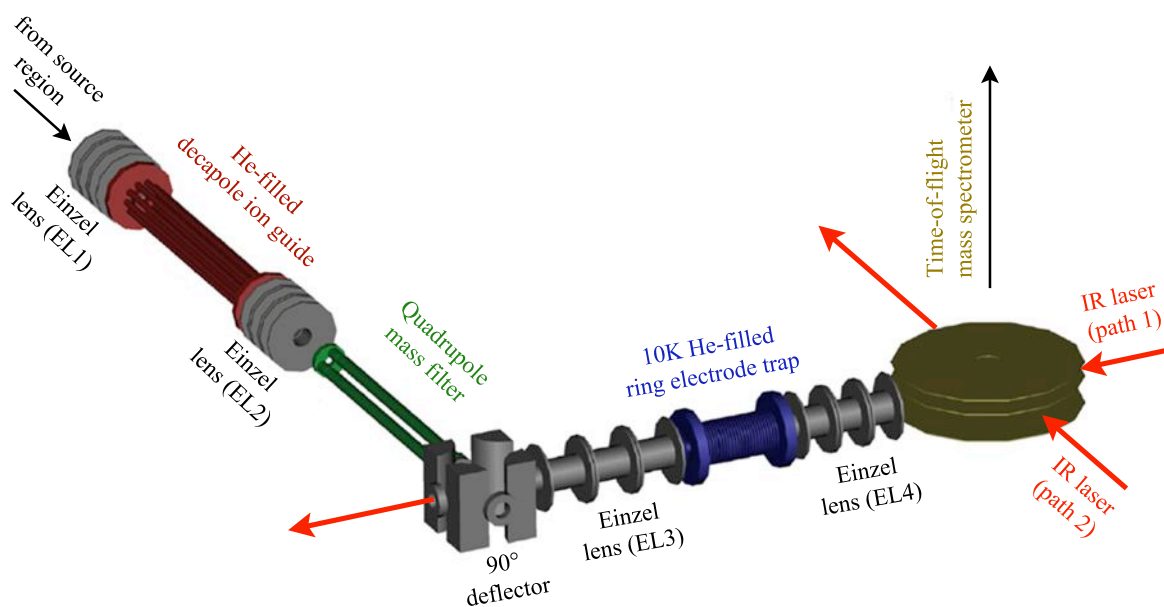
Figure 2.8: Schematic 3D-view of the ring electrode ion trap–tandem mass spectrometer. Adapted with permission from Ref. [31]. Copyright (2009) American Chemical Society.

The ion trap-tandem mass spectrometer described in this section was constructed in 2006 [65]. The general operating principle of the spectrometer can be divided into five stages: ion formation, ion guiding, mass selection, trapping and thermalization and detection. A schematic view of the instrument and its ion-optical elements is illustrated in Figure 2.8. Cluster ions are formed in the source region (not shown in Figure 2.8) as described in the previous section. The ion beam is sampled by a 4 mm skimmer and charged clusters are focused by an Einzel lens (EL1) into a RF decapole ion guide. Typically, the guide is filled

with helium buffer gas in order to collimate the beam. After passing a second Einzel lens (EL2), the collimated ion beam enters a quadrupole mass filter and ions of interest are mass-selected. Then, the ions are deflected over 90° by an electrostatic quadrupole deflector and focused by an Einzel lens (EL3) into a cryogenically-cooled RF ring electrode ion trap. The trap is mounted onto a cold head of a closed-cycle helium cryostat and its temperature can be controlled over the range from $10\,\mathrm{K}$ to $350\,\mathrm{K}$. A continuous flow of buffer gas inside the trap allows for accumulating and thermalizing the ions to the ambient temperature by means of multiple collisions. Ion trapping and extraction is controlled by a set of DC voltages applied to the trap electrodes. After the accumulation, all ions are extracted from the trap and pass an Einzel lens (EL4) and an ion beam deflector (not shown in Figure 2.8). This arrangement allows focusing the ion cloud both temporally and spatially into the center of the extraction region of an orthogonally mounted linear Wiley-McLaren time of flight mass spectrometer (TOF-MS). TOF mass spectra are measured by applying high-voltage pulses to the TOF electrodes and using a multichannel plate (MCP) detector mounted in a chevron configuration to detect ions. IR photodissociation of the ions is induced upon irradiation with an IR laser pulse when they reach the center of the TOF extraction zone. This ensures the collection of all ions arising from the IR-PD process in contrast to irradiation inside the trap. The orthogonal TOF arrangement allows for an IR laser access either collinear or perpendicular to the trap axis. Typically, the IR laser beam is aligned through the trap along the center line (path 1, Figure 2.8). This alignment faciliates the overlap of the IR laser pulse with the elongated ion packet. Depending on the divergence of the laser beam, the perpendicular alignment can be advantageous in order to prevent the laser from hitting the trap surfaces. In this case the laser beam is focused through the center of the extraction region of the TOF-MS (path 2, Figure 2.8). TOF mass spectra are measured for different wavelengths which are then converted into an IR spectrum.

Operating Pressures. All parts are housed in a vacuum chamber consisting of five stages. Each region is differentially pumped by means of a turbomolecular pump (TMP). The pressures are measured using full range hot cathode pressure gauges (*Pfeiffer*, PBR 260). The operating pressure in the source region depends on the implemented cluster source and typically varies between $10^{-5}\,\mathrm{mbar}$ (laser vaporization) and $10^{-3}\,\mathrm{mbar}$ (ESI). Due to the high gas ballast the source region is pumped by a $1600\,\mathrm{l/s}$ TMP (*Pfeiffer*, TMH 1601 P). The second stage contains the decapole ion guide operated at 10^{-6}–$10^{-4}\,\mathrm{mbar}$ depending on the introduced continuous flow of helium buffer gas. The next three stages, containing the quadrupole mass filter, the ion trap and the TOF-MS, are separated from the previous stages using a gate valve which is closed when the source region needs to be vented. Typical background pressures of 10^{-9}–$10^{-8}\,\mathrm{mbar}$ are achieved when all gas inlets are closed. The ion trap is typically operated at 10^{-6}–$10^{-5}\,\mathrm{mbar}$ determined by the continuous flow of the buffer gas. The trap region is pumped by a $230\,\mathrm{l/s}$ TMP (*Pfeiffer*, TMU 261 P) while all other regions are pumped by three $520\,\mathrm{l/s}$ TMPs (*Pfeiffer*, TMU 521 P).

IR Windows. Along both laser beam paths (path 1/2, Figure 2.8) the vacuum chamber is terminated by 3–$5\,\mathrm{mm}$ thick IR windows with a diameter of $25\,\mathrm{mm}$ allowing to couple the IR laser into the instrument. In order to cover the full mid-IR wavelength region (500–$4000\,\mathrm{cm^{-1}}$) several windows (CaF2, KBr, KRS-5) are available providing different IR transmission efficiency (see Appendix D).

2.3   Multipole RF Devices

The setup contains several multipole arrangements that are used in various ways to manipulate the motion of ions. A decapole is implemented to guide a broad mass range of ions while a quadrupole serves to mass-select ions of a certain mass-to-charge ratio. Furthermore, the ion trap confines the mass-selected ions in 3D space to form a dense ion cloud. In general, the functional principle of the various multipole devices depends on the geometrical arrangement and the application of fast oscillitary inhomogeneous RF fields. The first part of this section aims at providing some theoretical background. The question is addressed why RF fields are needed. Stability criteria for guiding ions are formulated on the basis of the adiabatic approximation in order to explain the operating conditions of the decapole ion guide. In the last part, the ring electrode trap (RET) and its operating principle are described.

2.3.1   Theoretical Insights

Electric Potential of Linear Multipoles.   The electric field within a linear $2n$–multipole, such as a quadrupole ($n = 2$) or decapole ($n = 5$), is generated by $2n$ parallel electrodes which are symmetrically arranged in a circle. The inscribed circle of this arrangement has a radius r_0. Each electrode is provided with the same electric potential Φ_0 whereas adjacent poles have opposite polarity. The essential equation for describing the corresponding electric potential is *Laplace's equation*

$$\Delta\Phi(r) = 0, \tag{2.1}$$

which can be derived from *Maxwell's equations in vacuum* [91]. According to the symmetry of the multipole geometry the potential Φ is best described in polar coordinates (r, ϕ). Assuming infinite long electrodes allows for neglecting the z-dependence. The solution of Eq. (2.1) has then to satisfy the boundary conditions $\Phi(r = r_0, \phi) = \Phi_0 \cos(n\phi)$ and $\Phi(r = 0, \phi) = 0$ which yields [51]

$$\Phi(r, \phi) = \Phi_0 \left(\frac{r}{r_0}\right)^n \cos(n\phi). \tag{2.2}$$

Figure 2.9 illustrates the potential surface of the quadrupole ($n = 2$) for different applied electrostatic potentials Φ_0. A characteristic feature is a saddle point in the center. It is a direct consequence of Laplace's equation that an electrostatic potential cannot have a local minimum in a charge-free two or three dimensional space.[2] A saddle potential is not appropriate for collimating or trapping ions because the potential is weakest at the surface of the electrodes. This results in unstable ion trajectories where the ions are deflected until they hit an electrode. This can be avoided if a fast oscillitary RF potential is applied to the electrodes which leads to a periodic *reversion* of polarity as illustrated by the sequence of potentials in Figure 2.9. The applied potential Φ_0 in Eq. (2.2) is then generally described as the sum of a DC and AC component

$$\Phi_0 = U + V cos(2\pi f t), \tag{2.3}$$

---

[2]This can be understood from the following mathematical point of view. Assuming a potential $\Phi(r)$ would have a local minimum in $\boldsymbol{u}$, its second partial derivatives along every single coordinate r_i would be greater than zero ($\frac{\partial^2 \Phi(\boldsymbol{u})}{\partial r_i^2} > 0$). Hence, their sum cannot be zero which is in conflict with Laplace's equation.
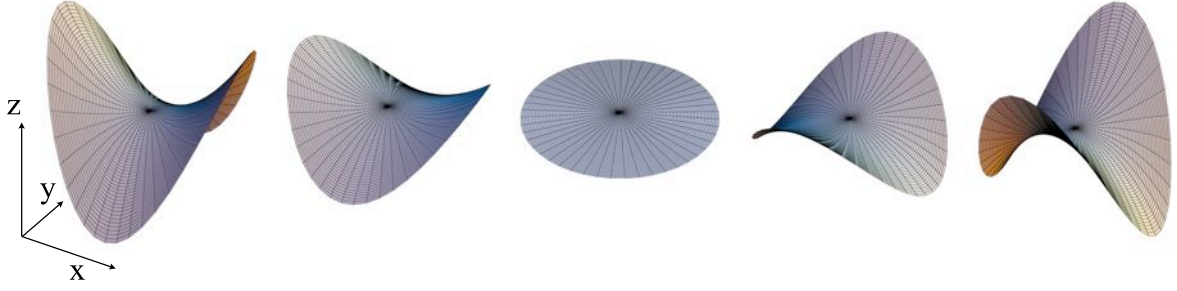
Figure 2.9: Electric potential surfaces of a quadrupole field according to Eq. (2.2).

where U is a DC voltage and V is the peak amplitude of a RF voltage with frequency f. The ions experience a time-averaged potential which shows a minimum in the center of the multipole. This so-called *effective potential* enables a confinement of the ions along the radial direction of the multipole. In practice, stable ion trajectories that allow the ions to pass the linear multipole depend on many parameters, e.g., the applied RF amplitude and frequency. These values have to be chosen in accordance to the ion mass and its initial kinetic energy which is the subject of the following subsection.

Safe Operating Conditions for Linear Multipoles. In order to find stable operating conditions to safely guide ions, stability criteria of the ion motion can be formulated. Note that analytical solutions only exist for oscillating quadrupole fields which lead to the fundamental properties of the quadrupole mass filter developed by W. Paul [92]. In contrast, for higher order multipole fields the ion trajectories are treated within the *adiabatic approximation* proposed by D. Gerlich [51]. Here, the ion motion is governed by the effective potential. According to Ref. [51] the effective potential of a linear multipole is given by

$$V^*(r) = \frac{n^2 q^2 V^2}{4m(2\pi f)^2 r_0^2} \left(\frac{r}{r_0}\right)^{2n-2} + qU \left(\frac{r}{r_0}\right)^n \cos(n\phi). \tag{2.4}$$

In order to derive operating conditions for guiding ions the DC potential U is omitted since this term is only relevant for the functionality of the quadrupole mass filter. Assuming an ion that enters the multipole at the distance r from the center it experiences a potential energy of $V^*(r)$. In the absence of the static potential the ion experiences a pure central force and it will be pushed towards the minimum field at $r = 0$. Thereby its potential energy is converted into kinetic energy and it starts to oscillate around $r = 0$ perpendicular to the multipole axis. In the adiabatic picture the kinetic energy and the potential energy are permanently exchanged. As long as the ion does not gain energy from the field the trajectory remains stable, i.e., it will not hit the electrodes. In contrast, presuming the ion has transverse energy E_t when it enters the field, which is the general case in the experiment, it will get lost if E_t exceeds the effective potential at the surface of the electrode $r = r_0$.

In order to prove the adiabaticity of the motion, a stability parameter η is introduced which mainly depends on the multipole parameters (n, r_0, f, V)

$$\eta(r) = 2n(n-1)\frac{qV}{m(2\pi f)^2 r_0^2} \left(\frac{r}{r_0}\right)^{n-2}. \tag{2.5}$$

In order to ensure stable trajectories the turning radius r/r_0 must be smaller than 1 and the following safe operating conditions are usually required [51]:

$$\eta \left(\frac{r}{r_0} = 0.8 \right) \leq 0.3,$$

$$V^* \left(\frac{r}{r_0} = 0.8 \right) \geq E_t. \tag{2.6}$$

The first criterion together with Eq. (2.5) allows estimating the smallest ion mass that is safely transmitted when a certain RF voltage V is applied:

$$m_{min}(V) = 2n(n-1) \frac{1}{r_0^2} \frac{V}{(2\pi f)^2} \frac{q}{0.3} (0.8)^{n-2}. \tag{2.7}$$

Furthermore, the second criterion allows calculating the minimum RF voltage which is necessary to safely guide an ion mass with a certain transverse energy E_t:

$$V_{min}(m, E_t) = \left(m \frac{4}{n^2} \frac{r_0^2 (2\pi f)^2}{(0.8)^{2n-2}} \frac{E_t}{q^2} \right)^{1/2}. \tag{2.8}$$

2.3.2   Decapole Ion Guide

In the experiment a homebuilt linear decapole ion guide is used which consists of 22 cm long circular electrodes arranged tangent to an inscribed circle with radius $r_0 = 10$ mm. The electrodes have a diameter of 5 mm. The guide is operated at a fixed RF frequency of 1.79 MHz provided by a commercial RF power supply (*Ardara Technologies*). The power supply is capable of supplying a maximum amplitude V_{max} of ± 850 V per electrode.

The decapole serves to guide and collimate the ions formed in the source region. In section 2.1 it has been shown that the ion distribution produced by laser vaporization or ESI covers a broad mass range typically from 50 to 1000 amu. The decapole is preferentially used for collecting the ions because of its capability to safely guide a broad mass range of ions at a time compared to for instance a quadrupole. This is illustrated in Eq. (2.8) which shows that the maximum guided mass for a fixed RF voltage increases with the number of poles n.

Example.   The transverse energy E_t of the ions is assumed to be 2 eV. Using Eq. (2.8) the minimum RF voltage required to safely guide the ions with $m = 1000$ amu is 500 V. This voltage corresponds to a minimum guided mass of 260 amu, according to Eq. (2.7). Therefore, operating with 500 V already covers a broad mass range. However, the transmission of ions can be further increased by filling helium buffer gas into the guide. The ions undergo many collisions with the gas which reduces the kinetic energy. The ions experience smaller oscillations around the center line of the guide leading to collimation of the ion beam. According to the stability criterion Eq. (2.8) the same maximum mass can then be guided at a lower RF voltage. Referring to Eq. (2.7) a lower RF voltage facilitates the transmission of smaller masses.
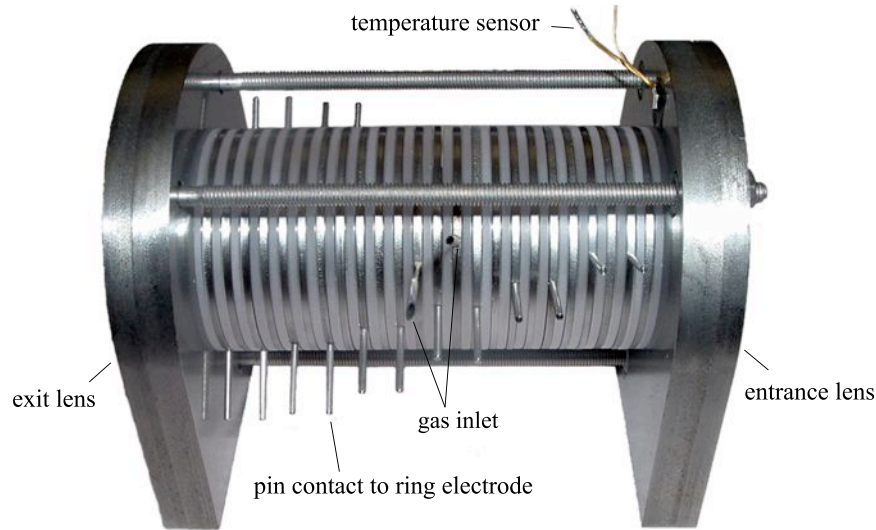
Figure 2.10: Assembly of the ring electrode ion trap.

2.3.3 Ring Electrode Ion Trap

In the IR-PD experiments trapping of the ions becomes necessary in order to accumulate the ions and increase the number density of ions. Furthermore, the stored ions are thermalized to cryogenic temperatures by means of collisions with a buffer gas.

Trap Design. The assembly of the RET is shown in Figure 2.10. It consists of 24 ring electrodes made of molybdenum. The electrodes are 1.5 mm thick and have an inner diameter of about 8.5 mm. Sapphire disks serve as 1 mm spacers in order to electrically isolate the electrodes from one another. All parts are stacked up to form a gas-tight cylinder which is a characteristic feature of this design. Two electrodes in the center contain a hole which allows introducing gas into the trap. Both ends of the cylinder are terminated by an entrance and exit lens. In order to cool the ion trap down to cryogenic temperatures, the assembly is mounted onto a cold head of a closed-cycle helium cryostat (*Sumitomo Heavy Industries*, RDK-205D) by means of an adapted copper block. The temperature of the trap and the cold head can be measured using two silicon diodes (*Lake Shore*, DT-670-SD) fixed to the entrance lens and the copper block, respectively. A heating cartridge (*Janis Research*, 50 W/50 Ω UHV heater) is installed between the ion trap and the cold head. This setup enables to continuously vary the temperature of the trap from approximately 10 K to 350 K using a temperature controller (*Lakeshore*, Model S331).

Electric Configuration. Generally, trapping of ions requires the confinement in three-dimensional space. As already discussed for the decapole ion guide in the previous subsection, confinement along the radial direction, i.e., perpendicular to the trap axis, is achieved by applying an appropriate RF field. For this purpose, the trap is operated at a constant frequency of 1.7 MHz while the RF amplitude can be varied from 0 V to 350 V. Adjacent ring electrodes are provided with opposite phases. In order to confine the ions in the third dimension, i.e., along the axial direction, appropriate electrostatic potentials are applied to the entrance and exit lens. Additionally, the ring electrode arrangement allows modifying the electric potential
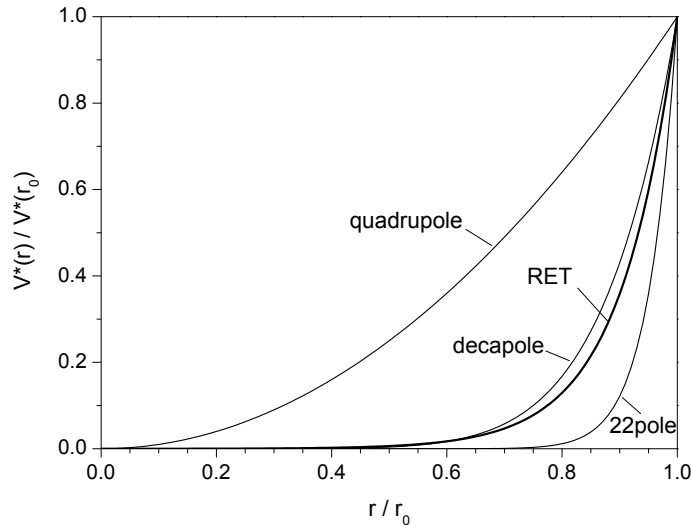
Figure 2.11: Radial dependence of the relative effective potentials $V^*(r)/V^*(r_0)$ of the ring electrode trap ($r_0 = 4.25\,\text{mm}$, $d_0 = 2.9\,\text{mm}$) in comparison to the quadrupole trap ($n = 2$), the decapole ion guide ($n = 5$) and the 22-pole trap ($n = 11$).

along the trap axis. To this end, the 24 electrodes are divided into six zones, i.e., each zone contains a set of four adjacent ring electrodes. Each zone is provided with an adjustable electrostatic potential, superimposed on the RF voltage, which creates an electric field gradient along the trap axis. This configuration offers a high flexibility in order to control the position of the ion packet inside the trap.

The Electric Potential.   In order to describe the electric potential of the RET one has to solve Laplace's equation (2.1). Due to the symmetry, the field geometry is best described in cylindrical coordinates with the radial component r and the axial component z. According to the theoretical description presented by D. Gerlich [51] the effective potential of the ring electrode arrangement is given by

$$V^*(r,z) = \frac{q^2 V^2 \pi^2}{4m\Omega^2 d_0^2} \left[I_1^2 \left(\pi \frac{r}{d_0} \right) \cos^2 \left(\pi \frac{z}{d_0} \right) + I_0^2 \left(\pi \frac{r}{d_0} \right) \sin^2 \left(\pi \frac{z}{d_0} \right) \right] / I_0^2 \left(\pi \frac{r_0}{d_0} \right), \quad (2.9)$$

whereas I_k (k integer) represents the modified Bessel functions of the first kind [93]

$$I_k(r) = \frac{1}{\pi} \int_0^\pi e^{r\cos\theta} \cos(k\theta) d\theta. \tag{2.10}$$

The parameters r_0 and d_0 are determined by the geometry and correspond to the inner radius of the trap and the center-to-center distance of the electrodes, respectively. Figure 2.11 illustrates the radial dependence of the effective potential of the RET (z is set to zero) compared to the quadrupole, decapole and 22-pole arrangement (according to Eq. (2.4)). A characteristic feature of the RET design is the large field-free region formed along the radial direction in contrast to the harmonic effective quadrupole potential. For collisional cooling a wide field-free region is preferred because the ions are quickly thermalized to the ambient temperature of the buffer gas. In a quadrupole trap the ions experience the high RF field close to the walls for longer times and are heated up [94]. A commonly used trap for studying low energy

collisions at very low temperatures is the 22-pole trap [94, 95]. This arrangement has an even steeper effective potential ($\sim r^{20}$) than the RET (Figure 2.11).

Trap Operation. A typical measurement cycle in the experiment involves two operating modes, i.e., loading the trap and extracting ions. During the operation, a constant flow of buffer gas, typically helium, inside the trap enables continuously filling and thermalizing ions. In the filling cycle, the applied DC potentials form a potential well along the trap axis in order to accumulate the ions. The potential of the entrance lens is determined by the kinetic energy of the incoming ions. It is chosen such that the ions can barely overcome the potential barrier at the entrance. A higher potential is applied to the exit lens such that all ions will be reflected back towards the entrance region. Due to multiple collisions with the buffer gas inside the trap, the ions lose sufficient kinetic energy which is then too low for leaving the trap. Thus, the ions are confined to the trap volume and can be accumulated. As the ion density increases, space charge effects arise usually limiting the number of accumulated ions to $10^6 \, \mathrm{cm}^{-3}$ [51]. Due to collisions with the buffer gas, the ions are internally cooled to the ambient temperature. After a filling time of typically about 100 ms, the ions are extracted from the trap by quickly switching the DC trap potentials to form a tailored voltage ramp. The ion packet passes an Einzel lens and is focused into the extraction region of the TOF-MS. The detection of the ions is the subject of Section 2.4.

In the following, some conditions for trapping ions shall be discussed in more detail. Important parameters are the applied DC trap potentials as they strongly influence the trapping performance. During the filling cycle, a smooth, flat potential well is required which ensures gentle trapping of the ions. In contrast, a steep potential causes higher acceleration of the ions which easily leads to collision-induced dissociation (CID) inside the trap, particularly affecting weakly-bound systems. For instance, microhydrated ions can lose one or more water molecules. The induced fragments would then contribute to the subsequent IR-PD process which hampers the measurement. Another example concerns the formation of messenger-tagged complexes in the trap which relies on three-body collisions (see below). The net formation can be substantially reduced when a steep voltage ramp is applied during the trap extraction. The ions gain sufficient kinetic energy resulting in the loss of the messenger due to CID. Table 2.1 shows different DC voltages which are typically applied for trapping messenger-tagged clusters and microhydrated ions. Zone B–C corresponding to the center of the trap are provided with equal potentials resulting in a broad, flat potential minimum along the trap axis. Note that the applied voltages are typically 3–4 V lower for ions formed by laser vaporization in comparison to ESI.

Formation of tagged complexes. The introduced buffer gas is relevant for several processes. For instance, the IR-VPD experiments on metal oxide clusters (Chapters $4-5$), involve the formation of rare gas-tagged species. These weakly bound complexes are formed in the cooled RET by collisions with the rare gas atoms (Rg) according to the following three-body association reaction [17],

$$\mathrm{AB^+ \cdot Rg_{n-1} + 2Rg \rightleftharpoons AB^+ \cdot Rg_n + Rg} \qquad n = 1, 2, \ldots. \tag{2.11}$$
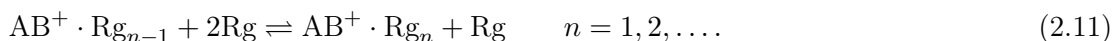
Helium has the smallest polarisability leading to low ion-He binding energies. Therefore, helium complex formation is not always observed, even at the lowest trap temperature. In this case, more polarisable rare gas atoms like neon, argon or krypton are used. The helium

	$Ce_3O_5^+ \cdot Ne$		$V_3O_7^+ \cdot Ar$		$(NaSO_4)_2^{2-} \cdot (H_2O)_5$	
	fill	extract	fill	extract	fill	extract
entrance	7.0	4.0	7.9	6.0	-11.5	-5.0
zone A	6.5	3.0	6.4	5.1	-9.2	-4.0
zone B	5.0	2.25	6.1	4.3	-9.0	-2.5
zone C	5.0	2.1	6.1	2.8	-9.0	-1.9
zone D	5.0	1.4	6.1	2.2	-9.3	-1.3
zone E	5.7	1.0	8.0	1.3	-14.0	-0.6
zone F	30.0	0.3	8.0	0.4	-14.0	0.0
exit	30.0	0.0	12.0	0.0	-15.0	0.0

Table 2.1: Various DC voltage sets (in volt) applied for trapping different ions. Three examples are shown corresponding to $Ce_3O_5^+ \cdot Ne$ (left) and $V_3O_7^+ \cdot Ar$ (middle) formed by laser vaporization and $(NaSO_4)_2^{2-} \cdot (H_2O)_5$ (right) formed with the electrospray source.

buffer gas is then mixed with a small amount, typically $\sim 1\%$, of the respective gas. In order to avoid condensation of these gases on the trap surface, the trap temperature has to be increased according to the freezing point of the gas (Ne: 20 K, Ar: 50 K, Kr: 65 K).

2.4 Detection Scheme

TOF Mass Spectrometer. The trapped ions are extracted from the RET and focused into the extraction region of a linear Wiley-McLaren TOF-MS [96]. The time that the ions need to travel from the trap to the TOF extraction region depends on their kinetic energy which is determined by the applied DC voltage ramp of the trap and the pressure of the buffer gas. During that time the TOF electrodes are grounded. Once the ions reach the extraction zone, short ($\sim$50 µs) high voltage pulses ($U_{max} = \pm 5$ kV) are applied to the TOF extraction and acceleration plates using two fast push-pull switches (*Behlke Power Electronics GmbH*, 6 kV HTS 61-03-GSM). During the extraction the ions are sampled by a large 20 mm aperture, then traverse a $\sim$1 m long field free region and separate out in time according to their mass-to-charge ratio. Ultimately, the ions are detected using a MCP detector and its signal is used to record the TOF spectrum. The output signal from the MCP is amplified by a fast pre-amplifier (*Ortec*, 9305 Fast Preamp) and sampled by a 300 MHz, 12 bit digitizer card (*Acquiris*, DP310) which is installed in the PC for real-time data collection.

Channeltron Detector. The voltages of all ion optics are optimized by monitoring the ion signal using a channeltron electron multiplier (*Burle*) which is installed along the trap axis, behind the TOF electrodes, in an off-axis configuration. In this mode of operation the TOF electrodes are grounded and the RET is operated in the RF-only mode so as to simply guide the mass-selected ions towards the channeltron detector. An amplifier discriminator receives the output signal from the channeltron and produces TTL pulses which are sent to a counter. The channeltron is used for recording quadrupole mass spectra.

IRPD Measurement Cycle. A typical measurement cycle is divided into three steps, i.e., extracting the ion packet from the trap, irradiation of the parent ions with the IR laser
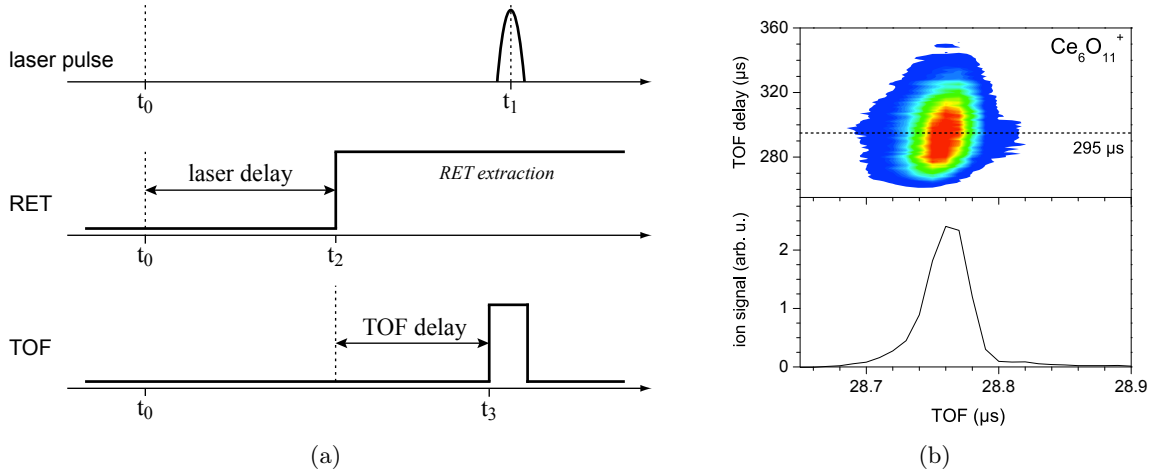
Figure 2.12: **(a)** Triggering scheme of the IR-PD experiment. **(b)** TOF delay scan of mass-selected $Ce_6O_{11}^+$ clusters (upper panel). A TOF delay scan represents a matrix comprising several TOF mass spectra (rows) measured for different TOF delay times. In the present scan the ion yield of $Ce_6O_{11}^+$ is plotted for different TOF delay times (rows) in the range from $255\,\mu s$ to $360\,\mu s$ (blue: low intensity, red: high intensity). Setting the TOF delay time to $295\,\mu s$ (dashed line) maximizes the ion yield (bottom panel).

pulse and subsequent recording of TOF mass spectra. Figure 2.12(a) illustrates the triggering scheme applied during the IR-PD experiments. A delay generator is used to control the triggers for the trap, the TOF high voltage switches and the digitizer card. The overall experiment is externally triggered by the applied IR laser system usually operating at a repetition rate of $10\,Hz$. Depending on the wavelength range one of two laser systems is used, i.e., either the free electron laser FELIX or a tabletop IR laser system (Section 2.5). At time t_0 the laser system provides an external trigger several hundreds of microseconds (FELIX: $500\,\mu s$, tabletop: $250\,\mu s$) prior to the IR laser pulse emission at time t_1 (top, Figure 2.12(a)). After a filling time of $98\,ms$ the ions are extracted from the trap by applying a DC voltage ramp for $2\,ms$ at time t_2 which is defined with respect to t_0 (middle, Figure 2.12(a)). Subsequently, the ions are transfered to the TOF extraction zone which typically takes $50\,\mu s$ to $200\,\mu s$. This time window is referred to as *TOF delay time* and defines the delay of the applied TOF high voltage pulses at time t_3 according to $t_3 = t_2 + $ TOF Delay (bottom, Figure 2.12(a)). The TOF delay time is fine adjusted to obtain a maximum TOF ion signal. To this end a TOF delay scan can be recorded shown in Figure 2.12(b). Keeping the TOF delay time fixed, the whole sequence comprising the trap extraction and ion detection is further shifted in time determined by the *laser delay time* according to $t_2 = t_0 + $ Laser Delay (middle, Figure 2.12(a)). This parameter delays the trap extraction and allows tuning the point in time when the ion packet is irradiated with the IR laser pulse. In the following, three cases will be discussed:

i) **$t_3 = t_1$**: The IR laser pulse emission and TOF high voltage pulses are triggered at the same time. The ion packet is irradiated in the TOF extraction zone at the very beginning of the acceleration phase. This mode can be viewed as the standard. Note that the photofragment ion yield can be measured background-free only in the absence of CID fragments. Otherwise the following mode is preferred.

ii) **$t_3 < t_1$**: The IR laser fires after the TOF high voltage pulses have been applied. The

ion packet is then irradiated in the TOF extraction zone *during* the acceleration phase. This scheme is advantageous if CID fragment ions are present in the ion packet. The "pre-acceleration" already separates the parent ions from the CID fragments prior to the irradiation according to their mass-to-charge ratio. As a consequence, the IR-PD and CID fragments are separated in time which allows measuring the photofragment ion yield background-free. This scheme is explained below based on background-free IR-VPD experiments on Kr-tagged suberate dianions (Subsection 2.4.1).

iii) $t_2 > t_1$: The IR laser fires prior to the trap extraction and the ion packet is irradiated directly in the trap.

Photodissociation Cross Section. An IR-PD spectrum is obtained by plotting the photodissociation cross section σ as a function of the laser frequency ν. It is generated from the TOF spectra which are measured as a function of the laser frequency ν. A time window Δt_i is defined for each mass channel i, corresponding to the parent and fragment ions, and the frequency-dependent ion yield $I_i'(\nu)$ is determined by integration. During the measurement each ion signal is subject to fluctuations in the source conditions. These fluctuations are canceled out by normalizing each ion yield to the total ion signal,

$$I_i(\nu) = \frac{I_i'(\nu)}{\sum_j^{all\ ions} I_j'(\nu)}. \tag{2.12}$$

According to Eq. (2.12) the normalized parent and fragment ion yield, $I_p(\nu)$ and $I_f(\nu)$, respectively, are given by

$$I_p(\nu) = \frac{I_p'(\nu)}{\sum_j^{all\ ions} I_j'(\nu)}, \tag{2.13}$$

$$I_f(\nu) = \frac{\sum_i^{all\ fragments} I_i'(\nu)}{\sum_j^{all\ ions} I_j'(\nu)}. \tag{2.14}$$

Ultimately, $\sigma(\nu)$ is determined from either the parent ion signal (Eq. (2.13)) or fragment ion signal (Eq. (2.14)) using the following equations,

$$\sigma_p(\nu) = -\ln[I_p(\nu)]/P(\nu), \tag{2.15}$$

$$\sigma_f(\nu) = -\ln[1 - I_f(\nu)]/P(\nu), \tag{2.16}$$

where the intensities are normalized to the frequency-dependent laser pulse energy $P(\nu)$. When the photofragment ion signals are measured background-free, the IR-PD spectrum is obtained from Eq. (2.16).

Alternatively, TOF mass spectra can be measured in the difference mode of operation, i.e., mass spectra are alternately measured with and without laser radiation. The integrated parent ion yield $I_p'(\nu)$ is then normalized to the parent ion yield I_0 measured without the IR laser applied. An IR-PD depletion spectrum is derived by plotting $\sigma_p(\nu)$ using the following equation [97],

$$\sigma_p(\nu) = -\ln\left[\frac{I_p'(\nu)}{I_0}\right]/P(\nu). \tag{2.17}$$

Remark. We often find a good agreement between experiment and theory by normalizing the IR-PD spectra to the variations in the pulse energy $P(\nu)$. Note that this approach differs from Eq. (1.7) which shows that the photon fluence $F(\nu)$ should actually be used. Basically, this normalization method assumes a single photon absorption process which is not the general case in the present experiments. $F(\nu)$ corresponds to the number of photons that pass the cross sectional area A of the geometrical interaction volume, which is determined by the overlap between the ion packet and the laser beam. However, A is not well-determined due to two reasons: (i) the size of the ion packet is not exactly known and (ii) the laser beam diameter changes with frequency. Thus, the determination of $F(\nu)$ is difficult. The pulse energy, on the other hand, can easily be measured. The laser beam is focused through the ion trap (beam path 1, Figure 2.8) and the pulse energy is then recorded behind the exit window.

Due to the collimation of the laser beam, we assume that A is limited by the laser beam diameter. The measured pulse energy may then be used to determine the (relative) number of photons n that penetrate the ion packet. However, normalizing the IR-PD spectra to n often underestimates the relative band intensities, especially in the low energy region of the covered spectral range (typically a factor of 2–3 in wavenumber). A better agreement with the simulated IR absorption spectra is often obtained, when the photon energy is additionally considered, that is using the pulse energy as described in Eq. 2.15–2.17. The good agreement may result from a partial compensation of several effects such as changes in the laser beam diameter or changes in the IR-PD efficiency due to multiple photon absorption.

2.4.1   Example: Background-free IR-PD Measurement

The IR-VPD experiments on Kr-tagged bare and monohydrated suberate dianions $^-$OOC– $(CH_2)_6$–COO$^-$ (SA^{2-}) nicely exemplify the procedure of a background-free measurement. For these experiments (Section 6.3), the monohydrated complexes $SA^{2-} \cdot H_2O$ are mass-selected by the quadrupole mass filter and accumulated in the RET containing a 1% Kr in He gas mixture at a temperature of 63 K. The TOF mass spectrum (a) in Figure 2.13 reflects the ion distribution inside the trap after an accumulation of 98 ms. The mass-selected ion peak $SA^{2-} \cdot H_2O$ is observed at 7.58 µs. Under the present experimental conditions some of the ions entering the trap undergo CID, forming the bare dianion SA^{2-} (7.22 µs). Both dianions, SA^{2-} and $SA^{2-} \cdot H_2O$, can also undergo three-body collisions involving a Kr atom, forming the corresponding Kr-tagged complexes $SA^{2-} \cdot Kr$ and $SA^{2-} \cdot H_2O \cdot Kr$, observed at $\sim$8.8 and $\sim$9.1 µs, respectively. These peaks consist of multiple masses and reflect the natural isotope distribution of Kr.

The next step of the experiment involves IR-VPD of the Kr-tagged complexes. Dissociation proceeds via loss of a Kr atom leading to the formation of SA^{2-} and $SA^{2-} \cdot H_2O$. Note, although Kr-complex formation is accomplished, there remains a significant amount of unreacted ions SA^{2-} and $SA^{2-} \cdot H_2O$ ((a), Figure 2.13). They contribute a background signal and small fluctuations of these intense peaks would introduce unwanted noise in the IR-VPD spectra. Therefore, in order to measure the photofragment ion signal background-free, the IR laser pulse is applied 1 µs after the high-voltage pulses have been applied to the TOF extraction plates, that is, *during* the acceleration phase of the ions. Prior to the irradiation all ions already gain velocity according to their mass-to-charge ratio and the parent (Kr-tagged species) and daughter ions (without Kr atom) become separated in space. The photofragment ion signal then leads to additional peaks (labeled with an asterisk) in the TOF mass spectra ((b), Figure 2.13). The peaks lie in-between the corresponding parent and daughter ion peaks. Their exact
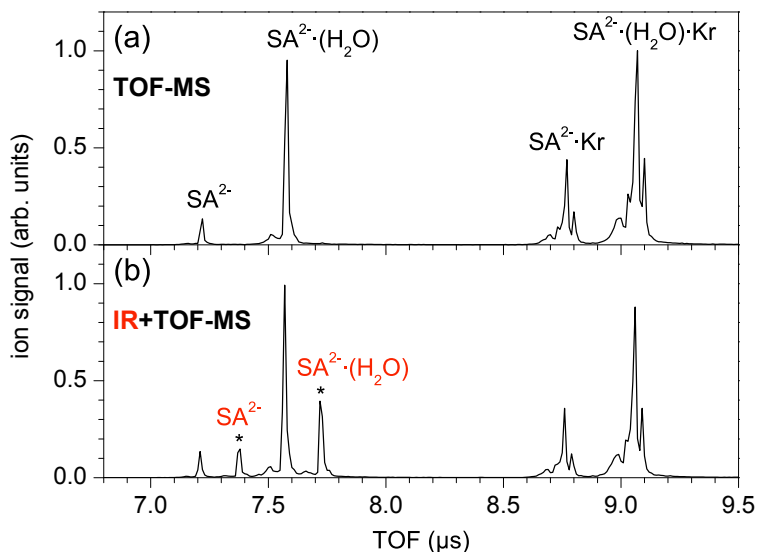
Figure 2.13: TOF mass spectra reflecting different stages of the background-free IR-PD measurement. Mass-selected monohydrated suberate dianions ($SA^{2-} \cdot H_2O$) are accumulated in the RET filled with a 1% Kr/He buffer gas mixture at $63\,K$. **(a)** Ion distribution inside the RET when no IR laser is applied. Bare suberate dianions (SA^{2-}) are formed by CID. Kr-complex formation is accomplished for both bare and monohydrated dianions. **(b)** TOF mass spectrum measured with the IR laser set on resonance ($2925\,cm^{-1}$, C–H stretching mode). Laser pulse is triggered shortly after the high-voltage pulses have been applied to the TOF extraction plates. The IR-VPD signals at 7.38 and $7.72\,\mu s$ (labeled with asterisk), arising from loss of Kr atoms, are detected background-free. Adapted with permission from Ref. [31]. Copyright (2009) American Chemical Society.

position depends on the adjusted *laser delay time.*

2.5 Infrared Light Sources

Different IR laser systems were used for the IR-PD experiments. The Free Electron Laser for Infrared eXperiments FELIX was primarily used. It is located at the FOM Institute for Plasma Physics in Nieuwegein (The Netherlands). The operating principle and its key features summarized here are based on Ref. [57, 98]. It will be followed by a description of a solid-state IR laser system available in our group at the Fritz-Haber-Institute in Berlin.

2.5.1 The Free Electron Laser for Infrared eXperiments (FELIX)

Operating Principles of a Free Electron Laser

In a FEL, light is generated from *free electrons* which pass a periodic magnetic field structure at relativistic energies. This approach offers great flexibility to produce intense light over a broad spectral range, in contrast to conventional laser systems where electrons are bound to atoms, molecules or crystals. Figure 2.14 illustrates the main components of a typical FEL. Electrons are produced by an electron gun and accelerated to relativistic energies. The beam is then injected into an *undulator* which is the central part of the FEL. The undulator is an assembly of alternating permanent magnets with period λ_u forming a periodic magnetic
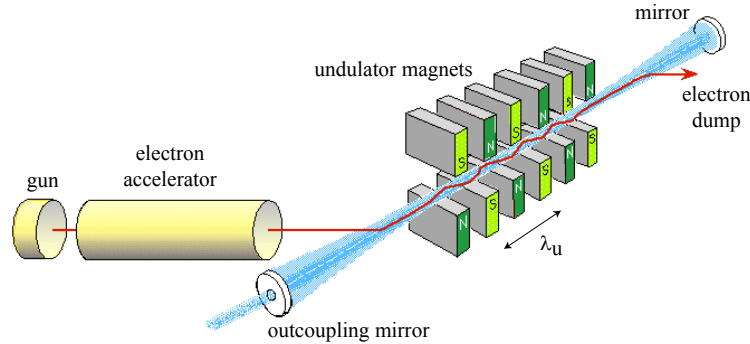
Figure 2.14: Generic layout of a free electron laser. Electrons are emitted from an electron gun, accelerated, and injected into an undulator. The permanent magnets produce a periodic magnetic field with period λ_u. The electrons pass the undulator and emit light which is stored in a resonator. A fraction of the light is coupled out. Adapted with permission from Ref. [57]. Copyright (2003) American Chemical Society.

field perpendicular to the direction of the electron beam (red trace, Figure 2.14). Obeying *Lorentz' force law*, the electrons experience a *wiggling* motion while traversing the undulator which results in the emission of radiation. The wavelength of the emitted light is determined by the path length traveled by the electrons per undulator period. Owing to the transverse motion, this path length is longer than the undulator period λ_u by a factor $(1 + K^2)$, where the dimensionless parameter K accounts for the magnetic field strength [57]. Moreover, since the electrons move with a velocity v_z close to speed of light c, the wavelength of the radiation is influenced by two relativistic effects. First, in the rest frame of an electron, the undulator assembly appears contracted and the period λ_u is reduced by the relativistic Lorentz factor

$$\gamma = \frac{E}{m_0 c^2} = \frac{1}{\sqrt{1 - \beta^2}} \qquad \text{with} \qquad \beta = v_z/c, \tag{2.18}$$

where E is the energy of the electron and m_0 its rest mass. Second, in the laboratory frame the wavelength of the emitted light is subject to a strong Doppler-shift and further reduced by a factor of 2γ. Furthermore, the energy of the radiation is concentrated in a narrow cone around the forward direction [57]. Considering all above-mentioned effects, the wavelength of the emitted radiation is given by the formula

$$\lambda_{emission} = \frac{\lambda_u}{2\gamma^2} \left(1 + K^2\right). \tag{2.19}$$

At the beginning of the emission, the spatial spread of the electrons inside the undulator is large compared to $\lambda_{emission}$. Therefore, the electrons do not emit coherently and the radiation is usually not very intense. In order to force the electrons to emit coherently, the undulator is placed inside an optical resonator comprised of two high-reflectivity mirrors at either side (Figure 2.14). In this configuration the emitted radiation is stored between both mirrors. When new electrons enter the cavity, they interact with the inhomogeneous electromagnetic field and experience a so-called *ponderomotive force*. This force modulates the density of the injected electrons along the longitudinal axis of the undulator. The electrons are bunched to equally spaced slices on the scale of the emitted wavelength. This effect is referred to as *microbunching* and causes all electrons to radiate in phase which leads to an increase of the
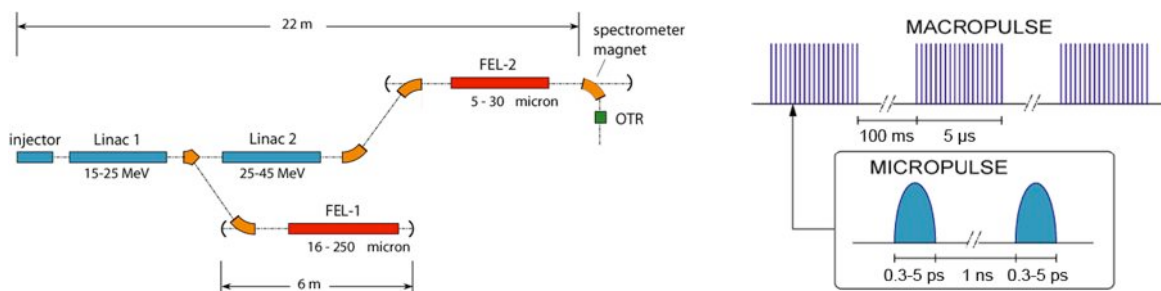
Figure 2.15: Left: Schematic View of the Free Electron Laser for Infrared eXperiments (FELIX). Two modes of operation are possible: The electrons are either accelerated only in the first stage (Linac 1) and steered into the undulator FEL 1 for the production of far-IR light, or they can be further accelerated in the second stage (Linac 2) enabling the production of mid-IR light inside the undulator FEL 2. **Right:** The pulse structure of the radiation produced by FELIX. Reprinted with permission from Ref. [57]. Copyright (2003) American Chemical Society.

radiation power by many orders of magnitude. The radiation power is proportional to N^2, where N is the number of undulator periods. Ultimately, a small fraction of the coherent radiation is coupled out by means of an outcoupling mirror (Figure 2.14).

Characteristics of FELIX

At FELIX electron pulses with an energy of 3.8 MeV are initially produced by an assembly consisting of an electron gun, modulated at 1 GHz, a prebuncher and a buncher. Two RF linear accelerators (Linac 1 and 2) are installed which allow accelerating the electrons to energies of 15–25 or 25–45 MeV (left, Figure 2.15). Behind each accelerator stage the electron beam can be steered into an undulator placed within an optical cavity which has a total length of 6 m (FEL-1 and FEL-2, Figure 2.15). The cavity length of the resonator is defined by two gold-plated copper mirrors, one attached to a translation stage. Each undulator contains two rows of 38 pairs of permanent magnets with a period length of 65 mm. Behind the undulator, the electron beam is bent out of the resonator and dumped. One mirror contains a small hole serving to couple out a small fraction of the radiation which is then guided through a vacuum system to the experiment.

FELIX is well suited to perform vibrational spectroscopy on molecules in the gas phase, because it provides tunability over a wide spectral range (5–250 µm) and high fluence on the microsecond time scale. In order to tune the emitted wavelength during the IR experiments, the magnetic field strength is varied by changing the gap between the pairs of magnets. According to the specified electron-beam energy, FEL-1 (lower electron energies) produces radiation in the far-IR region (16–250 µm) and FEL-2 (higher electron energies) provides light in the mid-IR region (5–30 µm). The latter is used for the experiments presented in this thesis. The experiments are performed on a moving ion packet. The packet moves with velocities on the order of several 1000 m/s and is irradiated by a collimated IR beam with a diameter of a few mm. The interaction time between a molecule and the light is thus on the order of microseconds. Therefore, high fluence on the microsecond time scale is important in order to drive the multiple photon absorption process (Section 1.3).

The time structure of the FELIX pulse (right, Figure 2.15) is determined by the time structure of the electron beam. FELIX is typically operated with a repetition rate of 10 Hz and a macropulse length of about 5 µs. Each macropulse consists of micropulses with a spacing

of 1 ns. The spectral bandwidth is determined by the micropulse length which can be adjusted from 300 fs to several picoseconds. In the present experiments, the bandwidth is about 0.2–0.3 % root mean square of the central wavelength. Such bandwidths correspond to typical output energies of up to 40 mJ per macropulse in the mid-IR region.

2.5.2   Nd:YAG Pumped OPO/OPA Infrared Laser System

The main component of this laser system is a tunable optical parametric oscillator (OPO)–optical parametric amplifier (OPA) converter system designed by Dean Guyer (*LaserVision*) [99]. The oscillator and amplifier stages contain a set of nonlinear crystals, KTP (Potassium Titanyl Phosphate, $KTiPO_4$) and KTA (Potassium Titanyle Arsenate, KTiOAsO4), respectively, where frequency conversion is accomplished by means of non-linear optical processes such as difference frequency mixing (DFM). In order to generate IR radiation the system requires a 1064 nm pump beam provided by a pulsed Nd:YAG laser. The pumped LaserVision system then converts the incoming 1064 nm radiation into mid-IR radiation which is tunable from 2.1 µm to 5.0 µm. The tunable range can be further extended to the far-IR region (5.0–16.0 µm) using an additional $AgGaSe_2$ crystal behind the OPA stage.

    Two OPO/OPA systems are available in our group. They differ in the number of crystals in the OPO stage and provide different laser pulse energies. The output specifications of both laser systems are summarized in Table 2.2. The high-power system (referred to as *double OPO*) contains two KTP crystals in the OPO stage. The 1064 nm pump light is provided by a pulsed, *seeded* Nd:YAG laser (*Continuum*, Powerlite DLS 8000). It operates at 10 Hz and produces 7 ns (FWHM) long pulses with pulse energies of up to 1.05 J. Using a pump energy of 550 mJ the power output can be as high as 34 mJ in the mid-IR region. The seeded pump beam results in a spectral bandwidth of about $1.3 \, cm^{-1}$. The second LaserVision system (referred to as *single OPO*) contains a single KTP crystal in the OPO stage and is pumped by a pulsed, *unseeded* Nd:YAG laser (*Innolas*, Spitlight 600). The pump laser is also operated at 10 Hz providing 7 ns (FWHM) long pulses with pulse energies up to 800 mJ. Using a pump energy of 550 mJ this system yields pulse energies of up to 12 mJ in the mid-IR. Owing to the unseeded pump, the spectral bandwidth is slightly increased to $3.6 \, cm^{-1}$. The operating

specification		double OPO	single OPO
tuning range	*mid-IR*	$2000 - 4700 \, cm^{-1}$	
	far-IR	$625 - 2000 \, cm^{-1}$	
pulse energy	*mid-IR*	$\leq 34 \, mJ$	$\leq 12 \, mJ$
	far-IR	$\leq 4 \, mJ$	$\leq 0.5 \, mJ$
spectral bandwidth	*mid-IR*	$\sim 1.3 \, cm^{-1}$	$\sim 3.6 \, cm^{-1}$
	far-IR	$\sim 1.8 \, cm^{-1}$	$\sim 5.1 \, cm^{-1}$
pump energy (1064 nm)		$\sim 550 \, mJ$ seeded	$\sim 550 \, mJ$ unseeded
pulse duration		7 ns	
repetition rate		10 Hz	

Table 2.2: Output specifications of the LaserVision IR OPO/OPA laser systems.

principle is the same for both laser systems and is explained in the following section based on the double OPO system.

Operating Principle

A schematic of the double OPO laser system is illustrated in Figure 2.16(a). The 1064 nm fundamental of the pulsed, seeded Nd:YAG laser is steered into the LaserVision system. A telescope at the entrance collimates the beam to fit the size of the crystals. A beam splitter divides the horizontally polarized incoming 1064 nm pump into two separate beam lines. Both components pass a beam attenuator containing a rotatable half-wave plate which allows continuous variation of the intensity. One third of the pump is directed into a KTP crystal for frequency doubling in order to produce 532 nm light serving as the pump for the OPO stage. The remainder of the 1064 nm beam is used as a pump source for the OPA stage. In both stages, each pump photon is converted into a signal and idler photon that sum in energy to that of the pump,

$$\frac{1}{\lambda_{\text{pump}}} = \frac{1}{\lambda_{\text{signal}}} + \frac{1}{\lambda_{\text{idler}}} \qquad (\lambda_{\text{signal}} < \lambda_{\text{idler}}) \,. \tag{2.20}$$

For the conversion process to be efficient, the phase matching condition $\boldsymbol{k}_{\text{pump}} = \boldsymbol{k}_{\text{signal}} + \boldsymbol{k}_{\text{idler}}$ needs to be fulfilled. In the LaserVision system phase matching is met by angle tuning the crystals in the horizontal plane by means of stepper motors. The 532 nm-pumped OPO stage contains two counter-rotated KTP crystals which produce signal radiation in the near-IR ($710 < \lambda_{\text{signal}} < 880$ nm) and idler radiation in the intermediate-IR ($1350 < \lambda_{\text{idler}} < 2120$ nm), illustrated in Figure 2.16(b). The idler wave (vertically polarized) from the OPO stage is used as the seed beam for the signal wave (horizontally polarized) of the OPA stage. Therefore, a variable waveplate is placed between both stages which rotates the polarization of the OPO idler beam. Thus, it becomes horizontally polarized and is then combined with the delayed 1064 nm beam for DFM in the OPA stage (Figure 2.16(b)). Two pairs of counter-rotated KTA crystals mix the OPO idler radiation with the 1064 nm pump light producing tunable radiation in the mid-IR region from 2136 nm to 5020 nm (OPA idler wave), given by

$$\bar{\nu}_{mid-IR} \left(\text{cm}^{-1} \right) = 10^7 \cdot \frac{1}{\lambda_{\text{idler}}^{OPA} \, (\text{nm})} = 10^7 \cdot \left(\frac{1}{1064 \, \text{nm}} - \frac{1}{\lambda_{\text{idler}}^{OPO} \, (\text{nm})} \right) . \tag{2.21}$$

As the mid-IR photons are created the OPO idler wave is amplified which then becomes the signal wave ($1350 < \lambda_{\text{signal}} < 2120$ nm) of the OPA stage. A Brewster plate polarizer is installed behind the OPA stage allowing to select either the signal or idler beam.

Both signal and idler from the OPA, become relevant for producing light in the longer wavelength region. Optionally, a AgGaSe$_2$ crystal can be installed behind the OPA stage. Here, the OPA idler wave undergoes DFM with the OPA signal wave generating tunable radiation covering part of the far-IR region ($5.0 - 16.0$ µm). This radiation is coupled out using either a Si (< 10 µm) or Ge (> 10 µm) filter.

(a)

(b)
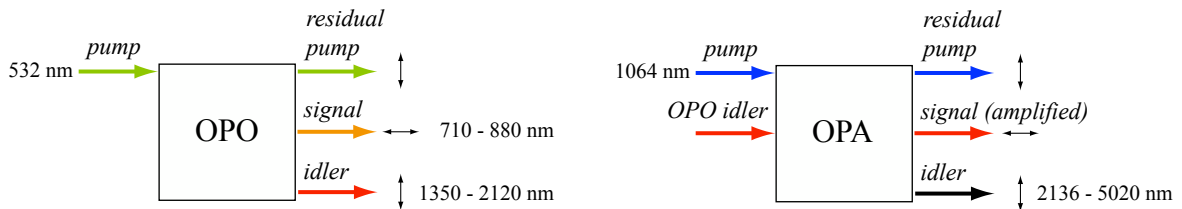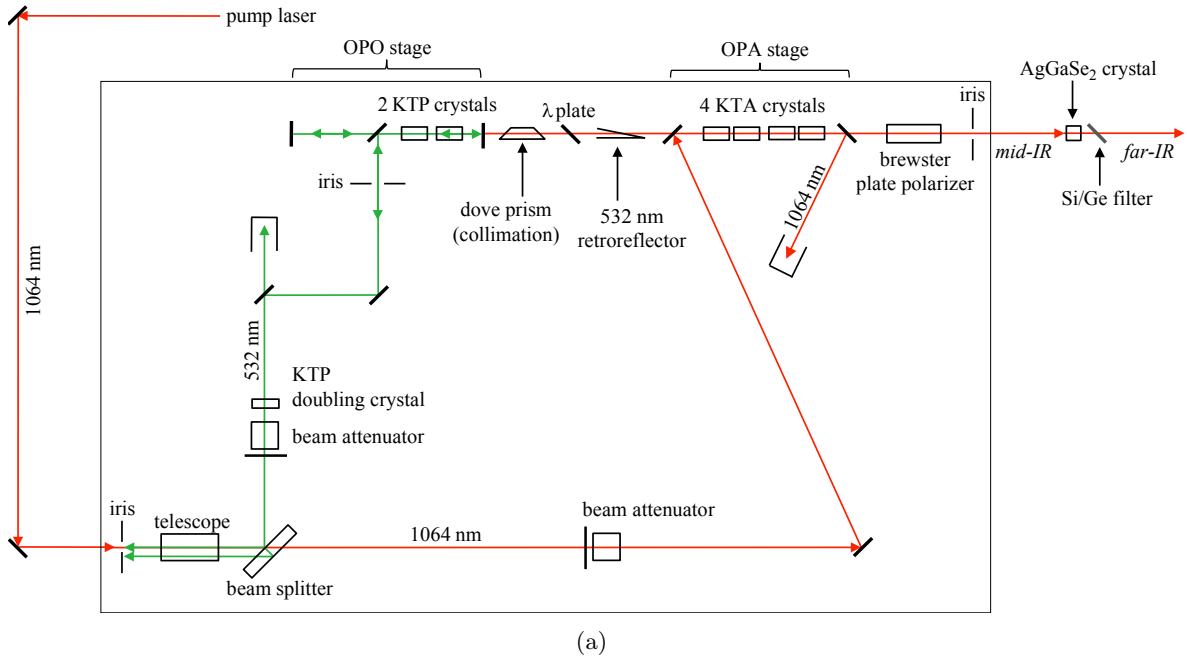
Figure 2.16: (a) Schematic overview of the OPO/OPA IR laser system from LaserVision. The 1064 nm pump beam, provided by a pulsed Nd:YAG laser, is efficiently converted into mid-IR radiation by means of non-linear optical processes in the OPO and OPA crystals. The colored arrows are used to depict the beam path and the wavelength of the light in each stage. **(b)** Frequency conversion processes occuring in the OPO and OPA stages of the laser system. The horizontal and vertical black arrows indicate the polarization of the laser beams with respect to the plane spanned by the laser system.

Chapter 3

Gas Phase Vibrational Spectroscopy of $V_3O_{6-8}^+$: Messenger Effects

IR-MPD of metal oxide cluster ions often yields vibrational spectra that are difficult to interpret, e.g., owing to broad absorption bands. Therefore, the messenger atom technique is used to investigate the structures of these ions. To this end a loosely bound rare gas atom is typically attached to the cluster ion and IR-PD experiments are then performed on this weakly bound complex. The ion-rare gas atom interaction is typically weak and the vibrational spectrum of the messenger complex is assumed to reflect the IR spectrum of the bare ion except for minor shifts in the vibrational frequencies. However, this assumption is not always appropriate, especially for cations and when heavier rare gas atoms are used. The positive charge can strongly polarize a rare gas atom resulting in an interaction that induces more dramatic effects on the cluster properties. Here, the IR signatures of messenger-tagged complexes $V_3O_{6-8}^+ \cdot M$ (M = He, Ne and Ar) are presented, demonstrating that a messenger atom can change the energetic ordering of the isomers. The study shows that the structure of $V_3O_{6-8}^+$ delicately depends on the type but also on the number of messenger atoms in the complex.

3.1   Introduction

Due to their structural variability and redox activity vanadium oxide containing materials are used in heterogeneous catalysis [12], predominantly in selective oxidation processes for the production of olefines. Recently, much effort has been directed towards the production of nanostructured vanadium oxide materials [101, 102], with the aim of optimizing their activity and selectivity. However, in most supported transition metal oxide catalysts, neither the size and distribution of the active particles on the support surface, nor their structure is sufficiently known [103]. Studies on size-selected transition metal oxide particles in the gas phase, i.e., in the absence of any interactions with a medium or support [104], allow for separation of the particle size from support effects, and, thereby lead to a better understanding of the structure-reactivity relationship. Ultimately, one would like to learn how the gas phase structures differ from those of supported clusters, the structure of bulk oxides and other aggregates such as thin films [19, 105, 106].

Preliminary structural investigations on trinuclear vanadium oxide cluster cations $V_3O_{6-8}{}^+$ were performed by M. Brümmer as part of his PhD research [61, 100]. Regarding the cluster $V_3O_7{}^+$, the study compared the vibrational spectrum of the bare ion to the spectrum of the Ar-complex $V_3O_7{}^+\cdot$Ar. Surprisingly, both IR spectra were distinctly different suggesting that the geometries of the bare and Ar-tagged cluster were different. These findings were supported by DFT calculations predicting a cage structure for bare $V_3O_7{}^+$ whereas a ring structure was found to be more stable in the presence of an Ar atom. Similar measurements were performed on $V_3O_8{}^+$. DFT calculations also predicted both cage and ring isomers for the bare ion. The IR-MPD spectrum of bare $V_3O_8{}^+$ provided evidence for a cage structure containing a peroxo group [100, 107]. Preliminary IR-VPD results were also reported for the Ar-tagged complex $V_3O_8{}^+\cdot$Ar [61]. However, the measured IR spectrum did not allow for a reliable structural assignment. IR-VPD experiments were also performed on the messenger complex $V_3O_6{}^+\cdot$Ar$_2$ [15, 61]. Its vibrational spectrum featured broad structured absorption bands making the structural assignment ambiguous. The IR spectrum was tentatively assigned to a chain-like structure, although some experimental bands were not reproduced by the simulated IR spectrum.

In the present study, complementary IR-VPD spectra of messenger-tagged $V_3O_{6-8}{}^+$ clusters are measured. In contrast to the preliminary experiments, different types of messengers (He, Ne, Ar) are used which allows examining their effects on the cluster properties in more detail, such as the relative stability of different isomers. For these investigations, a new instrument is used enabling to detect all ions simultaneously. The chapter aims at giving a phenomenological description of the observed messenger effects. The first section picks up on the previous investigation of $V_3O_7{}^+$. The former study indicates that the cation-Ar interaction induces a structural change of the bare ion, namely from a cage to a ring motif. However, some issues remain unexplained. For instance, what is the mechanism of the observed structural interconversion? How is this mechanism influenced by the type of the messenger atom, in particular when less polarisable rare gas atoms are used? To address these questions, the IR signature of the Ne-tagged complex $V_3O_7{}^+\cdot$Ne is investigated and compared to the IR-VPD spectrum of the Ar-tagged complex $V_3O_7{}^+\cdot$Ar that is remeasured in this work. Aided by DFT calculations on the bare as well as on the rare gas-tagged complexes, the interconversion between the cage and ring structure is discussed. Furthermore, the question is raised how the structure of a cluster is affected when multiple messenger atoms are attached. Several interesting effects are discussed based on IR-VPD measurements on $V_3O_8{}^+\cdot$Ar$_2$ and $V_3O_6{}^+\cdot$He$_{1,4}$.

3.2   Experimental Methods

The IR-VPD experiments are carried out on the ion trap–tandem mass spectrometer (Section 2.2). Vanadium oxide clusters are produced by laser vaporization. For the measurements the single rod target laser vaporization source was implemented (Section 2.1.1). In brief, the second harmonic (532 nm) of a pulsed Nd:YAG laser is used to vaporize the vanadium target material. The plasma is entrained in a carrier gas pulse of 0.25 % O_2 seeded in helium and vanadium oxide clusters are subsequently formed through expansion in a clustering channel held at a temperature of 250 K. A typical mass spectrum of cationic vanadium oxide clusters is presented in Section 2.1.1 (Figure 2.5). Mass-selected clusters $V_3O_n^+$ ($n = 6 - 8$) are accumulated and thermalized for 98 ms by multiple collisions with a helium buffer gas in an cryogenically-cooled ion trap. Here, the messenger-tagged complexes are formed by three-body association. Different rare gas atoms are used (He, Ne, Ar). To this end, a buffer gas of either pure He, a Ne/He or Ar/He gas mixture (typically 1 %) is introduced at ion trap temperatures of 15 K, 24 K and 55 K, respectively.

After the ion packet is extracted from the trap, it interacts with an IR laser pulse in the TOF extraction zone and high voltage pulses are applied for recording TOF mass spectra. Pulsed IR radiation is used from FELIX operated at 10 Hz in the spectral range from $350\,\mathrm{cm}^{-1}$ to $1250\,\mathrm{cm}^{-1}$. IR pulses are provided with average pulse energies of 5 mJ and a bandwidth of approximately 0.2 % root mean square of the central wavelength. FELIX is attenuated such that only rare gas loss channel(s) are observed in these experiments. TOF spectra are recorded for each wavelength step and IR-VPD spectra are obtained by plotting the photodissociation cross section σ as a function of the laser frequency ν according to Eq. (2.15) as described in Section 2.4.

## 3.3 $V_3O_7^+\cdot M$ (M = Ne, Ar): Cage vs. Ring Structure

Structural Assignments. Figure 3.1 presents the IR spectra of the bare $V_3O_7^+$ cluster and the rare gas-tagged complexes $V_3O_7^+\cdot M$ (M = Ne and Ar). As mentioned previously, the IR spectra of the Ar-tagged complex and the bare ion are distinctly different. For instance, the spectrum of $V_3O_7^+\cdot Ar$ reveals more structure and shows absorptions in different spectral regions (band c_4 and c_7), compared to the spectrum of bare $V_3O_7^+$. It suggests that both experiments (IR-MPD of bare ion vs. IR-VPD of Ar-tagged ion) actually probe different structural isomers. These observations are indeed supported by DFT calculations [100]. The spectrum of bare $V_3O_7^+$ is assigned to a cage structure predicted as the global minimum (top, Figure 3.1). In contrast, the absorptions of the Ar-tagged complex are attributed to a ring structure (bottom, Figure 3.1). In the presence of the Ar atom, the ring structure becomes more stable than the cage motif. The origin of this behavior lies in the charge distribution. In the ring structure, the Ar atom interacts with the total positive charge which is localized at the threefold coordinated V atom. Therefore, the Ar atom is strongly polarized resulting in a particular high binding energy ($\sim$55 kJ/mol). In the cage structure, the total positive charge is delocalized over all V atoms owing to the $C_{3\nu}$ symmetry of the cluster. Thus, the Ar atom becomes less polarized leading to a smaller binding energy ($\sim$23 kJ/mol). As a consequence, the relative stability of the two isomers is reversed: without Ar the cage is most stable by 7 kJ/mol, while in the presence of Ar, the ring structure is more stable by 25 kJ/mol.

What happens if the Ar atom is replaced by a less polarisable rare gas atom like neon? The
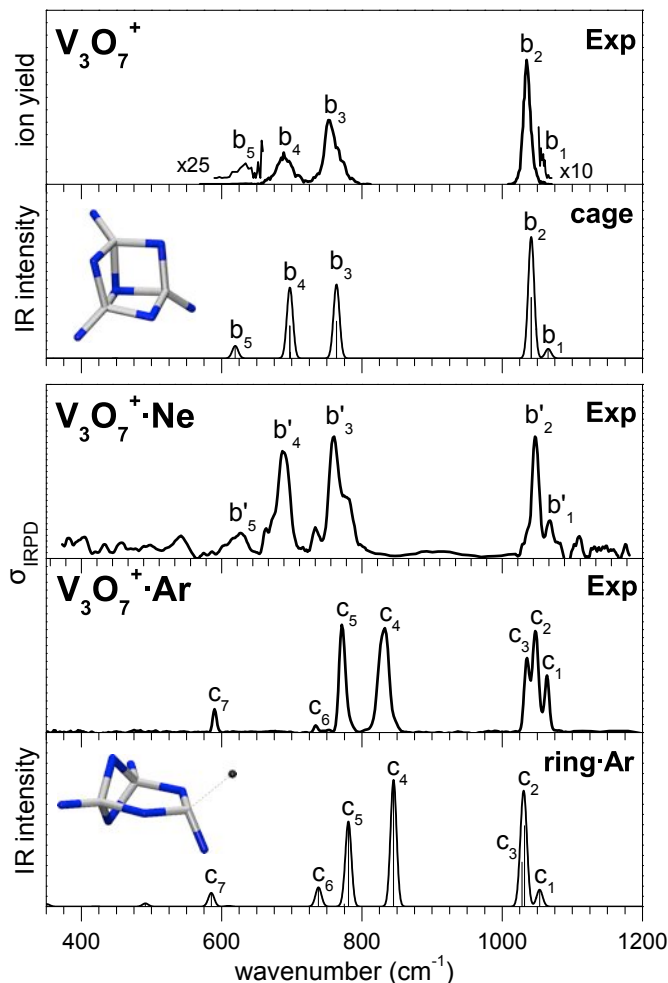
Figure 3.1: IR-MPD spectrum of bare $V_3O_7^+$ and IR-VPD spectra of rare gas-tagged complexes $V_3O_7^+ \cdot M$ (M = Ne and Ar) measured in the range from 350 to 1200 cm^{-1}. Experimental spectra are compared to simulated B3LYP/TZVP linear absorption spectra of the bare cage and ring·Ar isomers (V atoms: grey, O atoms: blue). The IR-MPD spectrum of bare $V_3O_7^+$ was measured by M. Brümmer and is taken from Ref. [100].

IR-VPD spectrum of the Ne-tagged complex $V_3O_7^+ \cdot Ne$ (middle panel, Figure 3.1) resembles the IR signature of the bare $V_3O_7^+$ ion regarding the number of bands (labeled b_1'–b_5') and their positions. Note that some deviations are observed which are attributed to the presence of the Ne atom. For instance, the bands b_1'–b_3' are sligthly blue-shifted by about 10 cm^{-1} and the relative intensities of bands b_3'–b_5' are enhanced. The latter effect arises from the lower dissociation energy of the cation-Ne complex compared to the bare ion. The pronounced similarity between both vibrational spectra indicate that the cage structure of bare $V_3O_7^+$ remains unchanged if neon is used as a messenger atom. DFT calculations, on the other hand, predict the ring·Ne complex to be more stable, similar to the cation-Ar complex [100]. This raises the question why the ring isomer is actually observed for $V_3O_7^+ \cdot Ar$ but not for $V_3O_7^+ \cdot Ne$? Apparently, the relative stability of the rare gas-tagged cage and ring isomers is not sufficient to understand the experimental observations.
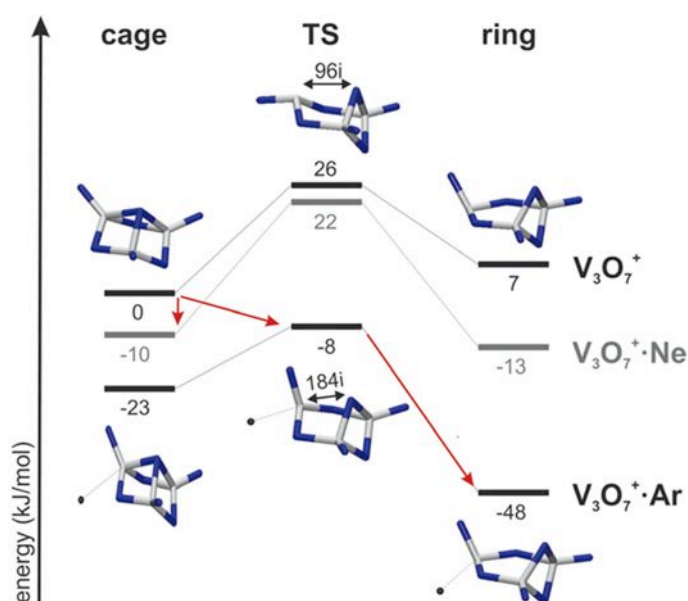
Figure 3.2: Schematic energy level diagram (B3LYP+D) of the cage (left) and ring (right) isomers of V$_3$O$_7^+$ as well as the transition structure TS (center) connecting the two isomers of the bare ions (top), the corresponding Ne- (center) and Ar-complexes (bottom). Structures, isomerization coordinate and imaginary frequency (in cm^{-1}) of the transition mode are indicated for the bare ions, as well as for the Ar-complexes. Red arrows indicate the formation path of experimentally observed complexes.

Formation Process. The structural assignments become understandable recalling how the rare gas-tagged complexes are actually formed. They are produced inside the ion trap, starting out from mass-selected, bare cations. The IR-MPD spectrum of bare V$_3$O$_7^+$ shows that the cluster has a cage-like structure (top, Figure 3.1). Inside the trap the bare ions undergo many collisions with the buffer gas atoms. These collisions can efficiently promote an interconversion from the cage isomer to the rare gas-tagged ring isomer. The efficiency of the process depends on the isomerization barrier. The IR-VPD experiments on V$_3$O$_7^+$·Ne and V$_3$O$_7^+$·Ar suggest that the barrier is influenced by the type of messenger atom used. The isomerization of V$_3$O$_7^+$ induced by Ar complex formation proceeds without a barrier or at least via a small barrier, i.e., comparable to the thermal energy of the buffer gas, which is held at 50 K. In contrast, using neon as a messenger seems to sufficiently increase the isomerization barrier such that interconversion into the ring·Ne complex is prevented.

Indeed, DFT calculations for V$_3$O$_7^+$ show that upon addition of Ar to the cage species, Ar complexes of the ring structure can be formed without a barrier (long red arrows, Figure 3.2). The formation of the ring·Ar complex proceeds *via* a negative barrier (-8 kJ/mol). This results from the strong cation-Ar interaction which reduces the energy of the cage-ring transition structure (TS) for the Ar complex below the energy of the cage structure plus the Ar atom at large distance (Figure 3.2). The reason is that Ar binds most strongly to the ring structure (55 kJ/mol) and less strongly to the cage-ring transition structure as well as the cage structure (34 and 23 kJ/mol, respectively). Figure 3.2 also shows the results for the Ne complex of V$_3$O$_7^+$ (gray energy levels). The cage·Ne complex will be formed in a direct process (short red arrow, Figure 3.2). In contrast to the cation-Ar complexes, the cage-ring transition structure binds the Ne atom more weakly. Consequently, it remains well above the energy

of the cage structure (plus the Ne atom at large distance). This high barrier (22 kJ/mol) prevents an isomerization from the cage to the ring isomer at an ion trap temperature of 20 K. Therefore, only the cage structure is expected to be predominantly formed which is what we find experimentally.

## 3.4 $V_3O_8{}^+\cdot Ar_2$: Restoration of the Cage Structure
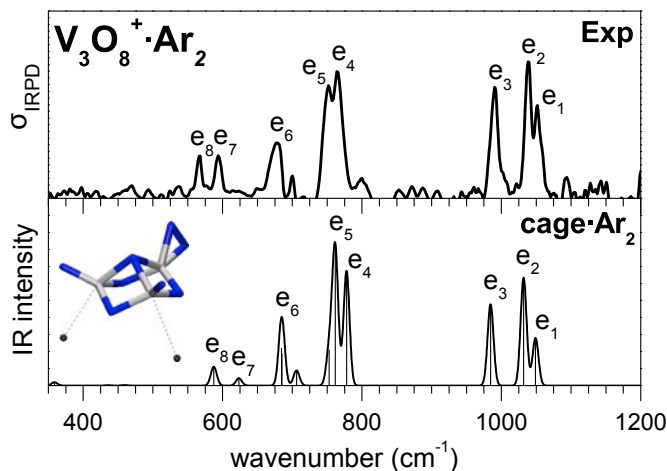
Figure 3.3: Experimental IR-VPD spectrum of the rare gas-tagged complex $V_3O_8{}^+\cdot Ar_2$ compared to simulated linear absorption spectra (B3LYP/TZVP) of the peroxo cage·Ar_2 isomer in the range from 350 to 1200 cm^{-1}.

The IR-VPD study on $V_3O_7{}^+\cdot Ne$ and $V_3O_7{}^+\cdot Ar$ revealed that the interconversion between the cage and ring isomers sensitively depends on the type of the messenger atom used. For the complex $V_3O_8{}^+\cdot Ar$ the situation is similar compared to $V_3O_7{}^+\cdot Ar$. The Ar atom binds stronger to the $V_3O_8{}^+$ ring isomer compared to the cage isomer, 31 kJ/mol and 21 kJ/mol respectively (Figure 3.4). The present section addresses the question how the isomerization is influenced by the presence of multiple messenger atoms. This shall be exemplified by the IR-VPD experiments on the Ar-tagged complex $V_3O_8{}^+\cdot Ar_2$. The experimental IR-VPD spectrum is shown in Figure 3.3. It exhibits eight absorption bands (labeled e_1–e_8) which are unambiguously assigned to a cage structure containing a peroxo group (bottom, Figure 3.3). In particular, band e_3 (991 cm^{-1}) represents a characteristic feature of this cage structure which is attributed to the O–O stretching mode of the peroxo group ($O_2{}^{2-}$). The same cage motif is assigned to the previously measured IR-MPD spectrum of the bare $V_3O_8{}^+$ ion [100]. These results indicate that addition of two Ar atoms to the bare cluster allows restoring the cage structure.

The observation of the cage structure for Ar_2 is also supported by theory illustrated by the energy level diagram in Figure 3.4. For the bare isomers, the peroxo cage structure is predicted 9 kJ/mol lower in energy than the peroxo ring structure. Upon addition of the first Ar atom to the cage structure the formation of both cage·Ar and ring·Ar complexes is possible, similarly to $V_3O_7{}^+$. While the cage·Ar complexes will be formed in a direct process, the ring·Ar complexes will be formed *via* a negative barrier (−9 kJ/mol, Figure 3.4). Both Ar complexes are predicted close in energy suggesting that both isomers could be probed in an IR-
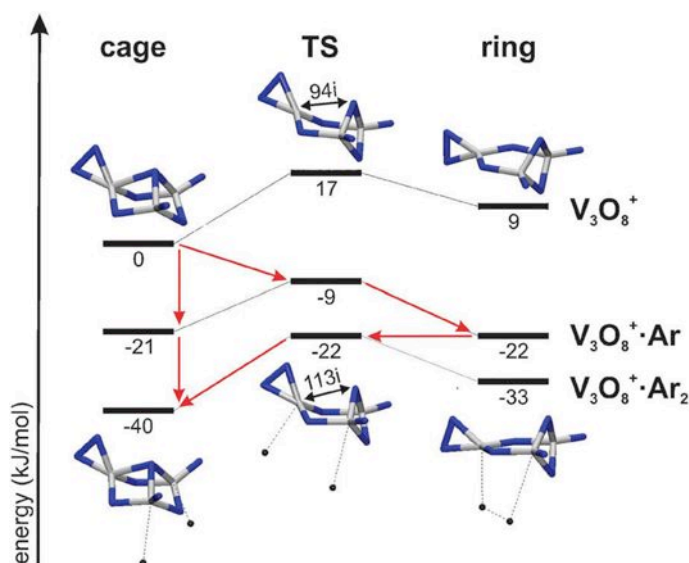
Figure 3.4: Schematic energy level diagram (B3LYP+D) of the peroxo cage (left) and ring (right) isomers of $V_3O_8^+$ as well as the transition structure TS (center) connecting the two isomers of the bare ions (top), the corresponding Ar- (center) and Ar$_2$-complexes (bottom). Structures, isomerization coordinate and imaginary frequency (in cm^{-1}) of the transition mode are indicated for the bare ions, as well as for the Ar$_2$-complexes. Red arrows indicate formation paths of the experimentally observed complexes.

VPD experiment on $V_3O_8^+\cdot Ar$. However, at the chosen experimental conditions, $V_3O_8^+\cdot Ar_2$ is efficiently formed. In contrast to the binding energy of the first Ar atom, the second Ar atom binds stronger to the cage structure (19 kJ/mol) compared to the ring structure (11 kJ/mol). As a consequence, the cage·Ar$_2$ complex becomes more stable (-7 kJ/mol) than the ring·Ar$_2$ complex (Figure 3.4). Furthermore, the transition structure of the Ar$_2$ complex has a similar energy as the ring·Ar complex (plus the second Ar atom at large distance). Hence, any ring·Ar complex formed can convert back into the more stable cage·Ar$_2$ complex (red arrow, Figure 3.4). One expects that the cage·Ar$_2$ complex is predominantly formed which is in agreement with the IR-VPD spectrum of $V_3O_8^+\cdot Ar_2$ (Figure 3.3).

3.5 $V_3O_6^+\cdot He_{1,4}$: Probing Multiple Isomers

The previous IR-VPD study on $V_3O_6^+\cdot Ar_2$ did not allow a clear structural assignment [15, 61]. Therefore, helium is used in the present work. Owing to its small polarisability, helium represents an ideal messenger exerting the smallest perturbation on the structure and vibrational properties of the bare ion. Due to its small size, helium-tagging often results in a distribution of messenger complexes. In the experiment, the complexes $V_3O_6^+\cdot He_n$ with $n = 1 - 4$ are formed in the ion trap. The IR-VPD spectrum of the largest complex $V_3O_6^+\cdot He_4$ (top, Figure 3.5) shows five narrow absorption bands and is considerably simpler than the previously reported spectrum of $V_3O_6^+\cdot Ar_2$. All peaks can unambiguously be assigned to a chain-like structure (Figure 3.5). The same structure is assigned to the IR-VPD spectra of the He-tagged complexes $n = 2$ and $n = 3$ [100].

Surprisingly, when just a single He atom is attached to $V_3O_6^+$, the IR-VPD spectrum
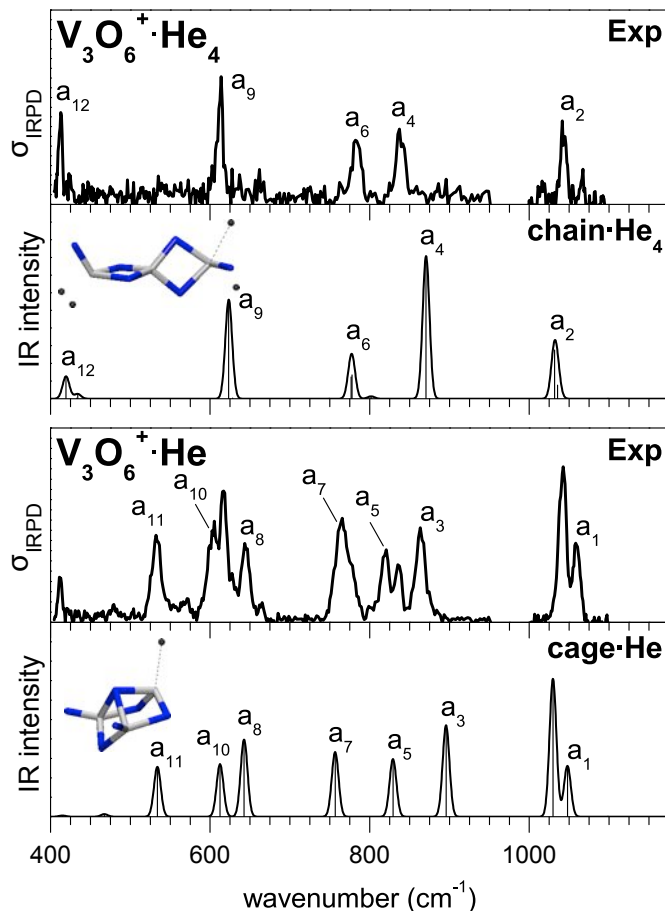
Figure 3.5: Experimental IR-VPD spectra of $V_3O_6^+ \cdot He_4$ (top) and $V_3O_6^+ \cdot He$ (bottom) compared to simulated linear absorption spectra (B3LYP/TZVP) of the chain$\cdot He_4$ and cage$\cdot He$ isomers, respectively, in the spectral range from 400 to 1175 cm^{-1}.

becomes much more complex (bottom, Figure 3.5). It still contains the characteristic features of the chain isomer observed in the $V_3O_6^+ \cdot He_4$ spectrum. Furthermore, several additional absorption peaks appear (a_1, a_3, a_5, a_7, a_8, a_{10}, a_{11}) which are not present in the spectrum of the $n = 4$ complex. These peaks are therefore attributed to the IR fingerprint of a second absorbing species probed in the experiment. Beside the chain isomer, DFT calculations also predict a cage-like structure. This species can account for all additional features (bottom, Figure 3.5).

Interestingly, the cage isomer is only probed for $n = 1$ whereas no indications are observed in the spectra of the He complexes $n = 2-4$ [100]. These differences in the IR-VPD spectra can be understood considering the sequential binding energies of the ion-He complexes calculated for both isomers [100]. One finds that the cage isomer binds a single He atom the strongest (11.8 kJ/mol). However, the sequential binding energy for the addition of a second He atom to the cage isomer (9.6 kJ/mol) is less than the calculated energies for the addition of the first, the second, the third or the fourth He atom to the chain isomer (11.3, 11.0, and 10.0 kJ/mol per He atom, respectively). Consequently, at a suitable partial pressure of helium in the ion trap, cage$\cdot He$ complexes will coexist with chain$\cdot He_{1-4}$ complexes which is observed in the

IR-VPD experiments.

3.6   Summary and Conclusions

The structure of trinuclear vanadium oxide clusters delicately depends on their oxygen content and their environment. $V_3O_7^+$, in which all atoms are either fully oxidized (vanadium) or reduced (oxygen), forms a stable cage structure of C_{3v} symmetry. Whereas the cage motif remains the global minimum energy structure in $V_3O_8^+$, removal of an oxygen atom from $V_3O_7^+$ results in a destabilization of this structure with respect to the other isomers, and the chain and ring motifs become more favourable in $V_3O_6^+$. The cage motif has also been identified as the most stable isomer for the isovalent $Nb_3O_8^+$, which exhibits a similar richness in energetically close-lying isomers [108]. Due to overlapping fragmentation channels resulting from the lack of mass-selection of the parent ions from the molecular beam prior to IR irradiation the vibrational spectra of $Nb_3O_6^+$ and $Nb_3O_7^+$ could not be assigned in those experiments, highlighting the increased sensitivity of the present tandem mass spectrometer approach.

The addition of rare gas atoms can markedly change the relative energies of different isomers, mainly due to rather strong polarization of the rare gas atom(s) by a localized and accessible positive charge. For $V_3O_6^+$ it was shown that by addition of He atoms that isomer (chain) can be discriminated from a mixture that binds more than two He atoms with almost the same energy per He atom.

Particularly noteworthy is the stabilization of the ring isomers over the cage isomers by addition of one Ar atom in $V_3O_{7,8}^+ \cdot Ar$ and the restoration of the cage structure in $V_3O_8^+ \cdot Ar_2$ While it is known that heavier rare gas atoms like Ar will shift vibrational frequencies and modulate intensities, for example in complexes with metal containing clusters [62], such dramatic effects on cluster energies as described here are rarely observed.

Given the fact that the energy differences between different isomers are at the accuracy limits of DFT calculations, one can also conclude that a firm determination of the most stable isomer structure of transition metal oxides is only possible by combining information from global structure optimization, QC calculations at different levels and IR-PD spectroscopy.

Chapter 4

IR-PD Spectroscopy of $Ce_mO_n{}^+$ Clusters

This work demonstrates that the most stable structures of even small gas phase aggregates of cerium oxide with 2–5 cerium atoms show structural motifs reminiscent of the bulk ceria. This is different from main group and transition metal oxide clusters, which often display structural features that are distinctly different from the bulk. The structures of $Ce_2O_2{}^+$, $Ce_3O_4{}^+$, and $(CeO_2)_mCeO^+$ clusters ($m = 0 - 4$) are unambiguously determined by global structure optimization using DFT combined with IR-VPD spectroscopy of the cluster-rare gas atom complexes. For $(CeO_2)_2CeO^+$ multiple isomers are observed. Their individual IR signatures are identified by tuning their relative population through the choice of Ne or Ar messenger atoms. The present results allow benchmarking a series of density functionals which yield different degrees of localization of unpaired electrons in Ce-4f states.

4.1 Introduction

Understanding how the structure and properties of a chemical compound change with its dimensionality, i.e., when passing from the three-dimensional bulk solid to two-dimensional thin films and to zero-dimensional nanosized clusters or small molecules, is of fundamental interest to physics and chemistry. Systems with reduced dimensionality can display unusual structural diversity even for metal oxides that have inherently stable bulk structures. A prominent example here are gas-phase aggregates of magnesium oxide [110]. Similarly, aluminum oxide (Al_2O_3), as low-dimensional material in form of thin films [111–113] and clusters [21, 23], exhibits new structural features that are not found in any of its known solid polymorphs. It is therefore not surprising that also small aggregates of transition metal oxides show unusual structural features. For example, both charged and neutral vanadium oxide clusters form polyhedral cages unknown in bulk V_2O_5 [19, 105]. Similar behavior was shown for bimetallic V-Ti oxide anion clusters [20] and neutral $(TiO_2)_m$ clusters [114]. For the latter even clusters of sizes $m = 9$-15 show geometrical structures which do not correspond to any of the known TiO_2 polymorphs.

The present study focuses on the structural characterization of cerium oxide clusters. Surprisingly, even the small cerium oxide clusters containing 2–5 Ce atoms show structural elements typical of bulk ceria (CeO_2). The structural properties are investigated based on a joint experimental-computational study. IR-VPD spectra are measured for the rare gas-tagged clusters $Ce_2O_2{}^+$, $Ce_3O_4{}^+$, and $(CeO_2)_mCeO^+$ ($m = 0 - 4$). Furthermore, global structure optimizations were performed for these compositions employing DFT. Since DFT calculations are of limited accuracy the final structure assignment is achieved by comparing the simulated IR absorption spectra of the lowest energy isomers with the experimental IR-VPD spectra. Previously, this approach was applied to determine the structures of other metal oxide cluster cations, including vanadium [18, 115], aluminum [21, 23], and magnesium oxide clusters [110]. Compared to previous work on cerium oxide clusters [116–129] there are two novel aspects to this study. First, the structures are computationally predicted using *ab initio* global structure optimizations. Second, vibrational spectra of mass-selected cluster cations are used to check the theoretical predictions and assign cluster structures on the basis of the comparison between the experimental and simulated IR spectra. The investigation of cerium oxide clusters represents the first step towards the structural characterization of binary cerium/vanadium oxide clusters reported in Chapter 5.

Ce-containing clusters have not been spectroscopically studied in the gas phase so far. The reactivity of small cerium oxide cations $Ce_mO_{2m}{}^+$ has been investigated, involving reactions with CO and small hydrocarbons, using mass spectrometry combined with DFT [119, 129]. IR spectra of small $Ce_mO_n{}^{+/0/-}$ ($m, n \leq 2$) clusters in an Ar matrix have also been measured [116, 120].

The clusters studied in the present work are not fully oxidized, i.e., there are Ce atoms in lower oxidation state than +IV. There is lively interest in partially reduced ceria [130–135] which arises from a broad range of industrial applications [136, 137] including heterogeneous catalysis [131, 138, 139]. Partially reduced ceria is formed when oxygen defects are created which leaves electrons in Ce-4f states. Whereas experiments point to localized Ce-4f states [134, 135] the theoretical prediction of the electronic distribution is challenging. The investigation of cerium oxide clusters in the gas phase is advantageous because a broad variety of DFT methods can be easily applied [119, 124, 125, 129] compared to extended systems such as nanoparticles and surfaces. Hence, the present combined experimental-computational

study of clusters not only contributes to a better understanding of the structural properties of partially reduced cerium oxide, but also serves as a benchmark for assessing the applicability of different computational methods to lanthanide oxide aggregates.

4.2 Experimental Methods
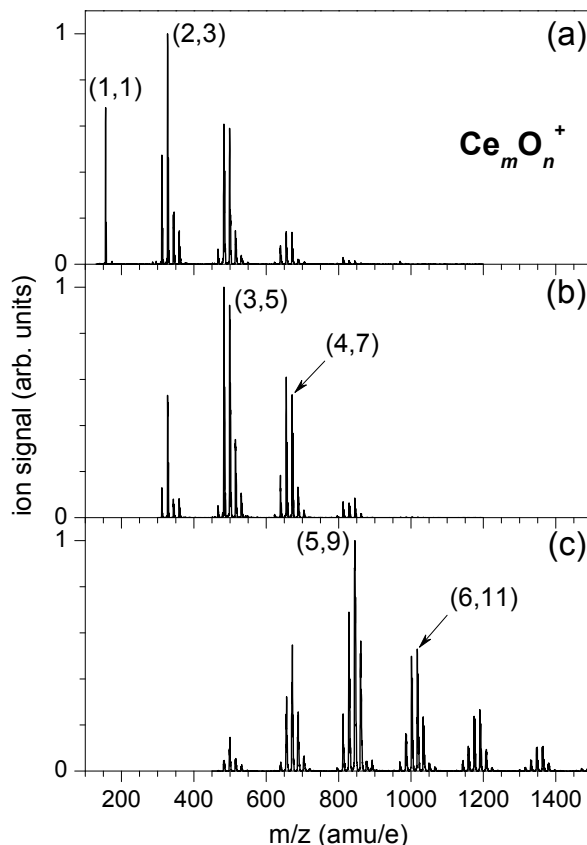
Figure 4.1: Typical mass spectra of cerium oxide cluster cations $Ce_mO_n^+$ (denoted (m, n)) formed by laser vaporization. The cluster distributions (a)–(c) depend on the *laser–valve* time delay as well as the ion optics parameters. The ion yield of cluster sizes $Ce_2O_3^+$ (a), $Ce_3O_5^+$ (b) and $Ce_6O_{11}^+$ (c) is maximized by tuning the time delay in the range from $200\,\mu s$ to $250\,\mu s$.

The IR-VPD experiments are carried out on the ion trap–tandem mass spectrometer (Section 2.2). For the production of the cerium oxide cluster cations the Leuven dual-target laser vaporization source was used (Section 2.1.1) [77]. The second harmonic (532 nm) of a pulsed Nd:YAG laser (*Spectra Physics*, Quanta Ray GCR Series) is used to vaporize the cerium target material. The formed plasma is entrained in a carrier gas pulse of $0.1\,\%$ O_2 seeded in helium and cerium oxide clusters are subsequently formed through expansion in a clustering channel held at a temperature of 120 K. The pulsed valve is operated at a backing pressure of $\sim$4 bar leading to a pressure of $\sim$10^{-5} mbar in the source region. Laser pulse energies of 10 mJ are sufficient to obtain a stable cluster signal. The firing of the laser is triggered with respect to the valve. Cluster sizes containing up to eight cerium atoms are easily produced by varying this time delay roughly between 200 and $250\,\mu s$ (Figure 4.1).

Mass-selected parent ions are accumulated and thermilized for 98 ms by multiple collisions with a buffer gas in an cryogenically-cooled ion trap. IR-VPD measurements are performed on ion-rare gas atom complexes which are formed in the trap. Different rare gas atoms are used (He, Ne, Ar). To this end, a buffer gas of either pure He, a mixture of 0.125% Ne, or 1% Ar in He is introduced at ion trap temperatures of 15 K, 24 K and 55 K, respectively.

After the ion packet is extracted from the trap, it interacts with an IR laser pulse in the TOF extraction zone and high voltage pulses are applied for recording TOF mass spectra. Pulsed IR radiation is used from FELIX which is operated in the spectral range from $400\,cm^{-1}$ to $1000\,cm^{-1}$ with average pulse energies of 10 mJ. TOF spectra are obtained in the difference mode of operation, i.e., mass spectra are alternately measured with and without laser radiation. Thereby, FELIX runs at a repetition rate of 5 Hz while clusters are produced at 10 Hz. The cycle is performed 50–70 times for each wavelength step. The ion signal intensity of a selected complex measured with and without IR radiation is integrated and depletion spectra are derived by plotting the photodissociation cross section σ as a function of the laser frequency ν according to Eq. (2.17).

4.3   Vibrational Spectra and Structural Assignment

In the following the experimental and theoretical results are presented for each cluster separately. First, the calculated structural motifs of the lowest energy isomers of the cluster are described. An overview of all optimized structures of cluster sizes containing 2–5 Ce atoms is shown in Figure 4.3(a). For the smallest clusters studied, CeO^+ und $Ce_2O_2^+$, only the lowest energy isomer is considered illustrated in Figure 4.2. Afterwards, the experimental IR-VPD spectrum is discussed and compared to simulated linear absorption spectra of the various isomers (Figures 4.2, 4.4–4.6). The subsequent assignment of a structure to the IR-VPD spectrum is based on the level of agreement between experiment and theory, e.g., number of absorption bands, their positions and relative intensities.

CeO^+. The experimental IR-VPD spectrum of $CeO^+ \cdot He$ is shown in Figure 4.2(a). The observed absorption band features three equally spaced peaks at 883, 891 and $900\,cm^{-1}$ which correspond to the P, Q and R branch of the cerium oxide stretching band. The presence of all three branches can be attributed to the structure of an asymmetric rigid rotor while, in contrast, a linear structure would lack the Q-branch and only two peaks would be expected [140]. Hence, these findings indicate a nonlinear structure of the $CeO^+ \cdot He$ complex which is confirmed by the calculations. The calculated structure (**1-1**) is illustrated in the top panel of Figure 4.2(a) along with the simulated IR absorption profile. The He atom is found to bind under an angle of 104° with respect to the Ce=O bond with a binding energy of 4.9 kJ/mol. The Ce=O bond length of the untagged CeO^+ cation (1.76 Å) remains unchanged upon tagging, demonstrating a negligible perturbation of the He atom on the structure of the ion. The corresponding simulated absorption spectrum including rotational transitions reproduces the observed band profile. Note that although the IR-VPD spectrum was measured at a trap temperature of 15 K, the rotational temperature of the complex is assumed to be 100 K in order to account for the width of the absorption band. For comparison, the rotational band contour simulated for 15 K is also shown in Figure 4.2(a). This finding suggests that the thermalization equilibrium of these complexes is not reached during the trapping cycle of 98 ms, or that the complexes heat up during the extraction from the trap.
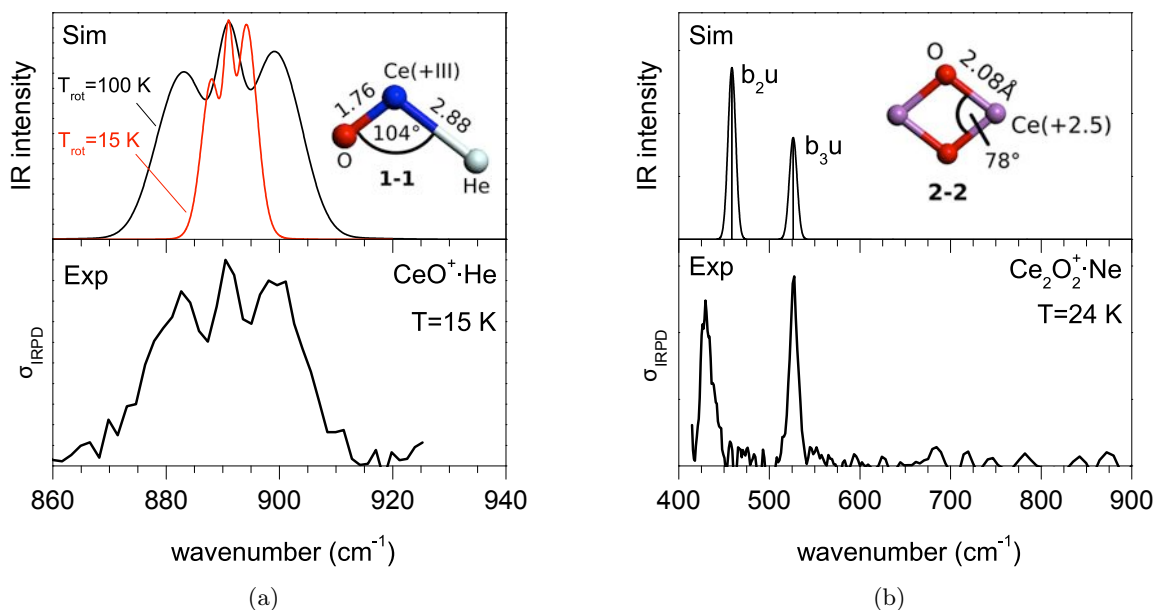
Figure 4.2: Comparison of experimental IR-VPD spectra to simulated B3LYP/TZVPP linear absorption spectra for the complexes $CeO^+\cdot He$ **(a)** and $Ce_2O_2^+\cdot Ne$ **(b)**. The simulated spectra of structure **1-1** include rotational transitions within the rigid rotor approximation using rotational constants $A = 0.65\,cm^{-1}$, $B = 0.32\,cm^{-1}$ and $C = 0.22\,cm^{-1}$. The calculated rotational band contours correspond to a temperature of $100\,K$ (black trace) and $15\,K$ (red trace). For better comparison the simulated spectra are shifted by $-19\,cm^{-1}$.

$Ce_2O_2^+$. The global minimum structure of the $Ce_2O_2^+$ cluster (**2-2**) is a D_{2h}-symmetric four-membered $Ce-(O)_2-Ce$ ring (Figure 4.2(b)). The cluster contains three unpaired electrons in the Ce f states which form a quadruplet spin state ($S = 4$, all spins parallel). All electrons are delocalized over both Ce atoms which are formally in the oxidation state $+2.5$.

The experimental IR-VPD spectrum of $Ce_2O_2^+\cdot Ne$ (bottom panel, Figure 4.2(b)) exhibits two absorption bands in the region below $600\,cm^{-1}$, namely at 430 and $531\,cm^{-1}$. The IR-VPD spectrum can unambiguously be assigned to structure (**2-2**) whose IR spectrum (top panel, Figure 4.2(b)) exhibits the same pattern. Two vibrational modes are predicted at 457 and $528\,cm^{-1}$ corresponding to in-plane deformation modes of the ring illustrated in Figure 4.3(b).

CeO_2CeO^+. The two most stable isomers of the CeO_2CeO^+ cation, **2-3a** and **2-3b**, are illustrated in Figure 4.3(a). Structure **2-3a** is of C_s symmetry and consists of a four-membered $Ce-(O)_2-Ce$ ring, similar to **2-2**, with an additional terminal O atom linked to one Ce atom. In the electronic ground state the unpaired electron is localized on the twofold coordinated Ce atom. The higher symmetric tribridged geometry (C_{3v}) found in isomer **2-3b** is $7\,kJ/mol$ less stable. It can be obtained from isomer **2-3a** where the terminal O atom in the Ce=O bond forms another Ce–O–Ce bridge with the Ce(+III) atom.

The experimental IR-VPD spectrum of $CeO_2CeO^+\cdot Ne$ (Figure 4.4(a)) exhibits four intense absorption bands at 528, 558, 673 and $838\,cm^{-1}$. Based on the IR-VPD spectrum of $CeO^+\cdot He$ the $838\,cm^{-1}$ band is assigned to the Ce=O stretching mode. The ring isomer **2-3a** can account for all observed bands. In particular, the characteristic Ce=O stretching

(a)

(b)
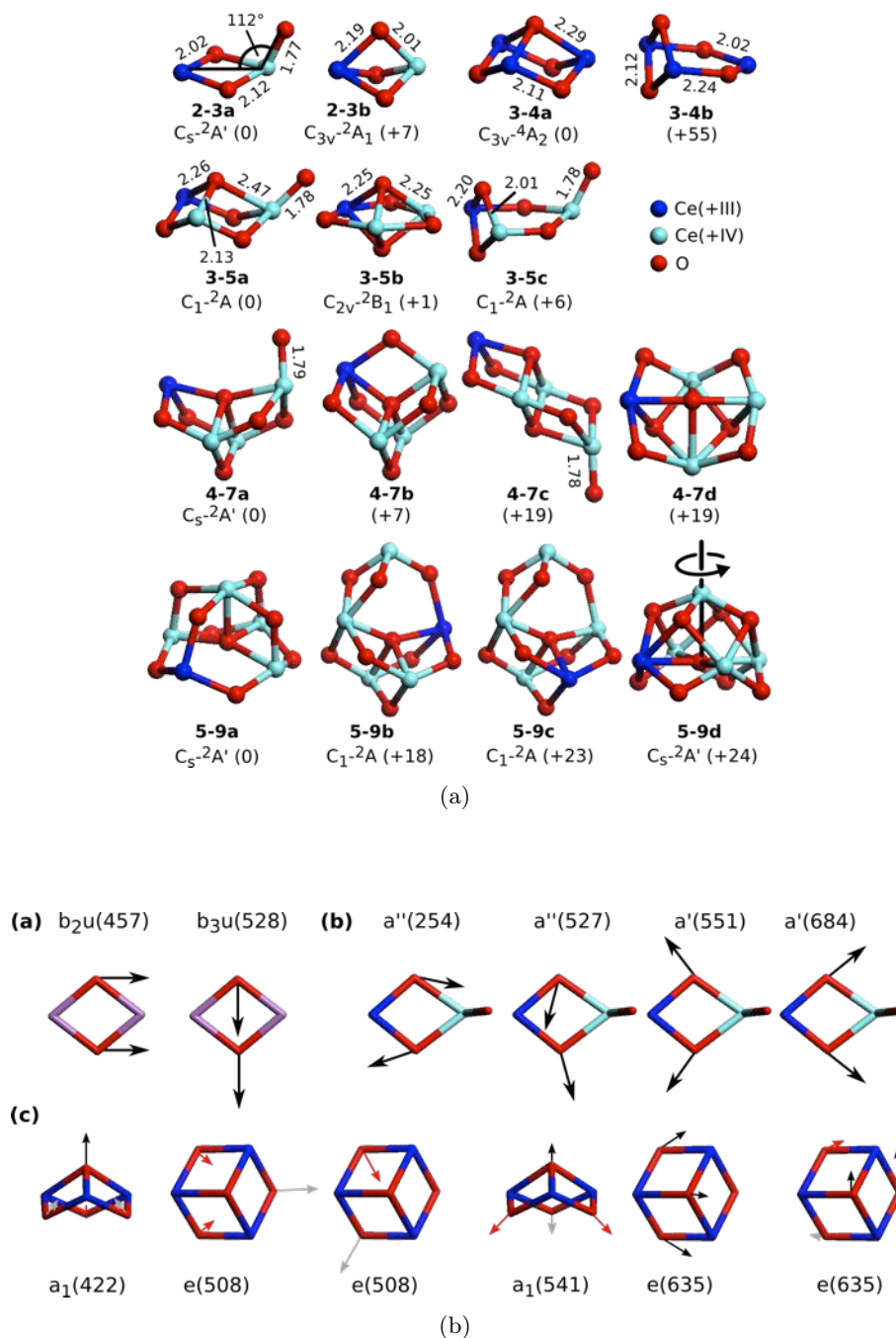
Figure 4.3: Top: Optimized B3LYP/TZVPP structures of relevant isomers investigated in this work. The oxidation states of the cerium atoms are indicated using different atom colors (Ce(+III): dark blue, Ce(+IV): cyan). Values in parentheses indicate relative total energies (kJ/mol), distances are given in Å. The black line in structure **5-9d** shows a rotation axis (see text). Bottom: IR active vibrational in-plane normal modes of (a) the structure **2-2** and (b) the structure **2-3a** and (c) selected vibrational normal modes of structure **3-4a**. Irreducible representations and simulated frequencies (cm^{-1}, in parentheses). Black arrows: motions in the drawing plane; Red and gray arrows: upwards and downwards motions, respectively.
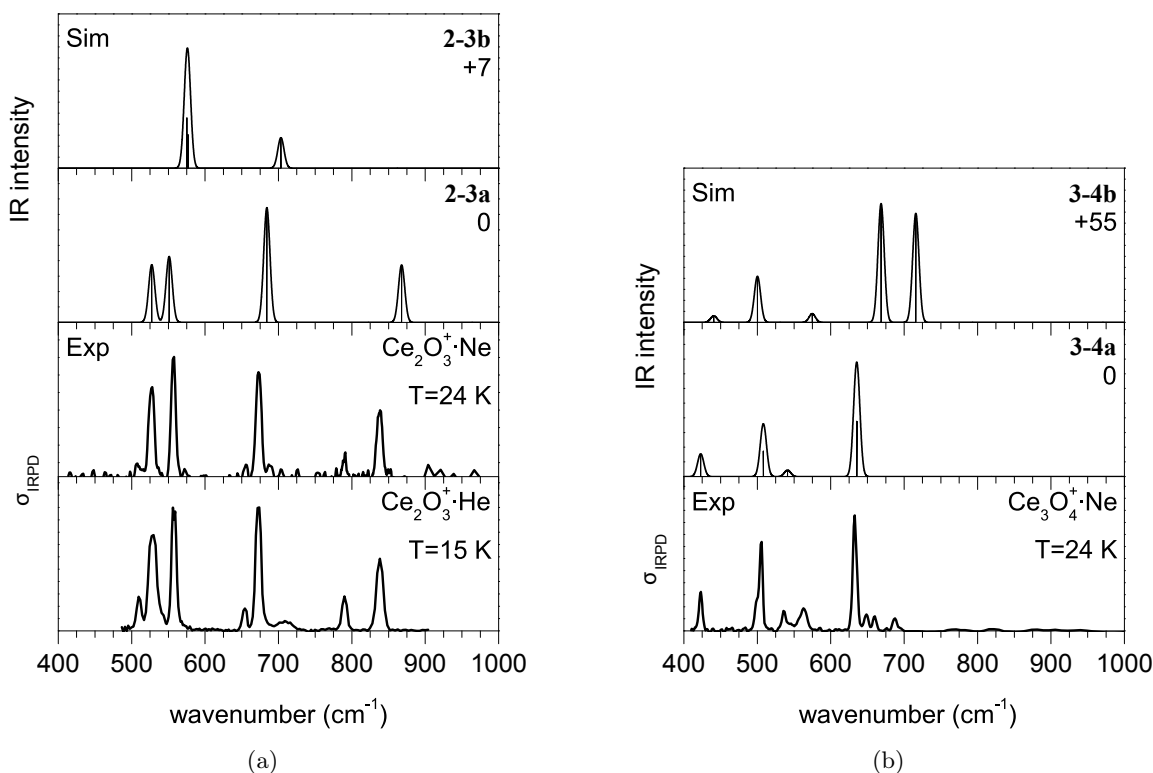
Figure 4.4: Comparison of experimental IR-VPD spectra to simulated B3LYP/TZVPP linear absorption spectra for the complexes CeO_2CeO^+ **(a)** and $Ce_3O_4{}^+$ **(b)**. Relative energies are given in kJ/mol.

band is predicted at $868\,cm^{-1}$. In contrast, the cage isomer **2-3b** ($+7\,kJ/mol$) yields only two IR bands. The strongest transition is predicted at $575\,cm^{-1}$ where no absorption is experimentally observed. Therefore, the cage structure is excluded from the assignment. The three experimental bands in the region below $700\,cm^{-1}$ are then assigned to in-plane modes of the ring (527, 551 and $684\,cm^{-1}$), illustrated in Figure 4.3(b). However, the $CeO_2CeO^+{\cdot}Ne$ spectrum shows additional weaker bands, e.g., at 506, 655 and $790\,cm^{-1}$. These bands are even more pronounced when helium is used as a messenger atom (bottom, Figure 4.4(a)). Unfortunately, these bands remain unassigned. They may indicate the presence of another energetically low-lying isomer that is not predicted by the present DFT calculations.

$Ce_3O_4{}^+$. The most stable isomer of the $Ce_3O_4{}^+$ cluster **3-4a** (Figure 4.3(a)) is of C_{3v} symmetry and contains three four-membered $Ce–(O)_2–Ce$ rings forming three faces of a rhombohedral prism. In its electronic ground state, three unpaired electrons in Ce f orbitals form a quadruplet spin state. Owing to the symmetry of the cluster, the electrons are delocalized over all Ce atoms which are formally reduced to Ce(+III). The next isomer, **3-4b**, is already predicted $55\,kJ/mol$ higher in energy and consists of a six-membered ring with one additional bridging O atom. In this structure one unpaired f electron is localized on one Ce atom and two unpaired f electrons are delocalized over the other two Ce atoms yielding three Ce(+III) atoms.

In the experimental IR-VPD spectrum of $Ce_3O_4{}^+{\cdot}Ne$ three intense absorption bands are

observed in the region below $700\,\mathrm{cm^{-1}}$ at positions 423, 506 and $633\,\mathrm{cm^{-1}}$ (bottom, Figure 4.4(b)). Additional absorption bands of less intensity emerge at 536 and $563\,\mathrm{cm^{-1}}$. The optimized structures **3-4a** and **3-4b** have characteristically different IR signatures (Figure 4.4(b)). Isomer **3-4a** yields three intense bands at 422, 508 and $635\,\mathrm{cm^{-1}}$ together with a weak vibrational transition at $541\,\mathrm{cm^{-1}}$. The two strong IR bands at 508 and $633\,\mathrm{cm^{-1}}$ result from two doubly degenerated normal modes (bottom row, Figure 4.3(b)). In contrast, the spectrum of isomer **3-4b** shows two intense peaks around $700\,\mathrm{cm^{-1}}$ where no IR bands are predicted for **3-4a**. Regarding the number of peaks and their positions, the IR-VPD spectrum is best reproduced by isomer **3-4a**. Since no to little absorption is observed around $700\,\mathrm{cm^{-1}}$ isomer **3-4b** is excluded from the assignment. Furthermore, this structure is predicted to lie too high in energy to be formed and is therefore not expected to be probed in the experiment.

$(CeO_2)_2CeO^+$. The three most stable structures of $(CeO_2)_2CeO^+$ are displayed in Figure 4.3(a). The isomers **3-5a** and **3-5b** are found close in energy, i.e., within $1\,\mathrm{kJ/mol}$, and can both be derived from structure **3-4a**. In **3-5a** the additional oxygen atom forms a terminal Ce=O bond on one Ce site. In **3-5b** the bottom side of structure **3-4a** is capped by the additional O atom leading to a distorted trigonal bi-pyramid with C_{2v} symmetry. The third isomer **3-5c** ($+6\,\mathrm{kJ/mol}$) can be obtained from structure **3-4b** by adding a terminal O atom to one Ce site. In each isomer, there is one unpaired electron in the 4f states localized at one Ce atom forming a doublet spin state ($S = 2$).

$(CeO_2)_2CeO^+$ shows different IR-VPD spectra depending on the messenger atom used. This dependence is illustrated in Figure 4.5(a) for the Ne-tagged and Ar-tagged clusters. The IR-VPD spectrum of the Ne-tagged cluster exhibits three bands above $600\,\mathrm{cm^{-1}}$, i.e., at 817, 721 and $655\,\mathrm{cm^{-1}}$ and a multiplet of three peaks emerges in the region below $500\,\mathrm{cm^{-1}}$. Furthermore, weak absorptions are observed in-between $500\text{--}600\,\mathrm{cm^{-1}}$. The IR-VPD spectrum of the Ar-tagged complex shows similar absorptions, but with different relative intensities. In particular, both spectra differ in the region of the Ce=O stretching vibrations ($>800\,\mathrm{cm^{-1}}$) where absorption is mainly observed for the Ne-tagged complex ($817\,\mathrm{cm^{-1}}$). Surprisingly, this band is rather weak in the spectrum of the Ar-tagged complex. This indicates that both IR-VPD experiments probe different isomers. More precisely, these observations suggest that the Ne atom preferentially stabilizes a structure containing a Ce=O moiety whereas the Ar atom binds to a structure without it.

Indeed, best agreement with the experimental spectrum of the neon complex is found for the simulated spectrum of structure **3-5a** containing a terminal O atom. It reproduces the three bands observed above $600\,\mathrm{cm^{-1}}$ (exp/sim: 817/845, 721/724, 655/655) and the characteristic triplet of peaks below $500\,\mathrm{cm^{-1}}$ (482/484, 466/469, 449/453). However, the weak bands in-between $500\text{--}600\,\mathrm{cm^{-1}}$ cannot be explained by **3-5a**, but can be attributed to **3-5b**. Isomer **3-5c** cannot account for the observed multiplet around $460\,\mathrm{cm^{-1}}$ and is therefore excluded from the assignment. In contrast, the spectrum of the Ar-tagged cluster shows good agreement with the simulated spectrum of isomer **3-5b** (exp/sim: 652/671, 571/568, 531/521). These assignments support that two isomers, i.e., **3-5a** and **3-5b**, are present in the IR-VPD experiment. The relative population of the isomers depends on the messenger atom used. This is further discussed below.

$(CeO_2)_3CeO^+$. Figure 4.3(a) shows the four most stable structures found for $(CeO_2)_3CeO^+$. The isomers **4-7b** to **4-7d** are located $+7$, $+19$, and $+19\,\mathrm{kJ/mol}$, respectively, above the global
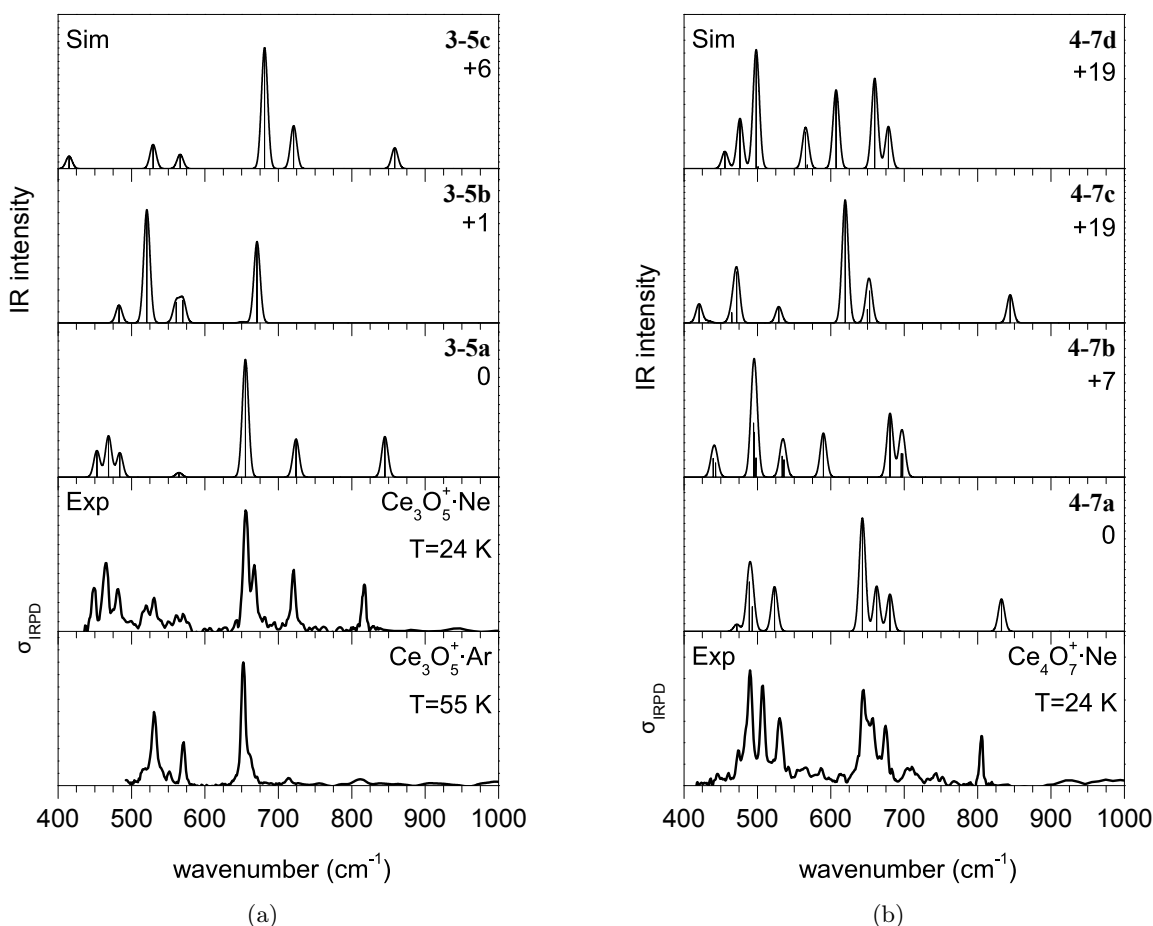
Figure 4.5: Comparison of experimental IR-VPD spectra to simulated B3LYP/TZVPP linear absorption spectra for the complexes $(CeO_2)_2CeO^+$ **(a)** and $(CeO_2)_3CeO^+$ **(b)**. Relative energies are given in kJ/mol.

minimum structure **4-7a**. The structure **4-7b** consists of three pyramidal units **3-4a** fused such that six twofold and one fourfold coordinated O atom are formed whereas all Ce atoms are fourfold coordinated. The topology of **4-7a** can be derived from **4-7b** by disconnecting one twofold coordinated O atom from one Ce atom. In this way, a terminal Ce=O bond and a threefold coordinated Ce atom are formed in the relaxed C_s-symmetric structure **4-7a**. **4-7c** is composed of two pyramidal units which share one edge yielding two fourfold and two threefold coordinated Ce atoms. One threefold coordinated Ce atom is connected to the terminal O atom. **4-7d** is formed by two bi-pyramidal units sharing one face. The most stable electronic state of all $(CeO_2)_3CeO^+$ isomers is a doublet state with a single unpaired electron in a Ce-4f orbital. In all structures the Ce(+III) site coincides with the Ce atom of lowest coordination.

The experimental IR-VPD spectrum of $(CeO_2)_3CeO^+\cdot Ne$ exhibits a terminal Ce=O stretching band at $805\,cm^{-1}$ and multiple peaks are observed around $650\,cm^{-1}$ and $500\,cm^{-1}$ (Figure 4.5(b)). The global minimum structure **4-7a** shows best agreement with the experiment. The present Ce=O moiety yields a stretching band at $832\,cm^{-1}$. At $650\,cm^{-1}$ three vibrational modes are predicted which nicely reproduce the experimental band positions (exp/sim: 675/681, 657/662, 645/643). In the region below $600\,cm^{-1}$ two strong bands are calculated
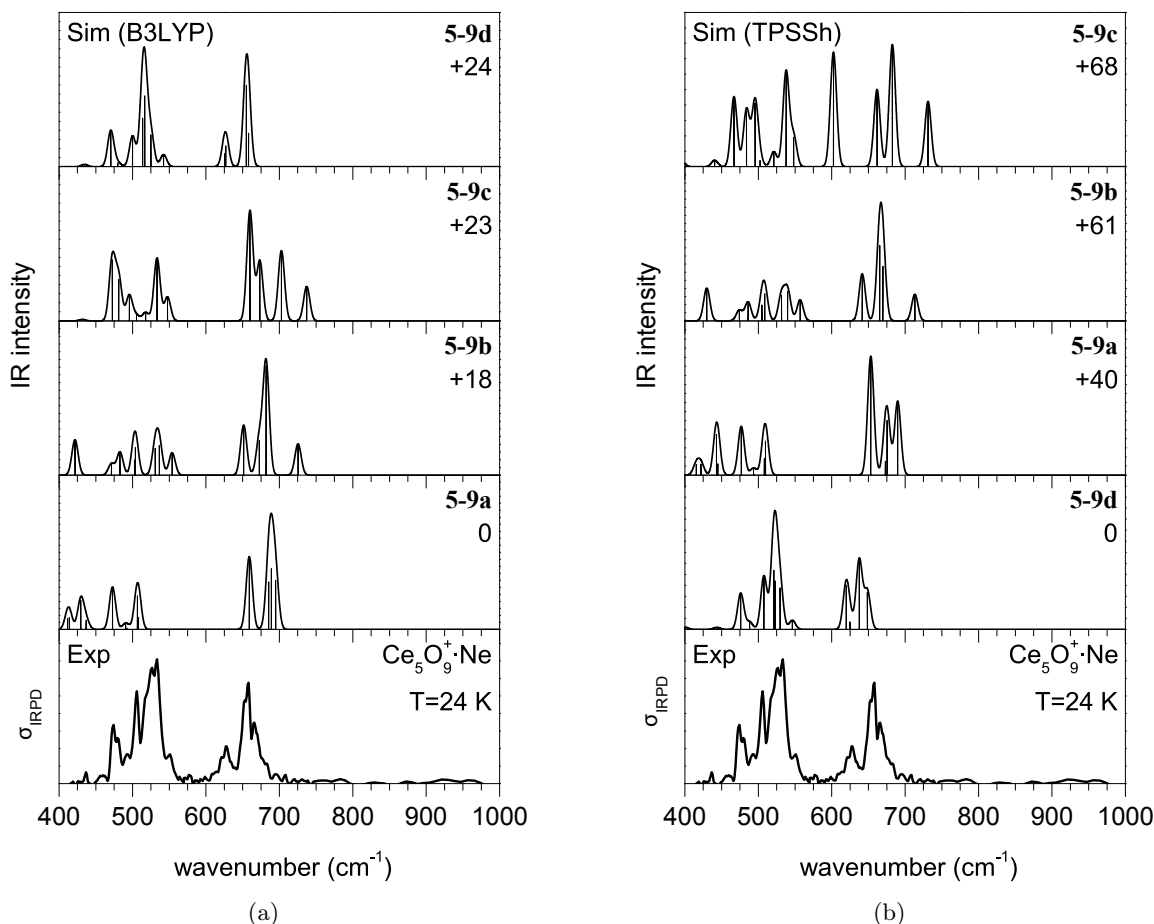
Figure 4.6: Comparison of the experimental IR-VPD spectra of $(CeO_2)_4CeO^+$ with simulated linear absorption spectra obtained from B3LYP/TZVPP **(a)** and TPSSh/TZVPP **(b)** calculations. Relative energies are given in kJ/mol.

at 523 and 490 cm^{-1} while three intense peaks are observed experimentally (530, 507 and 490 cm^{-1}). However, the predicted 490 cm^{-1} band contains two vibrational modes, i.e., at 493 and 489 cm^{-1}, which are assigned to the observed 507 and 490 cm^{-1} bands, respectively.

All energetically higher-lying isomers can be excluded from the assignment. The IR spectrum of isomer **4-7c** (+19 kJ/mol) can account for the Ce=O stretching band, but an intense band is predicted at 615 cm^{-1} where no absorption is observed experimentally. Isomers **4-7b** and **4-7d** contain no Ce=O moiety and, thus, cannot account for the observed Ce=O stretching band.

$(CeO_2)_4CeO^+$. Figure 4.3(a) shows the most stable structure types of $(CeO_2)_4CeO^+$. The most stable structure is **5-9a** while **5-9b**, **5-9c**, and **5-9d** are higher in energy by +18, +23 and +24 kJ/mol, respectively. None of the structures has a terminal O atom. **5-9d** consists of four fused bi-pyramidal units sharing two faces. The central Ce atom forms one of the pyramidal apexes. This yields four twofold, four threefold, and one fourfold coordinated O atoms. The structure **5-9a** can be derived from **5-9d** by 45° rotation of the threefold coordinated O atoms around the axis shown in Figure 4.3(a). **5-9a** is composed of four pyramidal units each of them

sharing two faces. **5-9b** and **5-9c** have common structural features with **3-4b** and **4-7a**, i.e., the six-membered ring and the two pyramidal units sharing one face. All structures have one unpaired electron in the Ce-4f states. The spin density resides almost completely on one Ce atom making it formally Ce(+III). Note that different spin localization for the same structure type leads to different stable minima, e.g., **5-9b** and **5-9c**.

The IR-VPD spectrum of the $(CeO_2)_4CeO^+ \cdot Ne$ complex (bottom panel, Figure 4.6(a)) exhibits two intense structured bands at ~ 650 and $\sim 520 \, cm^{-1}$. All optimized isomers, **5-9a** to **5-9d**, can account for the observed absorptions in these regions but their simulated IR spectra differ in particular in the lower wavenumber region ($< 600 \, cm^{-1}$) regarding the number of predicted modes and their intensities. An overall good agreement with the experiment is found only for isomer **5-9d**. But, this isomer is not predicted as the global minimum structure when the B3LYP functional is applied.

Interestingly, using a different functional, TPSSh instead of B3LYP, corrects this discrepancy. The TPSSh calculations change the energetic ordering of the isomers and **5-9d** becomes the lowest energy structure. Moreover, the simulated IR spectrum of **5-9d** shows excellent agreement with the experimental spectrum of $Ce_5O_9^+ \cdot Ne$ (bottom panel, Figure 4.6(b)).

4.4 Discussion

Regarding the IR signatures of the various cerium oxide clusters investigated in the present work several trends occur with increasing cluster size. Initially, in the spectral region below $800 \, cm^{-1}$, the small clusters containing 1–3 Ce atoms yield simple IR spectra showing few narrow ($< 10 \, cm^{-1}$) absorption peaks. For instance, $Ce_2O_2^+$ yields two characteristic peaks at 430 and $531 \, cm^{-1}$. Similarly, $Ce_2O_3^+$ absorbs around $530 \, cm^{-1}$, but yields an additional band around $670 \, cm^{-1}$. The IR spectra become more complex in these regions with growing cluster sizes. The larger clusters containing 4–5 Ce atoms mainly absorb around 500 and $650 \, cm^{-1}$ while broad, structured absorption bands are observed. Based on the structural assignment, these absorptions are assigned to vibrational modes of Ce–$(O)_2$–Ce four-membered rings representing subunits of the structures of the clusters. The spectral region from 800 to $900 \, cm^{-1}$ is characteristic for terminal Ce=O stretching vibration. It is a sensitive probe in order to distinguish between structural motifs containing a terminal Ce=O double bond or not. Such features are observed for the clusters $Ce_2O_3^+ \cdot Ne$, $Ce_3O_5^+ \cdot Ne$ and $Ce_4O_7^+ \cdot Ne$. The Ce=O bond length in the clusters varies from 1.76 to $1.79 \, Å$. The computational results show that the terminal O atom in the Ce=O moiety is always connected to a Ce(+IV) atom.

The simulated linear absorption spectra derived from B3LYP calculations show a good agreement with the experiment. In particular, the structures of the small clusters can unambiguously be assigned to the predicted lowest energy isomers. However, the B3LYP calculations for $Ce_5O_9^+$ are not confirmed by the measured IR-VPD spectrum. The B3LYP functional fails to predict the correct energetic ordering of the optimized structures. Best agreement is found with isomer **5-9d** which energetically lies $24 \, kJ/mol$ above the lowest energy structure. The origin of this discrepancy is the overestimation of the degree of localization of the unpaired electron occupying Ce-4f states by B3LYP [109]. In contrast, the TPSSh functional predicts the correct energetic ordering and isomer **5-9d** is found as the global minimum. The structural assignment of $Ce_5O_9^+$ nicely exemplifies that both experiment and theory are required for determining the correct lowest energy isomer.

The identified structures of the cerium oxide clusters reveal structural properties rem-
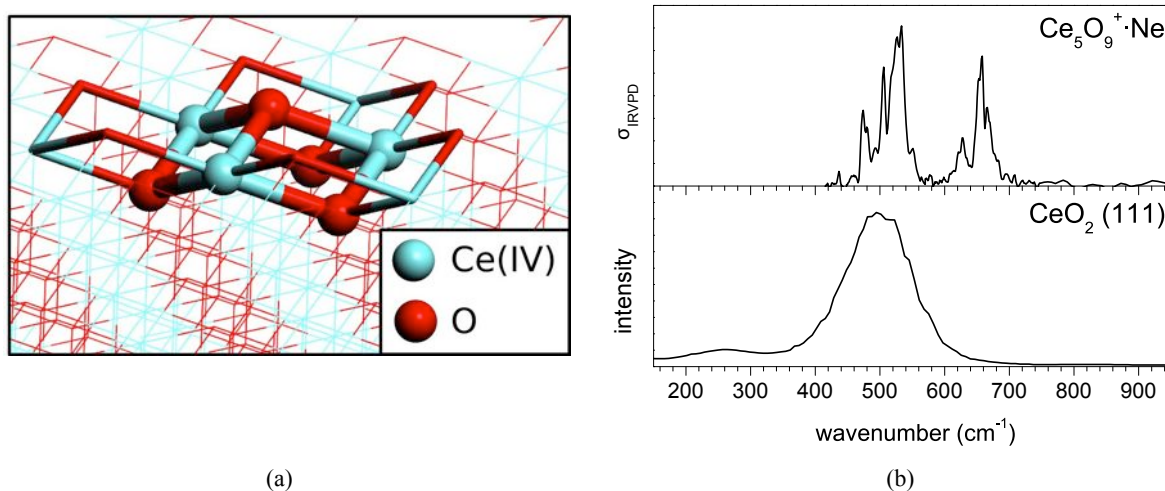
Figure 4.7: **(a)** Calculated oxygen-terminated (111) surface with the highlighted pyramidal Ce_3O_4 unit. **(b)** Experimental IR-VPD spectrum of $Ce_5O_9^+\cdot Ne$ (same as in Figure 4.6) compared to the experimental HREEL spectrum of the oxygen-terminated (111) surface of bulk ceria.

iniscent to bulk ceria. The smaller clusters, $Ce_2O_2^+$ and $Ce_2O_3^+$, contain a $Ce–(O)_2–Ce$ four-membered ring which is also part of the bulk structure (Figure 4.7(a)). This ring structure is similar to the $V_2O_2^+$ and $V_2O_3^+$ divanadium clusters which have been investigated before [18]. Similarly, the work on zirconium oxide clusters [141] gave experimental evidence for four-membered rings as a structural motif of small metal oxide clusters. The larger clusters with more than two Ce atoms are composed of pyramidal units which result in strong absorptions around 500 and $650\,cm^{-1}$ (see text above). The cluster $Ce_3O_4^+$ is assigned to isomer **3-4a** (see Figure 4.3(a)) which is also found in the oxygen-terminated (111) ceria surface (Figure 4.7(a)). Figure 4.7(b) compares the IR-VPD spectrum of the largest cluster studied here, $Ce_5O_9^+\cdot Ne$, to the high resolution electron energy loss (HREEL) spectrum of the CeO_2 (111) surface measured by Stubenrauch et al. [142]. The HREEL spectrum shows a single broad ($\sim 100\,cm^{-1}$) band at $500\,cm^{-1}$. This reveals that the spectral signatures of the gas phase $Ce_5O_9^+\cdot Ne$ cluster have not yet fully converged to that of the ceria surface. The absorption features around $500\,cm^{-1}$ are merely converged which correspond to out-of-plane deformation modes of the $Ce–(O)_2–Ce$ ring units. The additional IR absorption bands observed around $650\,cm^{-1}$ are attributed to in-plane modes of the ring units. They are expected to further red-shift in larger cerium oxide clusters. Similar results were previously reported for the cluster $V_8O_{20}^-$ [19]. Although this cluster size is still rather small, its IR-MPD spectrum already reflects the structural features of the vanadium oxide single-crystal surface.

For the $Ce_3O_5^+$ cluster the IR-VPD measurements show that two isomers are present. The IR-VPD spectrum of the neon-tagged complex shows contributions of both isomers, **3-5a** and **3-5b**. In contrast, when argon is used as a messenger atom isomer **3-5b**, containing no $Ce=O$ moiety, is mainly populated. Apparently, the choice of the messenger atom significantly influences the relative isomer populations. For the bare isomers, the calculations predict structure **3-5a** as the global minimum structure while **3-5b** ($+1\,kJ/mol$) lies higher in energy. The experimental findings suggest that structure **3-5b** is more stable in the presence of argon. Such energetic reordering of the isomers has also been observed for other metal oxide clusters like $V_3O_7^+$ and $V_3O_8^+$, discussed in Chapter 3 and in Ref. [100]. Compared to neon, the

Ar atom binds much stronger to the energetically higher-lying bare isomer which changes the energetic ordering of the isomers. Therefore the results support that, first, argon is not an appropriate spectator and, second, it is advisable to perform the calculations on the cluster-rare gas atom complexes, as well as on the bare cluster, whenever possible.

4.5   Summary and Conclusions

The structures of the partially reduced gas-phase cerium oxide clusters with compositions $Ce_2O_2^+$, $Ce_3O_4^+$, and $(CeO_2)_mCeO^+$ $(m = 0 - 4)$ are identified. The different predictions of different density functionals, in particular for the cluster $(CeO_2)_4CeO^+$, emphasize that both theory and experiment are required for determining the lowest energy isomers of these clusters. The dicerium clusters form Ce–$(O)_2$–Ce four-membered rings typical for small transition metal oxide clusters. The clusters containing more than two Ce atoms are composed of "pyramidal" structural subunits leading to intense IR signals around 500 and $650\,cm^{-1}$. Absorption signals in the range from 800 to $840\,cm^{-1}$ are fingerprints for terminal Ce=O double bonds in all clusters. Whereas smaller gas-phase metal oxide clusters often have quite different structural features and properties compared to the corresponding bulk metal oxides, the cerium oxide gas phase clusters are found to represent only "slightly modified" fragments of bulk ceria. This key finding supports the use of gas phase cerium oxide clusters in mass spectrometric reactions, e.g., as models for catalytic processes on ceria surfaces.

Chapter 5

IR-PD Spectroscopy of Ce$_m$V$_n$O$_o{}^+$ Clusters

IR-VPD spectra of rare-gas tagged $(CeO_2)(VO_2)^+$, $(CeO_2)(VO_2)_2{}^+$ and $(Ce_2O_3)(VO_2)^+$ clusters are measured in the 400–1200 cm^{-1} region. DFT is used to determine the geometric and electronic structure of low-energy isomers of the partially reduced clusters. The comparison between experimental and simulated spectra provides evidence for the larger stability of Ce^{+3}/V^{+5} compared to that of Ce^{+4}/V^{+4}, which confirms that the exceptionally high reducibility of Ce^{+4} accounts for the promoting role of ceria in supported vanadium oxide catalysts.

5.1   Introduction

Supported vanadia is an important solid catalyst for selective oxidations, for example, for the oxidative dehydrogenation (ODH) of alkanes and methanol [12, 24]. It has therefore been chosen as a material for examining the role of the supporting oxide on the catalytic activity [24, 25, 144, 145], and a strong dependence on the type of the supporting oxide has been found, the origin of which is still under debate. Among the factors discussed is the reducibility of the support material because hydrogen transfer, the rate-determining step in the ODH reaction [146–148], leaves an electron on the supported vanadium oxide catalysts. For vanadia supported on ceria, the catalytic activity is particularly high [24, 25, 149]. Although cerium oxide has been known for its ability to store, release, and transport oxygen ions for a long time [150], only recently, a combined experimental and computational investigation of VO_x/CeO_2-(111) model catalysts has shown that this remarkable activity is due to the ability of ceria to easily accommodate electrons in localized f-orbitals [146].

This raises the more general question of the role of the two metals in the partial reduction of a mixed metal oxide system. For VO_x particles on a $CeO_2(111)$ surface, photoelectron spectroscopy in agreement with DFT demonstrated that vanadium becomes fully oxidized (+5 oxidation state), whereas reduced cerium (+3) is formed [151]. DFT calculations for crystalline $CeVO_4$ also found that the $Ce^{(+3)}_2O_3 \cdot V^{(+5)}_2O_5$ form with reduced Ce is more stable than $Ce^{(+4)}O_2 \cdot V^{(+4)}O_2$ with reduced V, that is, the extra electron prefers the Ce-4f states rather than the V-3d states [152].

Here, three binary metal oxide gas-phase clusters, $Ce_mV_nO_o^+$, are investigated by IR-VPD spectroscopy in combination with DFT calculations. Charged species are required for mass selection. In $CeVO_4^+$ (**1**), both metal atoms are fully oxidized. There is no doubt about the $Ce^{(+4)}O_2 \cdot V^{(+5)}O_2^+$ electronic structure with all Ce-4f and V-3d states empty. For the $CeV_2O_6^+$ species (**2**), which can also be written as $(CeVO_4)(V^{(+5)}O_2^+)$, the same question arises as that for crystalline $CeVO_4$: Is the extra electron populating the Ce-4f or the V-3d states and does this lead to geometrically different isomers? The DFT calculations show that this is indeed the case and the measured IR spectra provide compelling evidence for electron localization in Ce-4f states. For the $Ce_2VO_5^+$ species (**3**), which can be written as $(CeVO_4)(Ce^{(+3)}O^+)$, we also find that vanadium is in the +5 oxidation state, whereas both cerium atoms are in the +3 oxidation state.

For comparison, DFT calculations are also made for the corresponding binary oxide clusters $M_mV_nO_o^+$ involving another redox-active oxide, M = Ti, and an inert oxide, M = Si, as models for vanadia supported by titania and silica, respectively.

5.2   Experimental Methods

The IR-VPD experiments are carried out on the ion trap-tandem mass spectrometer (Section 2.2). For the production of the binary cerium/vanadium oxide cluster cations the Leuven dual-target dual-laser vaporization source was implemented (Section 2.1.1) [77]. Two steps are required to achieve stable production of species **1**–**3**. First, the source parameters are optimized such that the formation of small cerium oxide clusters, CeO^+ and $Ce_2O_3^+$, is enhanced (top panel, Figure 4.1). A carrier gas mixture of 0.1 % O_2 in helium is used and the cerium target is vaporized by $\sim$10 mJ laser pulses. In the second step, a second laser is added to vaporize the vanadium target using $\sim$5 mJ laser pulses. Since both targets are mounted

close together both metal plumes are efficiently mixed in the formation chamber. The degree of mixing is controlled by the time delay ($10\,\mu s$) between both lasers.

Mass-selected parent ions are accumulated and thermilized for $98\,ms$ by multiple collisions with a buffer gas in an cryogenically-cooled ion trap. IR-VPD measurements are performed on ion–He atom (Ne atom) complexes which are formed in the trap using helium (neon) as a buffer gas at trap temperatures of $15\,K$ ($19\,K$).

The ion packet, extracted from the trap, interacts with the IR laser pulse in the TOF extraction zone and high voltage pulses are applied for recording TOF mass spectra. Pulsed IR radiation is used from FELIX which is operated in the spectral range from $400\,cm^{-1}$ to $1200\,cm^{-1}$ with average pulse energies of $10\,mJ$. TOF spectra are obtained in the difference mode of operation, i.e., mass spectra are alternately measured with and without laser radiation. Thereby, FELIX runs at a repetition rate of $5\,Hz$ while clusters are produced at $10\,Hz$. This cycle is performed 50–70 times for each wavelength step. The ion signal intensity of a selected complex measured with and without IR radiation is integrated and depletion spectra are derived by plotting the photodissociation cross section σ as a function of the laser frequency ν according to Eq. (2.17).

5.3   Results

In the first part of this section several optimized structures of energetically low-lying isomers for species **1**, **2** and **3** are introduced (Figure 5.1). In addition to the geometry, the spin density is plotted in order to provide insights on the localization of the unpaired electrons, in particular for species **2**, and **3**. From this, conclusions can be drawn about the oxidation states of the metal centers of the clusters. In the second part, the measured IR-VPD spectra are described. In order to test the computational predictions and to allow for a structural assignment, these spectra are compared to simulated IR absorption spectra of the various optimized structures (Figures 5.2–5.4). Particularly, the assignment of a certain isomer with a given oxidation state of the metal atoms involved is based on the agreement between experiment and theory together with the lowest energy criterion.

5.3.1   Structures and Energies of Isomers

The lowest-energy isomer found for **1** is characterized by a nearly planar, four-membered M–$(O)_2$–M ring with two terminal M=O bonds in trans configuration (**1A** in Figure 5.1). It is similar to the previously reported structures for Zr_2O_4 or $V_2O_4^+$ [18, 141, 153]. The V=O and Ce=O bond lengths are 1.57 and $1.75\,\text{Å}$, respectively. Other isomers, including one with the terminal M=O bonds in cis configuration (**1B**) and a scissor-like (**1C**) structure, lie +9 and $+55\,kJ/mol$, respectively, higher in energy than **1A**. Additionally, the geometry for the helium-tagged complex, **1A**·He, was optimized. The calculations predict that the He atom preferentially binds to vanadium, the positive charge center of **1A**, with a binding energy of $13\,kJ/mol$ (Figure 5.1).

The stablest geometry of **2** shows a cage-like structure which consists of two V=O groups and a three-fold coordinated Ce atom (**2A** in Figure 5.1). The chain-like (**2B**) and cage-like structures (**2C**) carrying single V=O and Ce=O subunits are found +113 and $+133\,kJ/mol$ higher in energy, respectively. Structure **2A** is similar to the structure reported for Zr_3O_6 [141] but is different from that of $V_3O_6^+$ [15], which prefers a **2B**-like structure. The unpaired electron in **2A** resides on the Ce atom, illustrated by the spin density isosurface in
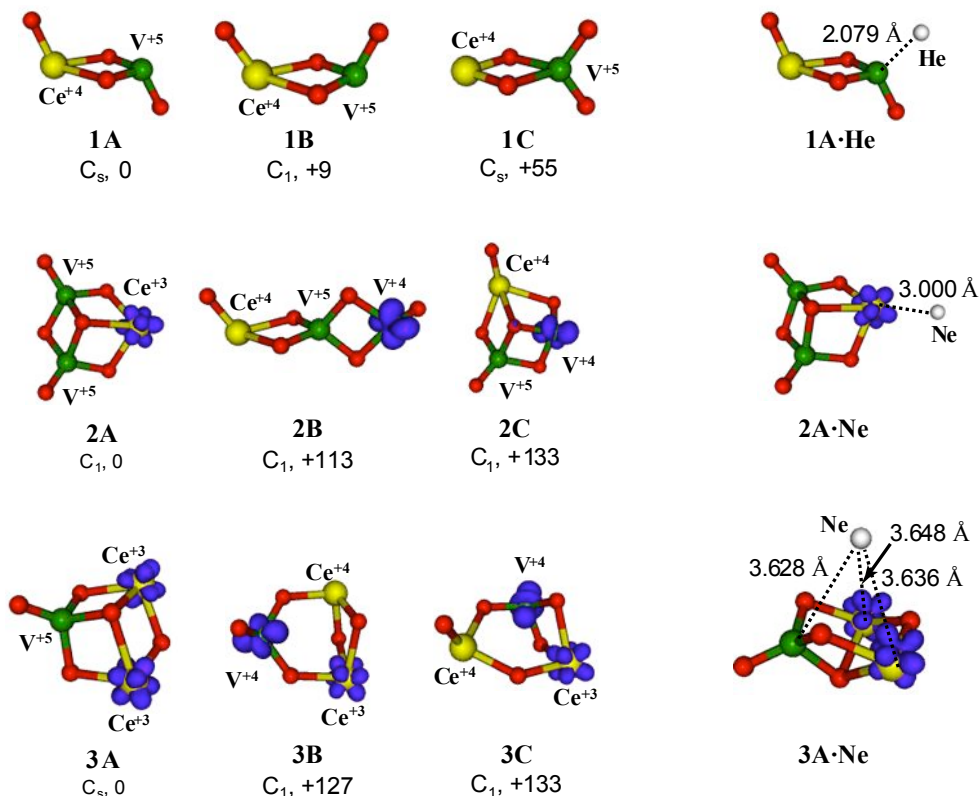
Figure 5.1: Optimized B3LYP/TZVPP structures and relative energies (in kJ/mol) of several low-lying isomers of $CeVO_4^+$ (**1**), $CeV_2O_6^+$ (**2**), and $Ce_2VO_5^+$ (**3**). (O red, V olive, Ce yellow). The oxidation state of each metal atom is specified. For the lowest-energy isomers helium- and neon-tagged structures are shown (right). The purple spin density isosurface indicates electron localization on either Ce or V.

Figure 5.1, which yields oxidation states of $Ce^{+3}/V^{+5}/V^{+5}$. This is contrary to the energetically higher-lying isomers, **2B** and **2C**, in which the extra electron resides on the V atom yielding the oxidation states $Ce^{+4}/V^{+4}/V^{+5}$. Additional structure optimizations for the neon-tagged complex **2A**·Ne reveal that the Ne atom prefers the low (three-fold)-coordinated Ce site ($E_{ion-Ne} = 9.1\,kJ/mol$) rather than the four-fold-coordinated V sites (Figure 5.1).

The cage-like structure **3A** (Figure 5.1) with C_s symmetry is predicted to be the lowest-energy isomer for **3**. It contains two unpaired electrons which are located on the Ce atoms. In the ground state both spins are anti-parallel, thereby forming a singlet spin state ($^1A'$). The next two low-lying isomers are the bicyclic triplet species **3B** (+127 kJ/mol) and **3C** (+133 kJ/mol). All three isomers contain one terminal oxygen atom, either in a V=O (**3A**, **3B**) or in a Ce=O (**3C**) double bond, and exhibit different oxidation states, $Ce^{+3}/Ce^{+3}/V^{+5}$ (**3A**) or $Ce^{+3}/Ce^{+4}/V^{+4}$ (**3B**, **3C**). Attachment of Ne to **3A** leads to structure **3A**·Ne (Figure 5.1), in which the Ne atom is located at a similar distance from all three metal atoms ($E_{ion-Ne} = 11\,kJ/mol$).

Summarizing, the present calculations predict ground-state structures for ions **1-3**, which are at least +55 kJ/mol more stable than other structural isomers. Whereas the electronic structure of **1** corresponds to fully oxidized metal centers (Ce^{+4}/V^{+5}), for the partially reduced species **2** and **3**, the most stable structures correspond exclusively to reduction of the Ce atoms

(Ce^{+3}), whereas the V^{+5} centers remain unaffected.
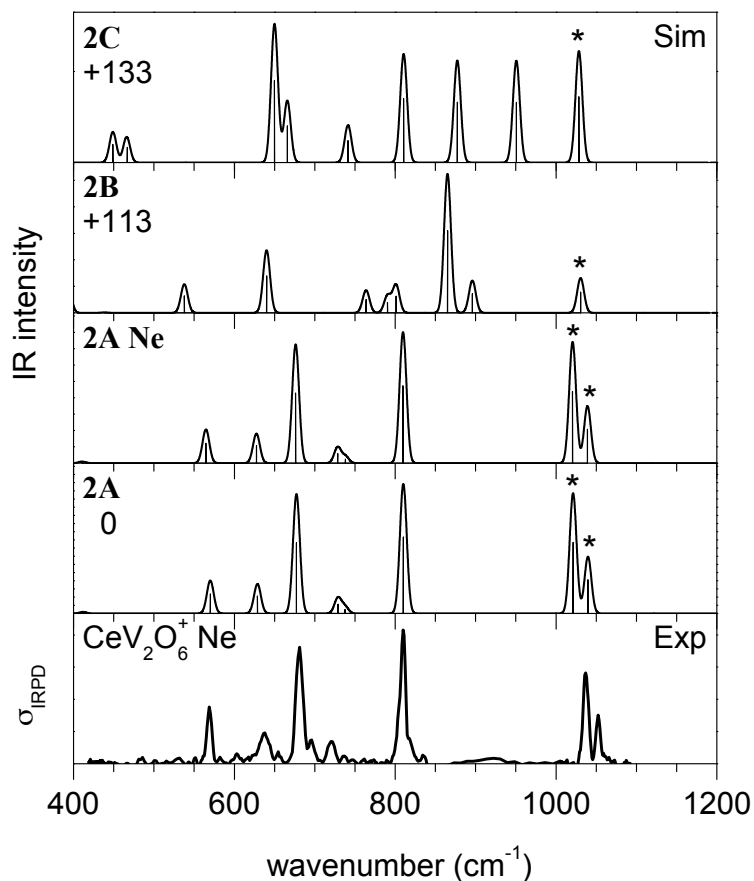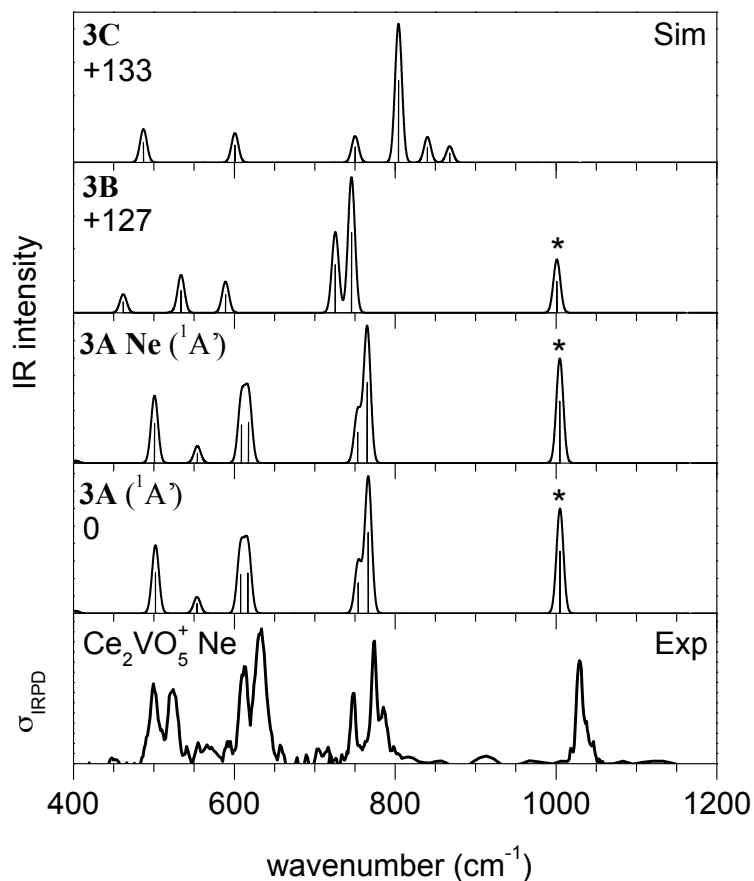
5.3.2 Vibrational Spectra and Structural Assignment
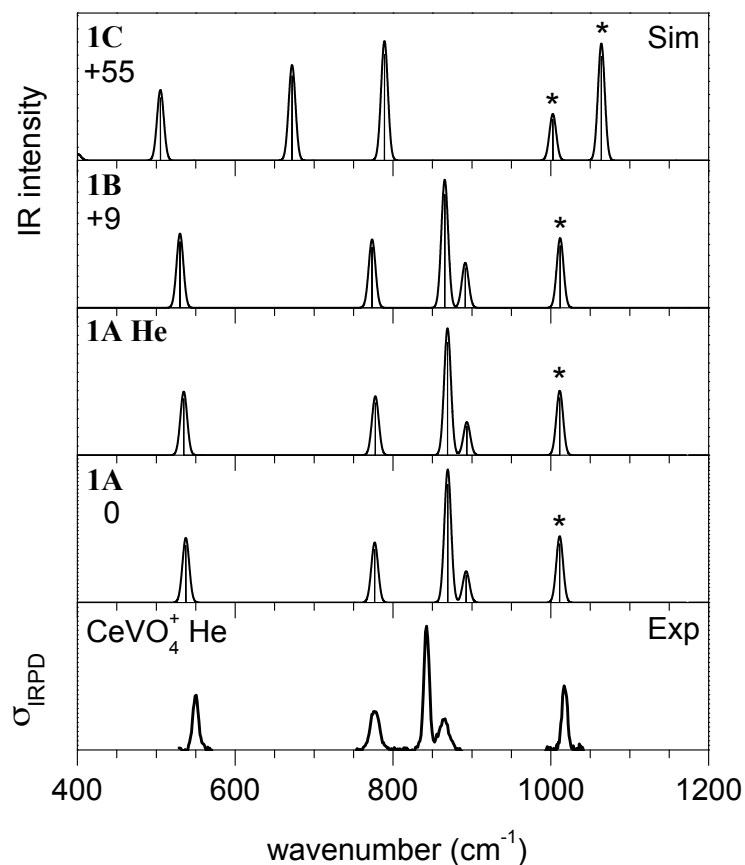
Figure 5.2: Comparison of experimental IR-VPD spectra of He-tagged $CeVO_4^+$ (bottom) to simulated B3LYP/TZVPP linear absorption spectra of isomers **1A**–**1C** and **1A**·He (upper panels). V=O modes are marked with an asterisk, and Ce=O modes are marked with an open circle. Relative energies are given in kJ/mol.

$CeVO_4^+$. Five absorption bands are observed at 1017, 866, 843, 776, and 551 cm^{-1} in the IR-VPD spectrum of **1**·He (bottom panel, Figure 5.2). The experimental spectrum shows excellent agreement with the simulated spectrum of the lowest-energy isomer **1A** both for band positions and relative intensities. The spectrum of **1A** remains nearly unaffected upon attachment of a He atom (spectrum **1A**·He, Figure 5.2). The deviations of the band positions are smaller than 5 cm^{-1}, suggesting that the influence of the messenger atom is negligible. The spectra of isomers **1A** and **1B**, the cis/trans isomers, are predicted to be very similar. The separation and relative intensities of the 843 and 866 cm^{-1} bands in the experimental spectrum (23 cm^{-1}, 1:0.25) are closer to those of the trans isomer **1A** (+24 cm^{-1}, 1:0.23) than those of the cis isomer **1B** (+26 cm^{-1}, 1:0.35), favoring an assignment to the trans isomer **1A**. The IR spectrum of the energetically higher-lying scissor-like (**1C**) structure (top panel, Figure 5.2) is markedly different from the experimental one, excluding it from the assignment.

The two highest-energy IR bands of **1**·He are assigned to the V=O ($\nu_{\text{exp}} = 1017\,\text{cm}^{-1}/\nu_{\text{calc}} = 1011\,\text{cm}^{-1}$) and Ce=O (866/893) stretching modes. Due to the 2.75 times higher mass of Ce compared to that of V, the Ce=O band is red-shifted relative to the vanadyl band, to a spectral region that overlaps with the M–(O)$_2$–M ring vibrations ($\sim$400–900\,cm^{-1}) [15], leading to substantial coupling between the Ce=O and the antisymmetric M–O ring stretching mode (843/869), in this particular case. The symmetric ring stretching (776/777) and breathing (551/537) modes are found at lower energies.

Figure 5.3: Comparison of experimental IR-VPD spectra of Ne-tagged CeV$_2$O$_6^+$ (bottom) to simulated B3LYP/TZVPP linear absorption spectra of the isomers **2A**–**2C** and **2A**·Ne (upper panels). V=O modes are marked with an asterisk, and Ce=O modes are marked with an open circle. Relative energies are given in kJ/mol.

CeV$_2$O$_6^+$. The IR-VPD spectrum of **2**·Ne (Figure 5.3) shows seven IR bands at 1052, 1037, 810, 720, 681, 638, and 569\,cm^{-1}. Excellent agreement is found with the simulated IR spectrum of the lowest-energy isomer **2A**. The doublet (1052 and 1037\,cm^{-1}) observed above 1000\,cm^{-1} is characteristic for structure **2A** because it unambiguously identifies the presence of two vanadyl groups, which yield a symmetric and an antisymmetric combination of the two V=O stretching modes (1040 and 1021\,cm^{-1}). Similar to **1A**, the addition of a Ne atom to structure **2A** has negligible effects on the IR spectrum (Figure 5.3). In contrast, isomers **2B** and **2C** exhibit a single V=O plus one Ce=O group. Consequently only a single band at

$1031 \, \text{cm}^{-1}$ ($1028 \, \text{cm}^{-1}$) is predicted for **2B** (**2C**). The Ce=O stretching modes at 896 (**2B**) and $877 \, \text{cm}^{-1}$ (**2C**) lie in a spectral region where no significant absorption is found in the experiment. The features below $800 \, \text{cm}^{-1}$ are attributed to stretching and bending vibrations involving the doubly coordinated O atoms.

Figure 5.4: Comparison of experimental IR-VPD spectra of Ne-tagged $Ce_2VO_5^+$ (bottom) to simulated B3LYP/TZVPP linear absorption spectra of the isomers **3A**–**3C** and **3A**·Ne (upper panels). V=O modes are marked with an asterisk, and Ce=O modes are marked with an open circle. Relative energies are given in kJ/mol.

$Ce_2VO_5^+$. The IR-VPD spectrum of **3**·Ne (bottom, Figure 5.4) exhibits seven peaks at 1029, 774, 748, 634, 612, 524, and $499 \, \text{cm}^{-1}$. The spectrum of the singlet ground state (^{1}A') of isomer **3A** reproduces six of these bands (1005, 767, 754, 617, 608, and $502 \, \text{cm}^{-1}$) satisfactorily and also accounts for the weak absorption band observed at $\sim560 \, \text{cm}^{-1}$ ($554 \, \text{cm}^{-1}$). The experimentally observed bands are assigned (in descending order with respect to energy) to one V=O stretching mode, three O–V–O stretching modes involving the doubly coordinated O atoms adjacent to the vanadium atom, as well as two more delocalized ring deformation modes. Unfortunately, the $524 \, \text{cm}^{-1}$ band remains unassigned. The initial assumption that this band may be attributed to the nearly isoenergetic triplet state (^{3}A') is not confirmed by the calculations, which yield identical vibrational frequencies for the ^{1}A' and ^{3}A' states [143]. The addition of a Ne atom has only minor effects on the IR absorption bands and cannot
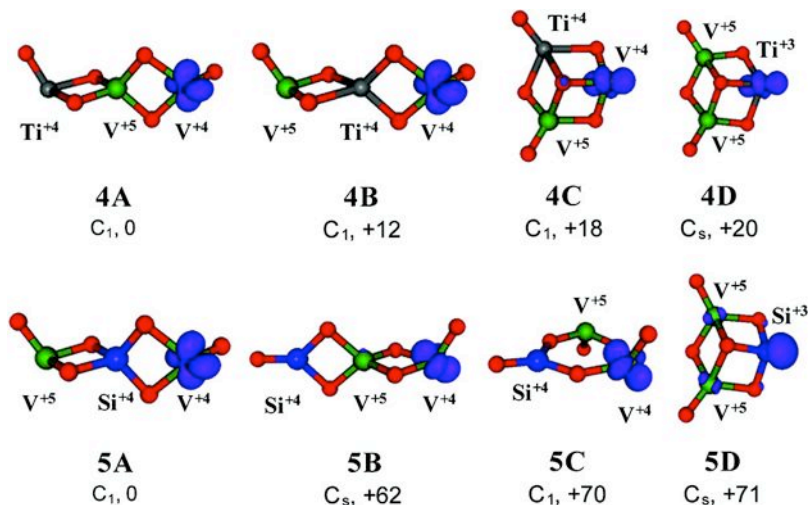
Figure 5.5: Optimized B3LYP/TZVPP structures and relative energies (in kJ/mol) of four low-lying isomers of $TiV_2O_6^+$ (**4A-4D**) and $SiV_2O_6^+$ (**5A-5D**). (O red, V olive, Ti dark gray, Si blue). The oxidation state of each metal atom is specified. The purple spin density isosurface indicates electron localization on either Ti/Si or V.

account for the observed $524\,cm^{-1}$ band (**3A**·Ne, Figure 5.4). The isomers **3B** (+127 kJ/mol) and **3C** (+133 kJ/mol) should lie too high in energy to be probed in the experiment. Their simulated IR spectra also fit less well with the experiment compared to the spectrum of **3A**. This allows to conclude that structures **3B** and **3C**, which contain a V^{+4} center, are not observed.

Summarizing, the best agreement of the experimental spectrum of **3**·Ne is found with the cage-like structure **3A** corresponding to oxidation states of $Ce^{+3}/Ce^{+3}/V^{+5}$. Both quasi-degenerate states ($^3A'$ and $^1A'$) contribute to the IR spectrum but cannot be differentiated due to their identical IR spectra.

5.4 Discussion

The good agreement between the experimental IR-VPD spectra and the simulated IR spectra of the lowest-energy structure for the three systems **1-3** considered here shows that the B3LYP/TZVPP calculations yield reliable relative energies and structures. On this basis, the calculations reproduce the vibrational properties of Ce-containing oxide clusters. In each case, the experiment confirms the predicted lowest energy structures for species **1** (Ce^{+4}/V^{+5}), **2** ($Ce^{+3}/V^{+5}/V^{+5}$), and **3** ($Ce^{+3}/Ce^{+3}/V^{+5}$). Specifically, one finds that in the gas phase binary metal oxide clusters studied here, the electron distribution leading to $Ce(f^1)^{+3}/V^{+5}$ is more stable than $Ce^{+4}/V(d^1)^{+4}$. These findings are consistent with previous experimental [154] and theoretical results [152] for crystalline $CeVO_4$, as well as with the preferential reducibility of cerium oxides over vanadium oxides reported previously [155–157]. It also agrees with a joint computational and surface science study [151] in which a solid ceria film was shown to stabilize vanadium oxide adspecies always in their highest oxidation state +5, whereas cerium was partially reduced.

For comparison, the reducibility of other typical support materials like titania and silica is studied based on additional DFT calculations using binary metal oxide clusters $MV_2O_6^+$ (M

= Ti, Si) as model systems. Figure 5.5 illustrates several optimized structures. In contrast to the cage-like structure of $CeV_2O_6^+$ (**2A**), the binary metal oxide clusters $TiV_2O_6^+$ (**4**) and $SiV_2O_6^+$ (**5**) prefer chain-like structures. Among the cage-like $MV_2O_6^+$ structures (M = Ti, Ce), **4C** with Ti^{+4}/V^{+4} is slightly (1.6 kJ/mol) more stable than **4D** with Ti^{+3}/V^{+5}, whereas **2C** with Ce^{+4}/V^{+4} is 133 kJ/mol less stable than **2A** with Ce^{+3}/V^{+5} (Figure 5.1). This suggests that the reduction of Ti^{+4} to Ti^{+3} is competitive with that of V^{+5} to V^{+4}. Comparing the Ce^{+4}/V^{+4} and Ti^{+4}/V^{+4} structures, the chain-like isomers **2B** and **4A**, respectively, are 20 and 18 kJ/mol more stable than the cage-like isomers with the same electron localization, **2C** and **4C**, respectively. They both have the V^{+5} species with the positive charge in the central four-fold-coordinated site. Only because of the unusual stabilization of vanadia in its highest oxidation state by cerium oxide does the cage-like structure **2A** with the Ce^{+3}/V^{+5} pair become the most stable isomer for $CeV_2O_6^+$. For Si, reduction to Si^{+3} is generally very unlikely, and structure **5D** is 71 kJ/mol less favorable than **5A**. Furthermore, the chain-like isomer **5A** with Si^{+4} in the middle is much more stable (62 kJ/mol) than the one with Si^{+4} in a terminal position (**5B**) because, in contrast to Ti, Si does not easily form terminal Si=O double bonds. A previous DFT study [158] also found that the structure of VO_x species supported on ceria is different from that supported on titania and also that their redox chemistry is different.

5.5   Summary and Conclusions

The experimental IR-VPD spectra of the cerium-vanadium oxide cluster cations **1-3** are well-reproduced by the simulated B3LYP/TZVPP IR spectra of the lowest-energy isomer, confirming that the B3LYP hybrid functional properly localizes electrons in the gas phase Ce-containing binary metal oxide clusters studied here. Experimental evidence is found for the predicted larger stability of Ce^{+3}/V^{+5} compared to that of Ce^{+4}/V^{+4}. We find crucial differences with respect to the relative reducibility in different binary metal-vanadium oxide clusters. Whereas in the vanadia-ceria clusters Ce^{+4} is easily reduced to Ce^{+3}, stabilizing the V^{+5} center, in vanadia-titania clusters, reduction of Ti^{+4} to Ti^{+3} is competitive with that of V^{+5} to V^{+4}, and in vanadia-silica clusters, Si^{+4} cannot be reduced. The present results confirm that an easily reducible support material, like ceria, may serve as an electron acceptor for the electron transferred to the active site in the rate-determining step [146–148]. Hence, IR-VPD spectroscopy on electronically tailored binary metal oxide clusters, combined with properly chosen QC calculations, may contribute to the understanding of complex solid catalysts.

Chapter 6

Solvent-Mediated Folding in Dicarboxylate Dianions

The water-induced conformational change in dicarboxylate dianions $^-$OOC–$(CH_2)_m$–COO$^-$ is investigated using IR-MPD spectroscopy combined with QC calculations. The vibrational signatures of microhydrated dianions containing up to 40 water molecules are studied in the region of the carboxylate stretching vibrations, by adding one water molecule at a time. The results reveal that the relative intensities of the symmetric (ν_S) verus antisymmetric (ν_A) stretching modes represent a sensitive probe for the conformation of the dianions. At sufficiently low solvent numbers the IR-MPD spectra exhibit a strong absorption for both ν_S and ν_A modes, indicating a linear conformation of the dianion. Once a critical number of water molecules are attached to the dianion, a significant drop of the ν_S band intensity is observed. This intensity drop is characteristic for a conformational transition of the dianions from a linear to a folded structure and markedly depends on the chain length. Aided by molecular dynamics (MD) simulations it is shown that the stability of the folded conformation is attributed to the formation of additional solute-solvent (rather than solvent-solvent) hydrogen bonds in the cluster.

6.1   Introduction

Dicarboxylate salts play an important role in many areas of science, including synthetic and atmospheric chemistry as well as biochemistry. For example, they are used as antitumor drugs [159] and as building blocks for metal-organic framework materials [160], and they are found in aerosol particles comprising photochemical smog [161]. Isolated dicarboxylate dianions ^-OOC-$(CH_2)_m$-COO^- are stable in the gas phase and serve as model systems for multiply charged anions [43, 162]. These dianions consist of two charged carboxylate groups which are separated by a hydrophobic, aliphatic chain which also makes them interesting for studying solvent-mediated effects.

The investigation of microhydrated dicarboxylate dianions by Wang et al. using anion photoelectron spectroscopy (PES) combined with MD simulation revealed that the conformation of the molecule is affected by the solvation environment [163]. The adiabatic detachment energy (ADE) of an anion typically increases with the degree of microhydration, i.e., with increasing number of water molecules n. Unexpectedly, for the suberate dianions ($m = 6$) the anion photoelectron spectra exhibit a characteristic decrease in the ADE from $n = 15$ to $n = 16$. Such behavior has never been observed in previous PES studies on solvated anions [163]. MD simulations were performed by P. Jungwirth in order to examine the population of different conformational states, i.e., linear and folded geometries of the dianion, as the number of water molecules increases. Interestingly, the simulations show that the folded structures are dominantly populated for $n > 18$. Ab initio calculations showed that the folded configurations have a significant lower ADE compared to the linear structures. Thus, the observed decrease in the ADE was attributed to a solvent-induced conformational transition of the dianion from a linear to a folded geometry. For $n = 0$ the Coulomb repulsion between the two charge centers is dominant and the dianion is linear. With increasing number of water molecules both negative charge centers of the dianion are solvated and two water clusters form. For the large solvated clusters both charges are shielded and a conformational transition occurs at $n \geq 16$. At those cluster sizes the water-water interaction is sufficiently large to overcome the Coulomb repulsion. Both solvation centers merge whereas the number of water-water H-bonds is increased which stabilizes the folded dianion [162, 163]. The critical cluster size for folding depends on the temperature [164] and the chain length m of the dianion [165]. The PES study of the adipate dianions ($m = 4$) found a drop in the ADE at 13 water molecules. In contrast, for the succinate dianion ($m = 2$), representing the smallest electronically stable dicarboxylate dianion in the gas phase, no indications of a conformational change are observed for up to 20 water molecules [165].

In order to develop a detailed understanding of the postulated hydration-mediated folding process, structural information is required which is challenging to extract from the photoelectron data. IR-PD spectroscopy combined with high-level QC calculations on microhydrated anions [38, 166, 167] is able to supply more information.

In the present study the vibrational signatures of microhydrated dicarboxylate dianions ^-OOC-$(CH_2)_m$-COO^- with different chain length $m = 2, 4, 6, 8$ are investigated employing IR-MPD spectroscopy. Aided by QC calculations relationships between conformational changes and spectroscopic features are established. The spectroscopic results allow analyzing how hydration can drive this conformational transition in a dianion and what role the hydrogen-bonded network plays. Previous structures of the suberate dianion derived by P. Jungwirth [163] simply represent snapshots of classical MD simulations. In contrast, in the present work a more demanding multi-stage protocol is employed to obtain the minimum-energy struc-

tures (Appendix C). First, classical MD simulations are used to search for several structural configurations. Second, these structures are further optimized using various high-level QC calculations in order to determine the lowest energy isomers and the harmonic vibrational frequencies.

6.2 Experimental Methods
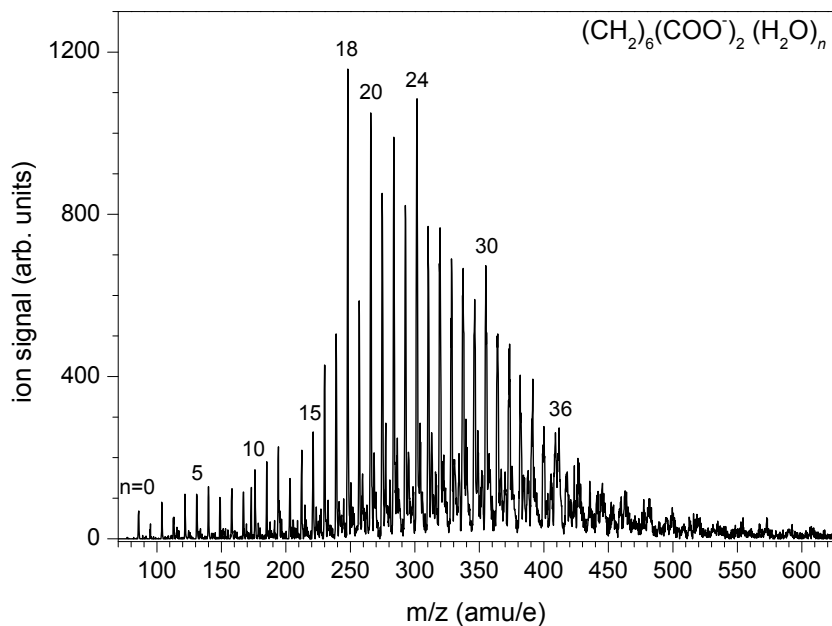
Figure 6.1: Typical mass spectrum of gas phase anions produced in a commercial Z-spray source from a solution of suberic acid (1 mM) and NaOH (2 mM) in a water/acetonitrile mixture (20/80). The source parameters have been tuned to optimize the formation of hydrated dianions with $n = 18$.

The IR-MPD experiments are carried out on the ion trap–tandem mass spectrometer (Section 2.2). Microhydrated dicarboxylate dianions are produced in a commercial Z-spray source (Subsection 2.1.2) from a solution containing 1 mM of the respective acid and 2 mM NaOH in a water/acetonitrile mixture (20/80). A typical cluster distribution of suberate dianions (mass $m = 172$ amu, charge $q = 2$ e) containing up to 40 water molecules is shown in Figure 6.1. Mass-selected parent ions are accumulated and thermilized for 98 ms by multiple collisions with a helium buffer gas in an ion trap held at 15 K. The ion packet, extracted from the trap, interacts with the IR laser pulse in the TOF extraction zone and high voltage pulses are applied for recording TOF mass spectra.

For the bare and monohydrated suberate dianions IR-VPD spectra are obtained from the corresponding Kr-tagged complexes. Those ion–Kr complexes are formed in the trap at a temperature of 63 K using a buffer gas mixture of ∼1 % Kr in helium.

Pulsed IR radiation is used either from FELIX or the "single" OPO/OPA IR laser system (Section 2.5). FELIX is used to probe the fingerprint region and operated in the spectral region from $650 \, \text{cm}^{-1}$ to $1800 \, \text{cm}^{-1}$ with average pulse energies of 30 mJ. The OPO/OPA laser system is operated in the spectral region from $2800 \, \text{cm}^{-1}$ to $3600 \, \text{cm}^{-1}$ covering the

region of the C–H and O–H stretching vibrations. TOF spectra are recorded 50–70 times for each wavelength step and subsequently averaged. IR-PD spectra are obtained by analyzing the normalized photofragment ion yield $I_f(\nu)$ and plotting the photodissociation cross section σ as a function of the laser frequency ν according to Eq. (2.16).

6.3   Bare and Monohydrated Suberate Dianions
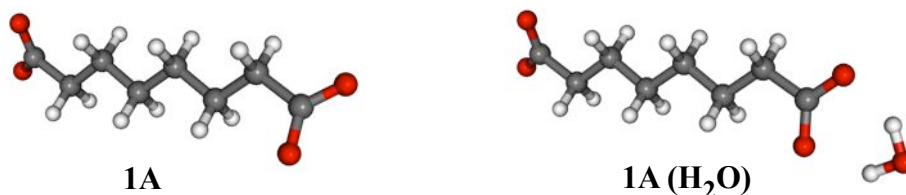

Scheme 1

As a first step towards the investigation of the folding transition in dicarboxylate dianions the vibrational signatures of the bare and monohydrated suberate dianion (SA^{2-}, $^-OOC–(CH_2)_6–COO^-$) are characterized. The measurement of the vibrational spectrum allows studying the influence of a single water molecule on the structure of the dianion. To this end IR-VPD spectra of the corresponding dianion-Kr atom complexes are measured in the range from $650\,cm^{-1}$ to $3600\,cm^{-1}$. This broad range covers several characteristic spectroscopic regions of the molecule including the C–O stretching vibrations of the carboxylate groups, the C–H stretching modes of the aliphatic chain and the O–H stretching region reflecting the vibrational modes of the water molecule. Based on these results a strategy is developed to investigate the spectroscopic features attributed to the solvent-mediated folding process.

Figure 6.2 shows the experimental IR-VPD spectra of the Kr-tagged bare dianion $SA^{2-}\cdot Kr$ and its monohydrated complex $SA^{2-}\cdot H_2O\cdot Kr$ (top part) measured in the region from $650\,cm^{-1}$ to $3600\,cm^{-1}$. The bottom part illustrates simulated linear absorption spectra which correspond to the bare and monohydrated all-trans isomer **A** (Scheme 1). This structure is predicted as the lowest energy isomer by MP2/aug-cc-pDVZ calculations in agreement with previously reported MP2/6-311+G* results of Wang and coworkers [162, 163].

6.3.1   Region of the C–H and O–H Stretching Vibrations

The IR-VPD spectrum of $SA^{2-}\cdot Kr$ exhibits a broad, structured C–H stretching band (labeled b in Figure 6.2) extending from 2800 to $2970\,cm^{-1}$ with five characteristic maxima observed at 2925, 2884, 2855, 2837 and $2818\,cm^{-1}$. The addition of a single water molecule to the suberate dianion leaves the shape and position of the C–H stretching band nearly unaffected (compare band b and b' in Figure 6.2), suggesting that the water molecule binds to one of the two carboxylate groups and leaves the C–C backbone structure unperturbed. For $SA^{2-}\cdot H_2O\cdot Kr$ a second absorption feature (denoted a') emerges in the O–H stretching region which is unusually broad and shows no structure. A similarly broad band is also observed in the IR-PD spectrum of $CH_3COO^-\cdot H_2O\cdot Ar$ [168, 169]. Here, the pronounced broadening is attributed to strong anharmonic coupling between the O–H stretching modes and intermolecular rocking motion which is found to be characteristic for a bidentate binding motif of the water molecule to the
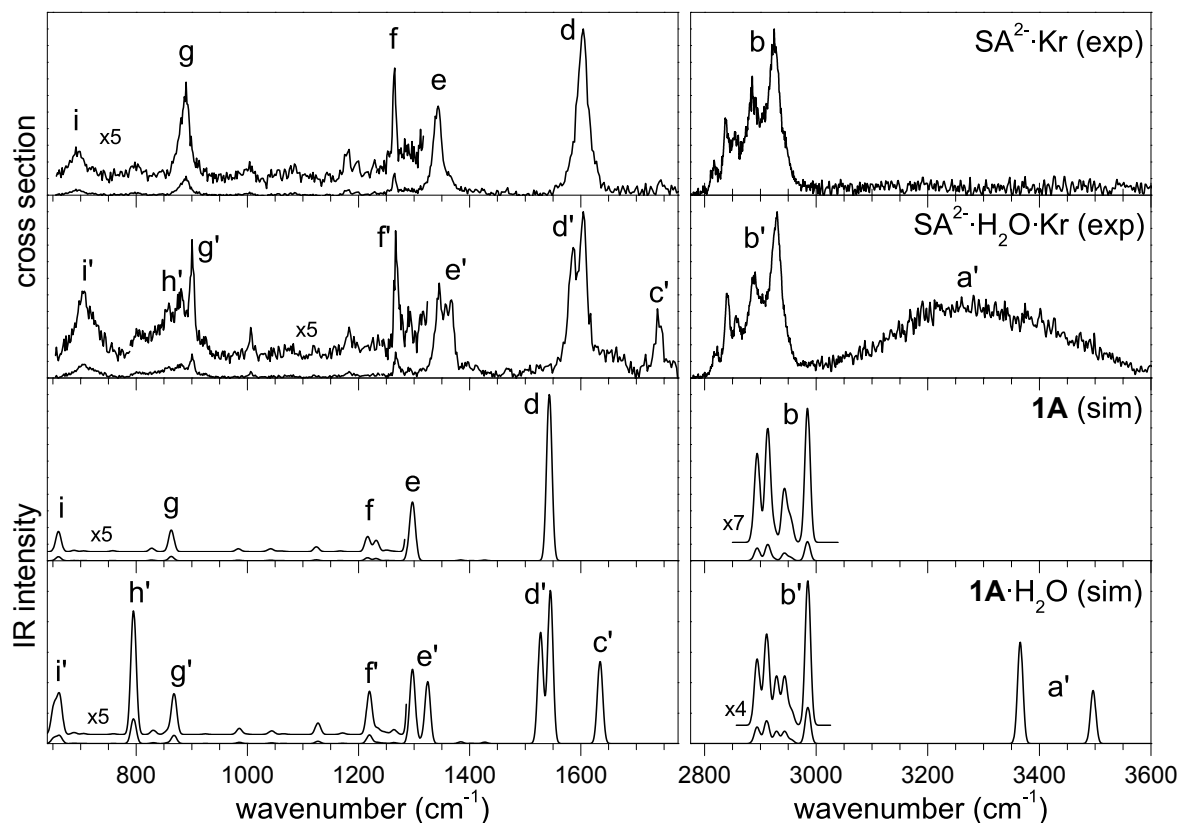
Figure 6.2: Top: IR-VPD spectra of the Kr-tagged suberate dianion (SA^{2-}·Kr) and the corresponding monohydrated dianion (SA^{2-}·H$_2$O·Kr) from 650 to 1800 cm^{-1} and 2775 to 3600 cm^{-1}, measured by monitoring the Kr atom loss channels as a function of the IR photon energy. The IR-VPD signal has been measured background-free as described in section 2.4. Bottom: Simulated linear absorption spectra of the lowest-energy isomers of the bare and monohydrated dianion obtained from MP2/aug-cc-pVDZ calculations. Harmonic frequencies are scaled by 0.959.

carboxylate group. Therefore, the observed spectra suggest that a similar coupling mechanism and thus a similar binding motif is present in SA^{2-}·H$_2$O·Kr (isomer **1A**·H$_2$O, Scheme 1).

The simulated spectra capture the main features in the C–H stretching region. The 12 C–H bonds in the dianion combine to yield 12 C–H stretching normal modes. The most intense vibrational mode observed in the IR spectra (b and b') is attributed to a combination of six antisymmetric CH$_2$ stretches, in which adjacent CH$_2$ units oscillate out-of-phase. The calculations also confirm that the presence of a water molecule in SA^{2-}·H$_2$O·Kr does not perturb the C–H stretching absorption region substantially. The broad feature a' observed in the O–H stretching region for SA^{2-}·H$_2$O·Kr is expectedly not well reproduced by the simulated spectrum. The two predicted harmonic frequencies fall within the range of the broad band, but the width is not reproduced because the broadening is governed by anharmonic coupling effects (see above).

Some discrepancies remain regarding the weak absorption band at 2818 cm^{-1} which is not reproduced by the all-trans isomer **A**. This could suggest that further isomers are present in the experiment and contribute to the IR-VPD spectrum. Indeed, the calculations predict low-energy isomers in cis configuration which can account for this weak red-shifted band [31].

The isomerization barrier between the trans- and cis-isomer is found to be rather low. Since the Kr-tagged complexes are formed at $63\,\mathrm{K}$ their internal energy is sufficiently high to allow for an interconversion between both conformations and consequently both species are probed in the IR-VPD experiment.

6.3.2   Fingerprint Region

The IR-VPD spectra of $SA^{2-}\cdot Kr$ and $SA^{2-}\cdot H_2O\cdot Kr$ in the fingerprint region are shown in the left part of Figure 6.2. The spectrum of $SA^{2-}\cdot Kr$ is essentially characterized by five bands at 1604 (d), 1343 (e), 1265 (f), 890 (g), and $697\,\mathrm{cm}^{-1}$ (i). The two most intense bands (d and e) are assigned to the antisymmetric (ν_A) and symmetric (ν_S) C–O stretching modes of the carboxylate groups, which are generally found in-between $1550\,\mathrm{cm}^{-1}$ and $1610\,\mathrm{cm}^{-1}$ and $1300\,\mathrm{cm}^{-1}$ and $1420\,\mathrm{cm}^{-1}$, respectively [170]. Note that the two carboxylate groups yield four stretching modes, i.e., a symmetric and an antisymmetric combination of the two types of carboxylate stretching modes.

Compared to $SA^{2-}\cdot Kr$, five bands of similar shape and relative intensity (d', e', f', g', and i') are also observed in the IR-VPD spectrum of $SA^{2-}\cdot H_2O\cdot Kr$ (Figure 6.2), suggesting that they are of similar nature. All additionally observed features can then be attributed to the presence of the water molecule. First, the band at $1738\,\mathrm{cm}^{-1}$ (c') corresponds to the water bending mode. It is well blue-shifted with respect to the H_2O bending frequency of an isolated water molecule ($1595\,\mathrm{cm}^{-1}$) [171]. A similarly blue-shifted band is observed in the IR spectrum of $NO_2{}^{-}\cdot H_2O$ ($\sim 1710\,\mathrm{cm}^{-1}$) [172], yielding additional support for the bidentate binding motif of the water molecule to the carboxylate group. Second, the broad feature observed between $820\,\mathrm{cm}^{-1}$ and $890\,\mathrm{cm}^{-1}$ (h') is tentatively assigned to the water rocking mode. As it is assumed that this intermolecular vibration is strongly coupled to the intramolecular O–H stretching modes (see above), one expects a broadened feature similar to band a'. Third, addition of one water molecule strongly affects the position of the C–O stretching bands (d' and e') which are split into multiple peaks. Binding of the water molecule to one carboxylate group leads to a shift of the associated carboxylate stretching modes, while the two corresponding modes of the unsolvated carboxylate group remain unchanged. Interestingly, this shift is toward the red for the ν_A mode (d' versus d), while it is toward the blue for the ν_S mode (e' versus e).

The comparison with the simulated IR spectra confirm the initial assignments. Band d is due to the excitation of the ν_A modes involving the two carboxylate groups. These yield a symmetric and an antisymmetric combination ($1543\,\mathrm{cm}^{-1}$), which are calculated within $0.1\,\mathrm{cm}^{-1}$ of each other and both with sizable IR intensity. This quasi-degeneracy reflects the weak coupling between each pair of modes owing to the large distance between the carboxylate groups. The corresponding combinations for the ν_S modes are also calculated quasi-degenerate in energy (1298 and $1300\,\mathrm{cm}^{-1}$), but only the antisymmetric combination is predicted to have significant IR intensity (band e). However, a CH_2 wagging mode is calculated within $2\,\mathrm{cm}^{-1}$ of the ν_S modes and contributes roughly 1/3 of the intensity of band e. All other IR-active modes have considerably smaller intensities. Band f is mainly due to CH_2 wagging ($1232\,\mathrm{cm}^{-1}$) and twisting modes ($1216\,\mathrm{cm}^{-1}$). Bands g and i correspond to modes that involve the O–C–O bending vibration with significant contributions from the terminal C–C stretching (g) and CH_2 rocking vibration (i), respectively.

## 6.4 Microhydration of Dicarboxylate Dianions

After the characterization of the vibrational signature of the bare and monohydrated suberate dianion, the microhydration is studied adding one water molecule at a time. The first water molecule preferentially binds to one carboxylate group which strongly affects the C–O stretching vibrations of that group only. One observes a red-shift of the corresponding ν_A mode and a blue-shift of the ν_S mode leading to a splitting of the carboxylate stretching bands in the vibrational spectrum. Additional water molecules are expected to further solvate the hydrophilic charge centers of the molecule. Therefore, the region of the carboxylate stretching vibrations is used as a probe for investigating the effects of microhydration on the structure of the dicarboxylate dianions. Several questions are addressed regarding the solvation motifs, e.g, are the carboxylate groups alternately solvated or do the water molecules preferentially bind to one group? How does the solvation environment affect the C–C backbone of the molecule?

### 6.4.1 Folding Transition in Suberate Dianions

Figure 6.3 shows IR-MPD spectra of microhydrated suberate dianions, $SA^{2-}(H_2O)_n$, which contain up to 28 water molecules. The spectra for $n = 0$ and $n = 1$ have been discussed in the previous section and are the same as those in Figure 6.2. The symmetric and antisymmetric carboxylate stretching bands undergo sequential shifts as a function of the number of water molecules which is shown in more detail in Figure 6.4 (left panel). One observes that the ν_A band shifts to lower (1603→1566 cm^{-1}) while the ν_S band shifts to higher frequencies (1344→1404 cm^{-1}) with increasing number of water molecules. This sequential shift is nearly monotonic and decreases gradually with increasing values of n. The frequency shifts are particularly strong in the range $0 \leq n \leq 10$ where the ν_S and ν_A bands shift by $+50$ cm^{-1} and -28 cm^{-1}, respectively. For $n = 10 - 28$ the band positions are less affected shifting by only $+10$ cm^{-1} (ν_S) and -9 cm^{-1} (ν_A). This indicates that for $n > 10$ the negative charge centers become fully solvated at a certain solvent number and additional water molecules have no direct interaction with the carboxylate groups. Wang et al. find a similar behavior in the ADE exhibiting a minor sequential increase beyond $n = 8$ [163]. The frequencies of aliphatic dicarboxylate dianions in bulk solution, for example, pimelate dianions $^-$OOC-(CH$_2$)$_5$COO$^-$ ($\nu_A = 1545$ cm^{-1}, $\nu_S = 1407$ cm^{-1}) [173], are reached for ν_S but not for ν_A, suggesting that ν_A is more sensitive to long-range solvent effects than ν_S.

While the sequential band shifts are rather regular in nature, the behavior of the band intensities shows an unexpected size dependence. This effect is best seen in Figure 6.3 for the IR-MPD spectra of $n \geq 14$. For hydrated clusters containing up to 15 water molecules similar peak intensities are observed for both the ν_A and ν_S bands. Interestingly, at $n = 16$ the intensity of the ν_S band drops significantly and remains low throughout the spectra of the larger clusters. A more quantitative analysis involves the normalized intensity $I(\nu_S) / [I(\nu_S) + I(\nu_A)]$ which is plotted in Figure 6.4 (right panel). The ratio increases from 0.32 at $n = 0$ to above 0.50 at $n = 11$, after which it drops down to 0.11 at $n = 16$ and remains small for all larger water clusters.

To elucidate the origin of this behavior, several minimum-energy structures for both linear and folded geometries for even values of n up to $n = 16$ have been determined. Figure 6.3 shows selected simulated IR spectra (blue traces) which agree best with the experiment together with the corresponding structures. For each cluster size with $n \leq 14$ the water molecules are predicted to symmetrically solvate both carboxylate groups. The first eight water molecules
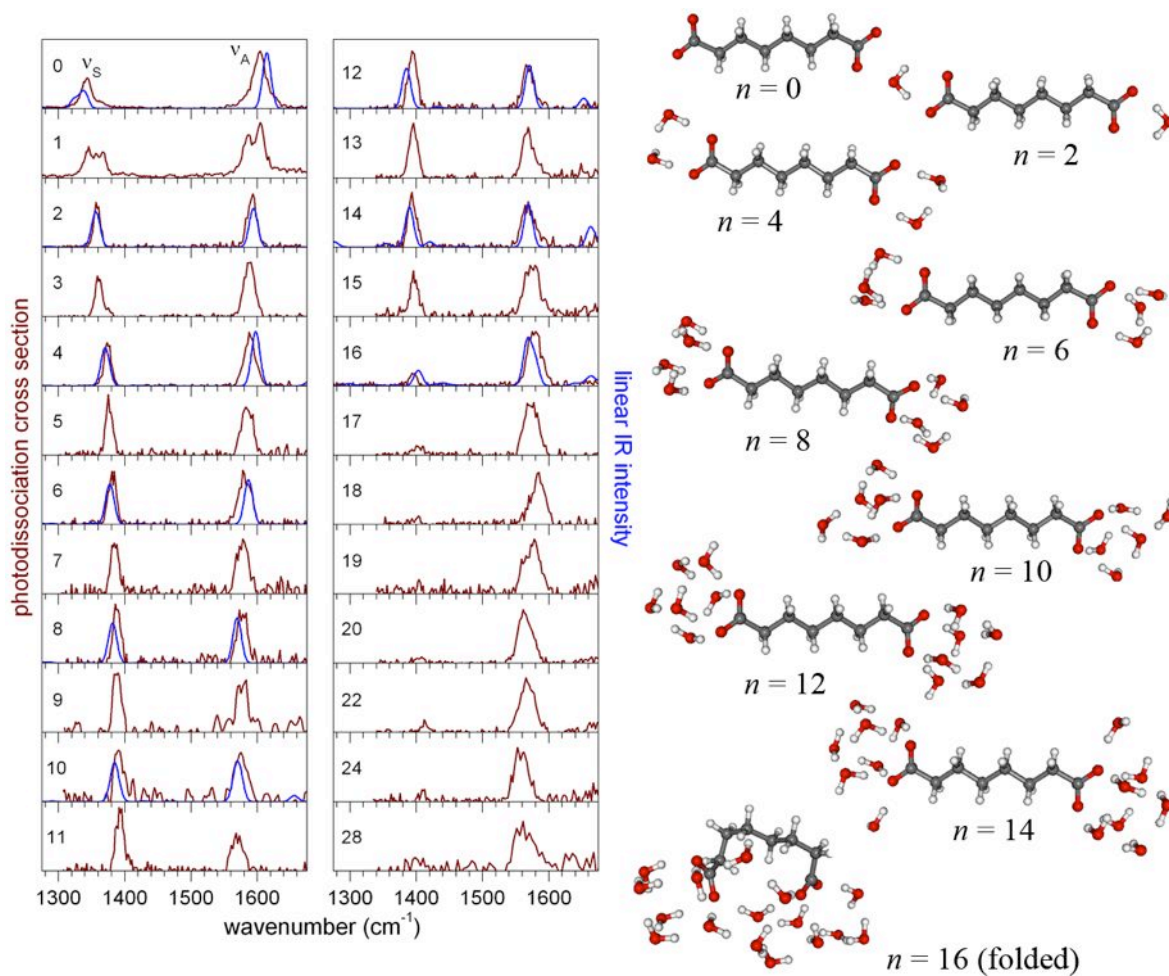
Figure 6.3: Experimental IR-MPD spectra (red traces) of $SA^{2-}(H_2O)_n$ clusters with $n = 0 - 28$ in the region of the symmetric (ν_S) and antisymmetric (ν_A) carboxylate stretching modes. The photodissociation cross section is plotted as a function of the photon energy (cm^{-1}). Simulated linear IR absorption spectra (blue traces) and optimized geometries are shown for $n = 0, 2, \ldots, 16$. Calculated harmonic frequencies are scaled by 1.025.
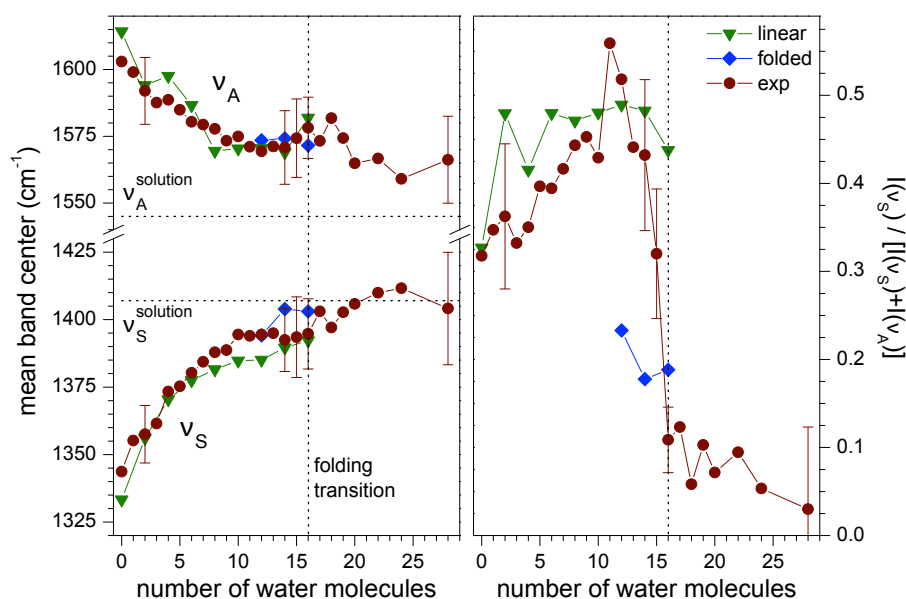
Figure 6.4: Center of the ν_S and ν_A bands (left) and the intensity ratio $I(\nu_S)/[I(\nu_S)+I(\nu_A)]$ (right) for microhydrated $SA^{2-}(H_2O)_n$ dianions as a function of n. Experimental values (red circles), as well as computed values for linear (green triangles) and folded (blue diamonds) geometries are shown. Lines connecting the symbols are drawn to guide the eye. Dotted horizontal lines indicate absorption frequencies in solution (see text).

directly interact with the carboxylate O atoms thereby constantly increasing the number of dianion-water H-bonds. Especially for $n = 6$ and $n = 8$ the formation of three-membered and four-membered water rings is predicted, respectively, where each water forms one H-bond with the dianion and another with an adjacent water (see Figure 6.3). Those solvation motifs are particularly stable, i.e., energetically favored, and are also found for hydrated bicarbonate [33] and nitrate anions [32]. For $n > 8$ additional water molecules extend the water network through formation of additional water-water H-bonds. For $n \leq 14$ the hydrated dianion has a linear all-trans configuration where both water clusters are separated. In contrast, at $n = 16$ the $(CH_2)_6$ chain of the molecule is strongly bent resulting in a reduced distance between the carboxylate groups. Interestingly, its IR spectrum exhibits a characteristic drop in the ν_S band intensity, whereas the ν_A mode remains intense. This is different for the linear configurations for $n < 16$ where both bands have similar intensities (see Figure 6.3 and 6.4). Note that stabilized folded geometries are also predicted for cluster sizes $n = 12$ and $n = 14$ whose IR spectra exhibit a similar intensity drop.

For $n < 16$ good agreement between experiment and theory is found for the linear geometries. The experimental frequency shifts and relative intensities of the ν_S and ν_A band are well reproduced by the simulated IR spectra (Figure 6.4). At $n = 16$ only the folded structure can account for the observed intensity drop of the ν_S band, which represents a characteristic spectroscopic feature of all folded geometries. Hence, the observed intensity drop at $n = 16$ is attributed to a conformational change of the dianion from a linear to a folded configuration. These results support the previous suggestions of a conformational transition reported by Wang et al. [163].

IR-MPD spectra of cluster sizes $n = 5 - 18$ have also been measured in the spectral region from 2500 to $3800\,cm^{-1}$ covering the region of the C–H and O–H stretching vibrations (Figure

C.1 in the appendix). Unfortunately, the IR spectra for $n \geq 14$ do not reveal significant changes that could be attributed to a folding transition at $n = 16$.

6.4.2   Origin of Folding and Intensity Quenching

The potential energy of a particular conformation can be decomposed into three different types of interactions involving the repulsive Coulomb potential between the charges as well as the attractive dianion-water and water-water interactions. For the unsolvated dianion the linear conformation is energetically favorable, because it minimizes the repulsive Coulomb interaction. In contrast, in the predicted folded geometry for $n = 16$ (Figure 6.3) the distance between the carboxylate C-atoms decreased from $9.2\,\text{Å}$ to $5.5\,\text{Å}$ and, consequently, the Coulomb repulsion strongly increases. Hence, in order to stabilize the folded state the enhanced Coulomb repulsion has to be compensated. Initially, the solvation of the dianion by the first few water molecules ($n \leq 8$) enhances the dianion-water interaction because these water molecules directly bind to the carboxylate groups (see structures in Figure 6.3). Simultaneously, the two charge centers are screened by the solvation shell which minimizes the Coulomb repulsion. As more water molecules are added ($n > 8$) the water clusters grow and the water-water interaction increases. At a critical size n the charges are sufficiently screened and the attractive interactions can overcome the Coulomb repulsion. One could assume that the enhanced water-water interaction stabilizes the folded state, as suggested by Wang and coworkers [162, 163], but this is not the case. Interestingly, the simulations reveal that the folded conformation is stabilized by the dianion-water interaction. For instance, at cluster size $n = 16$ the total number of H-bonds in the folded geometry is 31 compared to 28 for the linear structure; two additional *dianion-water* H-bonds are formed and only one *water-water* H-bond. Similar results are obtained for cluster sizes $n = 12$ and $n = 14$. Surprisingly, the water-water interaction does *not* contribute to folding, as the energy of the water cluster is not lowered by folding.

Another question concerns the origin of the intensity quenching of the ν_S band observed for the folded structures. Generally, the IR intensity of a vibrational mode is proportional to $|\partial M / \partial Q|^2$, the square of the change in dipole moment M as the geometry is displaced along the corresponding normal coordinate Q. As an example, the dipole moment has been analyzed for the linear and folded geometries of cluster $n = 12$ for the two symmetric and antisymmetric carboxylate stretching modes (Figure 6.5). For each mode, the intra-molecular charge density for both the minimized and displaced structure are calculated based on natural population analysis (NPA). These results are then employed to obtain the density difference which is plotted in Figure 6.5 using the colors *red* and *blue* to indicate an increased and decreased charge density, respectively. Displacement along the ν_A modes causes a strong charge transfer (CT) within a carboxylate. In the linear conformation the vibrations of both carboxylate groups are nearly decoupled. This is different in the folded geometry where the decreased distance between the carboxylate groups results in mutual polarization effects. However, owing to the local character of this CT, it is independent of the geometry of the polyethylene chain and is hence unaffected by the folding. Therefore both antisymmetric modes remain intense. This situation is in contrast to excitation of ν_S, where a smaller but long-range CT between the carboxylate moiety and the chain occurs, which is sensitive to changes in the dihedral angles upon folding (Figure 6.5, right). The excitation of the ν_S modes induces oscillating dipoles oriented along the aliphatic chain indicated by the colored arrows. In the linear conformation the antisymmetric combination strongly contributes to the IR spectrum ($I = 790\,\text{kJ/mol}$).
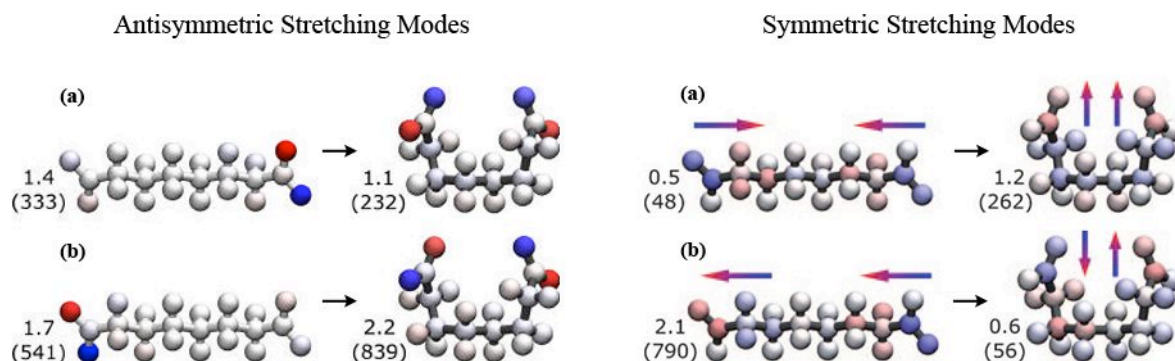
Figure 6.5: Intra-molecular charge density difference for the linear and folded $n = 12$ clusters (water molecules are not shown) induced by displacement along the antisymmetric ν_A modes (left) and symmetric ν_S modes (right). The symmetric combinations are shown on top (labeled (a)) while the antisymmetric combinations are shown at the bottom (labeled (b)). Results are obtained from natural population analysis (see text). $|\partial M / \partial Q|$ is given in $10^{-2}\,\mathrm{a.u.}$ Values in parentheses correspond to the IR intensity in kJ/mol.

Here, the induced dipoles are oscillating in phase resulting in a strong change of the dipole moment. In contrast, the symmetric combination has weak intensity ($I = 48\,\mathrm{kJ/mol}$) because the dipoles, oscillating in anti-phase, nearly cancel. This situation is reversed within the folded geometries. The intensiy of the antisymmetric combination significantly decreases by a factor of 14 while the symmetric combination is only enhanced by a factor of 5. Consequently, the intensity of the ν_S band drops. Note that the strength of this charge fluctuation strongly responds to hydration, and it will be affected by the mutual polarization of the carboxylates.

6.4.3 Folding Transition in Dependence on the Chain Length

The intensity of the ν_S band represents a sensitive probe to distinguish between linear and folded conformations of dicarboxylate dianions. The conformational transition from a linear to a folded state, is spectroscopically characterized by a sudden drop of the ν_S band intensity at a critical solvent number n. This spectroscopic tool is used to investigate how the conformational change is affected by the chain length m of the dianion. Several interesting questions arise, e.g., is a conformational transition observed for all chain lengths m and how does the critical solvent number n depend on m. To this end, the microhydration of $(CH_2)_m(COO^-)_2 \cdot (H_2O)_n$ clusters with $m = 8$ (Sebacate), $m = 4$ (adipate) and $m = 2$ (succinate) is studied. IR-MPD spectra are measured for dianions containing up to 40 water molecules (see Figures C.2–C.4 in the appendix). An overview of the sequential ν_A and ν_S band shifts as well as the normalized ν_S band intensities are plotted as a function of the number of water molecules in Figure 6.6. After the discussion of the experimental data, structures are assigned to microhydrated adipate and succinate dianions (Figure 6.7 and 6.8).

Adipate and Sebacate Dianions. For both dianions the sequential shift of the ν_A band shows a non-monotonic behavior when the number of water molecules n increases (top part, Figure 6.6). For $m = 4$, the ν_A band initially red-shifts from $1583 \rightarrow 1567\,\mathrm{cm}^{-1}$ between $n = 2 - 11$. From $n = 11$ to $n = 13$ one observes a blue-shift of about $10\,\mathrm{cm}^{-1}$. Eventually, for larger clusters with $n > 13$ the ν_A band red-shifts again reaching $1570\,\mathrm{cm}^{-1}$ at $n = 40$. For $m = 8$, the longest dianion studied here, one observes a similar trend. The addition of
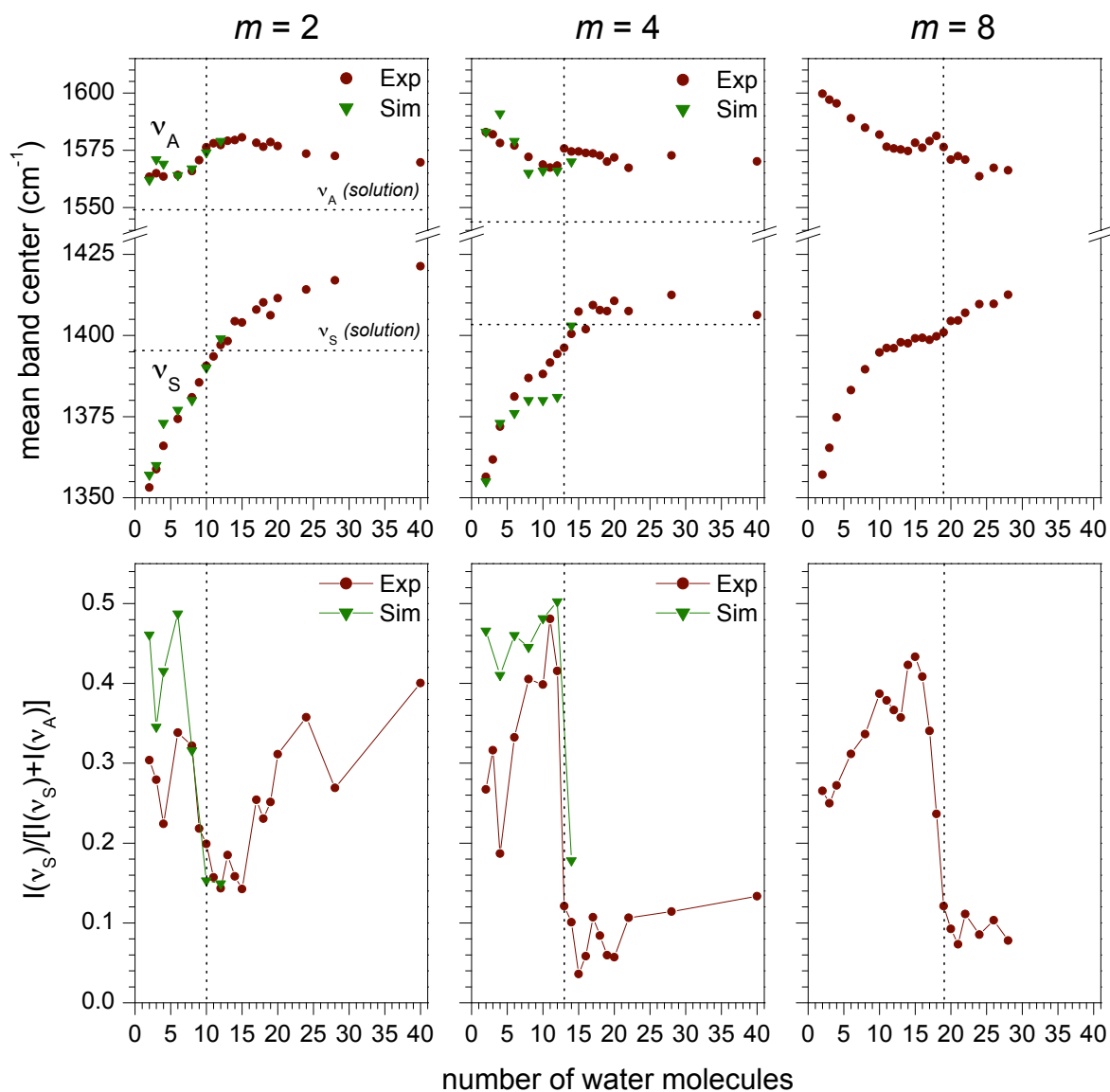
Figure 6.6: Sequential shifts of the ν_S and ν_A bands and the intensity ratio $I(\nu_S)/[I(\nu_S)+I(\nu_A)]$ as a function of the number of water molecules n for microhydrated $(CH_2)_m(COO^-)_2$ dianions with $m = 2, 4, 8$. Horizontal lines indicate the frequencies of the respective acid in solution. The vertical lines mark the critical solvent number n where the normilized ν_S intensity drops below 0.2. For $m = 2, 4$ the simulated normalized intensities are plotted (green triangles) corresponding to the best structural candidates (see also text).

the first 14 water molecules induces a red-shift from $1600 \rightarrow 1575\,\text{cm}^{-1}$ while from $n = 14$ to $n = 18$ a blue-shift of about $6\,\text{cm}^{-1}$ is observed. Then, for $n > 18$ the ν_A band monotonically red-shifts to $1566\,\text{cm}^{-1}$.

The ν_S band exhibits a monotonic blue-shift from $1357 \rightarrow 1413\,\text{cm}^{-1}$ and $1356 \rightarrow 1406\,\text{cm}^{-1}$ for $m = 8$ and $m = 4$, respectively. Similar to the suberate dianions, for $m = 4$ the ν_S band converges towards the frequencies of dianions in bulk solution ($1403\,\text{cm}^{-1}$), while the ν_A band does not reach the bulk limit ($1543\,\text{cm}^{-1}$).

In contrast to the band shifts, the normalized intensity of ν_S shows a stronger dependence on the chain length. Similar to the suberate dianion, a significant decrease of the intensity is observed for both dianions at a critical cluster size n. The normalized intensity drops below 0.2 at $n = 19$ ($n = 13$) for $m = 8$ ($m = 4$) and remains low for all larger clusters (bottom part, Figure 6.6). Note that the observed blue-shift of the ν_A band coincides with the intensity drop. Based on the results obtained for the suberate dianion, these observations are attributed to a conformational change. The findings show that the critical solvent number required for inducing the folding transition decreases when the chain length is reduced. More precisely, the critical solvent number n depends linearly on the chain length m, i.e., n reduces by three if m is reduced by two.

Succinate Dianion.   For the succinate dianion ($m = 2$), the shortest dianion studied here, several deviations occur from the general trends observed for dianions with longer chains. The shift of the ν_A band exhibits a non-monotonic behavior as well. The addition of up to 10 water molecules immediately induces a blue-shift ($1563 \rightarrow 1576\,\text{cm}^{-1}$) whereas for larger clusters with $n > 10$ the ν_A band slowly red-shifts to $1570\,\text{cm}^{-1}$ (Figure 6.6). Similar to dianions with $m > 2$, the frequency observed for dianions in solution ($1549\,\text{cm}^{-1}$) is not reached. In contrast, the frequency of the ν_S band monotonically increases ($1353 \rightarrow 1421\,\text{cm}^{-1}$) and reaches the bulk limit ($1395\,\text{cm}^{-1}$), which is even exceeded by about $26\,\text{cm}^{-1}$.

An interesting behavior is observed for the normalized ν_S intensity. Between $n = 8$ and $n = 10$ the intensity drops below 0.2 which is again accompanied with a blue-shift of the ν_A band. Surprisingly, the intensity remains small (< 0.2) only between $n = 10$ and $n = 15$ while it increases again to ~ 0.3 for larger clusters (Figure 6.6). This behavior is different compared to the results of the longer dianions. Although the intensity drop is less pronounced, this finding suggests that the $(\text{CH}_2)_2$ chain becomes slightly distorted at the cluster size $n = 10$. However, the increasing ν_S intensity indicates that the distorted geometry is not stabilized anymore when the hydration level increases and the molecule relaxes into the linear conformation. This aspect is discussed in more detail further below. First, structures will be assigned to the IR-MPD spectra in order to address the question if a folded geometry is still favorable for the short succinate dianion.

6.4.4   Structural Assignment

In the following, structures of microhydrated succinate and adipate dianions are assigned based on the comparison of experimental IR-MPD spectra with simulated linear absorption spectra of several low-energy isomers (Figures 6.7 and 6.8). Details on the computational methods are given in the appendix. In the first part, structures are assigned to adipate dianions ($m = 4$). Here, similar to suberate dianions, two structural motifs are predicted, i.e., linear (**lin**) and folded (**fold**) conformations. Afterwards, structural isomers are assigned to succinate dianions ($m = 2$). This assignment is more complex because an additional

structural motif is predicted. For the comparison, experimental and simulated IR spectra are arranged in columns with increasing cluster size n allowing for a two-dimensional comparison. Horizontally, for each n the experimental spectrum (left) is compared to two simulated IR spectra (middle and right). Furtermore, the vertical arrangement enables to compare the simulated sequential band shifts with the experimental trends. The IR spectra shown in the middle column are selected regarding the good agreement with the experiment.

Hydrated Adipate Dianions ($m = 4$). IR-MPD spectra and simulated IR spectra of hydrated adipate dianions containing an even number of water molecules $n = 2, 4, \ldots, 14$ are compared in Figure 6.7. In particular, the assignment relies on the observed sequential shifts and relative intensities of the ν_A and ν_S band. The experimental spectra show a monotonic blue-shift of the ν_S band ($45\,\mathrm{cm}^{-1}$) and a monotonic red-shift of the ν_A band (left panel, Figure 6.7). Initially, at $n = 2$ and $n = 4$, the ν_S band is weaker compared to the ν_A band whereas similar intensities of both bands are observed between $n = 6 - 12$. A striking feature is the significant intensity drop of the ν_S band at $n = 14$.

For $n \leq 8$ these experimental trends are well reproduced by the IR spectra of the symmetrically solvated structures (middle panel, Figure 6.7). For $n = 4$ and $n = 6$ the simulations also predict low-energy isomers with an asymmetric solvation environment, **lin-1** (1+3) and **lin-2** (2+4), respectively. For $n = 4$, this complex is found as the global minimum. However, its IR spectrum (right panel, Figure 6.7) exhibits a splitting of the ν_S band which is in conflict with the experiment. The situation is similar for $n = 6$. Here, the asymmetric solvation, **lin-2** (2+4), induces a splitting of the ν_A band which is not observed experimentally. For $n = 8$ two symmetrically solvated complexes, **lin-1** ($0.0\,\mathrm{kJ/mol}$) and **lin-2** ($+2.1\,\mathrm{kJ/mol}$), are predicted which differ in the arrangement of the solvating water molecules. Their IR spectra are very similar and cannot be differentiated. For $n = 10$ the asymmetrically solvated complex, **lin-1** (4+6), is the lowest energy isomer and predicted $1.3\,\mathrm{kJ/mol}$ more stable than the symmetrically solvated complex **lin-2** (5+5). This is attributed to the four-membered water ring which represents a particularly stable binding motif (see also structures for $m = 6$ in previous subsection). The IR spectrum of **lin-1** (4+6) shows good agreement with the experimental band positions and intensities (middle panel, Figure 6.7). In contrast, isomer **lin-2** (5+5) features a spectrum with a strongly blue-shifted ν_A band, in contradiction to experiment. For larger clusters ($n > 10$), the simulations predict linear and folded conformations to be close in energy. At $n = 12$ the folded structure, **fold-1**, is predicted $7.5\,\mathrm{kJ/mol}$ lower in energy than the linear complex **lin-1** (6+6). The IR spectrum of isomer **fold-1** shows a very weak ν_S band which is not observed in the experiment. Instead, the linear geometry, **lin-1** (6+6), can account for the observed relative intensities and is therefore assigned to the IR-MPD spectrum. For $n = 14$ the observed ν_S band intensity is strongly reduced which is assigned to the folded structure **fold-1**.

The band positions and normalized ν_S intensity of all assigned simulated IR spectra (middle panel, Figure 6.7) are plotted in Figure 6.6 (green triangles). The assigned structures can account for the observed red- and blue-shift of the ν_A and ν_S band, respectively, as the number of water molecules increases. The experimental trend of the normalized ν_S intensity is qualitatively reproduced by the simulated IR spectra. However, especially for the small clusters with $n < 6$ the deviations between experimental and simulated ν_S intensities are fairly high. In general, such deviations are expected owing to the multiple photon nature of the absorption process which lowers the IR-PD efficiency and results in smaller band intensities
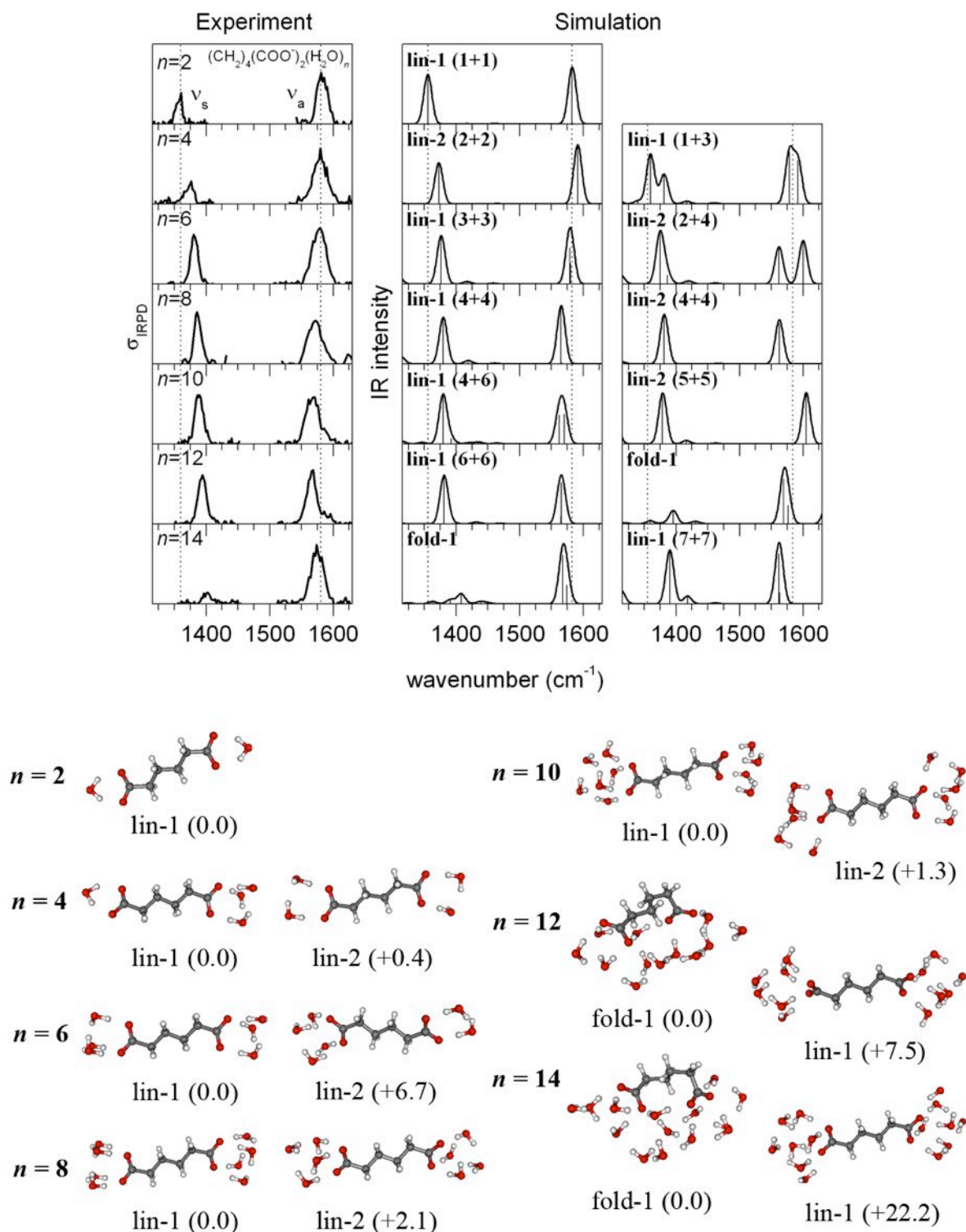
Figure 6.7: Experimental IR-MPD spectra (left panel) of microhydrated adipate dianions $(CH_2)_4(COO^-)_2 \cdot (H_2O)_n$ with $n = 2, 4, \ldots, 14$ compared to simulated linear IR absorption spectra (middle and right panel). Harmonic frequencies are scaled by 1.025. Optimized geometries are shown together with their relative energies (parentheses) given in kJ/mol.

[174]. This effect is more pronounced for the smaller hydrated complexes ($n < 6$) due to their higher dissociation energy, compared to the larger clusters, which requires the absorption of more photons to reach the dissociation limit. Furthermore, the intensity of the ν_S band may be stronger affected by the IR-MPD process since it falls in a lower frequency region than the ν_A band.

Summarizing, the comparison between experimental and simulated spectra allows distinguishing between symmetrically and asymmetrically solvated complexes based on energetic and spectroscopic reasons (e.g. band shape and shifts). For $n \leq 8$ one finds that the dianion is symmetrically solvated while for $n = 10$ an asymmetric solvation is preferred. However, the region of the carboxylate stretching vibrations is not sensitive to the arrangement of the water-water network. More important, the conformational states can be unambiguously assigned based on the relative band intensities. For $n \leq 12$ the observed ν_S and ν_A bands have similar intensity which is attributed to the linear conformation of the molecule. For $n > 12$ the observed ν_S band intensity is significantly decreased which is assigned to a folded geometry of the dianion similar to the suberate dianion.

Hydrated Succinate Dianions ($m = 2$). The succinate dianions differ from dianions with longer alkyl chains in one essential aspect. The separation of the two carboxylate groups is sufficiently small to allow water molecules to bind to both of them simultaneously without significant chain deformation. Such water molecules bridge both carboxylates which forms an additional solvation motif denoted as **bri** in the following structure assignment. The three possible structural motifs, i.e., **lin**, **bri** and **fold**, of the dianion are better classified by the C–C–C–C dihedral angle: (i) **lin** corresponds to a *trans* configuration with a dihedral angle of 180°, (ii) for **bri** the dihedral angle ranges from 130°–160°, (iii) **fold** is associated with a dihedral angle ≤100°. Therefore, the folding of the dianion is rather understood as a strong distortion of the inner C–C bond of the chain which decreases the distance of the two charge centers.

IR-MPD spectra and simulated IR spectra of hydrated succinate dianions containing $n = 2 - 4, 6, \ldots, 12$ water molecules are compared in Figure 6.8. The following experimental trends of the ν_A and ν_S band are considered for the structural assignment. The experimental spectra show a monotonic blue-shift of both bands (left panel, Figure 6.8). The ν_S band is observed to shift about $45\,\mathrm{cm}^{-1}$. The position of the ν_A band remains nearly constant between $n = 2 - 8$ while a blue-shift of about $12\,\mathrm{cm}^{-1}$ is observed for $n > 8$. The ν_S intensity noticeably drops at $n = 10$ and remains low at $n = 12$.

These experimental trends are well reproduced by the simulated IR spectra shown in the middle panel of Figure 6.8. In particular for the small clusters with $n \leq 6$ these IR spectra correspond to symmetrically solvated structures (see Figure 6.8). Nevertheless, this assignment is not always unambiguous as discussed in the following. For $n = 2$, the symmetrically solvated structure, **lin-1** (1+1), is the lowest-energy isomer whose IR spectrum exhibits a single peak for the ν_S and ν_A band in good agreement with the experiment. In contrast, the bridged structure **bri-1** (+9.6 kJ/mol) yields an IR spectrum (right panel, Figure 6.8) which features a splitting of the ν_A band in conflict with the experiment. For $n = 3$, the lowest-energy isomer **bri-1** represents a rather symmetric solvation motif whose IR spectrum agrees well with the experiment regarding the band positions and intensities. The linear (1+2) complex, **lin-1** (+7.1 kJ/mol), yields a similar IR spectrum, but differs in the shape of the ν_S band which features a small splitting. However, due to the width of the experimental band isomer **lin-1**
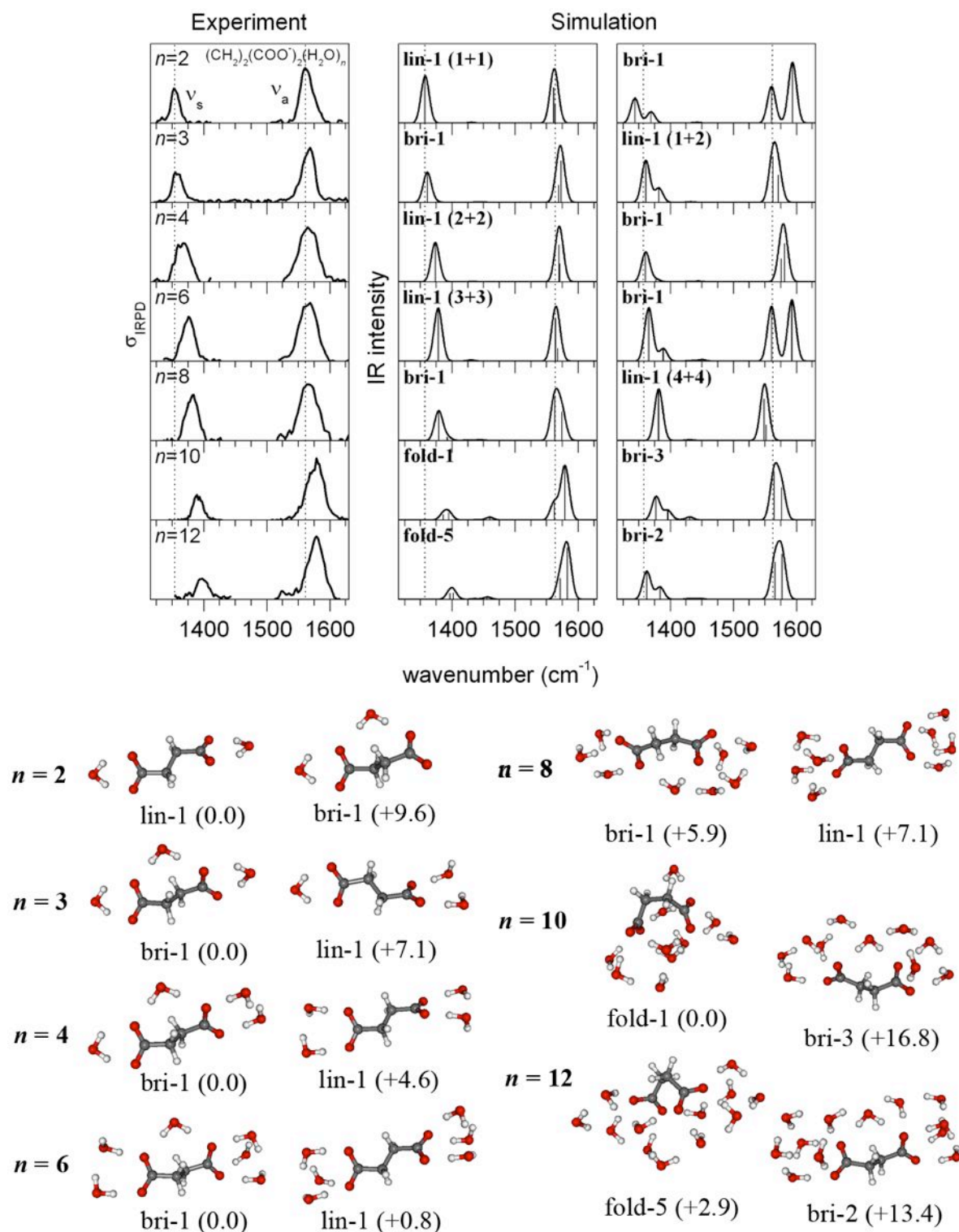
Figure 6.8: Experimental IR-MPD spectra (left panel) of microhydrated succinate dianions $(CH_2)_2(COO^-)_2 \cdot (H_2O)_n$ with $n = 2-4, 6, \ldots, 12$ compared to simulated linear IR absorption spectra (middle and right panel). Harmonic frequencies are scaled by 1.025. Optimized geometries are shown together with their relative energies (parentheses) given in kJ/mol.

cannot be excluded from the assignment. For $n = 4$ the situation is similar. Here, structure **bri-1** is predicted 4.6 kJ/mol lower in energy than the linear complex **lin-1** (2+2). Both IR spectra are similar and reproduce the experimental IR-MPD spectrum regarding the band shapes and intensities which does not allow for a clear assignment. However, regarding the sequential shifts of both bands the spectrum of isomer **lin-1** (2+2) agrees slightly better with the experiment (middle panel, Figure 6.8). For $n = 6$, the IR spectrum of the asymmetrically solvated complex **bri-1** shows a large splitting of the ν_A band (right panel, Figure 6.8) which is not observed experimentally. In contrast, the IR spectrum of the linear (3+3) complex, **lin-1** (+0.8 kJ/mol), shows a single peak for the ν_S and ν_A band in good agreement with the experiment. For $n = 8$, the asymmetrically solvated bridged isomer, **bri-1**, is found 1.2 kJ/mol lower in energy than the linear (4+4) complex, **lin-1**. The corresponding IR spectra are similar and reproduce the experimental spectrum. Neither of the structures can be excluded from the assignment. However, the spectrum of **bri-1** yields a slightly better agreement regarding the sequential shifts of the bands.

For $n = 10$, the simulations predict the folded geometry **fold-1** as the lowest-energy isomer. The bridged complex **bri-3** lies already 16.8 kJ/mol higher in energy. The IR spectrum of **fold-1** features a weak ν_S band in agreement with the observed intensity drop in the experiment. Furthermore, the sequential band shifts are well reproduced. The IR spectrum of **bri-3** is very similar in particular regarding the relative band intensities. Interestingly, even the brigded complex can account for the intensity drop owing to the strong distortion of the C–C–C–C chain (130°). Hence, the relative intensity does not allow to differentiate between both structural motifs. However, the bridged complex should lie too high in energy to be probed in the experiment and can therefore be excluded from the assignment. Similar to $n = 10$, for $n = 12$, the IR spectrum of the folded structure, **fold-5**, fits best the experimental trends of the ν_A and ν_S band. In contrast, the IR spectrum of the bridged structure, **bri-2**, shows a red-shifted ν_S band in conflict with the observed band shifts.

For a better comparison between experiment and theory, band positions and normalized ν_S band intensities of the IR spectra of the best structural candidates (middle panel, Figure 6.8) are plotted in Figure 6.6 (left panels). These spectra nicely describe the observed sequential band shifts and the trend of the ν_S band intensity. The deviations between experimental and simulated intensities especially for the small clusters ($n < 8$) are attributed to the multiple photon absorption process, similar to the adipate dianions (see above).

Summarizing, for the hydrated succinate dianions bridged structures form an additional structural motif. The structural assignment is ambiguous for certain cluster sizes n owing to similar vibrational signatures of the bridged structures compared to linear ($n \leq 8$) and folded complexes ($n \geq 10$). For the small clusters ($n < 8$) the observed blue-shifts of the ν_A and ν_S band are attributed to a symmetric solvation environment of the dianion. In contrast to the longer dianions with $m > 2$, the sudden decrease of the ν_S band intensity observed at $n = 10$ cannot exclusively be assigned to a folded conformation. The calculations reveal that the presence of a bridging water molecule can induce a significant distortion of the aliphatic chain which results in a noticeable quenching of the symmetric stretching band as well (see $n = 10$ and $n = 12$). However, comparing the predicted band shifts for both motifs supports that folded structures are probed in the experiment. For $n \geq 10$, in particular the blue-shift of the ν_S band is underestimated for the bridged structures. Furthermore, these bridged motifs should lie too high in energy (>10 kJ/mol) to be probed experimentally.

Folding in Succinate Dianions. Surprisingly, for succinate dianions the reduction of the ν_S band intensity is only observed in the range from $n = 10$ to $n = 15$ (left panels, Figure 6.6). Based on the calculations this intensity drop is attributed to a distorted C–C–C–C chain of the dianion predicted for folded and bridged complexes. However, the IR-MPD spectra reveal that the distorted geometry is not stabilized for larger clusters reflected in the increased normalized intensity for $n > 15$ (left panels, Figure 6.6). The observations confirm the previous findings of Wang and coworkers whose PES experiments show no indication of a folding for succinate dianions [165]. MD simulations performed by P. Jungwirth [165] reveal that succinate dianions have a propensity to be solvated in the bulk while larger dianions, e.g. suberate dianions, prefer the solvation at the water surface. Consequently, in solution the succinate dianion is equally surrounded by a solvation shell and the molecule is expected to be linear. The IR-MPD results suggest that the dianion is almost completely solvated at $n = 20$. At this cluster size, the ν_S band intensity is similar to intensities of the smaller clusters with $n \leq 6$ suggesting that the dianion relaxes into the linear conformation.

6.5 Summary and Conclusions

The water-mediated folding process of dicarboxylate dianions $^-$OOC-$(CH_2)_m$-COO$^-$ of different chain length $m = 2, 4, 6, 8$ has been investigated using IR-MPD spectroscopy combined with QC calculations. The results show that microhydration strongly affects the carboxylate stretching vibrations. In particular the intensity of the symmetric stretching modes (ν_S) shows a pronounced dependence on the cluster size. For sebacate ($m = 8$), suberate ($m = 6$) and adipate dianions ($m = 4$) the ν_S band intensity significantly drops at a critical number of water molecules n with $n = 19$, $n = 16$ and $n = 13$, respectively. Based on MD simulations this characteristic intensity drop is attributed to a conformational transition of the dianion from a linear to a folded configuration where the flexible $(CH_2)_m$ chain is strongly distorted. The calculations reveal that especially the intensity of the ν_S modes strongly responds to the distortion of the chain resulting in a quenching characteristic for a folded state. Furthermore, the critical solvent number n required for inducing the conformational transition depends linearly on the chain length m, i.e., if the $(CH_2)_m$ chain is reduced by two methylene groups n reduces by three. For dianions with $m \geq 4$ the folded state remains stabilized for larger water clusters which is essentially due to the formation of additional solute-solvent (rather than solvent-solvent) hydrogen bonds, based on the theoretical results. The findings confirm the previously reported PES results of Wang and coworkers [163, 165]. They observed a characteristic drop in the ADE for hydrated adipate and suberate dianions at $n = 13$ and $n = 16$, respectively, which is also assigned to a conformational change of the molecules. Recently, Demireva et al. studied the water-induced folding of 1,7-diammoniumheptane $NH_3^+(CH_2)_7NH_3^+$ using IR-PD spectroscopy combined with MD simulations [175]. The study reveals that 14 or more water molecules are required to induce a transition from a linear to folded conformation of the dication. However, the stability of the folded structure is attributed to additional solvent-solvent hydrogen bonds, in contrast to our results for dicarboxylate dianions. Both investigations thus show that the stabilizing forces significantly depend on the nature of the functional groups of the molecules.

A different behavior is observed for the succinate dianion ($m = 2$), the shortest dianion studied here. Although less pronounced, the intensity of the ν_S modes is observed to decrease at $n = 10$ but increases again for clusters with $n > 15$, in contrast to dianions with longer

alkyl chains. This suggests that the dianion is linear in larger clusters. These findings are in accordance with PES results from Wang and coworkers where no drop in the ADE was observed indicating that the hydrated dianion remains linear [165]. However, in-between $n = 10 - 15$ the ν_S band intensity is noticeably reduced indicating that the chain is distorted at these cluster sizes. Based on MD simulations, this intensity drop can be attributed to either folded or bridged complexes. These findings emphasize that IR-PD spectroscopy is more sensitive to changes in the dihedral angles of the alkyl chain.

Further spectroscopic features characteristic for the solute-solvent and solvent-solvent interaction are expected to be probed in the C–H stretching (2800–3000 cm^{-1}) and O–H stretching region ($>$3000 cm^{-1}), respectively. IR-MPD spectra of hydrated suberate dianions measured in the O–H stretching region exhibit no significant change for cluster sizes between $n = 13 - 18$ associated to a conformational transition. These results may indicate that the structure of the H-bonded water-water network remains nearly unaffected by folding of the molecule. Unfortunately, the extraction of structural informations within the C–H stretching region is challenging due to the weak vibrational transitions. Recently, Kamrath et al. have measured IR-VPD spectra of H$_2$-tagged mono- and dicarboxylate anions of dodecanedioic acid [176]. Using hydrogen as a messenger allows the formation of weakly-bound complexes ($E_{bind} \sim 600$ cm^{-1}) at trap temperatures still below 20 K. Owing to the low dissociation energy of those complexes the absorption of a single photon is sufficient to dissociate the molecule. Thereby the IR-PD process is strongly enhanced which would improve the measurements in the C–H stretching region.

Chapter 7

Outlook

IR-PD spectroscopy combined with QC calculation is a generally applicable method to investigate the structures of mass-selected gas phase cluster ions. In the present work, this method was successfully employed to characterize the structures of medium-sized clusters, involving transition metal oxide clusters of catalytic interest as well as microhydrated negative ions relevant in atmospheric processes. In the future, the investigation of larger clusters, containing several hundreds of atoms, is of great interest to illuminate the transition from microscopic to macroscopic behavior.

Cerium-Containing Clusters. The structural investigation of Ce-containing clusters reveals that even small gas phase clusters have properties similar to the bulk (Chapter 4–5). Regarding the structural evolution of cerium oxide clusters, IR spectra of larger clusters $(CeO_2)_m CeO^+$ ($m \geq 6$) will allow elucidating how many CeO_2 units are required to ultimately converge to the condensed phase, as observed for $V_8O_{20}^-$ [19]. In the present work, $(CeO_2)_4 CeO^+$ is the largest cluster for which a structure is assigned. However, at this size, the IR signature is not yet fully converged to the spectrum of the ceria surface.

Moreover, further spectroscopic data can aid to assess and improve the applicability of different DFT methods. The energetic ordering of the calculated isomers delicately depends on the description of the electron distribution, determined by the DFT functional used. The present study demonstrates that the B3LYP functional predicts the correct lowest energy structures for clusters containing less than five cerium atoms. In contrast, in larger clusters, like $(CeO_2)_4 CeO^+$, the TPSSh functional proves to be appropriate to predict the correct global minimum structure. This discrepancy emphasizes that the comparison between experiment and theory is essential for a reliable structural assignment. A consistent description of all cluster sizes based on one DFT functional is desirable and remains challenging.

Due to their bulk-like properties, gas phase Ce-containing clusters can serve as model systems for complex solid catalysts. In the future, it will be particularly interesting to extend our studies to adsorbate complexes formed between different metal oxide clusters, which, for instance, may contribute to a better understanding of the metal oxide support effect. The formation of such cluster aggregates requires a dual-target laser vaporization source which contains two separated vaporization channels in order to produce two different cluster beams. To this end, the existing single target source (Chapter 2.1.1) can be adapted by installing a second target drive assembly. Both formed cluster beams can be merged inside the cryogenically-cooled (20–300 K) aggregation chamber where multiple collisions promote the formation of

the adsorbate complexes. Alternatively, such complexes could be formed inside the cooled ion trap which offers more control over the thermalization of the cluster ions. To this end, two different cluster ions could be sequentially mass-selected in the quadrupole mass filter and accumulated in the trap. The storage time can be varied in order to facilitate the aggregation.

The aggregates $(Ce_mO_{2m-1})\cdot(VO_2)^+$, $(Ce_mO_{2m-1})\cdot(V_4O_{10})^+$ and $(Ce_mO_{2m})\cdot(V_4O_{10})^-$ would be suitable systems to mimic vanadium oxide clusters deposited on the ceria surface. The structural investigation of these systems will allow addressing various questions. These complexes are open-shell systems and the question arises whether the valence electrons still preferentially reside at the Ce atoms, as observed for the clusters $CeV_2O_6^+$ and $Ce_2VO_5^+$ studied in this thesis (Chapter 5). How does the metal oxide–metal oxide interaction affects the geometric structures of the bare cluster ions? In chapter 3 it has been shown that even rare gas atoms can markedly influence the geometric structure of vanadium oxide clusters. Thus, one expects a stronger influence from the "supporting" cerium oxide clusters, which are *not* chemically inert. The above-mentioned cluster series will allow studying these effects in detail, e.g., as a function of the cluster size and the charge state of the complex.

Structure-Reactivity Studies.   Besides the structural characterization of metal oxide clusters, IR-PD spectroscopy can be combined with reactivity measurements in order to elucidate structure-reactivity correlations. The ion trap-tandem mass spectrometer offers great flexibility to study the reaction of mass-selected ions with neutral reactants under thermalized conditions. This is demonstrated in our recent investigation of the reaction of $V_4O_{10}^+$ with propane [115], which shall be briefly summarized here. From mass spectrometry it is known that ODH is the main reaction channel which involves the transfer of two H atoms to $V_4O_{10}^+$, forming $[V_4O_{10}H_2]^+$ concomitant with the elimination of propene [177],

$$V_4O_{10}^+ + C_3H_8 \rightleftharpoons (V_4O_{10} \cdot C_3H_8)^+ \rightarrow [V_4O_{10}H_2]^+ + C_3H_6. \qquad (7.1)$$
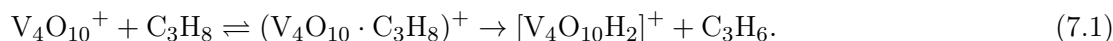
However, a more detailed understanding of the underlying reaction mechanism at the molecular level can be derived by characterizing the structure of the reaction product $[V_4O_{10}H_2]^+$. This can be accomplished via IR-MPD of the corresponding ion-propane complex, i.e., the propane molecule is used as a probe to measure an IR spectrum of $[V_4O_{10}H_2]^+$. Figure 7.1 shows the IR-MPD spectrum of $[V_4O_{10}H_2]^+ \cdot C_3H_8$ (bottom panel) together with simulated linear absorption spectra (upper panels) of three possible structural candidates (labeled A1, A2 and B). Structures A and B differ in the number of vanadyl (V=O) groups present in the $[V_4O_{10}H_2]^+$ moiety. While structure A contains two vanadyl and two V–OH groups, structure B contains three vanadyl and only one V–OH$_2$ group. Structures A1 and A2, on the other hand, differ in the way the propane molecule binds to the $[V_4O_{10}H_2]^+$ complex. Comparison of the experimental to the simulated spectra clearly favors an assignment to structures A1 and A2 rather than B. This is also in agreement with the calculated stabilities of A1 and A2, which differ by less than 1 kJ/mol, while B is 33 kJ/mol less stable [115]. The key finding in this study is that the abstraction of two H atoms from propane involves two vanadyl sites (structures A1 and A2) rather than a single one (structure B). It supports the assumption that polymeric vanadyl sites in vanadium oxide catalysts are essential in the ODH reaction.

Based on this initial structure–reactivity study, it will be interesting to investigate the same type of reaction in the presence of the supporting material. In this regard, the complexes $(Ce_mO_{2m-1})\cdot(V_4O_{10})^+$ are interesting species to elucidate the effects of cerium oxide clusters on the reaction mechanism.
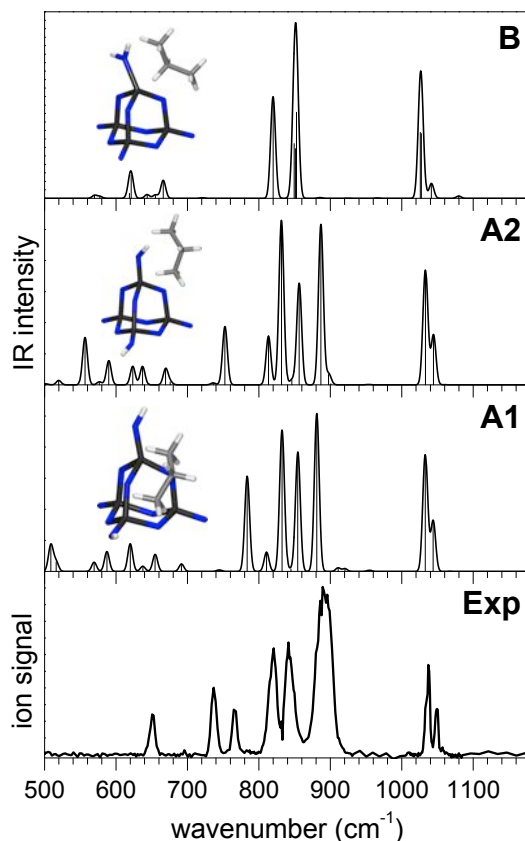
Figure 7.1: Experimental IR-MPD spectrum (bottom) of $[V_4O_{10}H_2 \cdot C_3H_8]^+$ (C_3H_8 loss channel) after trapping mass-selected $V_4O_{10}^+$ ions at $100\,K$ for $98\,ms$ in the ion trap filled with helium buffer gas seeded with $0.002\,\%$ propane. The IR-MPD spectrum is compared to simulated B3LYP/TZVP linear IR absorption spectra of three possible structural candidates (labeled B, A1 and A2).

Isomer-Selective Measurements. The increase in cluster size generally leads to an increase in the number of energetically low-lying isomers. Each of them may contribute to an IR spectrum which makes the interpretation and assignment challenging. In the present thesis, the IR-VPD experiments on the clusters $V_3O_6^+ \cdot He$ (Chapter 3) and $Ce_3O_5^+ \cdot Ne$ (Chapter 4) are two examples, where multiple isomers are spectroscopically probed. It will therefore be useful to employ experimental techniques which allow measuring IR spectra for each isomer individually. One possible strategy involves tuning of the relative isomer population. For example, for vanadium oxide clusters it has been demonstrated (Chapter 3), that the type and number of messenger atoms can markedly influence the relative stability of different isomers, which can lead to messenger-induced isomerization. Furthermore, the relative isomer population can be tuned by systematically varying the temperature of the trap which may result in thermally induced isomerization. This effect has been exploited in order to characterize the structural properties of carbon disulfide dimer anions $(CS_2)_2^-$ [178]. However, both approaches are not generally applicable, but rather depend on the properties of the clusters. Another technique is ion mobility mass spectrometry [179], which allows separating isomers that differ in their shape, leading to different collisional cross sections. Recently, Johnson et al. employed IR/IR double resonance spectroscopy which represents a more general scheme to measure vibrational spectra isomer-selectively [172, 180, 181].

Hydrated Acid Complexes.   The investigation of hydrated acid complexes is of particular interest in order to develop a deeper understanding of atmospheric processes [182, 183]. Small hydrated acid clusters have been intensively studied in order to gain insights in the acid molecule-solvent interaction. Future work will turn to larger complexes containing several tens of water molecules. The formation of large complexes thermalized to finite temperatures will aid to investigate complex surface phenomena under conditions relevant in the atmosphere. Ionization of acid molecules as well as ion-proton recombination are important processes occuring at the surface of aerosol particles. These processes are assumed to contribute to aerosol nucleation, which is still not well understood. Understanding the mechanism of acid dissociation represents thus a key goal. How many water molecules are needed to ionize the acid? This question has mostly been addressed by systematic computational studies on small hydrated acid clusters, revealing that three to five water molecules are typically required to stabilize an hydrated contact ion pair [182]. Experimental work, on the other hand, is still rather limited. IR studies, as recently performed for $(HCl)_m \cdot (H_2O)_n$ clusters in liquid helium droplets [184, 185] or for mass-selected $HSO_4^- \cdot (H_2O)_{1-16}$ clusters [36], can provide structural information necessary for a reliable structural assignment. Studying much larger hydrated complexes will allow elucidating the solvation behavior of the formed contact ion pair. Several hundreds of water molecules may be needed until water molecules intervene and induce bulk-like charge separation [182]. Depending on the nature of the ions, they either prefer solvation in the bulk or on the cluster surface. Ions present at the surface of aerosol particles can directly participate in chemical reactions and thus influence the earth's climate. Large hydrated complexes are therefore interesting systems to study reactions in the gas phase [183].

Appendix A

Single Target Laser Vaporization Source
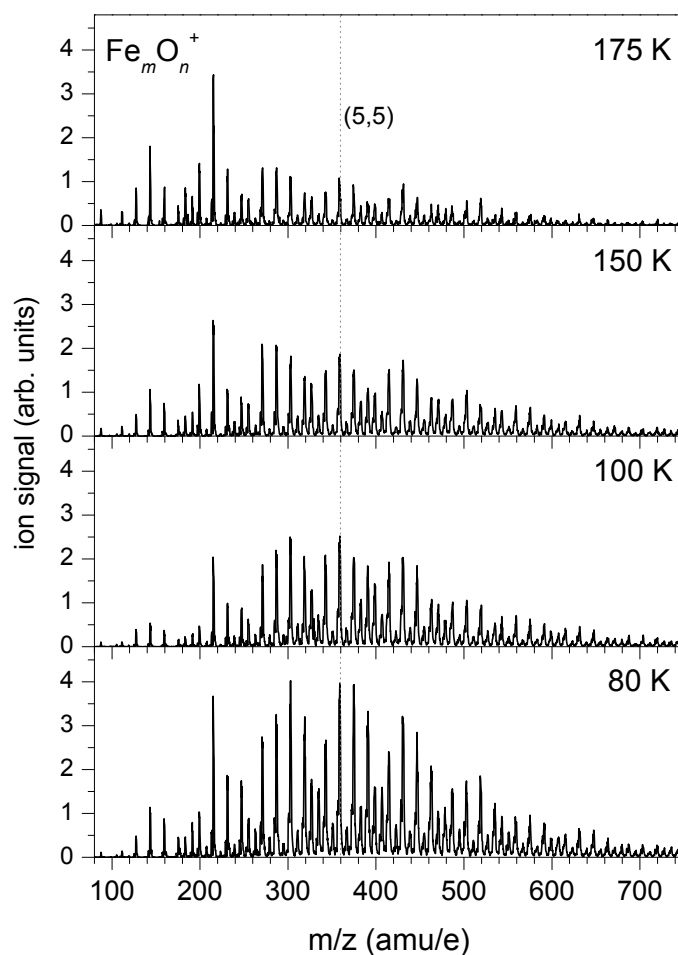
Figure A.1: Preliminary mass spectra of iron oxide clusters measured for different temperatures of the nozzle in the range from 175 K to 80 K. Ion optics have been slightly adjusted for each spectrum and optimized for cluster size $Fe_5O_5^+$ (360 amu, dashed line).
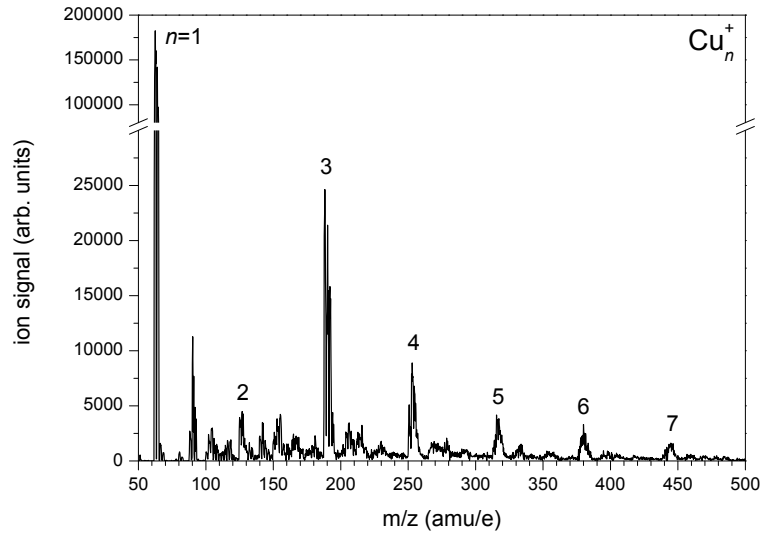
Figure A.2: Preliminary mass spectrum of metal copper clusters $Cu_n{}^+$.

Future Improvements

The performance of the drive assembly can be improved by implementing a gear unit which would offer several advantages. First, a gear reduction allows to increase the step resolution of the motor, for instance halfstep mode (note, this mode is optimal for the motor controller). Consequently, a higher torque can be applied which minimizes the risk of jamming. Second, the coupling of the nutation of the motor shaft to the thread screw would be reduced. In particular a worm gear mechanism is appropriate in order to achieve a compact setup. The current modular drive assembly allows for an implementation by basically replacing only the aluminum holders. In this new design the stepper motor would be mounted perpendicular to the rotation axis of the rod. Thereby the total length of the assembly would be reduced by about 20 mm which enables the installation of a precision shaft coupling between the thread screw and target holder. Thus the system gains higher flexibility in order to compensate tilting.

In an extended mode of operation the source unit can be cooled as well. But these experiments are currently hampered because the drive tends to jam when the source unit is cooled below 270 K. This is most likely induced by a distortion which is mainly driven by the temperature gradient throughout the drive assembly. In order to operate the whole source at low temperatures higher flexibility is important. To reduce the distortion, both aluminum holders have to be thermally decoupled from the source unit and the motor. Insulating material could be installed at both interfaces.

The current cryo stepper motor should be replaced by a motor which is suited for higher temperatures. Thus, an additional cooling of the motor would not be necessary anymore. Furthermore, the new motor should have a double shaft which allows for an implementation of an encoder providing information about the motion of the shaft and helps to detect jamming of the drive. Additionally a limit switch would allow to control the motion of the rod as it indicates an end of travel and prevents the motor from travelling too far. Both devices could be connected to the existing motor controller.

Appendix B

IR-PD Spectroscopy of $Fe_mO_n^+$ Clusters
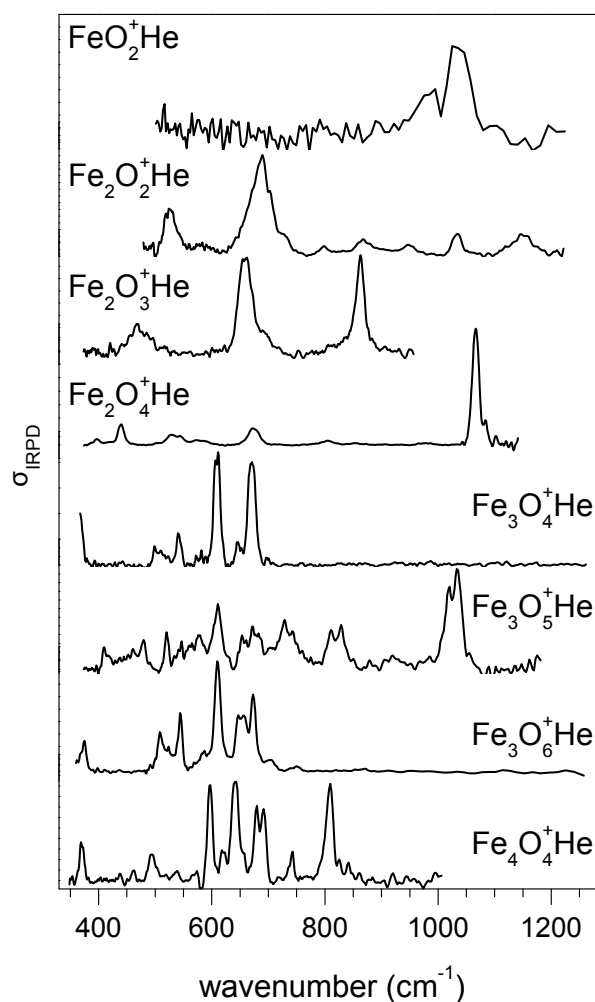
Figure B.1: Preliminary IR-VPD spectra of small helium-tagged iron oxide clusters measured in the range from 400 to $1200\,cm^{-1}$ using the free electron laser FELIX.

Appendix C

IR-PD Spectroscopy of Microhydrated Dicarboxylate Dianions

Computational Details for Structure Opimization[1]

To obtain the minimum-energy structure for the folded and linear configurations, a multi-stage protocol was used. Only the complexes with even number of water molecules were considered. First, the configuration space was roughly sampled by 5 ns of molecular dynamics (MD) simulation, after 1 ns of equilibration, using CHARMM with the TIP3P water model and force field parameters adopted from the CHARMM27 parameters for the glutamic acid side chain. At a later stage, these were repeated with harmonic constraints on the distance between the carboxylate carbon atoms (D), to effectively sample relevant regions of the configuration space. From each simulation, 500 random snapshots were optimized using the quantum mechanical (QM) SCC-DFTB method. Using ultra-tight optimization and appropriate energy thresholds, identical structures and local minima that are more than 5 kcal/mol higher in energy than the lowest one were discarded. The resulting minima (typically 20–200) were optimized with DFT using the PBE functional, the aug-cc-pVDZ basis set, and the RI approximation within turbomole. To gain confidence in the PBE structures and energies, geometries were further optimized with B3LYP/aug-cc-pVDZ and MP2/TZVP and their energies evaluated with CC2/aug-cc-pVDZ within turbomole. The aug-cc-pVDZ basis set was found necessary to reproduce all stable water configurations with PBE. The PBE/aug-cc-pVDZ geometries were found sufficiently accurate to evaluate the total energy at higher levels of theory. Structures were inspected and an energy threshold of 3-5 kcal/mol was chosen to select the PBE/aug-cc-pVDZ structures for further evaluation. Vibrational spectra and zero-point vibration energies (ZPVE) were calculated using PBE/aug-cc-pVDZ and total energies were re-evaluated using the CEPA/1 method in ORCA, corrected by the PBE ZPVE's. For the succinate dianions and up to $n = 10$ water molecules, total energies were obtained at the CEPA/1 level with aug-cc-pVTZ basis and ZPVE's from B3LYP/aug-cc-pVDZ.

---

[1] MD simulations and quantum chemical calculations were performed by Dr. Marius Wanko in the group of Prof. Angel Rubio (Universidad del País Vasco, Spain)

Microhydrated Suberate Dianions: C–H and O–H Stretching Vibrations

Figure C.1 shows IR-MPD spectra in the spectral region from 2500 to $3800\,\mathrm{cm^{-1}}$. A broad, intense absorption band (labeled B) emerges roughly from 3100 to $3700\,\mathrm{cm^{-1}}$ attributed to the hydrogen bonded O–H stretching modes. The position and shape are particularly affected by the size of the water clusters for $n \leq 11$. The maximum of band B exhibits a red-shift of about $110\,\mathrm{cm^{-1}}$ ($3325 \rightarrow 3435\,\mathrm{cm^{-1}}$) in-between $n = 5 - 8$. A shoulder (labeled A) appears around $3545\,\mathrm{cm^{-1}}$ at $n = 7$ and grows in intensity in-between $n = 7 - 11$. In contrast, another shoulder (labeled C) appearing around $3275\,\mathrm{cm^{-1}}$ at $n = 7$ slowly decreases in intensity when increasing the solvent number to $n = 15$. For larger clusters ($n > 12$) the absorption band becomes narrower and less structured. Contributions attributed to the C–H stretching modes ($<3000\,\mathrm{cm^{-1}}$) are weak and only observed for $n = 6 - 9$ (labeled D).
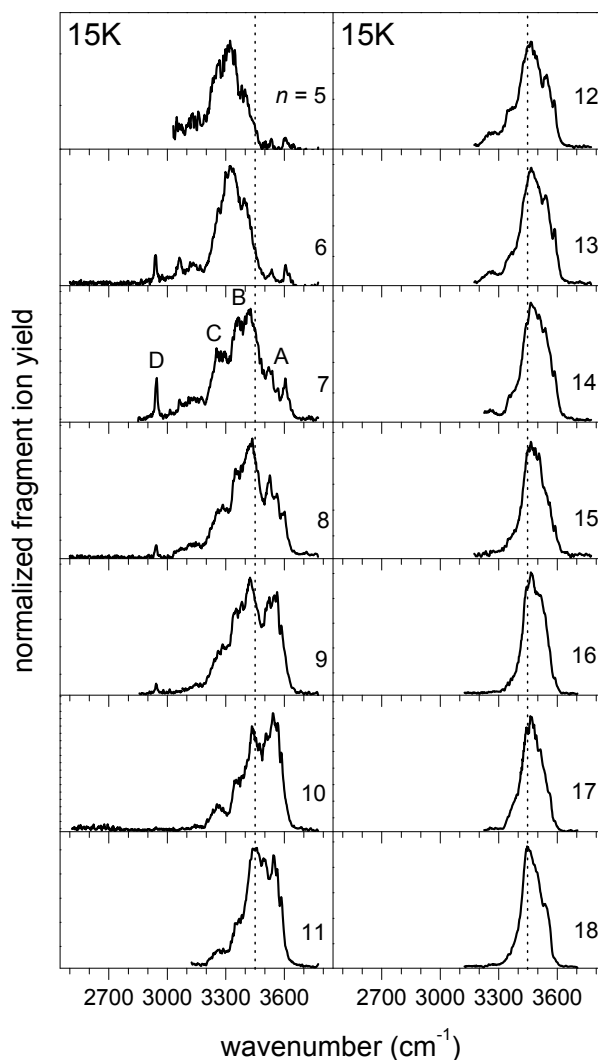
Figure C.1: Experimental IR-MPD spectra of $(CH_2)_6(COO^-)_2(H_2O)_n$ clusters with $n = 5 - 18$ in the region of the C–H and O–H stretching vibrations.

# Microhydrated Succinate Dianions: C–O Stretching Vibrations
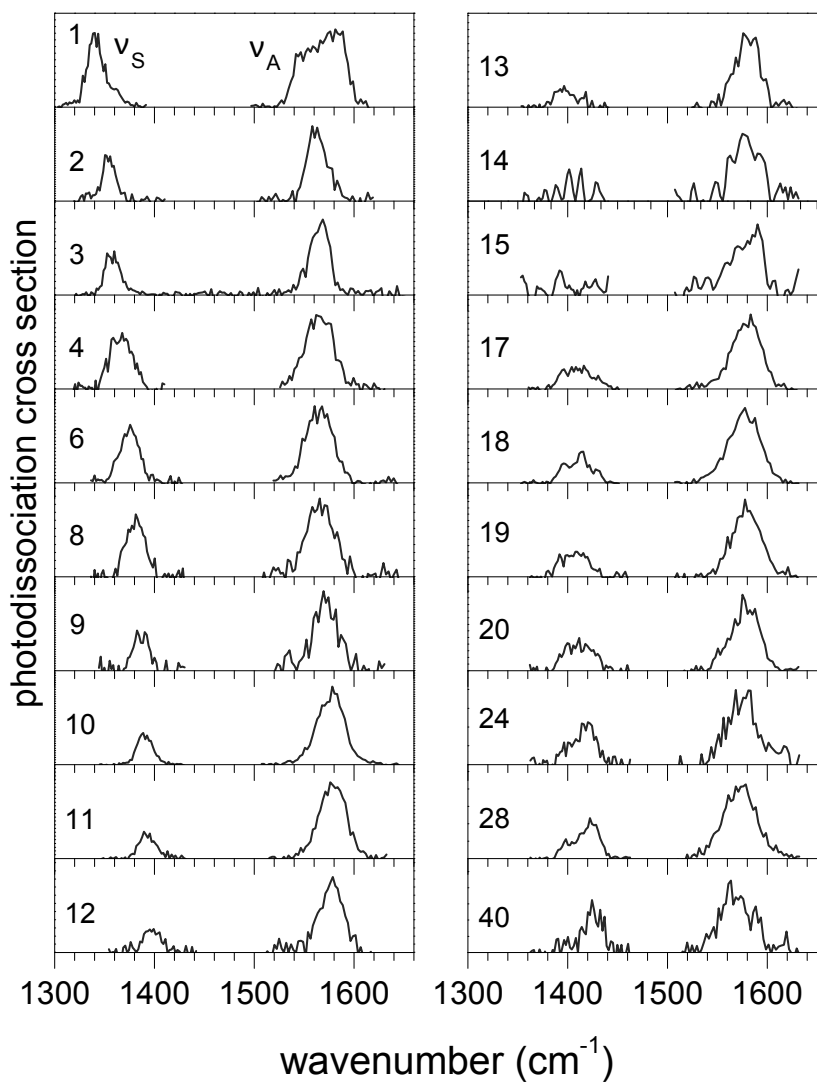
Figure C.2: Experimental IR-MPD spectra of $(CH_2)_2(COO^-)_2(H_2O)_n$ clusters with $n = 1 - 40$ in the region of the symmetric (ν_S) and antisymmetric (ν_A) carboxylate stretching modes. The photodissociation cross section is plotted as a function of the photon energy (cm^{-1}).

## Microhydrated Adipate Dianions: C–O Stretching Vibrations
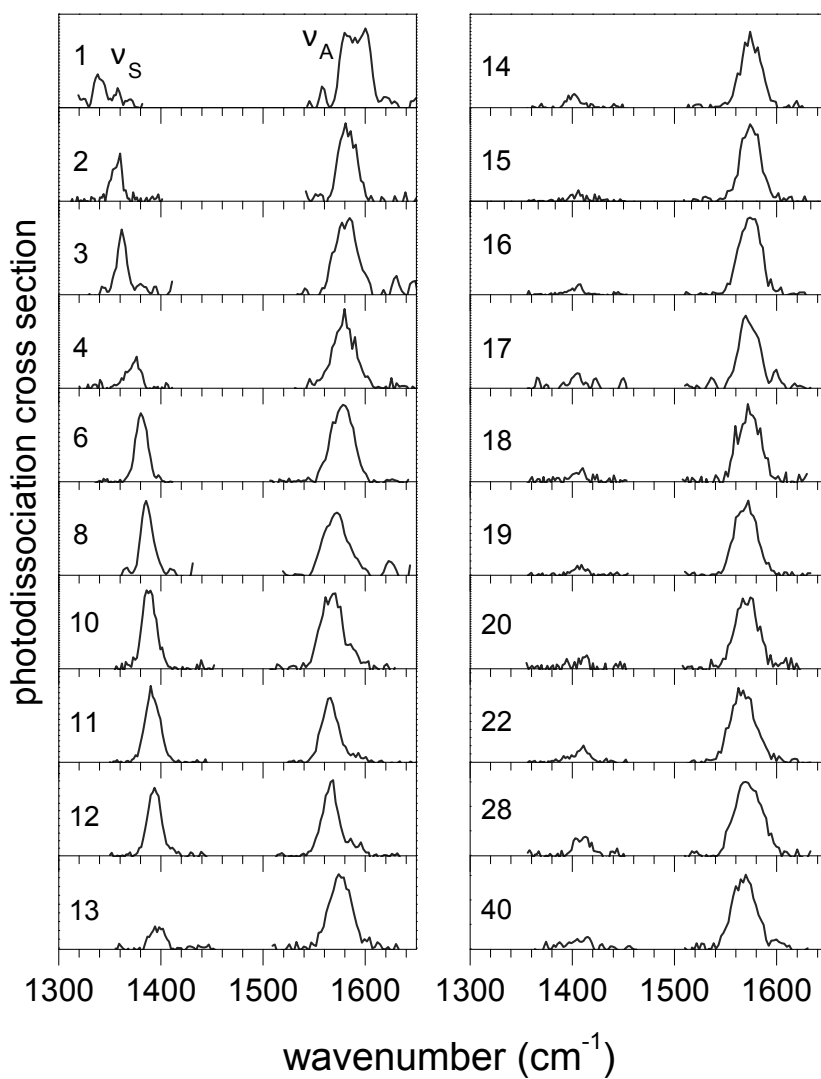
Figure C.3: Experimental IR-MPD spectra of $(CH_2)_4(COO^-)_2(H_2O)_n$ clusters with $n = 1 - 40$ in the region of the symmetric (ν_S) and antisymmetric (ν_A) carboxylate stretching modes. The photodissociation cross section is plotted as a function of the photon energy (cm^{-1}).

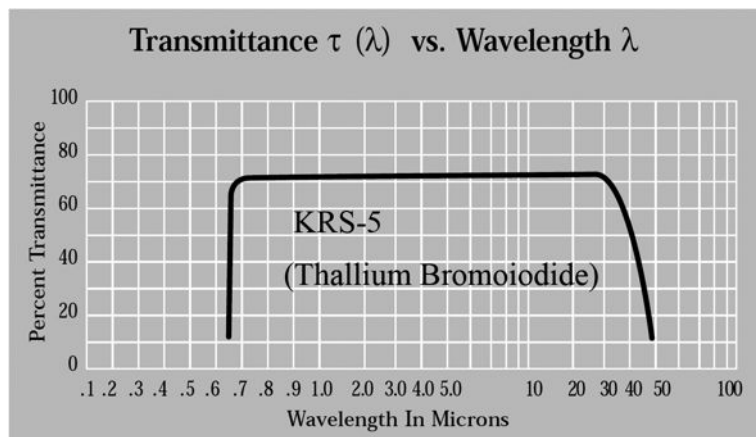# Microhydrated Sebacate Dianions: C–O Stretching Vibrations
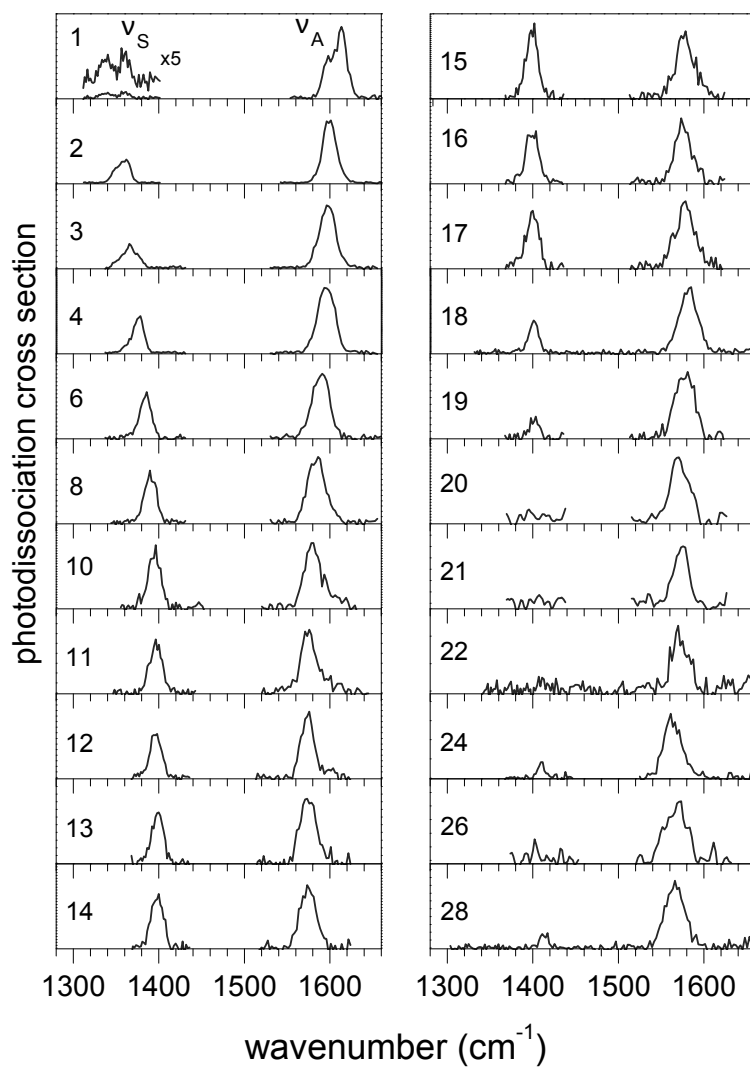
Figure C.4: Experimental IR-MPD spectra of $(CH_2)_8(COO^-)_2(H_2O)_n$ clusters with $n = 1 - 28$ in the region of the symmetric (ν_S) and antisymmetric (ν_A) carboxylate stretching modes. The photodissociation cross section is plotted as a function of the photon energy (cm^{-1}).

Appendix D

IR Transmission Curves
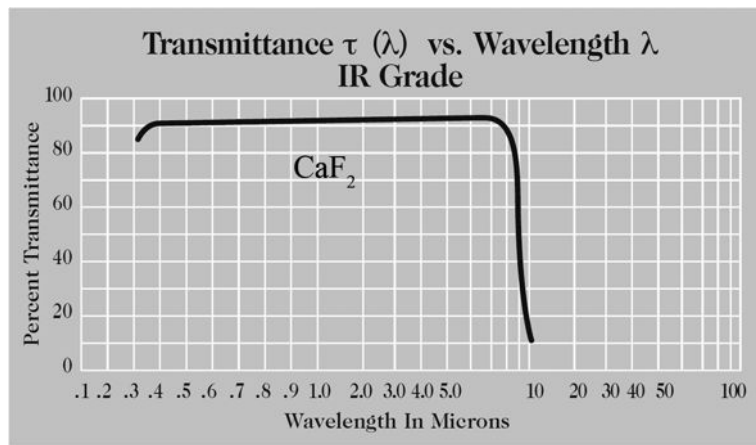
(a)
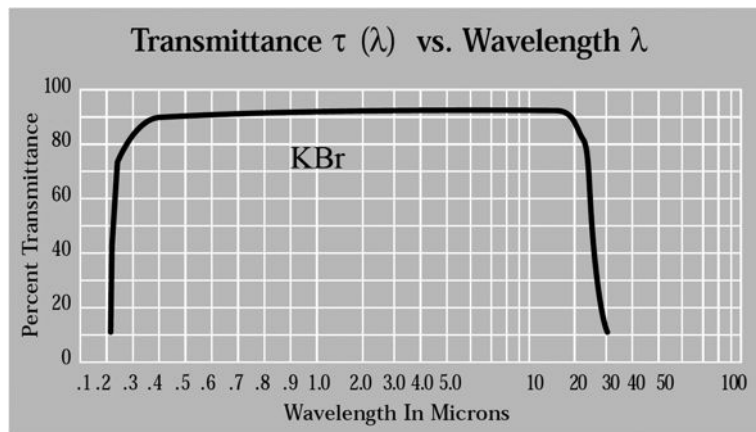
(b)

(c)

Figure D.1: Transmission curve for uncoated CaF_2 **(a)**, KBr **(b)** and KRS-5 **(c)** windows. Curves are provided by *ISP Optics*.[186]

Bibliography

[1] A. W. Castleman and R. G. Keesee, *Clusters: Bridging the Gas and Condensed Phases*, Acc. Chem. Res. **1986**, *19*, 413.

[2] W. A. de Heer, *The physics of simple metal clusters: experimental aspects and simple models*, Rev. Mod. Phys. **1993**, *65*, 611.

[3] M. A. Duncan, *Infrared spectroscopy to probe structure and dynamics in metal ion-molecule complexes*, Int. Rev. Phys. Chem. **2003**, *22*, 407.

[4] N. R. Walker, R. S. Walters, and M. A. Duncan, *Frontiers in the infrared spectroscopy of gas phase metal ion complexes*, New J. Chem. **2005**, *29*, 1495.

[5] R. Bogue, *Nanosensors: a review of recent research*, Sensor Review **2009**, *29*, 310.

[6] E. E. Chain, *Optical-properties of Vanadium Dioxide and Vanadium Pentoxide Thin-films*, Applied Optics **1991**, *30*, 2782.

[7] J. Garcia-Barriocanal, A. Rivera-Calzada, M. Varela, Z. Sefrioui, M. R. Diaz-Guillen, K. J. Moreno, J. A. Diaz-Guillen, E. Iborra, A. F. Fuentes, S. J. Pennycook, C. Leon, and J. Santarnaria, *Tailoring Disorder and Dimensionality: Strategies for Improved Solid Oxide Fuel Cell Electrolytes*, ChemPhysChem **2009**, *10*, 1003.

[8] A. T. Bell, *The impact of nanoscience on heterogeneous catalysis*, Science **2003**, *299*, 1688.

[9] D. Astruc, F. Lu, and J. R. Aranzaes, *Nanoparticles as recyclable catalysts: The frontier between homogeneous and heterogeneous catalysis*, Angew. Chem. Int. Ed. **2005**, *44*, 7852.

[10] F. Schüth, *Heterogene Katalyse. Schlüsseltechnologie der chemischen Industrie*, Chem. Unserer Zeit **2006**, *40*, 92.

[11] B. M. Weckhuysen, *Chemical Imaging of Spatial Heterogeneities in Catalytic Solids at Different Length and Time Scales*, Angew. Chem. Int. Ed. **2009**, *48*, 4910.

[12] B. M. Weckhuysen and D. E. Keller, *Chemistry, spectroscopy and the role of supported vanadium oxides in heterogeneous catalysis*, Catal. Today **2003**, *78*, 25.

[13] K. R. Asmis, *Infrared Photodissociation Spectroscopy of Mass-Selected Cluster Ions in the Gas Phase*, Habilitation, Freie Universität Berlin, **2005**.

[14] K. R. Asmis, *Structure characterisation of metal oxide clusters by vibrational spectroscopy: possibilities and prospects*, Phys. Chem. Chem. Phys. **2012**, *14*, 9270.

[15] K. R. Asmis and J. Sauer, *Mass-selective vibrational spectroscopy of vanadium oxide cluster ions*, Mass Spectrom. Rev. **2007**, *26*, 542.

[16] K. R. Asmis, M. Brümmer, C. Kaposta, G. Santambrogio, G. von Helden, G. Meijer, K. Rademann, and L. Wöste, *Mass-selected infrared photodissociation spectroscopy of $V_4O_{10}{}^+$*, Phys. Chem. Chem. Phys. **2002**, *4*, 1101.

[17] M. Brümmer, C. Kaposta, G. Santambrogio, and K. R. Asmis, *Formation and photodepletion of cluster ion-messenger atom complexes in a cold ion trap: Infrared spectroscopy of VO^+, $VO_2{}^+$, and $VO_3{}^+$*, J. Chem. Phys. **2003**, *119*, 12700.

[18] K. R. Asmis, G. Meijer, M. Brümmer, C. Kaposta, G. Santambrogio, L. Wöste, and J. Sauer, *Gas phase infrared spectroscopy of mono- and divanadium oxide cluster cations*, J. Chem. Phys. **2004**, *120*, 6461.

[19] K. R. Asmis, G. Santambrogio, M. Brümmer, and J. Sauer, *Polyhedral vanadium oxide cages: Infrared spectra of cluster anions and size-induced d electron localization*, Angew. Chem. Int. Ed. **2005**, *44*, 3122.

[20] E. Janssens, G. Santambrogio, M. Brümmer, L. Wöste, P. Lievens, J. Sauer, G. Meijer, and K. R. Asmis, *Isomorphous substitution in bimetallic oxide clusters*, Phys. Rev. Lett. **2006**, *96*, 233401.

[21] M. Sierka, J. Döbler, J. Sauer, G. Santambrogio, M. Brümmer, L. Wöste, E. Janssens, G. Meijer, and K. R. Asmis, *Unexpected structures of aluminum oxide clusters in the gas phase*, Angew. Chem. Int. Ed. **2007**, *46*, 3372.

[22] G. Santambrogio, M. Brümmer, L. Wöste, J. Döbler, M. Sierka, J. Sauer, G. Meijer, and K. R. Asmis, *Gas phase vibrational spectroscopy of mass-selected vanadium oxide anions*, Phys. Chem. Chem. Phys. **2008**, *10*, 3992.

[23] G. Santambrogio, E. Janssens, S. Li, T. Siebert, G. Meijer, K. R. Asmis, J. Döbler, M. Sierka, and J. Sauer, *Identification of Conical Structures in Small Aluminum Oxide Clusters: Infrared Spectroscopy of $(Al_2O_3)_{1-4}(AlO)^+$*, J. Am. Chem. Soc. **2008**, *130*, 15143.

[24] I. E. Wachs, *Recent conceptual advances in the catalysis science of mixed metal oxide catalytic materials*, Catal. Today **2005**, *100*, 79.

[25] A. Dinse, B. Frank, C. Hess, D. Habel, and R. Schomacker, *Oxidative dehydrogenation of propane over low-loaded vanadia catalysts: Impact of the support material on kinetics and selectivity*, J. Mol. Catal. A: Chem. **2008**, *289*, 28.

[26] D. A. Doyle, J. M. Cabral, R. A. Pfuetzner, A. L. Kuo, J. M. Gulbis, S. L. Cohen, B. T. Chait, and R. MacKinnon, *The structure of the potassium channel: Molecular basis of K^+ conduction and selectivity*, Science **1998**, *280*, 69.

[27] Y. F. Zhou, J. H. Morais-Cabral, A. Kaufman, and R. MacKinnon, *Chemistry of ion coordination and hydration revealed by a K^+ channel-Fab complex at 2.0 angstrom resolution*, Nature **2001**, *414*, 43.

[28] V. Ramanathan, P. J. Crutzen, J. T. Kiehl, and D. Rosenfeld, *Atmosphere - Aerosols, climate, and the hydrological cycle*, Science **2001**, *294*, 2119.

[29] B. J. Finlayson-Pitts, *The tropospheric chemistry of sea salt: A molecular-level view of the chemistry of NaCl and NaBr*, Chem. Rev. **2003**, *103*, 4801.

[30] K. R. Asmis and D. M. Neumark, *Vibrational Spectroscopy of Microhydrated Conjugate Base Anions*, Acc. Chem. Res. **2012**, *45*, 43.

[31] D. J. Goebbert, T. Wende, R. Bergmann, G. Meijer, and K. R. Asmis, *Messenger-Tagging Electrosprayed Ions: Vibrational Spectroscopy of Suberate Dianions*, J. Phys. Chem. A **2009**, *113*, 5874.

[32] D. J. Goebbert, E. Garand, T. Wende, R. Bergmann, G. Meijer, K. R. Asmis, and D. M. Neumark, *Infrared Spectroscopy of the Microhydrated Nitrate Ions $NO_3^-(H_2O)_{1-6}$*, J. Phys. Chem. A **2009**, *113*, 7584.

[33] E. Garand, T. Wende, D. J. Goebbert, R. Bergmann, G. Meijer, D. M. Neumark, and K. R. Asmis, *Infrared Spectroscopy of Hydrated Bicarbonate Anion Clusters: $HCO_3^-(H_2O)_{1-10}$*, J. Am. Chem. Soc. **2010**, *132*, 849.

[34] L. Jiang, T. Wende, R. Bergmann, G. Meijer, and K. R. Asmis, *Gas-Phase Vibrational Spectroscopy of Microhydrated Magnesium Nitrate Ions $[MgNO_3(H_2O)_{1-4}]^+$*, J. Am. Chem. Soc. **2010**, *132*, 7398.

[35] T. Wende, M. Wanko, L. Jiang, G. Meijer, K. R. Asmis, and A. Rubio, *Spectroscopic Characterization of Solvent-Mediated Folding in Dicarboxylate Dianions*, Angew. Chem. Int. Ed. **2011**, *50*, 3807.

[36] T. I. Yacovitch, T. Wende, L. Jiang, N. Heine, G. Meijer, D. M. Neumark, and K. R. Asmis, *Infrared Spectroscopy of Hydrated Bisulfate Anion Clusters: $HSO_4^-(H_2O)_{1-16}$*, J. Phys. Chem. Lett. **2011**, *2*, 2135.

[37] T. I. Yacovitch, N. Heine, C. Brieger, T. Wende, C. Hock, D. M. Neumark, and K. R. Asmis, *Vibrational spectroscopy of atmospherically relevant acid cluster anions: Bisulfate versus nitrate core structures*, J. Chem. Phys. **2012**, *136*, 241102.

[38] J. Zhou, G. Santambrogio, M. Brümmer, D. T. Moore, L. Wöste, G. Meijer, D. M. Neumark, and K. R. Asmis, *Infrared spectroscopy of hydrated sulfate dianions*, J. Chem. Phys. **2006**, *125*, 111102.

[39] Y. Miller, G. M. Chaban, J. Zhou, K. R. Asmis, D. M. Neumark, and R. B. Gerber, *Vibrational spectroscopy of $SO_4^{2-} \cdot (H_2O)_n$ clusters, $n = 1-5$: Harmonic and anharmonic calculations and experiment*, J. Chem. Phys. **2007**, *127*, 094305.

[40] A. I. Boldyrev and J. Simons, *Isolated SO_4^{2-} and PO_4^{3-} Anions Do Not Exist*, J. Phys. Chem. **1994**, *98*, 2298.

[41] J. Simons, P. Skurski, and R. Barrios, *Repulsive Coulomb barriers in compact stable and metastable multiply charged anions*, J. Am. Chem. Soc. **2000**, *122*, 11893.

[42] X. B. Wang, J. B. Nicholas, and L. S. Wang, *Electronic instability of isolated SO_4^{2-} and its solvation stabilization*, J. Chem. Phys. **2000**, *113*, 10837.

[43] L. S. Wang, C. F. Ding, X. B. Wang, J. B. Nicholas, and B. Nicholas, *Probing the potential barriers and intramolecular electrostatic interactions in free doubly charged anions*, Phys. Rev. Lett. **1998**, *81*, 2667.

[44] C. F. Ding, X. B. Wang, and L. S. Wang, *Photoelectron spectroscopy of doubly charged anions: Intramolecular Coulomb repulsion and solvent stabilization*, J. Phys. Chem. A **1998**, *102*, 8633.

[45] N. B. Colthup, L. H. Daly, and S. E. Wiberley, *Introduction to Infrared and Raman Spectroscopy*, Academic Press, **1990**.

[46] I. V. Hertel and C.-P. Schulz, *Atome, Moleküle und optische Physik 2: Moleküle und Photonen - Spektroskopie und Streuphysik*, Springer Berlin Heidelberg, **2010**.

[47] P. M. Morse, *Diatomic molecules according to the wave mechanics. II. Vibrational levels*, Physical Review **1929**, *34*, 57.

[48] K. Nakamoto, *Infrared and Raman Spectra of Inorganic and Coordination Compounds, Part A: Theory and Applications in Inorganic Chemistry*, Wiley-Interscience New York, **1997**.

[49] G. Berden, R. Peeters, and G. Meijer, *Cavity ring-down spectroscopy: Experimental schemes and applications*, Int. Rev. Phys. Chem. **2000**, *19*, 565.

[50] R. Casaes, R. Provencal, J. Paul, and R. J. Saykally, *High resolution pulsed infrared cavity ringdown spectroscopy: Application to laser ablated carbon clusters*, J. Chem. Phys. **2002**, *116*, 6640.

[51] D. Gerlich, *Inhomogeneous RF Fields - A Versatile Tool for the Study of Processes with Slow Ions*, Adv. Chem. Phys. **1992**, *82*, 1.

[52] J. Oomens, B. G. Sartakov, G. Meijer, and G. Von Helden, *Gas-phase infrared multiple photon dissociation spectroscopy of mass-selected molecular ions*, Int. J. Mass Spectrom. **2006**, *254*, 1.

[53] K. R. Asmis, A. Fielicke, G. von Helden, and G. Meijer, *Vibrational Spectroscopy of Gas-Phase Clusters and Complexes*, in *Atomic Clusters: From Gas Phase to Deposited Atomic Clusters*, vol. 12, edited by D. P. Woodruff, chap. 8, pp. 327–375, Elsevier, **2007**.

[54] P. Grüne, *Structure and Reactivity of Metal and Semiconductor Clusters in the Gas Phase*, Phd thesis, Technische Universität Berlin, **2009**.

[55] P. Gruene, J. Lyon, and A. Fielicke, *Vibrational Spectroscopy of Strongly Bound Clusters*, in *Handbook of Nanophysics*, pp. 1–14, CRC Press, **2010**.

[56] A. A. Makarov, I. Y. Petrova, E. A. Ryabov, and V. S. Letokhov, *Statistical Inhomogeneous Broadening of Infrared and Raman Transitions in Highly Vibrationally Excited XY_6 Molecules*, J. Phys. Chem. A **1998**, *102*, 1438.

[57] G. von Helden, D. van Heijnsbergen, and G. Meijer, *Resonant ionization using IR light: A new tool to study the spectroscopy and dynamics of gas-phase molecules and clusters*, J. Phys. Chem. A **2003**, *107*, 1671.

[58] M. Okumura, L. I. Yeh, J. D. Myers, and Y. T. Lee, *Infrared spectra of the cluster ions $H_7O_3^+ \cdot H_2$ and $H_9O_4^+ \cdot H_2$*, J. Chem. Phys. **1986**, *85*, 2328.

[59] M. Okumura, L. I. Yeh, J. D. Myers, and Y. T. Lee, *Infrared Spectra of the Solvated Hydronium Ion: Vibrational Predissociation Spectroscopy of Mass-Selected $H_3O^+ \cdot (H_2O)_n \cdot (H_2)_m$*, J. Phys. Chem. **1990**, *94*, 3416.

[60] M. A. Johnson, *Vibrational Predissociation Ion Spectroscopy*, in *The Encyclopedia of Mass Spectrometry: Theory and Ion Chemistry*, vol. 1, edited by P. B. Armentrout, M. L. Gross, and R. Caprioli, Elsevier: Oxford, UK, **2003**.

[61] M. Brümmer, *Spektroskopische Untersuchungen zur Struktur und Reaktivität von Vanadiumoxid-Clustern*, Doktorarbeit, Freie Universität Berlin, **2007**.

[62] R. Gehrke, P. Gruene, A. Fielicke, G. Meijer, and K. Reuter, *Nature of Ar bonding to small Co_n^+ clusters and its effect on the structure determination by far-infrared absorption spectroscopy*, J. Chem. Phys. **2009**, *130*, 034306.

[63] K. Mizuse and A. Fujii, *Infrared photodissociation spectroscopy of $H^+(H_2O)_6 \cdot M_m$ (M = Ne, Ar, Kr, Xe, H_2, N_2, and CH_4): messenger-dependent balance between H_3O^+ and $H_5O_2^+$ core isomers*, Phys. Chem. Chem. Phys. **2011**, *13*, 7098.

[64] J. Oomens, A. J. A. van Roij, G. Meijer, and G. von Helden, *Gas-phase infrared photodissociation spectroscopy of cationic polyaromatic hydrocarbons*, Astrophys. J. **2000**, *542*, 404.

[65] D. J. Goebbert, G. Meijer, and K. R. Asmis, *10K Ring Electrode Trap - Tandem Mass Spectrometer for Infrared Spectroscopy of Mass Selected Ions*, AIP Conf. Proc. **2009**, *1104*, 22.

[66] D. E. Powers, S. G. Hansen, M. E. Geusic, A. C. Puiu, J. B. Hopkins, T. G. Dietz, M. A. Duncan, P. R. R. Langridgesmith, and R. E. Smalley, *Supersonic Metal Cluster Beams: Laser Photoionization Studies of Cu_2*, J. Phys. Chem. **1982**, *86*, 2556.

[67] T. G. Dietz, M. A. Duncan, D. E. Powers, and R. E. Smalley, *Laser Production of Supersonic Metal Cluster Beams*, J. Chem. Phys. **1981**, *74*, 6511.

[68] R. E. Smalley, *Laser Studies of Metal Cluster Beams*, Laser Chemistry **1983**, *2*, 167.

[69] M. A. Duncan, *Invited Review Article: Laser vaporization cluster sources*, Rev. Sci. Instrum. **2012**, *83*, 041101.

[70] P. Milani and W. A. deHeer, *Improved Pulsed Laser Vaporization Source For Production of Intense Beams of Neutral and Ionized Clusters*, Rev. Sci. Instrum. **1990**, *61*, 1835.

[71] S. Maruyama, L. R. Anderson, and R. E. Smalley, *Direct Injection Supersonic Cluster Beam Source for FT-ICR Studies of Clusters*, Rev. Sci. Instrum. **1990**, *61*, 3686.

[72] P. Gangopadhyay and J. M. Lisy, *A Novel Target Manipulation Technique Used in Generating Bare Metal Cluster Ions for Catalytic Research*, Rev. Sci. Instrum. **1991**, *62*, 502.

[73] U. Heiz, F. Vanolli, L. Trento, and W. D. Schneider, *Chemical reactivity of size-selected supported clusters: An experimental setup*, Rev. Sci. Instrum. **1997**, *68*, 1986.

[74] H. Weidele, U. Frenzel, T. Leisner, and D. Kreisle, *Production of "cold/hot" metal cluster ions: a modified laser vaporization source*, Z. Phys. D **1991**, *20*, 411.

[75] C. M. Neal, G. A. Breaux, B. P. Cao, A. K. Starace, and M. F. Jarrold, *Improved signal stability from a laser vaporization source with a liquid metal target*, Rev. Sci. Instrum. **2007**, *78*, 075108.

[76] S. Nonose, Y. Sone, K. Onodera, S. Sudo, and K. Kaya, *Structure and Reactivity of Bimetallic $Co_n V_m$ Clusters*, J. Phys. Chem. **1990**, *94*, 2744.

[77] W. Bouwen, P. Thoen, F. Vanhoutte, S. Bouckaert, F. Despa, H. Weidele, R. E. Silverans, and P. Lievens, *Production of bimetallic clusters by a dual-target dual-laser vaporization source*, Rev. Sci. Instrum. **2000**, *71*, 54.

[78] M. Turra, B. Waldschmidt, B. Kaiser, and R. Schafer, *An improved time-of-flight method for cluster deposition and ion-scattering experiments*, Rev. Sci. Instrum. **2008**, *79*, 013905.

[79] L. S. Zheng, P. J. Brucat, C. L. Pettiette, S. Yang, and R. E. Smalley, *Formation and photodetachment of cold metal cluster negative ions*, J. Chem. Phys. **1985**, *83*, 4273.

[80] P. J. Brucat, L. S. Zheng, C. L. Pettiette, S. Yang, and R. E. Smalley, *Metal cluster ion photofragmentation*, J. Chem. Phys. **1986**, *84*, 3078.

[81] D. M. Cox, K. C. Reichmann, D. J. Trevor, and A. Kaldor, *CO chemisorption on free gas phase metal clusters*, J. Chem. Phys. **1988**, *88*, 111.

[82] E. Janssens, *Electronic and Geometric Structure of Transition Metal Doped Silver and Gold Clusters*, Phd thesis, Katholieke Universiteit Leuven, **2004**.

[83] T. Hihara, S. Pokrant, and J. A. Becker, *Magnetic moments and chemical bonding in isolated BiNCoM clusters*, Chem. Phys. Lett. **1998**, *294*, 357.

[84] J. B. Fenn, M. Mann, C. K. Meng, S. F. Wong, and C. M. Whitehouse, *Electrospray ionization–principles and practice*, Mass Spectrom. Rev. **1990**, *9*, 37.

[85] J. B. Fenn, M. Mann, C. K. Meng, S. F. Wong, and C. M. Whitehouse, *Electrospray Ionization for Mass Spectrometry of Large Biomolecules*, Science **1989**, *246*, 64.

[86] J. B. Fenn, *Electrospray Wings for Molecular Elephants (Nobel Lecture)*, Angew. Chem. Int. Ed. **2003**, *42*, 3871.

[87] R. B. Cole, *Electrospray Ionization Mass Spectrometry: Fundamentals, Instrumentation & Applications*, John Wiley & Sons, Inc., **1997**.

[88] P. Kebarle, *A brief overview of the present status of the mechanisms involved in electrospray mass spectrometry*, J. Mass Spectrom. **2000**, *35*, 804.

[89] W. D. Luedtke, U. Landman, Y. H. Chiu, D. J. Levandier, R. A. Dressler, S. Sok, and M. S. Gordon, *Nanojets, electrospray, and ion field evaporation: Molecular dynamics simulations and laboratory experiments*, J. Phys. Chem. A **2008**, *112*, 9628.

[90] J. L. P. Benesch, B. T. Ruotolo, D. A. Simmons, and C. V. Robinson, *Protein Complexes in the Gas Phase: Technology for Structural Genomics and Proteomics*, Chem. Rev. **2007**, *107*, 3544.

[91] M. H. Friedman, A. L. Yergey, and J. E. Campana, *Fundamentals of ion motion in electric radio-frequency multipole fields*, J. Phys. E: Sci. Instrum. **1982**, *15*, 53.

[92] W. Paul, *Electromagnetic Traps for Charged and Neutral Particles (Noble Lecture)*, Angew. Chem. Int. Ed. Engl. **1990**, *29*, 739.

[93] M. Abramowitz and I. A. Stegun, *Handbook of Mathematical Functions with Formulas, Graphs, and Mathematical Tables*, New York: Dover, **1972**.

[94] D. Gerlich and S. Horning, *Experimental Investigations of Radiative Association Processes As Related To Interstellar Chemistry*, Chem. Rev. **1992**, *92*, 1509.

[95] D. Gerlich, G. Borodi, A. Luca, C. Mogo, and M. A. Smith, *Reactions Between Cold CH_x^+ and Slow H and H_2*, Z. Phys. Chem. **2011**, *225*, 475.

[96] W. C. Wiley and I. H. McLaren, *Time-of-flight Mass Spectrometer with Improved Resolution*, Rev. Sci. Instrum. **1955**, *26*, 1150.

[97] A. Fielicke, G. von Helden, and G. Meijer, *Far-infrared spectroscopy of isolated transition metal clusters*, Eur. Phys. J. D **2005**, *34*, 83.

[98] D. Oepts, A. F. G. van der Meer, and P. W. van Amersfoort, *The Free-Electron-Laser user facility FELIX*, Infrared Phys. Technol. **1995**, *36*, 297.

[99] W. R. Bosenberg and D. R. Guyer, *Broadly tunable, single-frequency optical parametric frequency-conversion system*, J. Opt. Soc. Am. B **1993**, *10*, 1716.

[100] K. R. Asmis, T. Wende, M. Brümmer, O. Gause, G. Santambrogio, E. C. Stanca-Kaposta, J. Döbler, N. A., and J. Sauer, *Structural variability in transition metal oxide clusters: gas phase vibrational spectroscopy of $V_3O_{6-8}^+$*, Phys. Chem. Chem. Phys. **2012**, *14*, 9377.

[101] Y. S. Hu, X. Liu, J. O. Müller, R. Schlögl, J. Maier, and D. S. Su, *Synthesis and Electrode Performance of Nanostructured V_2O_5 by Using a Carbon Tube-in-Tube as a Nanoreactor and an Efficient Mixed-Conducting Network*, Angew. Chem. Int. Ed. **2009**, *48*, 210.

[102] F. Stavale, C. A. Achete, and H. Niehus, *Vanadium nanoclusters on Si(111) 7×7 surface studied by scanning tunneling microscopy*, Surf. Sci. **2007**, *601*, 4881.

[103] N. Magg, B. Immaraporn, J. B. Giorgi, T. Schroeder, M. Baumer, J. Dobler, Z. L. Wu, E. Kondratenko, M. Cherian, M. Baerns, P. C. Stair, J. Sauer, and H. J. Freund, *Vibrational spectra of alumina- and silica-supported vanadia revisited: An experimental and theoretical model catalyst study*, J. Catal. **2004**, *226*, 88.

[104] D. K. Böhme and H. Schwarz, *Gas-phase catalysis by atomic and cluster metal ions: The ultimate single-site catalysts*, Angew. Chem. Int. Ed. **2005**, *44*, 2336.

[105] S. F. Vyboishchikov and J. Sauer, *$(V_2O_5)_n$ gas-phase clusters ($n = 1 - 12$) compared to V_2O_5 crystal: DFT calculations*, J. Phys. Chem. A **2001**, *105*, 8588.

[106] J. Sauer and J. Döbler, *Structure and reactivity of V_2O_5: bulk solid, nanosized clusters, species supported on silica and alumina, cluster cations and anions*, Dalton Trans. **2004**, pp. 3116–3121.

[107] G. Santambrogio, *IR Photodissociation and Femtosecond Negative-Neutral-Positive Spectroscopy of Vanadium Oxide Clusters and Cluster Ions*, Diploma thesis, Università degli Studî di Milano, **2001**.

[108] A. Fielicke, G. Meijer, and G. von Helden, *Infrared spectroscopy of niobium oxide cluster cations in a molecular beam: Identifying the cluster structures*, J. Am. Chem. Soc. **2003**, *125*, 3659.

[109] A. M. Burow, T. Wende, M. Sierka, R. Wlodarczyk, J. Sauer, P. Claes, L. Jiang, G. Meijer, P. Lievens, and K. R. Asmis, *Structures and vibrational spectroscopy of partially reduced gas-phase cerium oxide clusters*, Phys. Chem. Chem. Phys. **2011**, *13*, 19393.

[110] K. Kwapien, M. Sierka, J. Döbler, J. Sauer, M. Haertelt, A. Fielicke, and G. Meijer, *Structural Diversity and Flexibility of MgO Gas-Phase Clusters*, Angew. Chem. Int. Ed. **2011**, *50*, DOI: 10.1002/anie.201004617.

[111] G. Kresse, M. Schmid, E. Napetschnig, M. Shishkin, L. Kohler, and P. Varga, *Structure of the ultrathin aluminum oxide film on NiAl(110)*, Science **2005**, *308*, 1440.

[112] M. Schmid, M. Shishkin, G. Kresse, E. Napetschnig, P. Varga, M. Kulawik, N. Nilius, H. P. Rust, and H. J. Freund, *Oxygen-deficient line defects in an ultrathin aluminum oxide film*, Phys. Rev. Lett. **2006**, *97*, 046101.

[113] Q. H. Wu, A. Fortunelli, and G. Granozzi, *Preparation, characterisation and structure of Ti and Al ultrathin oxide films on metals*, Int. Rev. Phys. Chem. **2009**, *28*, 517.

[114] S. Hamad, C. R. A. Catlow, S. M. Woodley, S. Lago, and J. A. Mejias, *Structure and stability of small TiO_2 nanoparticles*, J. Phys. Chem. B **2005**, *109*, 15741.

[115] T. Wende, J. Döbler, L. Jiang, P. Claes, E. Janssens, P. Lievens, G. Meijer, K. R. Asmis, and J. Sauer, *Infrared spectroscopic characterization of the oxidative dehydrogenation of propane by $V_4O_{10}{}^+$*, Int. J. Mass Spectrom. **2010**, *297*, 102.

[116] S. D. Gabelnick, G. T. Reedy, and M. G. Chasanov, *Infrared spectra and structure of some matrix-isolated lanthanide and actinide oxides*, J. Chem. Phys. **1974**, *60*, 1167.

[117] C. Linton, M. Dulick, and R. W. Field, *Laser Spectroscopy of CeO, Fluorescence of the $C_1 - X_1$ and $D_3 - X_3$ Systems*, J. Mol. Spectrosc. **1979**, *78*, 428.

[118] C. Linton, M. Dulick, R. W. Field, P. Carette, and R. F. Barrow, *Low lying electronic states of CeO*, J. Chem. Phys. **1981**, *74*, 189.

[119] C. Heinemann, H. H. Cornehl, D. Schröder, M. Dolg, and H. Schwarz, *The CeO_2^+ Cation: Gas-Phase Reactivity and Electronic Structure*, Inorg. Chem. **1996**, *35*, 2463.

[120] S. P. Willson and L. Andrews, *Characterization of the Reaction Products of Laser-Ablated Early Lanthanide Metal Atoms with Molecular Oxygen. Infrared Spectra of LnO, LnO^+, LnO^-, LnO_2, LnO_2^+, LnO_2^-, LnO_3^-, and $(LnO)_2$ in Solid Argon*, J. Phys. Chem. A **1999**, *103*, 3171.

[121] Z. L. Wang and X. D. Feng, *Polyhedral shapes of CeO_2 nanoparticles*, J. Phys. Chem. B **2003**, *107*, 13563.

[122] F. Zhang, Q. Jin, and S. W. Chan, *Ceria nanoparticles: Size, size distribution, and shape*, J. Appl. Phys. **2004**, *95*, 4319.

[123] C. Loschen, S. T. Bromley, K. M. Neyman, and F. Illas, *Understanding Ceria Nanoparticles from First-Principles Calculations*, J. Phys. Chem. C **2007**, *111*, 10142.

[124] C. Chen, H.-L. Chen, M.-H. Weng, S.-P. Ju, J.-G. Chang, and C.-S. Chang, *Structural Properties of $(CeO_2)_n$ ($n = 1 - 5$) Nanoparticle: Molecular Mechanics and First Principle Studies*, Chin. J. Catal. **2008**, *29*, 1117.

[125] S. F. Li, H. Lu, P. Li, Z. Yang, and Z. X. Guo, *First-principles local density approximation (generalized gradient approximation) +U study of catalytic Ce_nO_m clusters: U value differs from bulk*, J. Chem. Phys. **2008**, *128*, 164718.

[126] C. Loschen, A. Migani, S. T. Bromley, F. Illas, and K. M. Neyman, *Density functional studies of model cerium oxide nanoparticles*, Phys. Chem. Chem. Phys. **2008**, *10*, 5730.

[127] F. Aubriet, J.-J. Gaumet, W. A. de Jong, G. S. Groenewold, A. K. Gianotto, M. E. McIlwain, M. J. Van Stipdonk, and C. M. Leavitt, *Cerium Oxyhydroxide Clusters: Formation, Structure, and Reactivity*, J. Phys. Chem. A **2009**, *113*, 6239.

[128] A. Migani, K. M. Neyman, F. Illas, and S. T. Bromley, *Exploring Ce^{3+}/Ce^{4+} cation ordering in reduced ceria nanoparticles using interionic-potential and density-functional calculations*, J. Chem. Phys. **2009**, *131*, 064701.

[129] X.-N. Wu, Y.-X. Zhao, W. Xue, Z.-C. Wang, S.-G. He, and X.-L. Ding, *Active sites of stoichiometric cerium oxide cations ($Ce_mO_{2m}^+$) probed by reactions with carbon monoxide and small hydrocarbon molecules*, Phys. Chem. Chem. Phys. **2010**, *12*, 3984.

[130] A. Pfau and K. D. Schierbaum, *The electronic structure of stoichiometric and reduced CeO_2 surfaces: an XPS, UPS and HREELS study*, Surf. Sci. **1994**, *321*, 71.

[131] A. Trovarelli, *Catalytic Properties of Ceria and CeO_2-Containing Materials*, Catal. Rev. Sci. Eng. **1996**, *38*, 439.

[132] D. R. Mullins, P. V. Radulovic, and S. H. Overbury, *Ordered cerium oxide thin films grown on Ru(0001) and Ni(111)*, Surf. Sci. **1999**, *429*, 186.

[133] C. T. Campbell and C. H. F. Peden, *Oxygen Vacancies and Catalysis on Ceria Surfaces*, Science **2005**, *309*, 713.

[134] F. Esch, S. Fabris, L. Zhou, T. Montini, C. Africh, P. Fornasiero, G. Comelli, and R. Rosei, *Electron Localization Determines Defect Formation on Ceria Substrates*, Science **2005**, *309*, 752.

[135] J. F. Jerratsch, X. Shao, N. Nilius, H.-J. Freund, C. Popa, M. V. Ganduglia-Pirovano, A. M. Burow, and J. Sauer, *Electron localization in defective ceria films: An STM and DFT study*, Phys. Rev. Lett. **2011**, *106*, 246801.

[136] C. Pijolat, G. Tournier, and J. P. Viricelle, *Detection of CO in H_2-rich gases with a samarium doped ceria (SDC) sensor for fuel cell applications*, Sens. Actuators, B **2009**, *141*, 7.

[137] N. Izu, W. Shin, I. Matsubara, and N. Murayama, *Resistive Oxygen Sensor Using Ceria-Zirconia Sensor Material and Ceria-Yttria Temperature Compensating Material for Lean-Burn Engine*, Sensors **2009**, *9*, 8884.

[138] W. Z. Zhu and S. C. Deevi, *A review on the status of anode materials for solid oxide fuel cells*, Materials Science and Engineering A **2003**, *362*, 228.

[139] R. J. Gorte, *Ceria in Catalysis: From Automotive Applications to the Water Gas Shift Reaction*, AIChE J. **2010**, *56*, 1126.

[140] H. W. Kroto, *Molecular Rotation Spectra*, John Wiley & Sons, **1975**.

[141] G. von Helden, A. Kirilyuk, D. van Heijnsbergen, B. Sartakov, M. A. Duncan, and G. Meijer, *Infrared spectroscopy of gas-phase zirconium oxide clusters*, Chem. Phys. **2000**, *262*, 31.

[142] J. Stubenrauch, E. Brosha, and J. M. Vohs, *Reaction of carboxylic acids on $CeO_2(111)$ and $CeO_2(100)$*, Catal. Today **1996**, *28*, 431.

[143] L. Jiang, T. Wende, P. Claes, S. Bhattacharyy, M. Sierka, G. Meijer, P. Lievens, J. Sauer, and K. R. Asmis, *Electron Distribution in Partially Reduced Mixed Metal Oxide Systems: Infrared Spectroscopy of $Ce_m V_n O_o^+$ Gas-Phase Clusters*, J. Phys. Chem. A **2011**, *115*, 11187.

[144] M. A. Banares, *Supported metal oxide and other catalysts for ethane conversion: a review*, Catal. Today **1999**, *51*, 319.

[145] A. Khodakov, B. Olthof, A. T. Bell, and E. Iglesia, *Structure and catalytic properties of supported vanadium oxides: Support effects on oxidative dehydrogenation reactions*, J. Catal. **1999**, *181*, 205.

[146] M. V. Ganduglia-Pirovano, C. Popa, J. Sauer, H. Abbott, A. Uhl, M. Baron, D. Stacchiola, O. Bondarchuk, S. Shaikhutdinov, and H. J. Freund, *Role of Ceria in Oxidative Dehydrogenation on Supported Vanadia Catalysts*, J. Am. Chem. Soc. **2010**, *132*, 2345.

[147] J. Döbler, M. Pritzsche, and J. Sauer, *Oxidation of methanol to formaldehyde on supported vanadium oxide catalysts compared to gas phase molecules*, J. Am. Chem. Soc. **2005**, *127*, 10861.

[148] X. Rozanska, R. Fortrie, and J. Sauer, *Oxidative dehydrogenation of propane by monomeric vanadium oxide sites on silica support*, J. Phys. Chem. C **2007**, *111*, 6041.

[149] W. Daniell, A. Ponchel, S. Kuba, F. Anderle, T. Weingand, D. H. Gregory, and H. Knozinger, *Characterization and catalytic behavior of VO_x–CeO_2 catalysts for the oxidative dehydrogenation of propane*, Top. Catal. **2002**, *20*, 65.

[150] A. Trovarelli, *Catalysis by Ceria and Related Materials*, vol. 2, Imperial College Press: London, **2002**.

[151] M. Baron, H. Abbott, O. Bondarchuk, D. Stacchiola, A. Uhl, S. Shaikhutdinov, H. J. Freund, C. Popa, M. V. Ganduglia-Pirovano, and J. Sauer, *Resolving the Atomic Structure of Vanadia Monolayer Catalysts: Monomers, Trimers, and Oligomers on Ceria*, Angew. Chem. Int. Ed. **2009**, *48*, 8006.

[152] J. L. F. Da Silva, M. V. Ganduglia-Pirovano, and J. Sauer, *Formation of the cerium orthovanadate $CeVO_4$: DFT+U study*, Phys. Rev. B **2007**, *76*, 125117.

[153] M. Pykavy, C. van Wullen, and J. Sauer, *Electronic ground states of the $V_2O_4^{+/0/-}$ species from multireference correlation and density functional studies*, J. Chem. Phys. **2004**, *120*, 4207.

[154] R. F. Reidy and K. E. Swider, *Determination of the Cerium Oxidation-state in Cerium Vanadate*, J. Am. Ceram. Soc. **1995**, *78*, 1121.

[155] M. V. Ganduglia-Pirovano, A. Hofmann, and J. Sauer, *Oxygen vacancies in transition metal and rare earth oxides: Current state of understanding and remaining challenges*, Surf. Sci. Rep. **2007**, *62*, 219.

[156] B. M. Reddy, A. Khan, Y. Yamada, T. Kobayashi, S. Loridant, and J. C. Volta, *Structural Characterization of CeO_2–TiO_2 and V_2O_5/CeO_2–TiO_2 Catalysts by Raman and XPS Techniques*, J. Phys. Chem. B **2003**, *107*, 5162.

[157] M. V. Martinez-Huerta, J. M. Coronado, M. Fernandez-Garcia, A. Iglesias-Juez, G. Deo, J. L. G. Fierro, and M. A. Banares, *Nature of the vanadia-ceria interface in V^{5+}/CeO_2 catalysts and its relevance for the solid-state reaction toward $CeVO_4$ and catalytic properties*, J. Catal. **2004**, *225*, 240.

[158] V. Shapovalov and H. Metiu, *VO_x ($x = 1 - 4$) submonolayers supported on rutile $TiO_2(110)$ and $CeO_2(111)$ surfaces: The structure, the charge of the atoms, the XPS spectrum, and the equilibrium composition in the presence of oxygen*, J. Phys. Chem. C **2007**, *111*, 14179.

[159] M. Gielen, *Tin-based antitumour drugs*, Coord. Chem. Rev. **1996**, *151*, 41.

[160] C. N. R. Rao, S. Natarajan, and R. Vaidhyanathan, *Metal carboxylates with open architectures*, Angew. Chem. Int. Ed. **2004**, *43*, 1466.

[161] D. Grosjean, K. van Cauwenberghe, J. P. Schmid, P. E. Kelley, and J. N. Pitts, *Identification of C_3–C_{10} Aliphatic Dicarboxylic Acids in Airborne Particulate Matter*, Environ. Sci. Technol. **1978**, *12*, 313.

[162] X. B. Wang and L. S. Wang, *Photoelectron Spectroscopy of Multiply Charged Anions*, Annu. Rev. Phys. Chem. **2009**, *60*, 105.

[163] X. Yang, Y. J. Fu, X. B. Wang, P. Slavicek, M. Mucha, P. Jungwirth, and L. S. Wang, *Solvent-mediated folding of a doubly charged anion*, J. Am. Chem. Soc. **2004**, *126*, 876.

[164] X. B. Wang, J. Yang, and L. S. Wang, *Observation of entropic effect on conformation changes of complex systems under well-controlled temperature conditions*, J. Phys. Chem. A **2008**, *112*, 172.

[165] B. Minofar, M. Mucha, P. Jungwirth, X. Yang, Y. J. Fu, X. B. Wang, and L. S. Wang, *Bulk versus interfacial aqueous solvation of dicarboxylate dianions*, J. Am. Chem. Soc. **2004**, *126*, 11691.

[166] J. M. Weber, J. A. Kelley, S. B. Nielsen, P. Ayotte, and M. A. Johnson, *Isolating the spectroscopic signature of a hydration shell with the use of clusters: Superoxide tetrahydrate*, Science **2000**, *287*, 2461.

[167] M. F. Bush, R. J. Saykally, and E. R. Williams, *Evidence for water rings in the hexahydrated sulfate dianion from IR spectroscopy*, J. Am. Chem. Soc. **2007**, *129*, 2220.

[168] E. M. Myshakin, K. D. Jordan, E. L. Sibert, and M. A. Johnson, *Large anharmonic effects in the infrared spectra of the symmetrical $CH_3NO_2^-{\cdot}(H_2O)$ and $CH_3CO_2^-{\cdot}(H_2O)$ complexes*, J. Chem. Phys. **2003**, *119*, 10138.

[169] W. H. Robertson, E. A. Price, J. M. Weber, J. W. Shin, G. H. Weddle, and M. A. Johnson, *Infrared signatures of a water molecule attached to triatomic domains of molecular anions: Evolution of the H-bonding configuration with domain length*, J. Phys. Chem. A **2003**, *107*, 6527.

[170] M. Hesse, H. Meier, and B. Zeeh, *Spektroskopische Methoden in der organischen Chemie*, Georg Thieme Verlag: Stuttgart, Germany, **1987**.

[171] T. Shimanouchi, *Tables of Molecular Vibrational Frequencies, Consolidated*, vol. 1, National Bureau of Standards: Washington, DC, **1972**.

[172] B. M. Elliott, R. A. Relph, J. R. Roscioli, J. C. Bopp, G. H. Gardenier, T. L. Guasco, and M. A. Johnson, *Isolating the spectra of cluster ion isomers using Ar-"tag" -mediated IR-IR double resonance within the vibrational manifolds: Application to $NO_2^-{\cdot}H_2O$*, J. Chem. Phys. **2008**, *129*, 094303.

[173] S. E. Cabaniss, J. A. Leenheer, and I. F. McVey, *Aqueous infrared carboxylate absorbances: aliphatic di-acids*, Spectrochim. Acta, Part A **1998**, *54*, 449.

[174] J. Oomens, A. G. G. M. Tielens, B. G. Sartakov, G. von Helden, and G. Meijer, *Laboratory infrared spectroscopy of cationic polycyclic aromatic hydrocarbon molecules*, Astrophys. J. **2003**, *591*, 968.

[175] M. Demireva, J. T. O'Brien, and E. R. Williams, *Water-Induced Folding of 1,7-Diammoniumheptane*, J. Am. Chem. Soc. **2012**, *134*, 11216.

[176] M. Z. Kamrath, R. A. Relph, T. L. Guasco, C. M. Leavitt, and M. A. Johnson, *Vibrational predissociation spectroscopy of the H_2-tagged mono- and dicarboxylate anions of dodecanedioic acid*, Int. J. Mass Spectrom. **2011**, *300*, 91.

[177] S. Feyel, D. Schröder, and H. Schwarz, *Gas-phase oxidation of isomeric butenes and small alkanes by vanadium-oxide and -hydroxide cluster cations*, J. Phys. Chem. A **2006**, *110*, 2647.

[178] D. J. Goebbert, T. Wende, L. Jiang, G. Meijer, A. Sanov, and K. R. Asmis, *IR Spectroscopic Characterization of the Thermally Induced Isomerization in Carbon Disulfide Dimer Anions*, J. Phys. Chem. Lett. **2010**, *1*, 2465.

[179] G. von Helden, M. T. Hsu, P. R. Kemper, and M. T. Bowers, *Structures of Carbon Cluster Ions from 3 to 60 atoms: Linears to Rings to Fullerenes*, J. Chem. Phys. **1991**, *95*, 3835.

[180] T. L. Guasco, B. M. Elliott, M. A. Johnson, J. Ding, and K. D. Jordan, *Isolating the Spectral Signatures of Individual Sites in Water Networks Using Vibrational Double-Resonance Spectroscopy of Cluster Isotopomers*, J. Phys. Chem. Lett. **2010**, *1*, 2396.

[181] C. M. Leavitt, A. B. Wolk, J. A. Fournier, M. Z. Kamrath, E. Garand, M. J. Van Stipdonk, and M. A. Johnson, *Isomer-Specific IR–IR Double Resonance Spectroscopy of D_2-Tagged Protonated Dipeptides Prepared in a Cryogenic Ion Trap*, J. Phys. Chem. Lett. **2012**, *3*, 1099.

[182] K. R. Leopold, *Hydrated Acid Clusters*, Annu. Rev. Phys. Chem. **2011**, *62*, 327.

[183] V. Vaida, *Perspective: Water cluster mediated atmospheric chemistry*, J. Chem. Phys. **2011**, *135*, 020901.

[184] A. Gutberlet, G. Schwaab, O. Birer, M. Masia, A. Kaczmarek, H. Forbert, M. Havenith, and D. Marx, *Aggregation-Induced Dissociation of $HCl(H_2O)_4$ Below 1 K: The Smallest Droplet of Acid*, Science **2009**, *324*, 1545.

[185] S. D. Flynn, D. Skvortsov, A. M. Morrison, T. Liang, M. Y. Choi, G. E. Douberly, and A. F. Vilesov, *Infrared Spectra of HCl-H_2O Clusters in Helium Nanodroplets*, J. Phys. Chem. Lett. **2010**, *1*, 2233.

[186] http://www.ispoptics.com.

Danksagung

In der Schulzeit habe ich meinen Weg zur Physik erst über einen Umweg gefunden. Bei der Wahl des ersten Pflichtfaches entschied ich mich zunächst für Biologie. In der ersten Stunde erhielten wir damals die Aufgabe Zusammenspiele zwischen Bäume, Pflanzen und Tiere *pantomimisch* darzustellen. Ich gebe an dieser Stelle gerne zu, dass ich meine Schwierigkeiten hatte, diese Aufgabe überzeugend umzusetzen. Im anschließenden Schuljahr wechselte ich daher in den Physikunterricht, um vielmehr die Vorgänge der unbelebten Natur verstehen zu lernen. Meine damalige Lehrerin, Frau Hoffmann, füllte dieses Fach mit Leben und weckte somit die Neugier auf mehr. Sie hat mich insbesondere ermutigt, dieser Neugierde auch nach der Schulzeit nachzugehen. Dies war sicher ein erster entscheidender Impuls ein Physikstudium aufzunehmen, welches nun sogar in diese Doktorarbeit mündete. Zum Gelingen dieser Arbeit haben viele Personen maßgeblich beigetragen, bei denen ich mich im Folgenden herzlich bedanken möchte.

Bei meinem ersten Besuch des Fritz-Haber-Instituts hat mich die Vielzahl an spannenden Experimenten sehr beeindruckt. Ebenso bemerkenswert war die angenehme Atmosphäre innerhalb der Abteilung Molekülphysik sowie die Begeisterung, mit der die verschiedenen Projekte vorgestellt wurden. Ich bin Prof. Gerard Meijer sehr dankbar für die Möglichkeit, dass ich meine Doktorarbeit in dieser tollen Arbeitsumgebung durchführen konnte sowie für sein Interesse, mit dem er die Entwicklung meiner Projekte verfolgt hat. Prof. Ludger Wöste möchte ich für die Übernahme des Zweitgutachtens danken.

Mein besonderer Dank gilt meinem Gruppenleiter Knut Asmis für die Betreuung meiner Arbeit. Er hat sich in allen Phasen meiner Arbeit immer Zeit für mich genommen. Unsere Zusammenarbeit an den vielen interessanten Projekten hat mir große Freude bereitet und ich konnte fortlaufend viel Nützliches über die Experimente von ihm lernen. Ich möchte mich bei allen ehemaligen und aktuellen Mitgliedern unserer Arbeitsgruppe für die tolle Zusammenarbeit und gegenseitige Unterstützung bedanken: Daniel Goebbert, Risshu Bergmann, Ling Jiang, Nadja Heine, Claudia Brieger, Matias Fagiani, Tim Esser. Unsere vielen gemeinsamen Messphasen am Freien Elektronenlaser FELIX waren für mich besonders reizvoll und spannend. Es war immer ein Abenteuer die gesamte Laborausrüstung, von der Vakuumapparatur bis zur kleinsten Ersatzschraube, in Berlin zu verladen und im Keller des FOM Instituts Rijnhuizen wieder aufzubauen. Hier waren Tetris-Kenntnisse absolut von Vorteil und das Space Shuttle haben wir jedes mal erfolgreich starten lassen. Der Enthusiasmus und die Euphorie, die ich in unserem Team während den verschiedenen Messzeiten erlebt habe, waren für mich eine wundervolle Erfahrung. Ich werde viele schöne Momente stets in Erinnerung behalten. Mein Dank gilt auch André Merli und Philipp Müller, die den LKW samt Labor stets sicher von A nach B manövriert haben.

Ich bin äußerst dankbar für die großartige technische Unterstützung am Institut. Die Erfahrungen und handwerklichen Geschicke vieler Kollegen sind unverzichtbar für die Entwicklung

Lebenslauf

Der Lebenslauf ist in der Online-Version aus Gründen des Datenschutzes nicht enthalten.

For reasons of data protection, the curriculum vitae is not included in the online version.

List of Publications

1. T. Wende, L. Jiang, N. Heine, T. I. Yacovitch, G. Meijer, K. R. Asmis, and D. M. Neumark, *Gas Phase Infrared Spectroscopy on Microhydrated Sodium Sulfate Dimer Dianions*, in preparation **2012**.

2. N. Dietl, T. Wende, K. Chen, L. Jiang, Y.-D. Wu, M. Schlangen, G. Meijer, X. Zhang, K. R. Asmis, and H. Schwarz, *Structure and Chemistry of the Small Mixed-Oxo-Cluster $[VPO_4]^{\bullet+}$ as a model system for the Oxidation of Small Hydrocarbons*, in preparation **2012**.

3. M. Wanko, M. M. Saralegui, T. Wende, A. Rubio, L. Jiang, G. Meijer, and K. R. Asmis, *Infrared Spectroscopy on Microsolvated Carboxylate Dianions*, in preparation **2012**.

4. L. Jiang, N. Heine, J. Liu, T. I. Yacovitch, T. Wende, F. Mohamed, G. Meijer, D. M. Neumark, J. Sauer, and K. R. Asmis, *Infrared Spectroscopy of the Microhydrated Dihydrogen Phosphate Anion Clusters $H_2PO_4^-$ $(H_2O)_{0-12}$*, in preparation **2012**.

5. T. I. Yacovitch, N. Heine, C. Brieger, T. Wende, C. Hock, D. M. Neumark, and K. R. Asmis, *Communication: Vibrational spectroscopy of atmospherically relevant acid cluster anions: Bisulfate versus nitrate core structures*, J. Chem. Phys. **2012**, *136*, 241102–(1–4).

6. K. R. Asmis, T. Wende, M. Brümmer, O. Gause, G. Santambrogio, E. C. Stanca-Kaposta, J. Döbler, A. Niedziela, and J. Sauer, *Structural variability in transition metal oxide clusters: gas phase vibrational spectroscopy of $V_3O_{6-8}^+$*, Phys. Chem. Chem. Phys. **2012**, *14*, 9377–9388.

7. L. Jiang, T. Wende, P. Claes, S. Bhattacharyya, M. Sierka, G. Meijer, P. Lievens, J. Sauer, and K. R. Asmis, *Electron Distribution in Partially Reduced Mixed Metal Oxide Systems: Infrared Spectroscopy of $Ce_mV_nO_o^+$ Clusters*, J. Phys. Chem. A **2011**, *115*, 11187–11192.

8. T. I. Yacovitch, T. Wende, L. Jiang, N. Heine, G. Meijer, D. M. Neumark, and K. R. Asmis, *Infrared Spectroscopy of Hydrated Bisulfate Anion Clusters: $HSO_4^- \cdot (H_2O)_{1-16}$*, J. Phys. Chem. Lett. **2011**, *2*, 2135–2140.

9. M. Savoca, T. Wende, L. Jiang, J. Langer, G. Meijer, O. Dopfer, and K. R. Asmis, *Infrared Spectra and Structures of Silver-PAH Cation Complexes*, J. Phys. Chem. Lett. **2011**, *2*, 2052–2056.

10. T. Wende, M. Wanko, L. Jiang, G. Meijer, K. R. Asmis, and A. Rubio, *Spectroscopic Characterization of Solvent-Mediated Folding in Dicarboxylate Dianions*, Angew. Chem. Int. Ed. **2011**, *50*, 3807–3810.

11. A. M. Burow, T. Wende, M. Sierka, R. Włodarczyk, J. Sauer, P. Claes, L. Jiang, G. Meijer, P. Lievens, and K. R. Asmis, *Structures and vibrational spectroscopy of partially reduced gas-phase cerium oxide clusters*, Phys. Chem. Chem. Phys. **2011**, *13*, 19393–19400.

12. L. Lin, P. Claes, T. Höltzl, E. Janssens, T. Wende, R. Bergmann, G. Santambrogio, G. Meijer, K. R. Asmis, M. T. Nguyen, and P. Lievens, *The structure of Au_6Y^+ in the gas phase*, Phys. Chem. Chem. Phys. **2010**, *12*, 13907–13913.

13. T. Wende, J. Döbler, L. Jiang, P. Claes, E. Janssens, P. Lievens, G. Meijer, K. R. Asmis, and J. Sauer, *Infrared spectroscopic characterization of the oxidative dehydrogenation of propane by $V_4O_{10}{}^+$*, Int. J. Mass Spectrom. **2010**, *297*, 102–106.

14. D. J. Goebbert, T. Wende, L. Jiang, G. Meijer, A. Sanov, and K. R. Asmis, *IR Spectroscopic Characterization of the Thermally Induced Isomerization in Carbon Disulfide Dimer Anions*, J. Phys. Chem. Lett. **2010**, *1*, 2465–2469.

15. L. Jiang, T. Wende, R. Bergmann, G. Meijer, and K. R. Asmis, *Gas-Phase Vibrational Spectroscopy of Microhydrated Magnesium Nitrate Ions $[MgNO_3 \cdot (H_2O)_{1-4}]^+$*, J. Am. Chem. Soc. **2010**, *132*, 7398–7404.

16. E. Garand, T. Wende, D. J. Goebbert, R. Bergmann, G. Meijer, D. M. Neumark, and K. R. Asmis, *Infrared Spectroscopy of Hydrated Bicarbonate Anion Clusters: $HCO_3{}^- \cdot (H_2O)_{1-10}$*, J. Am. Chem. Soc. **2010**, *132*, 849–856.

17. D. J. Goebbert, E. Garand, T. Wende, R. Bergmann, G. Meijer, K. R. Asmis, and D. M. Neumark, *Infrared Spectroscopy of Microhydrated Nitrate Ions $NO_3{}^- \cdot (H_2O)_{1-6}$*, J. Phys. Chem. A **2009**, *113*, 7584–7592.

18. D. J. Goebbert, T. Wende, R. Bergmann, G. Meijer, and K. R. Asmis, *Messenger-Tagging Electrosprayed Ions: Vibrational Spectroscopy of Suberate Dianions*, J. Phys. Chem. A **2009**, *113*, 5874–5880.

Eidesstattliche Erklärung

(gemäß §7, Ziffer (4) der Promotionsordnung vom 05.02.2010 des Fachbereichs Physik an der Freien Universität Berlin)

Die Disseration habe ich selbstständig angefertigt. Alle Hilfsmittel und Hilfen habe ich angegeben, insbesondere habe ich die wörtlich oder dem Sinne nach anderen Veröffentlichungen entnommenen Stellen kenntlich gemacht.

Die Dissertation hat bisher weder in der gegenwärtigen noch in einer anderen Fassung weder dem Fachbereich Physik der Freien Universität Berlin noch einer anderen Fakultät oder Universität vorgelegen.

_____
Ort, Datum

_____
Unterschrift